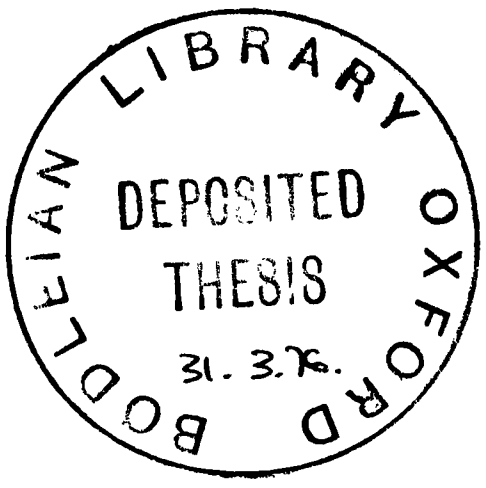
SOME APPLICATIONS OF THE THEORY OF ELECTRON DIFFRACTION CONTRAST

- by -

D.K. Saldin, B.A.

Thesis submitted for a degree of Doctor of Philosophy in the University of Oxford



St.Catherine's College

October 1975

"They have heard the Music of the Spheres, yet they know that Science is made for Man and not Man for Science."

- J.M. Ziman on Some Eminent Physicists

ABSTRACT

The theory of the diffraction of electrons from crystals originated in the classical paper of Bethe (1928) very shortly after the enunciation of the principles of quantum mechanics. The use of the electron microscope as a practical tool for studying crystal structures (and their defects) led to the development of the theory in forms suitable for the explanation of contrast effects on micrographs. The fundamental problem is the calculation of the electron wave-function emerging from the exit force of the crystal.

Broadly speaking, the two types of electron diffraction theory are the quantum mechanical and the wave optical. Chapter 1, which begins with a review of the development of diffraction theories since the early years of this century, is mainly concerned with the quantum mechanical approach. The elegant formulation of Yoshioka (1957) in which the phenomenon of absorption is shown to be capable of explanation by the use of a complex potential is outlined, and the usefulness of the dispersion surface construction is demonstrated. The conditions under which the Bloch wave and the Darwin (1914) formulations are equivalent are discussed, as is the validity of various approximations normally used in the theory as applied to deformed crystals.

The wave-optical approach is discussed in Chapter 2 with particular reference to Sturkey's (1962) theory. It is shown that the discrepancy

noted by Fukuhara (1966) between the results of Sturkey's and Bethe's theories may be explained by the fact that Sturkey's theory is concerned with positron diffraction. Numerical calculations are given to support this explanation and a corrected form of Sturkey's theory is given.

The theory of the weak-beam technique (Cockayne, Ray and Whelan 1969) is discussed in Chapter 3. It is shown that under such conditions the dynamical theory expressed in the Darwin formalism asymptotically approaches the form of a kinematical theory modified to take account of the effects of absorption. Under such conditions it is shown that only two Bloch waves contribute appreciably to the image contrast of defects and that as a result, a theory based on the kinematical scattering of Bloch waves gives results identical with those of kinematic theory applied to diffracted wave amplitudes. For particular experimental situations, such as contrast from extended dislocation nodes in silicon, numerical calculations, which confirm excellent agreement between the results of dynamical theory and kinematical theory are described.

Applications of the kinematical Bloch wave scattering theory to the predictions of the main features of contrast from small defects, such as dislocation loops, are reviewed in Chapter 4. The computer program used for calculating the image contrast from defects is described in Chapter 5. Also given is a critical discussion of numerical methods of solving a set of coupled ordinary differential equations, such as the Howie-Whelan equations (1961), for complicated strain-fields.

A method of generating computer simulated electron microscope images is discussed with careful attention to the simulation of the photographic processes involved.

Chapter 6 begins with a review of linear elasticity theory and its application to the theory of dislocations. It is shown how integration around a suitably chosen Burgers' circuit yields the formulae derived by Yoffe (1960) for the displacement field, and how these formulae may be used to compute the displacement field due to a regular polygonal dislocation loop of an arbitrary number of sides. This field is expressed in terms of its components in the directions of the cube axesof the crystal in a form convenient for its use in a dynamical theory computer program.

An introduction to the theory of point defects and their mechanisms of clustering during annealing and after particle irradiation is given in Chapter 7. The reasons for the observation of dislocation loops and stacking-fault tetrahedron are discussed. The electron microscope contrast features of such defects as well as others, such as voids and spherical inclusions, under both kinematical and dynamical imaging conditions are considered. The various methods used so far for the evaluation of the displacement fields due to dislocation loops and previous computer simulation work on the images due to such defects are reviewed. Finally a description of the present investigations of image contrast carried out using the polygonal loop model of Chapter 6 is described. The computer simulated images and their corresponding experimental images are displayed, and the effects of varying parameters such as the loop size, depth in the foil, operating Bragg reflection etc. are studied. Such computer simulation work is shown to be helpful in the identification not only of Frank loops, which are common in f.c.c. metals, but also of perfect loops (with shear components of Burgers vector) which are common in b.c.c. metals.

Chapter 8 begins with a consideration of the various mechanisms of formation of a stacking-fault tetrahedron in an f.c.c metal and contains a discussion of the nature of the displacement field around it, including the nature of its stacking-faults. A method of constructing its displacement field from four triangular edge loops on $\{111\}$ planes is described. The constituent triangular loops may be constructed by the methods outlined in Chapter 6. Finally the results of computations of the image contrast due to stacking-fault tetrahedra are shown and discussed. It is shown, for instance, that interstitial and vacancy-type tetrahedra may be distinguished by essentially the same methods as those used for dislocation loops.

The main conclusions of this thesis and remaining problems are discussed in Chapter 9.

PREFACE

This dissertation describes research carried out independently by the author, under the supervision of Dr.M.J.Whelan, in the Department of Metallurgy and Science of Materials, University of Oxford, since October 1971. It is not substantially the same as one submitted at this or any other university. The thesis is original although due reference to the work of others has been made where appropriate. Such references have been listed alphabetically at the end of this thesis. Some parts of this dissertation have been already published as follows:

J.Phys. C. (1973) 6, L215

J.Microsc.(1973) 98, 116

Proceedings of the 8th International Congress on Electron Microscopy,Canberra (1974) p.458.

Collected Abstracts of the 10th International Congress on Crystallography, Amsterdam (1975), S265.

Proceedings of the meeting of the Electron Microscopy and Analysis Group of the Institute of Physics (EMAG 75), Bristol (1975, in press).

The author would like to express his gratitude to the following for their contributions:

Professor Sir Peter Hirsch, F.R.S. for the provision of laboratory facilities and for many useful discussions.

Dr.M.J.Whelan for much help and guidance and a careful reading of the manuscript.

Professor L.Fox for permission to use the University Computing facilities.

The Director of the Atlas Computer Laboratory, Chilton, Didcot, Oxfordshire for the use of the Stromberg-Carlson 4020 plotting device.

Many thanks are also due to the following:

Dr.D.J.H. Cockayne for much advice and encouragement and for conveying a feeling for the excitement of research.

Dr.Adrienne Hart-Davis for assistance with the computer simulation programme.

Mr.A.Stathopoulos, Dr.C.A.English and Dr.A.G.Cullis for providing the experimental micrographs appearing in this thesis.

Mr.A.MacKnight for his photographic work.

Mrs.Toni Tattersall for her excellent typing of the thesis.

Dr.M.L.Jenkins, Dr.J.C.H.Spence, Dr.E.Johnson, Dr.Elizabeth Hewat, Mr.S.M.Holmes, Mr.P.Rez and others, too numerous to mention, for many stimulating discussions.

Dr.R.S.Nelson of the Atomic Energy Research Establishment, Harwell for providing financial support for this work.

Finally the author is grateful to his parents for making it all possible.

D.K.Saldin.

St.Catherine's College,
Oxford.
October 1975

TABLE OF CONTENTS

CHAPTER 1: AN INTRODUCTION TO THE DYNAMICAL THEORY OF ELECTRON DIFFRACTION CONTRAST - THE QUANTUM MECHANICAL APPROACH

1.1 Introduction

1.2.1 Theories for perfect non-absorbing crystals

1.2.2 The phenomenon of absorption

1.3 Early experimental support

1.4 Applications of the theory to defect scattering

1.5 Types of electron diffraction theories

1.6.1 Quantum Mechanical treatment

1.6.2 Lattice periodicity conditions

1.6.3 Need for a complex potential

1.6.4 The high-energy approximation

1.6.5 The eigenvalue equation

1.7.1 Propogation of wave in the crystal

1.7.2 The shape transform

1.7.3 Boundary condition at exit surface

1.8.1 The column approximation

1.8.2 Deformed crystals

1.8.3 Differential equations for Darwin wave amplitude

1.8.4 Differential equations for Bloch wave amplitudes

1.9 Exact treatment (without column approximation).

CHAPTER 2: WAVE OPTICAL DYNAMICAL THEORY AND A MODIFICATION TO STURKEY'S THEORY

2.1 Scattering from an isolated atom

2.1.1 Born Approximation

2.1.2 Relation between scattering factor and Fourier transform of potential

2.2 Valicity of First Born Approximation for crystals

2.3 Development of a Wave-Optical theory

2.3.1 Fresnel Zone Calculation

2.3.2 Origin Shift Term
2.4 Sturkey's Theory
2.4.1 Dynamic equilibrium equation
2.4.2 Errors in Sturkey's equilibrium equation
2.4.3 Correction to Sturkey's theory
2.4.4 Solution for perfect crystal
2.4.5 Evaluation of Reflection coefficients
2.5 Consequences of Sturkey's error
2.5.1 Application of Sturkey's original and corrected methods
2.5.2 Matrix diagonalization calculations
2.5.3 Explanation of discrepancy in terms of Bloch waves

CHAPTER 3: IMAGE CONTRAST UNDER "WEAK-BEAM" CONDITIONS
3.1 Historical Introduction
3.2 Interpretation of Weak-Beam Images
3.3 Kinematical Limit of Dynamical Theory
3.3.1 The Darwin picture
3.3.2 The Bloch wave picture
3.4 Kinematical Bloch Wave scattering
3.4.1 The effect of absorption
3.5 The criterion of Cockayne et al. for image peak positions
3.6 Comparison of image peak positions on various theories
3.7 Weak-Beam contrast from extended nodes in silicon (comparison kinematical and dynamical theory image profiles)

CHAPTER 4: THEORY OF CONTRAST FROM SMALL DEFECT CLUSTERS
4.1 Introduction
4.2 Bloch Wave scattering at lattice defects
4.2.1 First Born Approximation applied to Bloch Wave scattering
4.3 The two-beam case
4.3.1 Black-White images of small defects
4.2.2 Absorption

4.3.3 General Expressions for Amplitudes with large absorption
4.3.4 Defects near the electron entry surface
4.3.5 Defects near the electron exit surface
4.4 Contrast from some special defects
4.4.1 Edge-on Frank Loop
4.4.2 Edge-on pure shear loop
4.4.3 Flat-on pure shear loop
4.5 Summary

CHAPTER 5 COMPUTER SIMULATION OF ELECTRON MICROSCOPE IMAGES
5.1 Introduction
5.2 The dynamical theory computer program
5.2.1 The MASTER Segment
5.2.2 The PRINC subroutine
5.2.3 Subroutine DSLV
5.2.4 Subroutine DRIV
5.2.5 Subroutine DISP
5.3 Methods for numerically solving coupled ordinary differential equations
5.3.1 Runge-Kutta methods
5.3.2 Kutta-Merson process
5.3.3 Gill's process
5.3.4 Comparison of Kutta-Merson and Gill's processes
5.4 Interpolation Scheme
5.5 Relationship between photographic density and electron intensity
5.5.1 In the electron microscope
5.5.2 In the enlarger
5.5.3 On the final (positive) point
5.6 The SC4020 Plotter
5.7 Adjustment of Contrast Levels

CHAPTER 6: DISPLACEMENT FIELDS FOR POLYGONAL LOOPS DISLOCATION LOOPS

6.1 Introduction

6.2 Brief Review of Elasticity Theory

6.2.1 Stresses and Strains

6.2.2 Linear Elasticity

6.3 Green's Function of Elasticity

6.4 Applications of the Green's Function method for curved dislocations

6.5 Isotropic case

6.6 The Angular Dislocation

6.6.1 Burgers vector in the x-direction

6.6.2 " " " y "

6.6.3 " " " z "

6.6.4 Angular Dislocation with general Burgers' vector

6.7 Displacement field due to a polygonal loop

6.7.1 Position and Orientation of the loop in the foil

6.7.2 Coordinate systems for individual angular dislocations

6.7.3 Displacement field due to each angular dislocation

6.7.4 Burgers vector components for each angular dislocation

6.7.5 Displacement field due to whole loop

6.7.6 Insertion of correct stacking-fault

6.7.7 Components of displacements in crystallographic directions

6.8 Summary

CHAPTER 7 COMPUTER SIMULATED IMAGES OF POLYGONAL LOOPS DISLOCATION LOOPS

7.1 Introduction

7.2 The most likely form of vacancy clusters

7.3 Irradiation by high-energy particles

7.4 Dissociation of loops

7.5 Images from small defect clusters

7.5.1 "Kinematic" Images

7.5.2 "Dynamic" Images

7.5.3 Qualitative features of contrast

(i) Voids

(ii) Spherical Inclusions

(iii) Dislocation loops

7.5.4 Depth dependence of $\vec{g} \cdot \vec{l}$
7.5 Dispalcement field due to a dislocation loop-(review)
(a) Isotropic Media
7.6.1 The infinitesimal loop
7.6.2 Finite Circular Edge Loop
7.6.3 Finite circular shear loop
(b) 7.6.4 Anisotropic Media
7.7 Computer Simulation of Images (Review)
7.8 Computer Simulation of Dark-Field Images (Present Work)
7.8.1 Hexagonal Frank loops in Cooper
(a) Edge-on loops
(b) Inclined loops
7.8.2 Loops in B.C.C. metals

CHAPTER 8: IMAGE CONTRAST FROM STACKING FAULT TETRAHEDRA
8.1 Introduction
8.2 The Nature of the stacking faults.
8.3 The displacement field
8.3.1 Position of tetrahedron in foil
8.3.2 Coordinate axes for each triangular face
8.3.3 Insertion of correct fault vectors
8.4 Alternative method for construction of the displacement field
8.5 Computer simulated images
8.5.1 Vacancy-type tetrahedra
(a) ⟨110⟩ orientation
(b) ⟨100⟩ orientation
8.5.2 Comparison between Frank loops and Tetrahedra at ⟨100⟩ orientation
8.5.3 Depth Dependence
8.5.4 The interstitial-type tetrahedron
8.5.5 Differentiation between interstitial and vacancy tetrahedron.

CHAPTER 9: PRESENT CONCLUSION AND REMAINING PROBLEMS

Appendix 1: Derivation of the integral equation of scattering

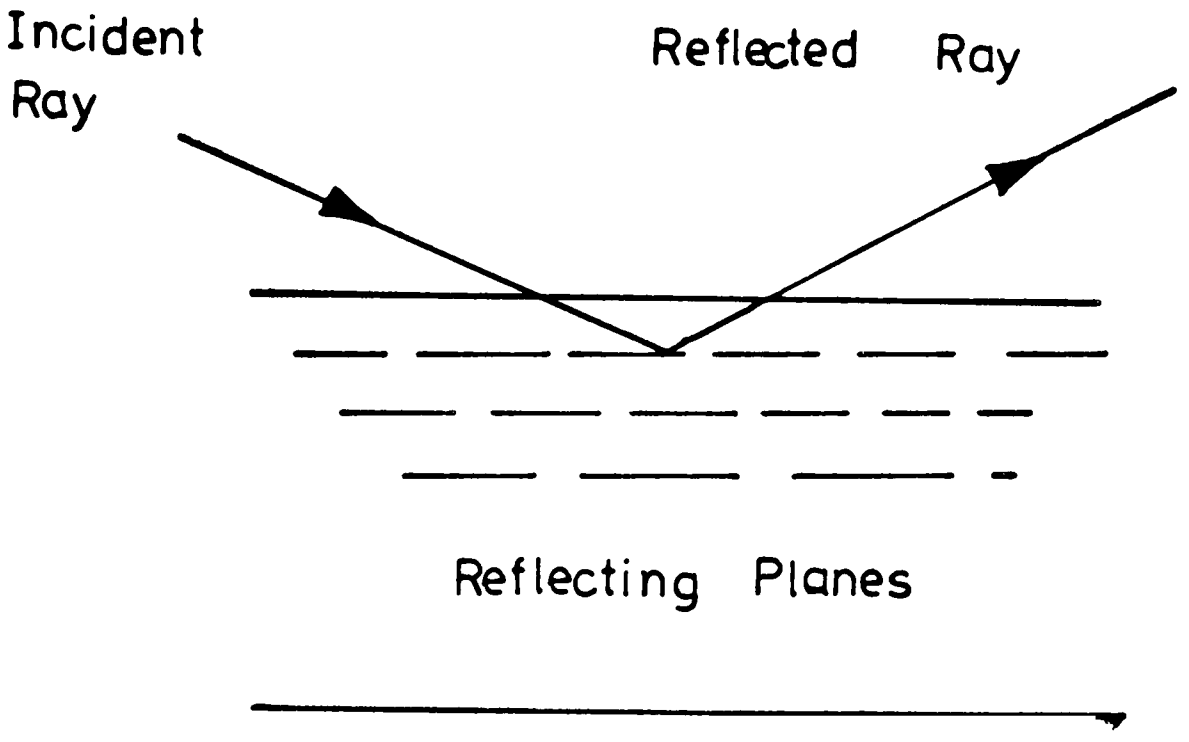
Appendix II: Solid Angle subtended by an angular dislocation

Appendix III: The matrix of the eigenvectors C for different types of fundamental matrix $\underline{A}$

References

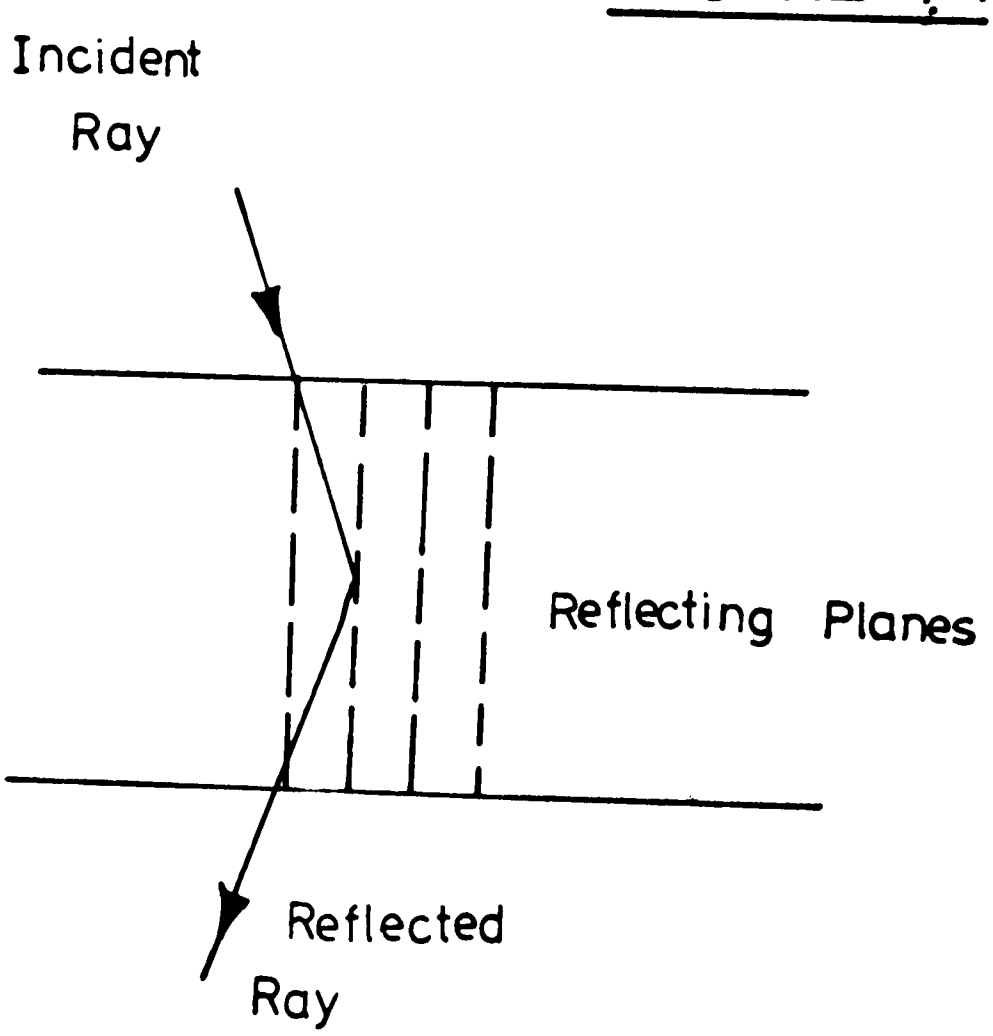
Chapter 1

AN INTRODUCTION TO THE DYNAMICAL THEORY OF ELECTRON DIFFRACTION CONTRAST - THE QUANTUM MECHANICAL APPROACH



(a) BRAGG CASE

FIGURE 1.1



(b) LAUE CASE

1.1 Introduction

The rapid proliferation in the use of the electron microscope for the study of crystalline materials, ranging from lattice defects in metals and semi-conductors, and lattice images from metallic oxides, to the structure of proteins and viruses in molecular biology, has been the main stimulant to the development of an adequate theory of electron diffraction contrast. Although arising in part from its parent subject, the theory of X-ray diffraction, it incorporates many interesting and novel features.

Historical Review

1.2.1 Theories for perfect non-absorbing crystals

The earliest dynamical theories of diffraction were developed by Darwin (1914, a,b, 1922) and Ewald (1916, 1917). These theories describe the propogation of X-rays through crystals. Darwin used the view of diffraction held by the Braggs, namely that atomic planes behave essentially as mirrors for the X-rays. His theory thus employs terms like the "transmission coefficient" and "reflection coefficient". He considered mainly the Bragg case (illustrated in Fig.1.1(a)). In this case waves are incident at a glancing angle to the crystal surface and the propogation of the waves in the direction perpendicular to the surface is attenuated (even in the absence of absorption). The theory was able to predict the phenomenon of "primary extinction" (nowadays simply called extinction). The term "secondary extinction" used by Darwin described diminution of the incident beam due to the presence of a mosaic structure in the material, such that at any orientation of the crystal, some of the mosiacs would be

at the Bragg reflecting position and thus diffract strongly.

The physical basis of Ewald's theory is (at least superficially) quite different. He was concerned with the problem of determining the normal modes of electrical vibration of the crystal, which he considered to be a collection of resonators. He was thus able to construct the now familiar "dispersion surfaces" which determine the allowed wave-vectors of the crystal waves of a given energy. The problem of a X-ray beam incident on the crystal from a vacuum was dealt with by an appropriate wave-matching method at the surface. Ewald studied mainly the Laue case (see Fig.1.1(b)) which considers almost normal incidence of the vacuum wave. In this case crystal waves travelling normal to the surface are not attenuated (except by the phenomenon of absorption).

A similar theory for electrons had, of course, to wait until the enunciation of the principles of wave mechanics for particles which was provided by Schrodinger (1926). Bethe (1928) developed a wave mechanical theory for electron diffraction, which he applied mainly to the Bragg case. MacGillavry (1940) extended Bethe's work to cover the Laue case.

1.2.2 The Phenomenon of Absorption

The attenuation of an elastically scattered wave in a crystal, due to the loss of electrons which are scattered in directions appreciably different from those predicted by Bragg's Law is known as "absorption". It is particularly important in electron microscopy where frequently small apertures are placed around particular Bragg spots in the diffraction plane. Similar considerations apply to electron microscopy of amorphous materials, except of course that Bragg's Law is inapplicable. Molière (1939) described absorption by means of a phenomenological theory.

In 1941 the "Borrmann effect" of X-ray diffraction was discovered. This was the observation (Borrmann 1941, 1950) that the apparent absorption of a beam of X-rays traversing a crystal at the Bragg angle is greatly reduced. A similar effect was shown to exist for electrons by Honjo (1953) and Honjo and Mihama (1954) who noticed an intensity difference between the spots of a doublet in the electron diffraction pattern from a wedge crystal. This is now known as "anomalous"absorption, and was described by von Laue (1946) on Molière's theory. Yoshioka (1957) was able to put Molière's phenomenological theory on a proper quantum mechanical basis for electron diffraction by considering the effect of inelastically scattered electrons on the attenuation of the elastically scattered waves.

1.3 Early Experimental Support

During the early years of the development of the electron microscope, decisive experimental support for these theories came from Hillier and Baker (1942) who observed thickness (extinction) fringes in $Al_2O_3.H_2O$, Heidenreich and Sturkey (1945) and Heidenreich (1949) who observed both thickness and bend contours in such materials as MgO, CdO, aluminium and aluminium-copper alloys. The last two papers explain these effects on the basis of dynamical theory. Similar work was also reported by Boersch (1942, 1943, 1944). Another dynamical effect which was experimentally observed was the presence of kinematically forbidden reflections in diffraction patterns from crystalline specimens.

1.4 Application of the theory to defect scattering

Whelan and Hirsch (1957) applied the dynamical theory to a stacking-fault and introduced the concept of the column approximation. Hirsch, Howie and Whelan (1960) applied a kinematical theory to dislocations using the column approximation. Hashimoto, Howie and Whelan (1962) treated absorbtion for perfect crystals and faults. Finally Howie and Whelan (1961, 1962) developed the dynamical theory for absorbing, imperfect crystals, using the column approximation. They showed the equivalence of Darwin's method applied to the Laue case and Bethe's eigenvalue approach.

1.5 Types of electron diffraction theories

Since the early 1950's a host of different dynamical theories of electron diffraction have been proposed. An admirable review of these theories is contained in the paper by Goodman and Moodie (1974) who also demonstrate their essential equivalence. Most of these formulations are reported in the Proceedings of the International Conference on Magnetism and Crystallography, Kyoto (1961).

The two main categories of electron diffraction contrast theories are; the wave-optical and the quantum mechanical approaches. Into the former type fall the theories of Darwin, Ewald, Cowley and Moodie (1957) and Sturkey (1962). The theories of Bethe (1928) Fujiwara (1959), Fujimoto (1959) and Tournarie (1962) fall into the latter category. The work of Howie and Whelan (1961) incorporated both types of approach.

In this chapter the more formal quantum mechanical approach is dealt with, while in the next chapter, the more physically visualizable

wave optical methods are considered (with particular reference to Sturkey's method). The multi-slice method of Cowley and Moodie is not considered in this thesis.

The quantum mechanical approach has the advantage of naturally being able to predict the electron microscope phenomenon of "absorption". It can be shown that depends on the effect of inelastically scattered electrons on the elastically scattered wave field.

We therefore pursue the method due to Yoshioka (1957) which is a generalization of Bethe's (1928) approach, which only dealt with elastically scattered electrons.

Quantum Mechanical Treatment

The Schrodinger equation which describes the interaction of an incident electron with a crystal is,

$$\left(-\frac{\hbar^2}{2m}\nabla^2 + H_c + H'\right)\Phi = E\Phi \qquad (1.1)$$

where H_c and H' are the quantum mechanical operators for the energy of the crystal, and that for the interaction energy of the incident electron with the crystal respectively, m is the mass of the incident electron, and E is the total energy.

Now if the perturbation H' is small compared to $\left(-\frac{\hbar^2}{2m}\nabla^2 + H_c\right)$, it is possible to a first order, to make the expansion

$$\Phi(\underline{r}, \underline{r}_1, \underline{r}_2, \ldots, \underline{r}_N) = \varphi_n(\underline{r})\, a_n(\underline{r}_1, \underline{r}_2, \ldots, \underline{r}_j, \ldots \underline{r}_N) \qquad (1.2)$$

where $\underline{r}$ is the coordinate of the incident electron and $\underline{r}_j$ that of the j^{th}.

crystal electron. Here a_n is the wave-function of the n th excited state of the crystal and φ_n the inelastically scattered wave that raises the crystal to that state. φ_o represents the elastically scattered electron and a_o the initial state of the crystal. a_n satisfies the eigenvalue equation

$$H_c\, a_n = E_n\, a_n \qquad (1.3)$$

Substituting (1.2) into (1.1), multiplying by a_n and integrating over the $\underline{r}_j$'s gives with the aid of (1.3)

$$\nabla^2\varphi_o + \left(\chi_o^2 - \frac{2m}{\hbar^2} H'_{oo}\right)\varphi_o = \frac{2m}{\hbar^2}\sum_{m\neq o} H'_{om}\,\varphi_m \qquad (1.4)$$

$$\nabla^2\varphi_n + \left(\chi_n^2 - \frac{2m}{\hbar^2} H'_{nn}\right)\varphi_n = \frac{2m}{\hbar^2}\sum_{m\neq n} H'_{nm}\,\varphi_m \qquad (1.5)$$

where $\chi_n^2 = \frac{2m}{\hbar^2}(E - E_n)$

and $H'_{nm} = \int a_n^*\, H' a_m\, d\tau$, where $d\tau = d\underline{r}_1\, d\underline{r}_2 \ldots d\underline{r}_N$

Terms in $H'_{nm}\varphi_m\ (m\neq o)$ in (1.5) give only second order corrections to Bethe's theory since φ_n is small compared to φ_o and $|2m\, H'_{nm}/\hbar^2| \ll \chi_n^2$, and are neglected. The Equation (1.5) becomes

$$\nabla^2\varphi_n + \chi_n^2\,\varphi_n = \frac{2m}{\hbar^2} H'_{no}\,\varphi_o \qquad (n \geq 1)$$

The solution in terms of the Green's function is

$$\varphi_n(\underline{r}) = -\frac{m}{2\pi\hbar^2}\int \frac{\exp\left(i\chi_n|\underline{r}-\underline{r}'|\right)}{|\underline{r}-\underline{r}'|} H'_{no}(r')\,\varphi_o(r')\,d\underline{r}' \qquad (1.6)$$

Substitution of (1.4) into (1.6) gives

$$\nabla^2 \phi_o + \left(\chi_o^2 - \frac{2m}{\hbar^2} H_{oo}'(\underline{r})\right) \phi_o + \frac{2m}{\hbar^2} \int B(\underline{r}, \underline{r}') \phi_o(\underline{r}') \, d\underline{r}' = 0 \qquad (1.7)$$

where $B(\underline{r}, \underline{r}') = \frac{m}{2\pi\hbar^2} \sum_{n \neq o} H_{on}'(\underline{r}) H_{no}'(\underline{r}) \frac{\exp(i\chi_n |\underline{r} - \underline{r}'|)}{|\underline{r} - \underline{r}'|}$

1.6.2 Lattice periodicity conditions

$B(\underline{r}, \underline{r}')$ satisfies the condition

$B(\underline{r}, \underline{r}') = B(\underline{r} + \underline{a}, \underline{r}' + \underline{a})$ where a is the unit cell vector of the lattice. Now $H_{oo}'(\underline{r})$ represents the periodic crystal potential and the integral over the infinite domain in (1.7) can be restricted to over the crystal volume due to the short range of $B(\underline{r}, \underline{r}')$ Then since $\phi_o(\underline{r} + \underline{a})$ is a solution of (1.7) as well as $\phi_o(\underline{r})$ we can write

$$\phi_o(\underline{r}) = \sum_g C_g \exp(2\pi i \, \underline{k}_g \cdot \underline{r}) \qquad (1.8)$$

where $\underline{k}_g = \underline{k} + \underline{g}$ (where $\underline{g}$ is a reciprocal lattice vector) by Bloch's Theorem. These are the so-called "Bloch-waves" of the system, and we shall hope to be able to determine the allowed wave-vectors $\underline{k}_o$ (and hence $\underline{k}_g$) of the fast incident electrons travelling in the crystal. We similarly hope to determine the Bloch-wave excitation coefficients C_g corresponding to each permissible wave-vector of the electrons.

For a perfect crystal we can expand the crystal potential $H_{oo}'(\underline{r})$ in a Fourier series,

$$H_{oo}'(\underline{r}) = \sum_g V_g \exp(2\pi i \, \underline{g} \cdot \underline{r}) \qquad (1.9)$$

1.6.3 Need for a complex potential

Substituting (1.8) and (1.9) into (1.7), multiplying by $\exp(-2\pi i\, \underline{k}_g . \underline{r})$ and integrating over the whole volume V of the crystal, we have,

$$-\frac{\hbar^2}{2m}\left(k_g^2 - \chi_o^2\right)C_g - \sum_h V_{g-h}\, C_h - \sum_h W_{gh}\, C_h = 0$$

where $$W_{gh} = \frac{1}{V}\int_V\int_V B(\underline{r},\underline{r}')\exp\left(2\pi i\left[\underline{k}_g . \underline{r} + \underline{k}_h . \underline{r}'\right]\right)d\underline{r}\,d\underline{r}' \qquad (1.10)$$

By expressing the Green's function in (1.6) namely

$$\frac{1}{4\pi}\,\frac{\exp\left[2\pi i\left(\chi_n|\underline{r}-\underline{r}'|\right)\right]}{|\underline{r}-\underline{r}'|}$$

in the integral form, $\frac{1}{(2\pi)^3}\int\frac{\exp\left[2\pi i\, \underline{K}'.(\underline{r}-\underline{r}')\right]}{(K'^2-\chi_n^2)}\,dK'$,

Yoshioka was able to show that

$$W_{hg} = W_{hg}^r + i\, W_{hg}^i$$

The real part was obtained by integrating a function over a real axis and the imaginary part from the principal part due to a singularity on this axis. He also showed that W_{hg}^r and W_{hg}^i are real and that,

$$\left.\begin{aligned} W_{hg}^r &= (W_{hg}^r)^* \\ W_{hg}^i &= -(W_{hg}^i)^* \end{aligned}\right\} \text{ and } \quad \begin{aligned} W_{hg}^r &= W_{gh}^r \\ W_{hg}^i &= W_{gh}^i \end{aligned}$$

Putting $$\tilde{U}_{g-h} = \frac{2m}{\hbar^2}\left(V_{g-h} + W_{gh}^r\right)$$

And $$U'_{gh} = \frac{2m}{\hbar^2}\, W_{gh}^i$$

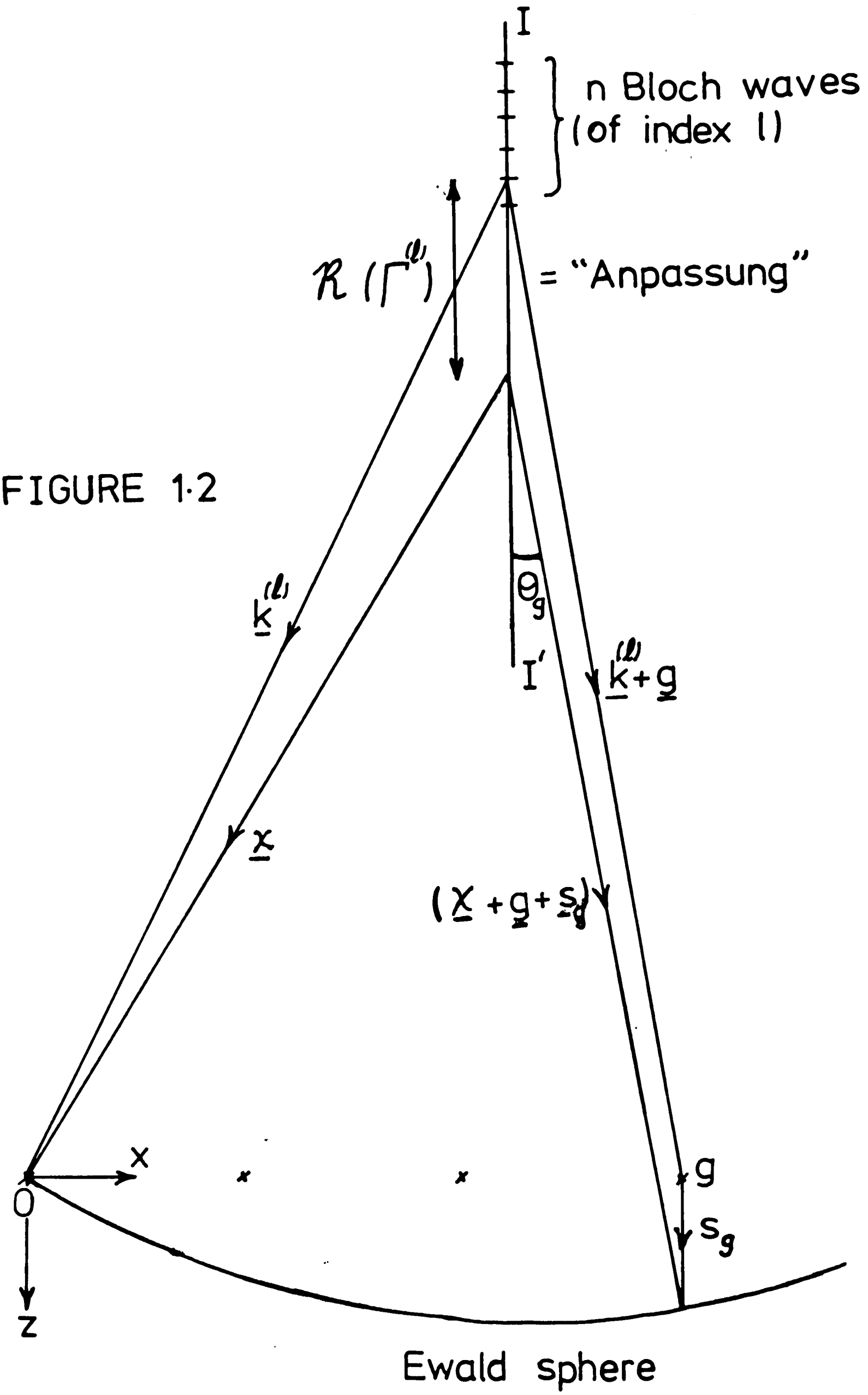

I
n Bloch waves
(of index l)
$\mathcal{R}(\Gamma^{(l)})$
= "Anpassung"
$\underline{k}^{(l)}$
θ_g
I'
$\underline{k}^{(l)}+\underline{g}$
$\underline{\chi}$
$(\underline{\chi}+\underline{g}+\underline{s}_g)$
x
O
z
g
s_g
Ewald sphere

FIGURE 1·2

equation (1.10) becomes

$$(\chi_o^2 - k_g^2)\, C_g - \sum_h \tilde{U}_{g-h}\, C_h - i \sum_h U'_{g-h}\, C_h = 0$$

where the summations are over all the reciprocal lattice points considered. χ_o is the wave-vector of the incident electron in vacuo. This shows that we may obtain the effect of the inelastic scattering on the elastically scattered wave by considering the motion of Bloch waves in a complex potential. We have thus,

$$(\chi^2 - [\underline{k} + \underline{g}]^2)\, C_g - \sum_h \tilde{U}_{g-h}\, C_h - i \sum_h U'_{g-h}\, C_h = 0 \qquad (1.11)$$

1.6.4 The high-energy approximation

Now in the Laue case $\underline{k}$ has a large component perpendicular to $\underline{g}$ and a small one parallel to $\underline{g}$, $\underline{k}_z$ and $\underline{k}_x$ respectively, say.

Then
$$\begin{aligned}(\chi^2 - [\underline{k}^2 + \underline{g}^2]) &= \chi^2 - (\chi + [\Gamma - s_g]\cos\theta_g)^2 \\ &\simeq 2\chi (s_g - \Gamma)\cos\theta_g\end{aligned}$$

where $\Gamma = k_z - \chi_z$

(see the dispersion surface construction) (Fig. 1.2)

We can therefore re-write (1.11) in the form:

$$s_g C_g + \sum_h \frac{\tilde{U}_{g-h}}{2\chi} C_h + \sum_h \frac{U'_{g-h}}{2\chi} C_h = \Gamma C_g \qquad (1.12)$$

1.6.5 The Eigenvalue equation

Now if we consider n reciprocal lattice vectors g in the series (1.8) and (1.9) there are clearly n equations of the type (1.12), one for each g. Equation (1.12) can be written in matrix form,

$$(\underline{\underline{U}} + [S_g]_D)\{C_g\} = \Gamma\{C_g\} \qquad (1.13)$$

In this notation a matrix $\underline{\underline{M}}$ is constituted by elements M_{ik} where the horizontal and vertical columns are labelled by the subscripts i and k respectively. A diagonal matrix $\underline{\underline{D}}$ with elements a_k is denoted by $[a_k]_D$

with $D_{ik} = \delta_{ik} a_k$ (δ_{ik} is the Kronecker symbol

The Einstein notation is not used here so the R.H.S. is not summed over K). A vertical column vector is written $\{v_g\}$ or $\{w^l\}$ where g or l is the running index of the vector components.

In equation (1.13) the matrix $\underline{\underline{U}}$ can be written as $\underline{\underline{\tilde{U}}} + i\,\underline{\underline{U}}'$ where $\underline{\underline{\tilde{U}}}$ and $\underline{\underline{U}}'$ are themselves Hermitian matrices defined by

$$\tilde{U}_{g,h} = U_{g-h}/2\chi$$

$$U'_{g,h} = U'_{g-h}/2\chi$$

Now equation (1.13) is in the form of a matrix eigenvalue equation and has n eigenvalues $\Gamma^{(l)}$ Let the corresponding eigenvectors be $\{C_g^l\}$. The real parts of the $\Gamma^{(l)}$ are what Bethe calls the "anpassung". As can be seen from the dispersion surface construction, they measure the differences between the z-components of the crystal wave vectors and that of the vacuum wave-vector. The imaginary parts of $\Gamma^{(l)}$ give rise to attentuation of each Bloch wave by a different amount.

1.7.1 Propagation of waves in the crystal

We see therefore that the electron wave-vector in the crystal can be regarded as lying on n discrete branches in reciprocal space, and gives rise to the so-called dispersion surface (Fig.1.2).If x is the coordinate parallel to the foil surface,then in general the crystal wave ($\underline{k} + \underline{g}$) and the emergent vacuum wave $(\underline{\chi} + \underline{g} + \underline{s}_j)$ have, identical x-components, due to the wave matching boundary condition at the surface. Thus the ends of these vectors all lie on lines parallel to the z-direction.

The wave-function in the crystal can be written.

$$\Psi = \sum_l \psi^{(l)} b^{(l)} (\Gamma^{(l)}, z)$$

$\psi^{(l)}$ being the amplitude of the Bloch-wave solution

$$b^{(l)} (\underline{k}, z) = \sum_g C_g^l \exp \left(2\pi i \left[(\underline{\chi} + \underline{g}) . \underline{r} + \Gamma^{(l)} z \right]\right) \qquad (1.14).$$

The $b^{(l)}(\underline{k},z)$ are the exact solutions of Schrodinger's equation and Ψ is a linear sum of them where the coefficients $\psi^{(l)}$ are to be determined by the boundary conditions at the electron incident surface. If only waves travelling in one particular direction are incident, then we can write the incident wave as

$\Psi_{inc} = \phi_0(0) \exp(2\pi i \underline{\chi} . \underline{r})$ where the origin is taken in the first layer. On emerging from the foil, the total wavefunction can be written as the sum of plane waves in the directions $(\underline{\chi} + \underline{g} + \underline{s}_j)$. The vector $\underline{g}$ clearly arises from the need to satisfy the Bragg condition. The vector $\underline{s}_j$ is necessary in order to make $|\underline{\chi} + \underline{g} + s_j| = |\underline{\chi}|$. This is clearly the condition to make the emergent electron wave-vectors lie on the

Ewald Sphere. It is found that appreciable amplitude exists in emergent waves for which S_g is a small vector not equal to zero. This is due to the so-called shape transform effect that arises since the crystal is not infinite in spatial extent.

1.7.2 The shape transform

In the derivation of the dynamical scattering equations by wave-optical arguments (see Chapter 2), kinematical scattering conditions are considered to hold in each scattering layer (which lie perpendicular to the incident electron beam). Now each of these layers is thin in the direction of propogation of the incident beam, but are considered to be of effectively infinite extent in directions lying in their planes. The distribution of intensity in reciprocal space from a parallelpiped crystal is given, on kinematical theory, (see Hirsch et al, 1965, p.97) by

$$\phi_g = \frac{F_g}{V_g} \frac{\sin(\pi A u)}{\pi u} \cdot \frac{\sin(\pi B v)}{\pi v} \frac{\sin(\pi C w)}{\pi w}$$

where F_g is the structure factor for the reflection g, V_c is the volume of a unit cell, A, B and C are the linear dimensions of the crystal in the x, y and z directions respectively and u, v and w are coordinates in reciprocal space with origin at the reciprocal lattice point g, and measured in the x, y and z directions respectively.

Figure 1.3 shows the intensity distribution in the x-direction. It is clear that since B and C are very large, the intensity distribution in the y and z directions around any diffraction spot in reciprocal space would be very narrow. Thus each reciprocal lattice point can be regarded as smeared out in thez-direction when considering scattering at each layer. In other words, the Ewald

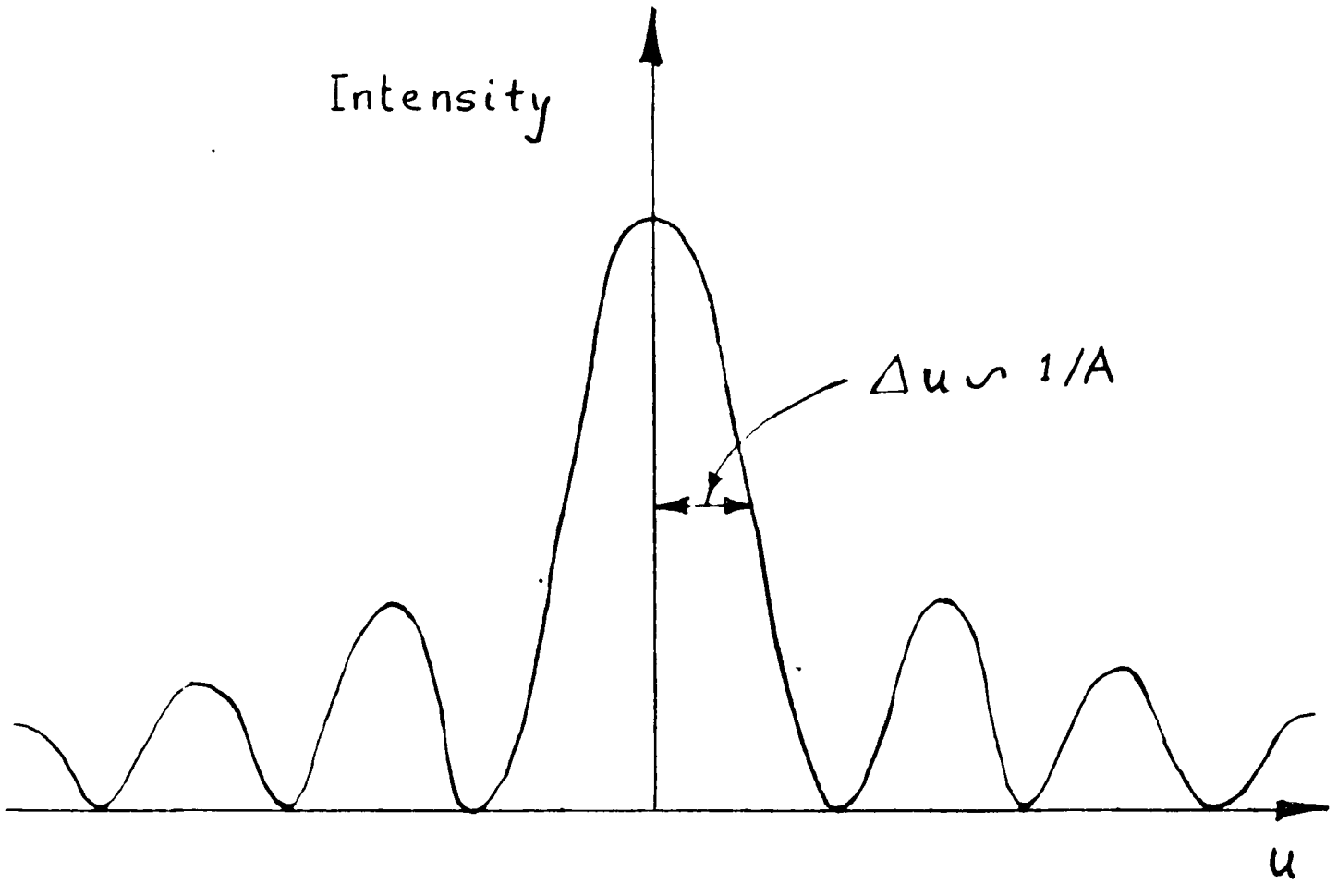


FIGURE 1.3

sphere does not have to pass through the centre of a reciprocal lattice spot to excite the corresponding reflection, since Bragg's Law is only strictly valid for crystals infinite in all directions, and since for finite crystals perfect destructive interference does not occur for all directions not exactly satisfying the Bragg Law.

1.7.3 Boundary conditions at Exit Surfaces

We may write the wavefunction for electrons emerging from the crystal of thickness t as

$$\psi = \sum_g \phi_g(t) \exp\left[2\pi i \left(\underline{\chi} + \underline{g} + \underline{s}_g\right).\underline{r}\right] \qquad (1.15)$$

As a boundary condition at the emergent surface, we may equate this to the wave-function in the crystal at the emergent surface, given by equation (1.14) and obtain

$$\Phi_g(t) = \sum_\ell \psi^\ell C_g^\ell \exp\left[2\pi i \Gamma^{(\ell)} t\right] \exp\left[-2\pi i s_g t\right] \quad (1.16a)$$

(since s_g is a vector in the z-direction, from the argument above we can write this as

$$\{\Phi_g(t_1)\} = \left[\exp(-2\pi i s_g t_1)\right]_D \cdot \underline{\underline{C}} \cdot \left[\exp\left(2\pi i \Gamma^{(\ell)} t_1\right)\right]_D \{\psi^{(\ell)}\} \quad (1.16)$$

for a thickness t_1. Also for a thickness t_2,

$$\{\Phi_g(t_2)\} = \left[\exp(-2\pi i s_g t_2)\right]_D \cdot \underline{\underline{C}} \left[\exp\left(2\pi i \Gamma^{(\ell)} t_2\right)\right]_D \{\psi^{(\ell)}\}$$

By combining these two expressions, we obtain

$$\{\Phi_g(t_2)\} = \left[\exp(-2\pi i s_g t_2)\right]_D \cdot \underline{\underline{C}} \left[\exp\left(2\pi i \Gamma^{(\ell)}\{t_2 - t_1\}\right)\right] \times \cdot$$
$$\cdot \times \underline{\underline{C}}^{-1} \left[\exp(2\pi i s_g t_1)\right]_D \{\Phi_g(t_1)\}$$

The matrix that related $\{\Phi_g(t_1)\}$ and $\{\Phi_g(t_2)\}$ is called the scattering matrix and can be written

$$P(t_2, t_1) = \left[\exp(-2\pi i s_g t_2)\right]_D \cdot \underline{\underline{C}} \cdot \left[\exp\left(2\pi i \Gamma^{(\ell)}\{t_2 - t_1\}\right)\right] \times \cdot\cdot$$
$$\cdots \times \underline{\underline{C}}^{-1} \left[\exp(2\pi i s_g t_1)\right]_D \quad (1.17)$$

1.8.1 The Column Approximation

It is seen that in the above treatment, only the dependence of Φ_g with z is considered. This is justified for a perfect crystal since the crystal is laterally uniform and the quantities Φ_g are in

fact independent of the other coordinates x and y. When however a crystal contains lattice defects, such as dislocations, lateral uniformity is destroyed and the solution of Schrodinger's equation must be dependent on x and y. The equations relating the quantities $\psi_g(\underline{r})$ will then be partial differential equations and not amenable to easy treatment. The column approximation consists of dividing the crystal up into very thin columns such that the lateral variation of all variables across them can be ignored. The partial differential equations then become ordinary differential equations with Z as the independent variable.

1.8.2 Deformed Crystals

In defected crystals the deformable ion approximation is invoked. This states that when the displacement of an atom at a point r is R(r), the potential in the imperfect crystal is the same as that in the perfect crystal at the point $[\underline{r} - \underline{R}(\underline{r})]$. This is clearly only valid when the displacent $\underline{R}(\underline{r})$ is slowly varying. Then equation (1.9) has to be modified to

$$H_{oo}' = \frac{\hbar^2}{2me} \sum_g U_g \exp\{2\pi i\, \underline{g} . [\underline{r} - \underline{R}(\underline{r})]\}$$

In fact one can use the formalism of the preceding theory if one makes the identification

$$U_g(\underline{r}) \Rightarrow U_g \exp[-2\pi i\, \underline{h} . \underline{R}(\underline{r})] \qquad (1.18)$$

1.8.3 Differential equation for Darwin wave amplitudes in deformed crystal

From (1.18) it is easy to see that for a deformed crystal, the matrix U of equation (1.13) has to be replaced by (in the column

approximation)

$$\left[\exp\{-2\pi i\, u_h(z)\}\right]_D \underline{\underline{\zeta}} \left[\exp\{2\pi i\, u_g(z)\}\right]_D$$

where $u_g(z) = g \cdot \underline{R}(z)$

From the eigenvalue equation (1.13) we see that for a particular z, the eigenvectors are now

$$\left[\exp\{-2\pi i\, u_g(z)\}\right]_D \{c_g\}$$

Then the scattering matrix for an infinitesimal slab of thickness $\delta z = z_2 - z_1$ is

$$P(z_2, z_1) = \left[\exp\{-2\pi i [S_g z_2 + u_g(z_2)]\}\right]_D \cdot \underline{\underline{\zeta}} \cdot \left[\exp\{2\pi i \Gamma^{(l)} \delta z\}\right]_D \times \ldots$$

$$\ldots \times \underline{\underline{\zeta}}^{-1} \left[\exp\{2\pi i [S_g z_1 + u_g(z_1)]\}\right]_D$$

Now

$$\lim_{\delta z \to 0} \left(\left[\exp\{2\pi i \Gamma^{(l)} \delta z\}\right]_D \right)$$

$$= 2\pi i\, dz \left[\Gamma^{(l)}\right]_D + \underline{\underline{I}}$$

where $\underline{\underline{I}}$ is the unit matrix.

Then,

$$\Phi_g(z_2) = \left[\exp(-2\pi i S_g \delta z)\right]_D \Phi_g(z_1)$$

$$+ 2\pi i\, \delta z \left[\exp\{-2\pi i [S_g z_2 + u_g(z_2)]\}\right]_D \cdot \underline{\underline{\zeta}} \cdot \times \ldots$$

$$\ldots \times \left[\Delta k^{(l)}\right]_D \underline{\underline{\zeta}}^{-1} \left[\exp\{2\pi i [S_g z_1 + u_g(z_1)]\}\right]_D \Phi_g(z_1)$$

Also expanding $\left[\exp(-2\pi i S_g \delta z)\right]$ as

$$\underline{\underline{I}} - 2\pi i\, \delta z \left[S_g\right]_D$$

and since $\underline{\underline{\zeta}} \cdot \left[\Delta k^{(l)}\right]_D \underline{\underline{\zeta}}^{-1} = \underline{\underline{u}} + \left[S_g\right]_D$ from (1.13)

we have

$$\lim_{\delta z \to 0} \left[\frac{\{\phi_g(z_2)\} - \{\phi_g(z_1)\}}{\delta z} \right] = -2\pi i \, [S_g]_D \{\phi_g(z)\}$$

$$+ 2\pi i \left[\exp\{-2\pi i [s_g z + u_g(z)]\} \right]_D \underline{\underline{U}} \times \cdots$$

$$\cdots \times \left[\exp\{2\pi i [s_g z + u_g(z)]\} \right]_D \{\phi_g(z_1)\}$$

$$+ 2\pi i \, [S_g]_D \{\phi_g(z)\}$$

Thus,

$$\frac{d}{dz}\{\phi_g(z)\} = 2\pi i \left[\exp\{-2\pi i [s_g z + u_g(z)]\} \right]_D \underline{\underline{U}} \times \cdots$$

$$\cdots \times \left[\exp\{2\pi i [s_g z + u_g(z)]\} \right]_D \{\phi_g(z)\}$$

(1.19)

This is the standard equation relating the amplitudes in a plane wave leaving the crystal in the direction $(\underline{\chi} + \underline{g} + \underline{s}_g)$ to the amplitudes of the plane waves of different values of g. This equation is used in this thesis for all dynamical theory computations of $\{\phi_g(z)\}$ for continuously varying $u_g(z)$.

1.8.4 Differential equations for Bloch-Wave Amplitudes

In the case of a deformed crystal equation (1.16) relating the Darwin amplitudes to the Bloch wave amplitudes for each thickness t is,

$$\{\psi_g(t)\} = \left[\exp\left(-2\pi i\left[s_g t + u_g(t)\right]\right)\right]_D \subseteq \left[\exp\left(2\pi i \Gamma^{(l)} t\right)\right]_D \{\psi^{(l)}(t)\}$$

Substitution of this expression into (1.19) changing the variable t to z since we are now interested in the waves in the crystal, we obtain,

$$\frac{d}{dz}\{\psi^{(l)}\} = 2\pi i \left[\exp\left(-2\pi i \Gamma^{(l)} z\right)\right]_D \cdot \underline{\underline{C}}^{-1} \times \ldots$$

$$\ldots \times \left(\left[u_g, z\right]_D \cdot \underline{\underline{C}} + \left\langle\left(\underline{\underline{u}} + \left[s_g\right]_D\right)\underline{\underline{C}} - \underline{\underline{C}}\left[\Delta k^{(l)}\right]_D\right\rangle\right) \times \ldots$$

$$\ldots \times \left[\exp\left(2\pi i \Gamma^{(l)} z\right)\right]_D \cdot \{\psi^{(l)}\}.$$

But the expression within the brackets $\langle \ldots \rangle$ is in the form of one side of the eigenvalue equation. Therefore if the matrices $\underline{\underline{C}}$ and $\underline{\underline{D}}$ ($\Gamma^{(l)}$) used in the above equation are those obtained by solving the eigenvalue equation exactly, the above expression reduces to

$$\frac{d}{dz}\{\psi^{(l)}(z)\} = 2\pi i \left[\exp\left(-2\pi i \Gamma^{(l)} z\right)\right]_D \cdot \underline{\underline{C}}^{-1} \left[u_g, z\right]_D \times \ldots$$

$$\ldots \times \underline{\underline{C}} \cdot \left[\exp\left(2\pi i \Gamma^{(l)} z\right)\right]_D \{\psi^{(l)}(z)\} \qquad (1.21)$$

where $u_{g,z} = \frac{d}{dz}\left[g \cdot \underline{\underline{R}}(z)\right]$

This equation is very useful for the study of small defect clusters and will be considered again in chapter 4.

1.9 Exact Treatment (NOT using the Column approximation) of the Darwin amplitudes

If χ_o is the incident wave-vector in vacuo, we can write

$$\psi(\underline{r}) = \sum_g \phi_g(\underline{r}) \exp\left[2\pi i(\underline{\chi} + \underline{g} + \underline{s}_g).\underline{r}\right] \qquad (1.22)$$

and

$$V(\underline{r}) = \frac{\hbar^2}{2m} \sum_g U_g(\underline{r}) \exp(2\pi i\, \underline{g}.\underline{r})$$

Substituting into the Schrodinger equation,

$$-\frac{\hbar^2}{2m} \nabla^2 \psi(\underline{r}) + V(\underline{r})\psi(\underline{r}) = E\,\psi(\underline{r})$$

we obtain

$$\sum_g \exp(2\pi i\, \underline{g}.\underline{r})\left[\nabla^2 \phi_g(\underline{r}) + 4\pi i(\underline{\chi} + \underline{g} + \underline{s}_g)\nabla \phi_g(\underline{r})\right.$$
$$\left. + \sum_h 4\pi^2 U_{g-h}(\underline{r})\,\phi_h(\underline{r}) \exp\left[2\pi i(s_h - s_g)z\right] = 0\right.$$

Equating each coefficient of the exponential to zero

$$(\underline{\chi} + \underline{g} + \underline{s}_g)_z \frac{\partial \phi_g}{\partial z} = \pi i \sum_h U_{g-h}(\underline{r})\,\phi_h(\underline{r}) \exp\left[2\pi i(s_h - s_g)z\right]$$
$$-(\underline{\chi} + \underline{g})_x \frac{\partial \phi_g}{\partial x} - (\underline{\chi}_o + \underline{g})_y \frac{\partial \phi_g}{\partial y} + \frac{i}{4\pi}\nabla^2 \phi_g \qquad (1.23)$$

where $\phi_g(\underline{r})$ and $U_g(\underline{r})$ are slowly varying over a unit cell.

The column approximation consists of neglecting the last three terms on the R.H.S. This is usually valid since due to the smallness of the Bragg angle $\chi_z \gg \chi_x$ or χ_y

Equation (1.21) can be rewritten,

$$(\underline{\chi} + \underline{s}_g)_z \frac{\partial \phi_g}{\partial z} = \pi i \sum_h U_{g-h}\,\phi_h(\underline{r}) \exp\left[2\pi i\left\{(\underline{h} - \underline{g}).\underline{R}(\underline{r}) + \ldots\right.\right.$$
$$\left.\left. \ldots + (s_h - s_g)z\right\}\right] \qquad (1.24)$$

This equation still contains dependencies on z and y. One overcomes this problem by only considering the variation of the ϕ_g's down a narrow column, over which the ranges of x and y are small. Then $\phi_h(\underline{r})$ and $\underline{R}(\underline{r})$ can be re-written $\phi_h(z)$ and $R(z)$ and (1.24) becomes in the usual notation of the Howie-Whelan theory,

$$\frac{d}{dz}\phi_g(z) = \pi i \sum_h \frac{\phi_h(z)}{\xi_{g-h}} \exp\left\{2\pi i\left[(s_h - s_g)z + (\underline{h} - \underline{g}).\underline{R}(z)\right]\right\} \qquad (1.25)$$

where ξ_{g-h} are the so-called "two beam extinction distances". Equation (1.23) is clearly identical with (1.19).

It is rather interesting that in equation (1.22) we expand the wave function in terms of the vacuum wave-vectors, and then substitute this expression into Schrodinger's equation for a crystal. Of course just because we make an expansion in terms of such plane waves does not imply that this is the form in which the waves propogate in the crystal. On the contrary, we know from solid state theory that the crystal waves are best described as Bloch waves. However, in an electron microscope we only select those waves with wave-vectors that lie on the Ewald Sphere when they emerge from the crystal. Since we are then only interested in the amplitudes (and usually only the intensities) of these waves, we naturally expand the crystal wave function in the form of linear combinations of these "Darwin" waves.

Chapter 2

WAVE-OPTICAL DYNAMICAL THEORY AND A MODIFICATION TO STURKEY'S THEORY

2.1 Scattering from an isolated atom

The starting point in a wave-optical theory is the consideration of the manner of scattering of an electron by an atom.

The spatial part ψ of the wave-function of an electron travelling at a non-relativistic velocity satisfies the time-independent Schrodinger equation,

$$(\nabla^2 + 4\pi\chi^2)\,\psi(\underline{r}) = -4\pi^2\, u(\underline{r})\,\psi(\underline{r}) \qquad (2.1)$$

where $\chi = (2mE/h^2)^{\frac{1}{2}}$, E being the energy of the electron. $u(\underline{r}) = \frac{2m}{h^2} V(\underline{r})$ where $V(\underline{r})$ is the atomic potential.

The incident electron wave-function $\psi_o(\underline{r})$ satisfies the Schrodinger equation with the potential switched off,

i.e. $$(\nabla^2 + 4\pi\chi^2)\,\psi_o(\underline{r}) = 0 \qquad (2.2).$$

Thus $$\psi_o(\underline{r}) = A \exp(2\pi i\, \underline{\chi}.\underline{r}) \qquad (2.3)$$

where A is some constant. This is a plane wave whose direction of propagation is that of the wave-vector $\underline{\chi}$.

It can be shown (see Appendix I) that the wave-function after scattering can be expressed in terms of ψ_o in the integral equation of scattering,

$$\psi(\underline{r}) = \psi_o(\underline{r}) + 4\pi^2 \int u(\underline{r}')\,\psi(\underline{r}')\,G(\underline{r},\underline{r}')\,d^3\underline{r}' \qquad (2.4).$$

$G(\underline{r},\underline{r}')$ is known as the Green's function of the operator $(\nabla^2 + 4\pi^2\chi^2)$ and has the form $G(\underline{r},\underline{r}') = \dfrac{\exp(2\pi i \chi |\underline{r}-\underline{r}'|)}{4\pi|\underline{r}-\underline{r}'|}$

(2.5).

2.1.1 Born Approximation

Equation (2.4) immediately suggests an iterative method of solution. We can write,

$$\psi_1(\underline{r}) = \psi_0(\underline{r}) + 4\pi^2 \int u(\underline{r}')\,\psi_0(\underline{r}')\,G(\underline{r},\underline{r}')\,d^3\underline{r}' \qquad (2.6)$$

On the R.H.S. under the integral sign, we take $\psi_0(\underline{r}')$ as a first order estimate of the wave-function after scattering. We obtain thus a better approximation to $\psi(\underline{r})$, namely $\psi_1(\underline{r})$ This is known as the first Born Approximation to the wave-function after scattering.

By iteration we can find the N_{th} order Born Approximation to the final wave-function by the use of the general recurrence relation,

$$\psi_N(\underline{r}) = \psi_0(\underline{r}) + 4\pi^2 \int u(\underline{r}')\,\psi_{N-1}(\underline{r}')\,G(\underline{r},\underline{r}')\,d^3\underline{r}' \qquad (2.7)$$

2.1.2 Relation between scattering factor and Fourier transform of potential

In the first order Born Approximation we can write,

$$\psi_s(\underline{r}) = 4\pi^2 \int u(\underline{r}')\exp(2\pi i\,\underline{\chi}.\underline{r}')\frac{\exp(2\pi i\,\underline{\chi}.|\underline{r}-\underline{r}'|)}{4\pi|\underline{r}-\underline{r}'|}\,d^3\underline{r}'$$

where $\psi_s(\underline{r})$ is the scattered wave (i.e. $\psi(\underline{r}) - \psi_0(\underline{r})$)

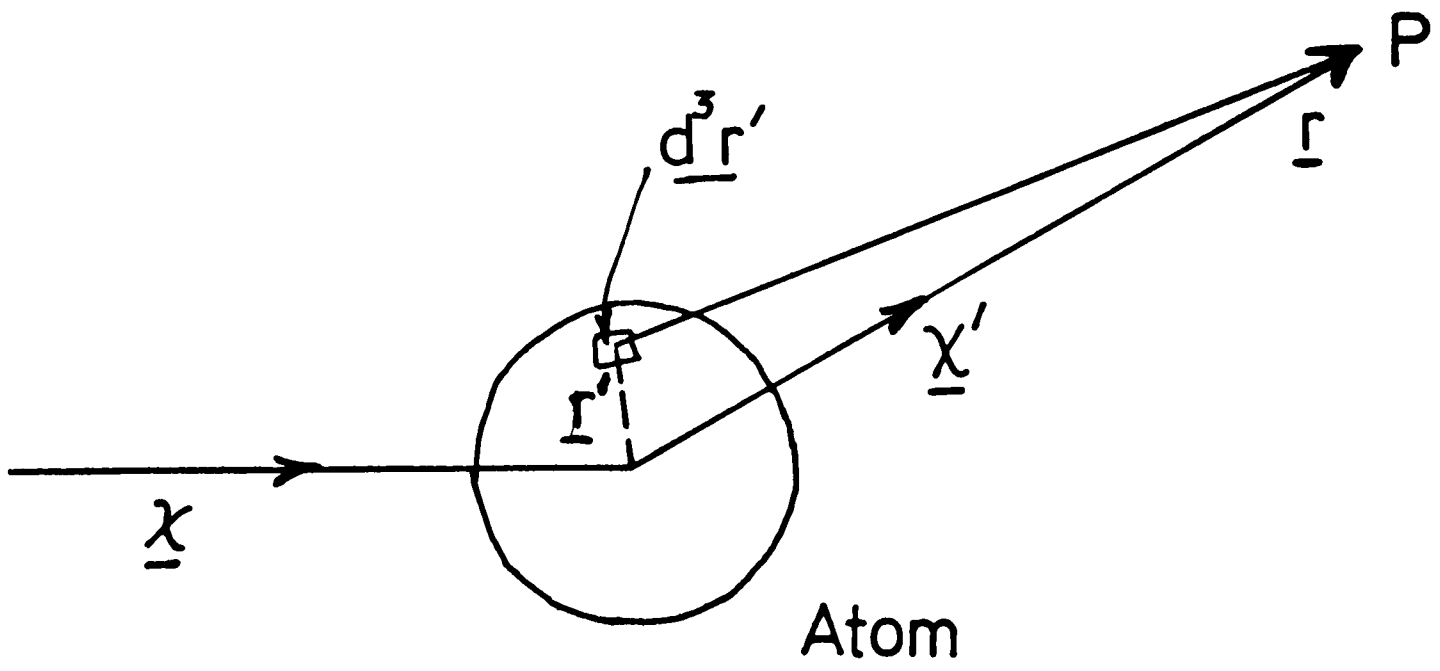

P
$d^3\underline{r}'$
$\underline{r}$
$\underline{\chi}'$
$\underline{r}'$
$\underline{\chi}$
Atom

FIGURE 2·1

Now $U(\underline{r}')$ is only appreciable for values of $|\underline{r}'| \ll |\underline{r}|$ in the case of a small scattering centre whose effect is observed at a point P appreciably distant from it. Then the integral above need only be performed for values of $|\underline{r}'| \ll |\underline{r}|$. As can be seen from Figure 2.1, we can then write,

$$\chi|\underline{r} - \underline{r}'| = \chi r - \underline{\chi}'.\underline{r}'$$

where $\underline{\chi}'$ is the wave-vector of the scattered ray. Thus we obtain, since we may also put $|\underline{r} - \underline{r}'| \rightarrow r$,

$$\psi_s(\underline{r}) = \frac{\pi \exp(2\pi i \chi r)}{r} \int U(\underline{r}') \exp[2\pi i (\underline{\chi} - \underline{\chi}').\underline{r}'] d^3\underline{r}'$$

Putting $\underline{\chi}' - \underline{\chi} = K = 2(\sin\theta)/\lambda$

$$\psi_s(\underline{r}) = \frac{2\pi m}{h^2} \frac{\exp(2\pi i \chi r)}{r} \int V(\underline{r}') \exp(-2\pi i \underline{K}.\underline{r}') d^3\underline{r}'$$

Now the electron scattering factor $f_e(\underline{K})$ is defined by the asymptotic relationship,

$$\psi_s(\underline{r}) = f_e(\underline{K}) \frac{\exp(2\pi i \chi r)}{r}.$$

Therefore,

$$f_e(\underline{K}) = \frac{2\pi m}{h^2} \int V(\underline{r}') \exp(-2\pi i \underline{K}.\underline{r}') d^3\underline{r}' \qquad (2.6).$$

Thus the electron scattering factor is proportional to the Fourier Transform of the atomic potential.

The validity of the Born Approximation for isolated scattering centres has been discussed by various authors (e.g. Mott and Massey, 1949). In general it is valid when $E \gg V(\underline{r}_i)$ and when the spatial extent of $V(\underline{r}_i)$ is small.

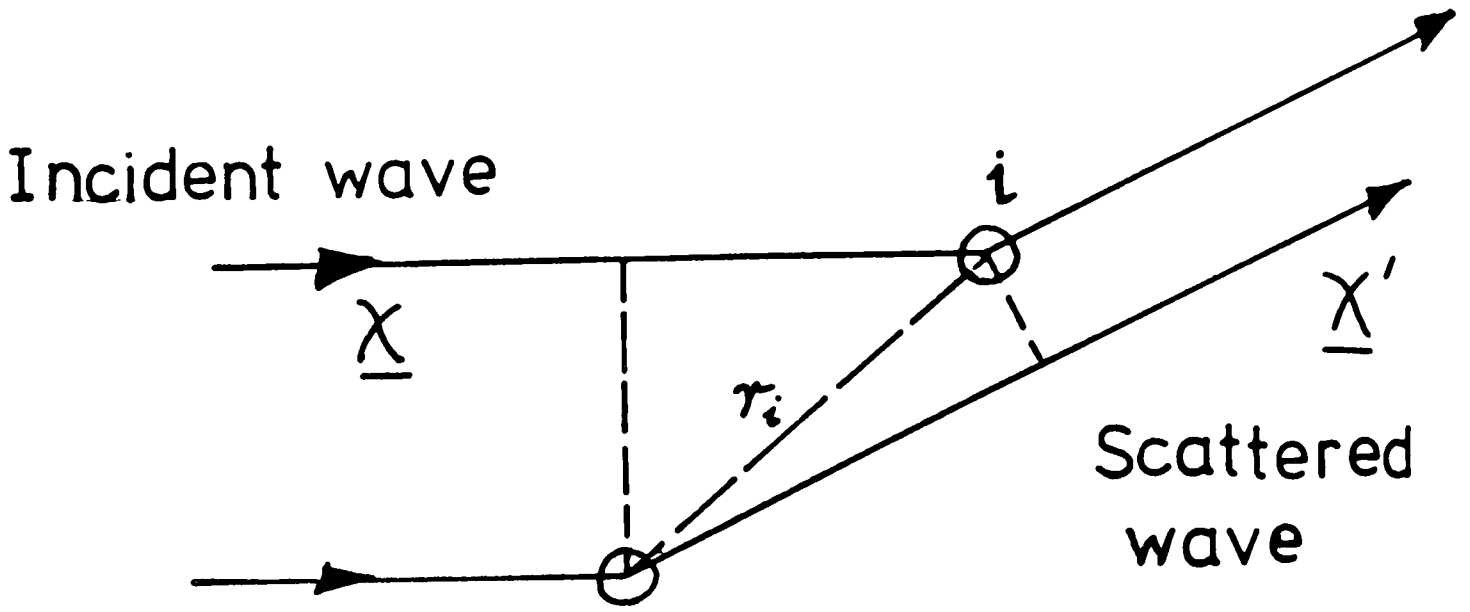


FIGURE 2·2

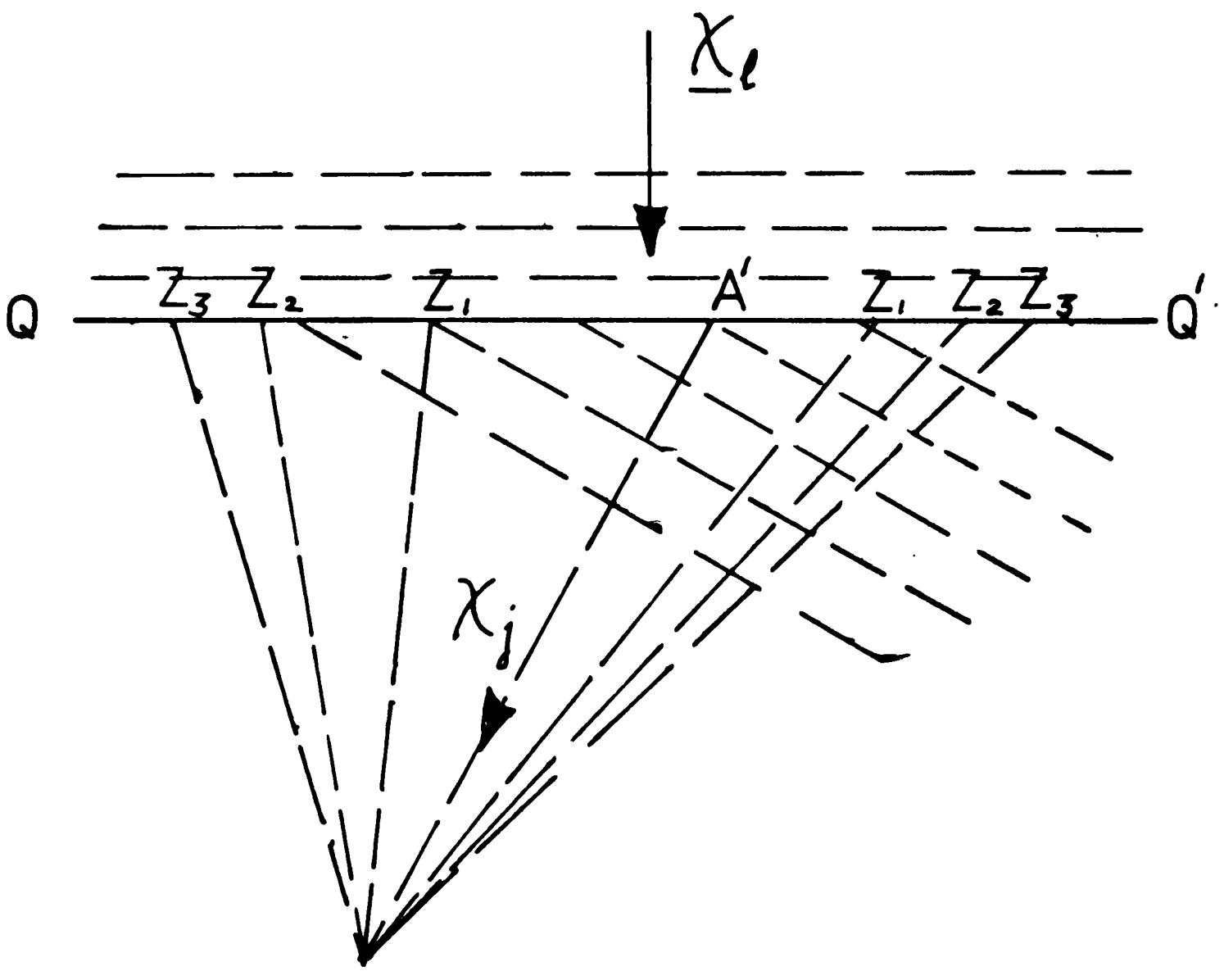


FIGURE 2·3

2.2 Validity of First Born Approximation for crystals

Fukuhara (1965) has shown that for elastic scattering, the value of $f_e(\underline{K})$ that enters into the equations of diffraction theory is that calculated according to equation (1.6). The reason is that in diffraction theory of periodic lattices, the quantities of interest are the Fourier Transforms of the lattice potential, namely expressions like $\int V(\underline{r}') \exp(2\pi i \underline{g} \underline{r}') d^3\underline{r}'$ where $\underline{g}$ is a reciprocal lattice vector. But these are the very expressions that enter into equations like (1.6). Now it is well known that higher order Born Approximations lead to expressions containing imaginary parts of $f_e(K)$. Fukuhara was able to show that the imaginary parts calculated in this way do not lead to attenuation of the waves calculated on the basis of electron diffraction theory.

2.3 Development of a Wave-Optical Theory

From figure 2.2 it is easy to see that the amplitude A_o scattered by a unit cell with atoms at positions τ_i is given by

$$A_o = \frac{\exp(2\pi i \chi r)}{r} \sum_{i\ (\text{unit cell})} f_e(\underline{K}) \exp(-2\pi i \underline{K}.\underline{\tau}_i)$$

where the summation is over all the atoms in the unit cell.

The structure factor $F(\underline{K})$ is defined by

$$F(\underline{K}) = \sum_{i\ (\text{unit cell})} f_e(\underline{K}) \exp(-2\pi i \underline{K}.\underline{\tau}_i)$$

The amplitude due to scattering by a whole crystal can similarly be shown to be

$$A = \frac{\exp(2\pi i \chi r)}{r} \sum_{j} F(\underline{K}) \exp(-2\pi i \underline{K} \underline{\tau}_j) \qquad (2.7)$$

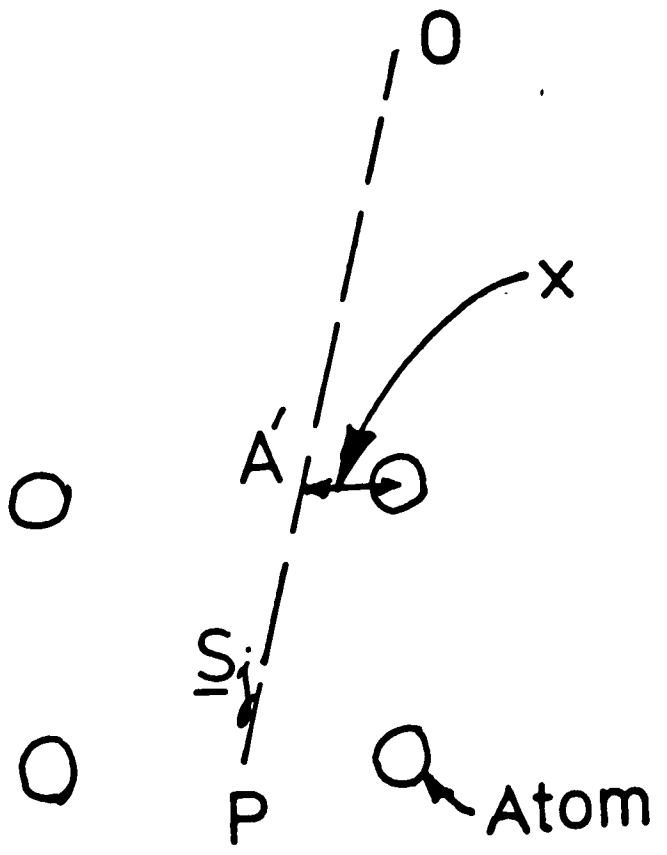


FIGURE 2·4

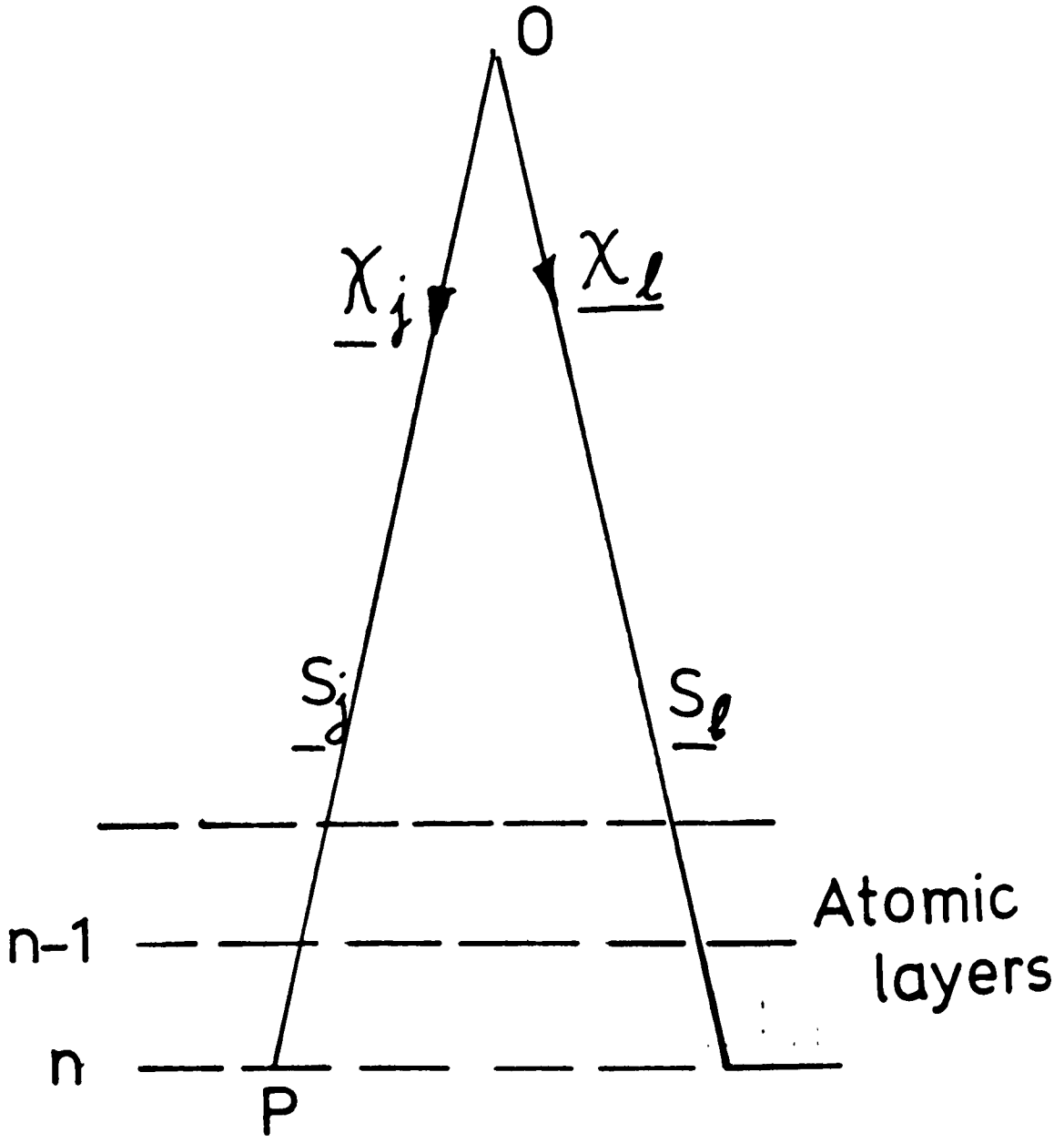


FIGURE 2·5

where τ_j is the position of the unit cell, and the summation is over all the unit cells in the crystal.

2.3.1 Fresnel Zone Calculations

Figure 2.3 shows how this may conveniently be done. Let P be a point at which we require to calculate the amplitude of a wave travelling in a direction $\underline{\chi}_j$. This wave is regarded to have formed as a result of scattering at the plane $\varphi\varphi'$ of a wave of vector $\underline{\chi}_l$.

Now if A' corresponds to an atomic centre we can conveniently use it to mark the centre of a series of Fresnel zones on the plane QQ'. It is well known from the theory of optics that the amplitude of the wave at Pis equal to half the contribution made by the first Fresnel Zone. It is also known that this contribution is out of phase by $\pi/2$ relative to the phase of the incident wave at P, so long as the phases of the incident and scattered waves are equal at A'. If the incident and scattered waves are both regarded as plane, this will clearly only be so if A' is coincident with an atomic position. If it is not, an additional phase difference equal to $2\pi(\underline{\chi}_j - \underline{\chi}_l).\underline{x}$ is introduced in the phase of the scattered wave at P. ($\underline{x}$ is the displacement in the plane QQ' of A' from an atomic centre (see figure 2.4)). This is the so-called "origin-shift" term.

2.3.2 Origin Shift Term

Let us choose the origin of our position vector to be situated at the top of the foil and at an atomic centre. Let $\underline{S}_j$ be the distance from the origin in the direction of the jth diffracted beam.

We write $\underline{\chi}_\ell = \underline{\chi}_0 + \underline{g}_\ell + \underline{S}_\ell$ where g_ℓ is the reciprocal lattice vector for the reflection and $\underline{S}_\ell$ is the deviation measured in the z direction of the reciprocal lattice point from the Ewald Sphere. Then the phase change due to "origin shift" can be written $2\pi(\underline{g}_j - \underline{g}_\ell).\underline{S}_j$. Due to the smallness of the Bragg angle, this can be regarded as slowly varying from one atomic plane to the adjacent one in theLaue case. If $i r^0_{j\ell}$ is the reflection coefficient per unit length for the plane through the origin, then the reflection coefficient for the mth plane can be written

$$i r^m_{j\ell} = i r^0_{j\ell} \exp\left[2\pi(\underline{g}_j - \underline{g}_\ell).\underline{S}_j\right] \qquad (2.8)$$

The factor i is used to represent the $\pi/2$ charge of phase from the Fresnel Zone calculation.

2.4 Sturkey's Theory

A scattering matrix formulation of the dynamical theory was developed by Sturkey during the 1950's, and was published in full in 1962. A similar theory was developed by Howie and Whelan (1961) In 1966 Fukuhara compared five-beam dynamical theory calculations based on the Bethe theory described in Chapter 1, with results predicted by Sturkey's theory for the same case. He described the discrepancy as "appalling". His explanation of this difference was that it was due to certain approximations made by Sturkey, meaning presumably the fact that Sturkey only considered the effect of the first nine terms of his matrix power series. It is shown in this chapter that Sturkey's error was more fundamental and involved an incorrect derivation of the scattering equilibrium equations.

Sturkey's theory considered the case of a perfect crystal with no "absorption" of electrons. If $\phi_i(z)$ is the Darwin amplitude of the ith diffracted beam at a depth z, conservation of electron flux through the crystal demands that $\sum_i \phi_i^*(z)\,\phi_i(z)$ is invariant with respect to z. If the beam travelling in the incident direction is $\phi_0(z)$

then $$\sum_i \phi_i^*(z)\,\phi_i(z) = \phi_0^*(0)\,\phi_0(0) = 1$$

for unit incident amplitude. In matrix form

$$\{\phi_i(z)\} = \underline{\underline{B}}\,\{\delta_{0,i}\}$$

where $\underline{\underline{B}}$ is a square unitary matrix.

By elementary matrix theory $\underline{\underline{B}}$ must have the form

$$\underline{\underline{B}} = \exp[i\,\underline{\underline{R}}(z)]$$
$$= \underline{\underline{I}} + i\,\underline{\underline{R}} - \frac{1}{2!}\underline{\underline{R}}^2 + \ldots + \frac{(i\underline{\underline{R}})^n}{n!} + \ldots$$

where R is Hermitian (i.e. $R_{ij} = R_{ji}^*$)

Sturkey calls $\underline{\underline{R}}(z)$ the scattering matrix. It will be noted that this is not the same as the scattering matrix defined in Chapter 1. The components of this matrix are evaluated by wave-optical arguments similar to those used by Darwin (1914) for the X-ray case.

2.4.1 Sturkey's dynamic equilibrium equation

The crystal is regarded as made up of identical equally spaced layers, and the incident electron beam is in a direction close to the normals to these layers (see Figure 2.5). $\underline{\chi}_0$ is the wave-vector (of magnitude $2\pi/\lambda$) in vacuo of the incident ray. $\underline{\chi}_\ell$ are the wave vectors of the diffracted rays. Let $\gamma_{j\ell}$ be the amplitude reflection coefficient per unit thickness for a beam reflected from a direction 1 into a direction j. Let T_{jj} be the transmission coefficient for a beam travelling in the direction χ_j,

and let $\underline{S}_j$ be the distance from the origin (in the first layer) in the direction of the j^{th}. diffracted beam. ϕ_{nj} is the amplitude of the beam passing the n^{th} layer in the direction j. Sturkey obtains the equilibrium equation,

$$\phi_{n,j} = T_{jj}\ \phi_{(n-1),j} \exp\left(i \underline{\chi}_j . \underline{\Delta S}_j\right) + i \sum_{l \neq j} r_{jl}\, \Delta z\, \phi_{n,l} \cdot \ldots \times \exp\left(i \underline{\chi}_l . \underline{\Delta S}_l\right) \qquad (2.9)$$

In the limit of narrowly spaced layers, Sturkey lets $T_{jj} \rightarrow 1$ This equation appears to be incorrect for several reasons.

2.4.2 Errors in Sturkey's equilibrium equation

Firstly since the summation on the R.H.S.does not include the term for which $l = j$ effects due to forward scattering are excluded. In addition, if all phases are measured relative to the origin O (in figure 2.5), then the correct phase propogation factor at the point P due to a wave travelling in the l direction is $\exp\left(i \underline{\chi}_l . \underline{S}_j\right)$ not $\exp\left(i \underline{\chi}_l . \underline{S}_l\right)$. Thirdly, the reflection coefficient r_{jl} is not identical for each plane but varies with depth since the direction j is not exactly perpendicular to the lattice planes. This is the "origin-shift" effect described earlier.

2.4.3 Correction to Sturkey's Theory

The reflection coefficient should be described by a further index (we write it as r^n_{jl}). Then the fundamental equilibrium equation becomes (where Z is the coordinate normal to the layers)

$$\phi_{n+1,j} = \phi_{n,j} + i\, \Delta z \sum_l r^n_{jl}\, \phi_{n,l} \exp\left[i \left(\underline{\chi}_l - \underline{\chi}_j\right) . \underline{S}_j\right]$$

This can be written as the differential equation

$$\frac{d}{dz}\phi_j = i \sum_l r^n_{jl}\, \phi_l \exp\left[i \left(\underline{\chi}_l - \underline{\chi}_j\right) . \underline{S}_j\right] \qquad (2.10)$$

But from equation (2.8) we see that

$$r^{n}_{jl} = r^{o}_{jl} \exp\left[-2\pi i \left(g_l - g_j\right).\underline{S}_j\right]$$

Putting $r^{o}_{jl} = r_{jl}$ and substituting into (2.10) we have

$$\frac{d\Phi_j}{dz} = i \sum_l r_{jl}\, \phi_l \exp\left[i\left(\chi_o - \chi_j\right)_z z\right] \qquad (2.11)$$

Now making the substitution,

$$\phi_j = \phi_j' \exp\left[i\left(\chi_o - \chi_j\right)_z z\right] \qquad (2.12)$$

we obtain,

$$\frac{d\Phi_j'}{dz} = i\left(\chi_j - \chi_o\right)_z \phi_j' + i \sum_l r_{jl}\, \phi_l' \qquad (2.13)$$

The transformation (2.11) only affects the phase of the amplitude ϕ_l. The amplitudes ϕ_l' calculated from (2.12) are therefore just as valid for the calculation of intensities. Now equation (2.12) with the primes dropped for convenience, is the same as that given by Howie and Whelan (1961) with $r_{jl} = \pi/\xi_{j-l}$ for a perfect crystal.

2.4.4 Solution for perfect crystal

Equation (2.12) can be written in matrix form with the primes dropped as

$$\frac{d}{dz}\{\phi_j\} = i\,\underline{R}\,\{\phi_j\} \qquad (2.14)$$

Now it is well known from the theory of differential equations that the solution of (2.14) is

$$\{\phi_j(z)\} = \exp\left[-i\,\underline{R}\,z\right]\{\phi_j(0)\} \qquad (2.15)$$

$$\text{if} \quad \frac{d}{dz}\left(\underline{R}\right) = 0 \qquad (2.16)$$

and since $\{\phi_j(0)\}$ is completely known, this is the explicit solution.

Equation (2.16) requires that $\underline{\underline{R}}$ should be a constant matrix (i.e. independent of z) if the solution to (2.14) can be written in the form (2.15). If the crystal contains lattice defects such as dislocations, the reflection coefficients r_{jl} will be functions of z and therefore $\underline{\underline{R}}$ will be a function of z. In that case (2.15) is inadmissible as a solution and equation (2.14) has in general to be solved by numerical computation. It is also easy to see that $\underline{\underline{R}}$ is the "scattering matrix" of Sturkey's theory and must in the case of non-absorbing crystals be Hermitian.

2.4.5 Evaluation of reflection coefficients

Values of the off-diagonal elements of the matrix $\underline{\underline{R}}$, namely the r_{jl} coefficients, are obtained by comparing equation (2.11) with (1.21). For the case of a perfect crystal $\underline{\underline{R}}(z) = 0$ in equation (1.25). That equation can then be written, since the deviation parameter s is small compared to χ_z

$$\frac{d\phi_j}{dz} = i \sum_l \frac{\pi U_{j-l}}{\chi_z} \phi_l \exp\left[2\pi i (s_l - s_j) z\right]$$

Here χ_z is the z-component of the vacuum wave vector.

Also $$2\pi i (s_l - s_j) = i (\chi_l - \chi_j)_z$$

and therefore by direct comparison with (2.11)we obtain

$$r_{jl} = \frac{\pi U_{j-l}}{\chi_z}$$

We thus see that the off-diagonal elements of the matrix $\underline{\underline{R}}$ are proportional to Fourier coefficients of the lattice potential

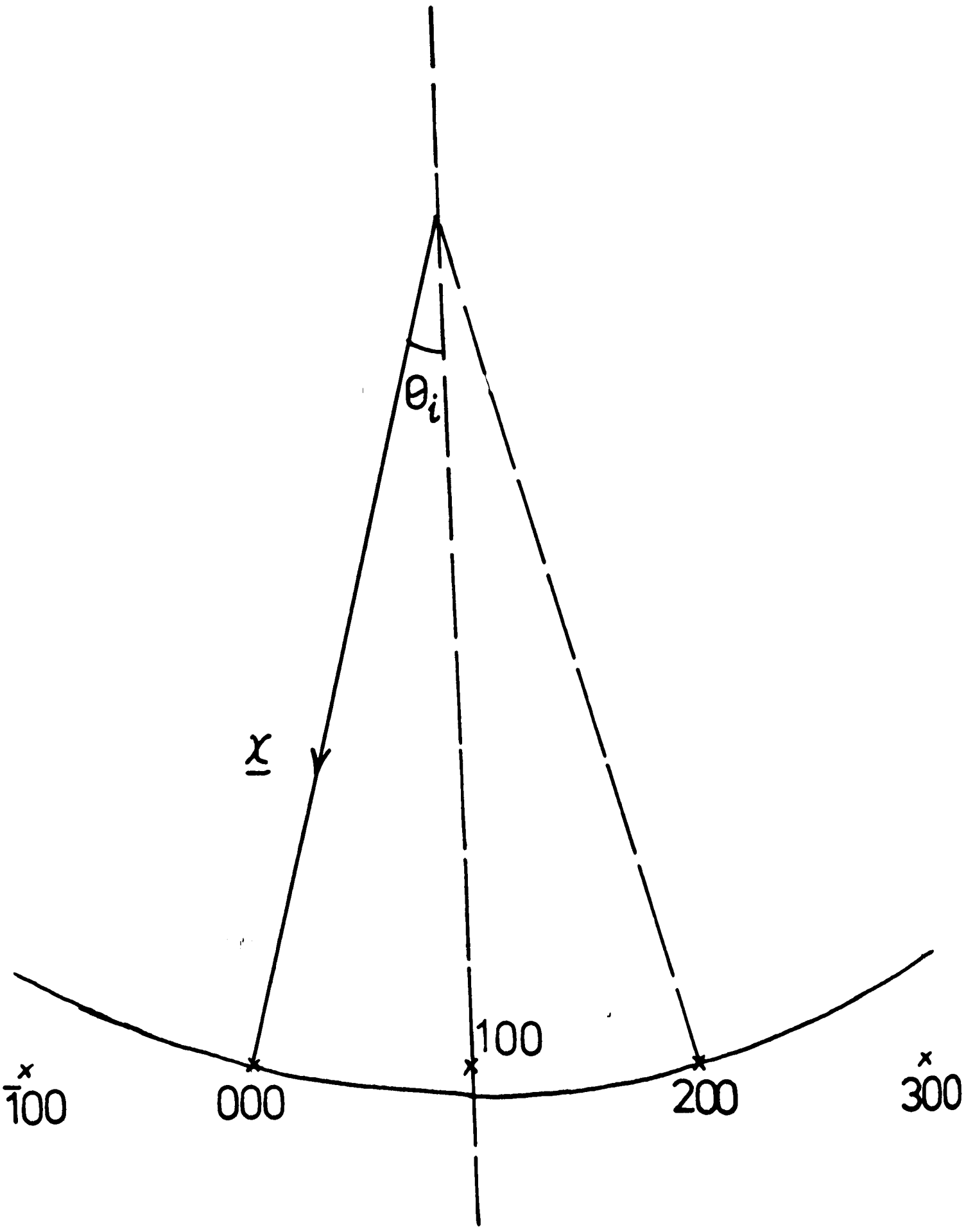


FIGURE 2·6

as seen by an incident particle.

2.5 Consequences of Sturkey's error

The scattering matrix given by Sturkey and derived from his incorrect equation (2.9) is identical to that calculated above except for the sign of the diagonal terms. Now in the calculation of intensities, a matrix which is identical to our matrix $\underline{\underline{R}}$ except for the sign of the off-diagonal terms, would give the same results as Sturkey's matrix. It is thus clear that any calculation of intensities based on Sturkey's matrix would describe the effects (apart from particle anti-particle annihilation) of positrons in the crystal. Alternatively they would describe the motion of electrons in a crystal composed of anti-matter. Sturkey could therefore be regarded as the (unwitting) theoretical pioneer of a subject whose experimental techniques still lie mostly in the future. However, it must be mentioned that some studies have already taken place, of the preferential trapping of positrons at dislocations in ordinary matter.

2.5.1 Application of Sturkey's original and corrected method

A special case studied by both Sturkey (1962) and Fukuhara (1966) was re-examined in the light of the above considerations. The case is illustrated in Figure 2.6. The five reciprocal lattice points corresponding to the five diffracted beams considered are shown, together with the Ewald Sphere. Sturkey was able to show that the diagonal terms of his scattering matrix $\underline{\underline{R}}(z)$ are $\frac{\pi}{\lambda}\sin^2\theta_j$ and the off-diagonal terms γ_{jl}. Now $\exp(i\underline{\underline{R}}z)$ is only defined in terms of a matrix power series. However,

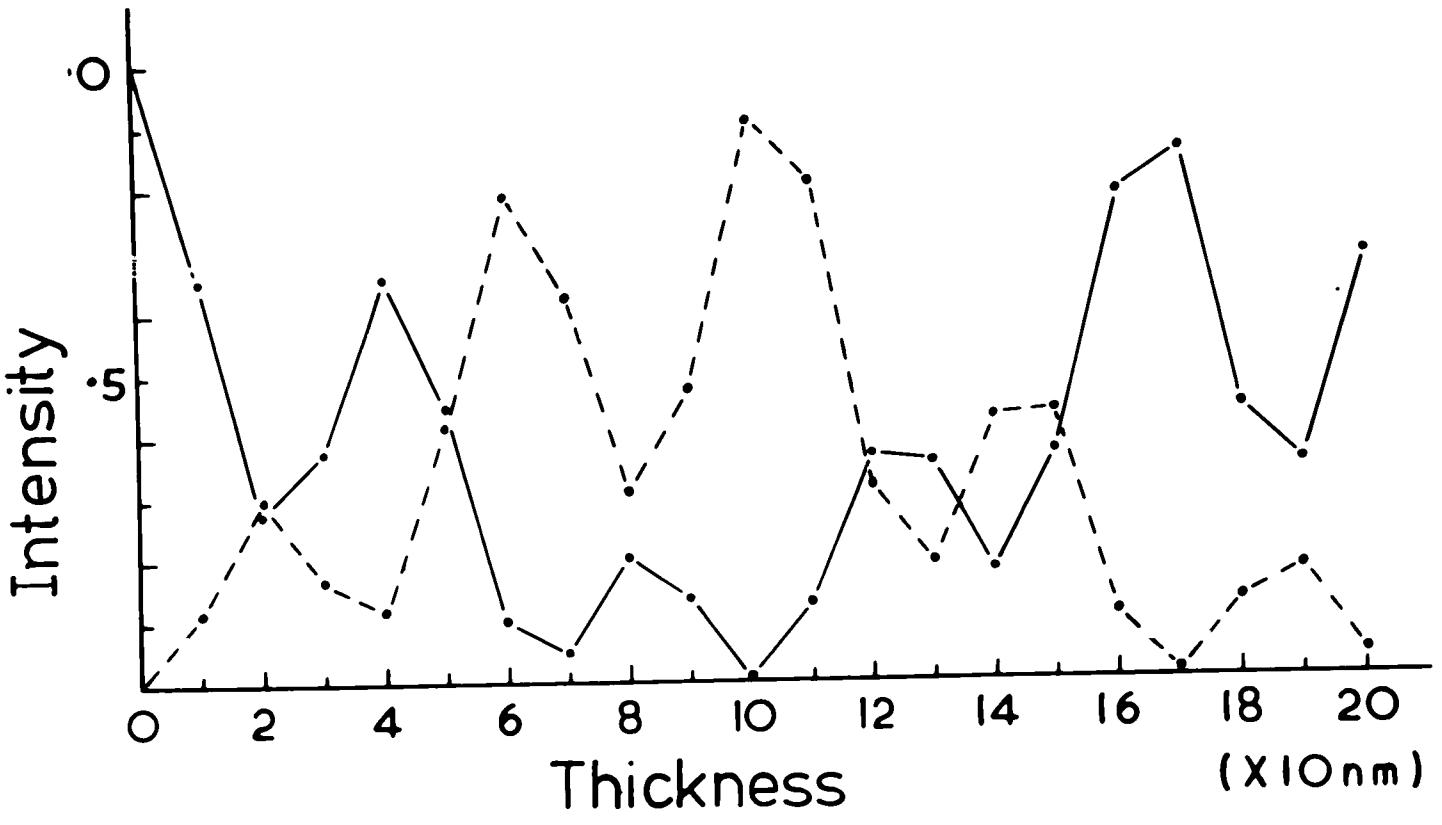


FIGURE 2.7

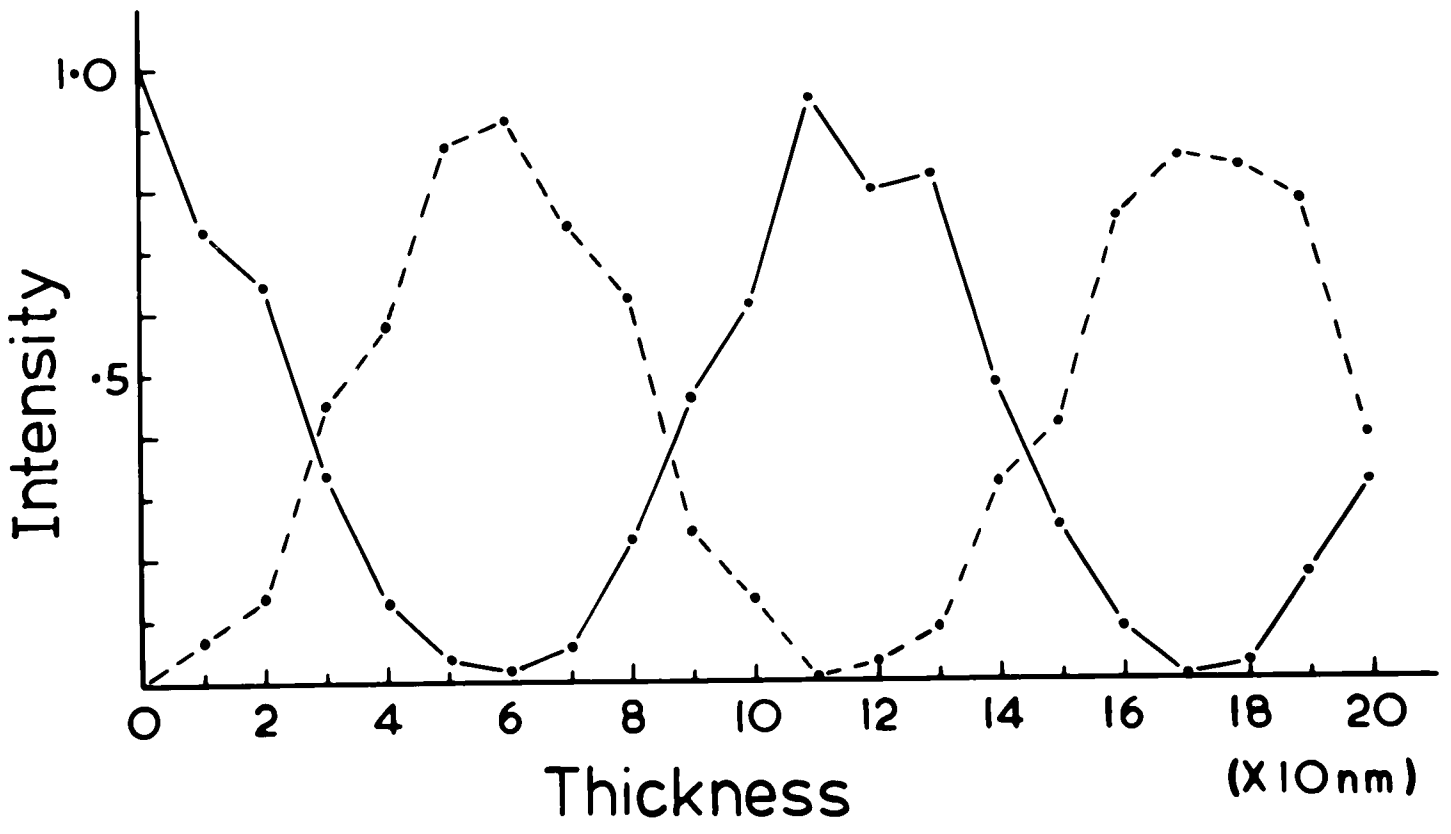


FIGURE 2.8

convergence of this series is only rapid if z is small. Sturkey took the thickness of his slab to be 100Å. He estimated that only nine terms in the matrix power series were necessary for reasonable convergence at this thickness. Calculations for multiples of this thickness were carried out by raising the matrix $\exp(i \underline{R} z)$ to the nth power. Using the data $|U_g| = 2.12 \times 10^{18}\ m^{-2}$, $K = 4\pi\ 10^{11}\ m^{-1}$ and $g_{100} = 2 \times 10^{9}\ m^{-1}$ the following equation was obtained, for a thickness (100n)Å

$$\begin{bmatrix} (100n) \\ (100n) \\ (100n) \\ (100n) \\ (100n) \end{bmatrix} = \left[\exp i \begin{pmatrix} 0.628 & 0.333 & 0.333 & 0.333 & 0.333 \\ 0.333 & 0 & 0.333 & 0.333 & 0.333 \\ 0.333 & 0.333 & 0.628 & 0.333 & 0.333 \\ 0.333 & 0.333 & 0.333 & 2.51 & 0.333 \\ 0.333 & 0.333 & 0.333 & 0.333 & 2.51 \end{pmatrix} \right]^{n} \times \ldots$$

$$\ldots \times \begin{bmatrix} 1 \\ 0 \\ 0 \\ 0 \\ 0 \end{bmatrix}$$

The column vector on the L.H.S. gives the amplitudes of the electron waves at a depth of 100nA. The column vector on the R.H.S. gives the amplitudes at the top of the crystal.

Figure 2.8 shows the results obtained by Sturkey. Sturkey's procedure was repeated escept that the signs of the off-diagonal terms in the matrix abovewere charged. The results are shown in Figure 2.7. These results are identical with those reported by Fukuhara based on the matrix diagonalization method for electrons.

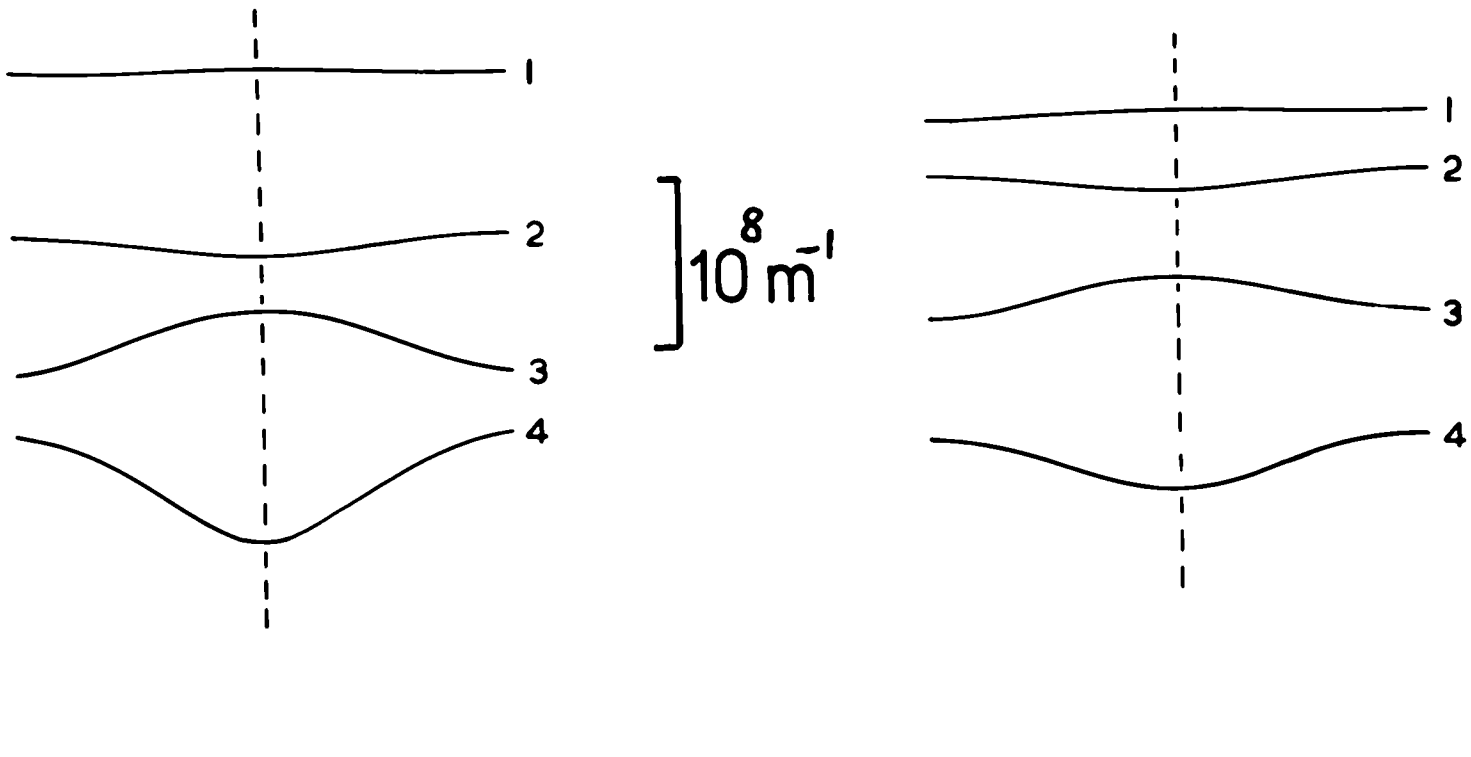


FIGURE 2·9

2.5.2 Matrix diagonalization calculations

The matrix diagonalization method has been described in Chapter 1. This procedure also gives information concerning the dispersion surface (figure 2.9). In particular we are interested in the permitted values of the Bloch wave-vectors at the Brillouin zone boundary (broken lines).

The sign of the U_g's were changed in this treatment also (to give results for positron diffraction) and the corresponding dispersion surface is given in figure 2.9(b). The intensities calculated on this basis were in perfect agreement with Sturkey's original results, thus proving the hypothesis beyond all doubt.

2.5.3 Explanation of the discrepancy in terms of Bloch waves

An understanding of the marked differences between figures 2.7 and 2.8 can be seen from a consideration of the beating between the Bloch waves on the dispersion surfaces 2.9(a) and 2.9(b) respectively.

In both cases, the most strongly excited branches are 2 and 3 (see Metherell and Fisher 1969). In 2.9(a) branch 1 is well separated from branches 2 and 3 at the Brillouin zone boundary. This gives rise to two periodicities in figure 2.7. The long wave-length ($\sim$ 180 nm) variation arises from interference between Bloch waves on branches 2 and 3 while the short wavelength ($\sim$ 40 nm) variation arises from interference between Bloch waves on branches 1 with these on branches 2 and 3. On the other hand in figure 2.9(b) the amplitude on branch 1 is small compared with those on branches 2 and 3 and we thus only see the "periodicity " of about 120 nm in figure 2.8. In this case any contribution from Bloch waves on branch 1 will produce periodicities of this order of magnitude.

Chapter 3

IMAGE CONTRAST UNDER "WEAK-BEAM" CONDITIONS

The germ of the idea of a weak-beam technique is found in early kinematical calculations of images from dislocations (Hirsch, Howie and Whelan, 1960). The experimental facilities available at the time however prevented it from coming into practical use until the late nineteen-sixties. The calculations of Hirsch et al. predicted images with narrow, high contrast intensity peaks near the cores of the projected dislocation positions when the images are formed by weakly excited reflections. It was shown that for dislocations with $\underset{\sim}{g}.\underset{\sim}{b} = 2$ (where $\underset{\sim}{g}$ is the reciprocal lattice vector of the operating reflection and $\underset{\sim}{b}$ the Burgers vector of the dislocation) the distance of the average kinematical peak position from the projected core of the dislocation is approximately $\frac{1}{2\pi s}$ for a screw dislocation and Gevers (1962) showed that the corresponding distance for an edge dislocation is about $\frac{2.1}{2\pi s}$ This indicates that the larger the value of s, the more closely the image peak position corresponds to the projected position of the core.

Subsequently the many beam dynamical calculations of Cockayne, Ray and Whelan (1968), and Howie and Basinski (1968) confirmed that these weak-beams form images of dislocations of higher resolution and contrast (though of lower intensity) than images formed from strongly excited reflections.

Cockayne, Ray and Whelan (1969) employed the weak-beam technique for the study of the dissociation of dislocations into partials.

This and subsequent work by Ray and Cockayne (1970, 1971, 1973) Cockayne, Jenkins and Ray (1971), Jenkins (1972) and Stobbs and Sworn (1971) has proved successful in the estimation of the important metallurgical parameter known as the stacking-fault energy, from the equilibrium separation of the partial dislocations. Similarly, the higher resolution afforded by this technique has been exploited (see e.g. Jenkins, Cockayne and Whelan (1973), Jenkins (1973)) to obtain considerable new information about the nature of small defect clusters produced by ion irradiation.

3.2 Interpretation of weak-beam images

It is well known that in high-resolution electron microscopy there is not necessarily a simple relationship between the object and the image. In fact the lack of phase information in the images make the unique reconstruction of the object from the image extremely difficult. We therefore need to work in the reverse direction, namely to make some guess as to the nature of the object and to use some form of electron diffraction theory to simulate the image for comparison with the experimental image. The dynamical theories described in Chapters 1 and 2 form our most refined and complete description of electron scattering in crystals. However the fact that no reflection is strongly excited under weak-beam conditions suggests that the kinematical theory might form a simpler but adequate description.

3.3 The kinematical limit of dynamical theory

In this section we investigate in what sense kinematical theory can be regarded as a limiting case of dynamical theory. We may do this either by following the Darwin approach of §1.8.3 or the Bloch wave formulation of 1.8.4.

3.3.1 The Darwin picture

Under weak beam conditions, no Bragg reflection is strongly satisfied. In terms of equation (1.25) $\Phi_h \ll \Phi_0$ for all h. In that case, equation (1.25) can be rewritten without terms involving Φ_h as,

$$\frac{d\Phi_0}{dz} = \frac{\pi i}{\xi_0}\Phi_0 \qquad (3.1)$$

and $$\frac{d\Phi_g}{dz} = \pi i \frac{\Phi_0}{\xi_g} \exp[2\pi i(s_g z + \underline{g}.\underline{R})] + \ldots + \frac{\pi i}{\xi_0}\Phi_g \qquad (3.2)$$

From equation (3.1) we obtain-

$$\Phi_0 = \exp(\pi i z/\xi_0)\ \Phi_0(0) \qquad (3.3)$$

and rearranging equation (3.2) we have

$$\exp(\pi i z/\xi_0)\frac{d}{dz}\left(\Phi_g \exp[-i\pi z/\xi_0]\right) = \frac{\pi i}{\xi_g}\Phi_0 \exp[2\pi i(s_g z + \underline{g}.\underline{R})]$$

Hence $$\left[\Phi_g \exp(-\pi i z/\xi_0)\right]_0^t = \pi i/\xi_g \int_0^t \Phi_0 \exp(-\pi i z/\xi_0)\exp[2\pi i(s_g z + \underline{g}.\underline{R})]\,dz$$

and using (3.3) we have (since $\phi_g(o) = o$)

$$\phi_g(t) = \frac{\pi i}{\xi_g} \exp(\pi i t/\xi_o)\, \phi_o(0) \int_o^t \exp[2\pi i(s_g z + g.\underline{R})]\, dz \qquad (3.4)$$

for a foil of thickness t

Now in general $1/\xi_o$ and $1/\xi_g$ are complex. Let us write these quantities as

$$(1/\xi_o + i/\xi_o') \quad \text{and} \quad (1/\xi_g + i/\xi_g')$$

Then equation (3.4) becomes

$$\phi_g = \pi i (1/\xi_g + i/\xi_g') \exp(-\pi t/\xi_o')\, \phi_o(0) \int_o^t \exp[2\pi i(s_g z + g.\underline{R})]\, dz \qquad (3.5)$$

if we drop the unimportant phase factor

$$\exp(\pi i t/\xi_o)$$

This can be regarded as a modified kinematical theory, resonably valid for the computation of weak-beam images. It differs from the expression given by Hirsch, Howie and Whelan (1960) by the term involving $(-\pi/\xi_g')$ which acts to increase the intensity in the reflection g and the factor $\exp(-\frac{\pi t}{\xi_o'})$ which reduces it. The former factor gives only a very small correction to ϕ_g and can usually be neglected. The latter factor is necessary however since weak-beam images are often obtained from crystal thickness of the same order as the "absorption length" ξ_o'. Thus absorption effects become very important in determining intensities. The expression of Hirsch, Howie and Whelan (1960) is only valid when $t \ll \xi_o'$ and when $\xi_g' \gg \xi_g$

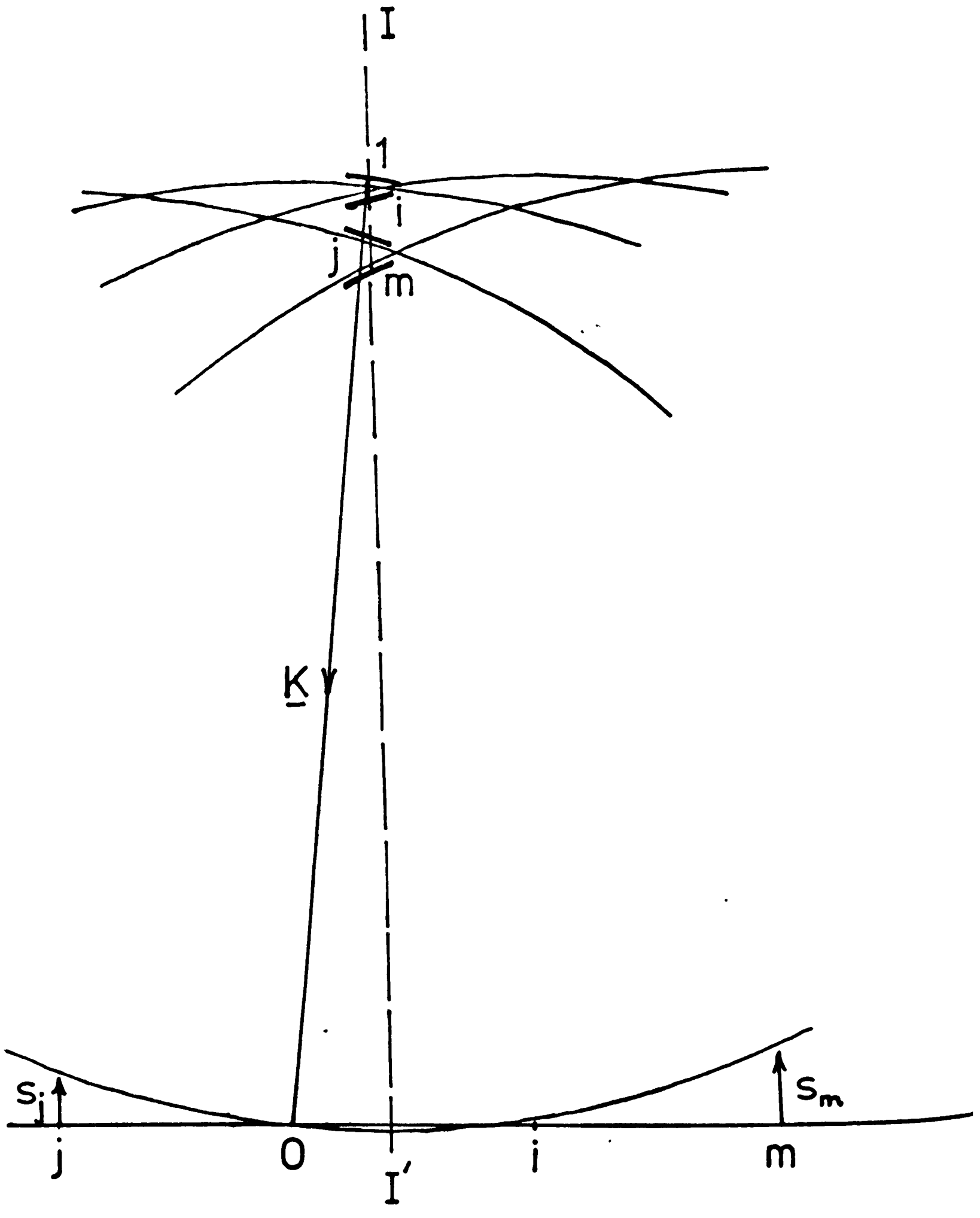


FIGURE 3·1

3.3.2 The Bloch wave picture

Let us rewrite the eigenvalue equation (1.13) as

$$\left(\underline{\underline{U}} + [S_h]_D\right)\{C_h\} = \Gamma\{C_h\}$$

Under weak-beam conditions the elements S_h become much larger than the elements of the matrix $\underline{\underline{U}}$. Then the matrix on the L.H.S. of (1.13) becomes nearly diagonal, the matrix of the eigenvectors approaches the unit matrix, and the eigenvalues $\Gamma^{(l)}$ approximate the elements of the diagonal matrix $[S_h]_D$. In this limit then, each $\{C_h^{(l)}\}$ and $\Gamma^{(l)}$ can be associated with a particular reflection $\underline{h}$ such that $\Gamma^{(l)} = S_h$. We may then use the notation of Cockayne (1972) and label the Bloch indices by means of the reflection that is associated with the corresponding Bloch wave. We can thus form a matrix of the eigenvectors $\{C_{h'}^{(h)}\}$ where h' characterises the rows and h the columns, and the eigenvectors can be written $\Gamma^{(h)}$.

In terms of the dispersion surface (fig.3.1) the branch corresponding to a particular reflection is the one closest to a sphere of radius $\underline{\chi}$ whose centre lies on the reciprocal lattice vector of that reflection, when the surface cuts the line II'.

We may now regard the matrix $\underline{\underline{U}}$ as a perturbation to the matrix $[S_h]_D$. Using the familiar methods of quantum mechanical perturbation theory (see Dicke and Wittke, 1960, Ch.14) we find that to first order,

$$C_{h'}^{(h)} = \frac{U_{h-h'}}{S_h - S_{h'}} \qquad (3.6)$$

for $h' \neq h$.

and that $C_{h'}^{(h')} \simeq 1$. (3.7)

This indicates that the off-diagonal terms of the matrix $\underline{\underline{C}}$ are still small compared to the diagonal terms. Now from equation (1.16) we see that a boundary condition at the electron entry surface of the foil is

$$\{\phi_h(0)\} = \underline{\underline{C}}\,\{\psi^{(h)}(0)\}$$

and hence

$$\{\psi^h(0)\} = \underline{\underline{C}}^{-1}\{\phi_h(0)\}$$

$$= \underline{\underline{C}}^{-1}\{\delta_{h,0}\}$$

and thus

$$\psi^h(0) = C_0^h \qquad (3.8)$$

since if an origin of coordinates is taken at an atomic centre of symmetry, $\underline{\underline{A}} = \left(\underline{\underline{U}} + [S_h]_D\right)$ is symmetric and thus $\underline{\underline{C}}^{-1} = \underline{\underline{C}}^T$ (see Appendix III for proof, and also consideration of the case of Hermitian $\underline{\underline{A}}$). So we see that the Bloch wave excitation coefficient $\psi^{(0)}(0)$ is much largerthan all the $\psi^h(0)$'s where $h \neq 0$ (Since the diagonal term $C_0^{(0)}$ is much larger than the non-diagonal terms $C_0^{(h)}$ where $h \neq 0$).

Now in a deformed crystal, scattering causes redistribution of amplitudes amongst the various branches of the dispersion surface. Thus at the electron exit surface of the crystal we would expect $\psi^{(h)}(t)$'s with $h \neq 0$ to have appreciable amplitude.

From (1.16a) we find that the amplitude in the "Darwin" wave of reflection $\underline{g}$ at depth t in a deformed crystal is,

$$\phi_g(t) = \sum_h \psi^{(h)}(t)\, C_g^{(h)} \exp\left[2\pi i \gamma^{(h)} t\right] \exp\left[-2\pi i \underline{g}\cdot\underline{R}(t)\right] \qquad (3.9)$$

where we have omitted the unimportant phase factor $\exp(-2\pi i s_g z)$.

Of the terms $C_g^{(h)}$, $C_g^{(g)}$ is much larger than all the others. Of the terms $\psi^{(h)}(t)$ we would still expect $\psi^{(o)}(t)$ to be much the largest if we assume that the amount of interbranch scattering is small. Thus we would expect only two terms to contribute appreciably to $\phi_g(t)$ from equation (3.6), namely the term containing $C_g^{(g)}$ and that containing $\psi^{(o)}(t)$. Then we may write

$$\phi_g(t) = \left\{ \psi^{(o)}(t)\, C_g^{(o)} \exp\left[2\pi i \gamma^{(o)} t\right] + \ldots \right.$$
$$\left. + \psi^{(g)}(t)\, C_g^{(g)} \exp\left[2\pi i \gamma^{(g)} t\right] \right\} \exp\left(-2\pi i \underline{g}\cdot\underline{R}(t)\right) \qquad (3.10).$$

3.4 Kinematical Bloch wave scattering

The conditions described in the last section, where near the electron entry surface, a particular Bloch wave has much larger amplitude then any of the others is very reminiscent of kinematical conditions for Darwin wave scattering. One is led to expect that a theory based on the kinematical scattering of Bloch waves would have some validity. In this section we explore the consequences of such a theory under weak-beam conditions.

Equation (1.21) may be written

$$\frac{d\psi^{(i)}}{dz} = \sum_j A_{ij}\,\psi^{(j)}$$

where $$A_{ij} = 2\pi i \sum_g g \cdot \frac{dR}{dz}\; C_g^{(i)} C_g^{(j)} \exp\left[2\pi i \left(\Gamma^{(j)} - \Gamma^{(i)}\right) z\right]$$

Putting $$T^{ij}(z) = 2\pi i \sum_g g \cdot \underline{R}(z)\, C_g^{(i)} C_g^{(j)}$$

and $$\Delta\Gamma^{ji} = \Gamma^{(j)} - \Gamma^{(i)}$$

Whelan (1972) has shown that for systematic reflections, if we consider the scattering from the branch j to branch i to be kinematical, then

$$\psi^{(i)}(t)\exp\left(-T^{ii}(t)\right) = \psi^{(i)}(0) + \sum_{j\neq i} D_{ij}(t)\,\psi^{(j)}(0) \qquad (3.11)$$

where

$$D_{ij} = 2\pi i\, B^{ij}\, \Delta\Gamma^{ji}\left[\frac{1-\exp\left[2\pi i\,\Delta\Gamma^{ji} t - T^{ii}(t)\right]}{2\pi i\,\Delta\Gamma^{ji}} + \cdots\right.$$

$$\left. \cdots + \int_0^t \exp\left(2\pi i\,\Delta\Gamma^{ji} - T^{ii}\right) dz\right]$$

where $$B^{ij} = \frac{T^{ij}}{T^{ii}} = \frac{\sum_g g\, C_g^{(i)} C_g^{(j)}}{\sum_g g\, C_g^{(i)} C_g^{(i)}}$$

Let us consider only the interaction between the Darwin waves corresponding to reciprocal lattice vectors 0 and g
Also let us again use the notation of Cockayne (1972) and associate Bloch waves with corresponding Darwin waves, as in the last section. In that case we make the identifications $i \Rightarrow g$ and $j \Rightarrow 0$ and we obtain,

$$B^{g0} = C_g^{(0)} / C_g^{(g)} .$$

From equation (3.11) we may find an expression for $\psi^{(g)}(t)$ from the known values of $\psi^{(0)}(0)$ and $\psi^{(g)}(0)$ obtained from (3.6), (3.7) and (3.8). In keeping with the kinematical approximation, we assume $\psi^{(0)}(t) = \psi^{(0)}(0)$. Substitution of these values of $\psi^{(0)}(t)$ and $\psi^{(g)}(t)$ into equation (3.10) and subsequent simplification gives

$$\phi_g(t) = -\frac{\pi i \, \Delta\Gamma^{(0g)}}{\xi_g s_g} \int_0^t \exp\left\{2\pi i \, \Delta\Gamma^{(0g)} - T^{(gg)}\right\} dz$$

Now $T^{(gg)} = 2\pi i \, g . \underline{R}(z)$

and under weak-beam conditions, $\Delta\Gamma^{(0g)} \rightarrow -s_g$ and thus,

$$\phi_g(t) = \frac{\pi i}{\xi_g} \int_0^t \exp\left\{-2\pi i \, (s_g z + g . \underline{R}(z))\right\} dz$$

which is precisely the kinematical amplitude in the absence of absorption. This result has been obtained independently by Holmes (private communication).

3.4.1 The effect of absorption

Incorporation of absorption into this theory is very straightforward. Hirsch et al (1965) show that the absorption coefficients of the two Bloch waves are

$$q^{(0)} = \frac{1}{2\xi_0'} - \frac{1}{2\xi_g'\sqrt{1+w^2}}$$

$$q^{(g)} = \frac{1}{2\xi_0'} + \frac{1}{2\xi_g'\sqrt{1+w^2}}$$

Under weak-beam conditions, $w \gg 1$ and thus,

$$q^{(0)} \rightarrow q^{(g)}$$

That is, the absorption coefficients of the two Bloch waves become nearly equal. Since $\phi_g(t)$ has been calculated above as a linear sum of Bloch waves, it is clear that the expression for $\phi_g(t)$ corrected for absorption should be

$$\phi_g(t) = \pi i \left(\frac{1}{\xi_g} + \frac{i}{\xi_g'}\right) \exp\left(-\pi t/\xi_0'\right) \times \ldots$$

$$\ldots \times \int_0^t \exp\left\{-2\pi i\left[s_g z + \underline{g}\cdot\underline{R}(z)\right]\right\} dz$$

which is effectively identical to (3.5) (Remembering that we are interested in amplitudes and not intensities). This is a very interesting result for it shows that under weak-beam conditions, a kinematical theory describing Darwin wave scattering and one describing Bloch wave scattering give identical results. It will be seen in the next chapter that although many details of contrast

from small defects observed under strong-beam conditions can be described by a kinematical Bloch wave theory, the scattering of the Darwin waves can only be accurately described by the dynamical theory.

3.5 The criterion of Cockayne et al for image peak positions

Cockayne et al (1969) gave an approximate criterion for determining the position of the peak in the image of a dislocation when a line profile perpendicular to the dislocation is considered. On kinematical theory the weak-beam peak occurs at the column for which the kinematical integral

$$\int_0^t \exp\left\{2\pi i \left[s_g z + \underline{g} \cdot \underline{R}(z) \right] \right\} dz$$

is a maximum. One would expect this to occur at a column for which the argument $\left[s_g z + \underline{g} \cdot \underline{R}(z)\right]$ was reasonably constant for a considerable range of depth. Mathematically these conditions may be written

$$s_g + \underline{g} \cdot \frac{d}{dz} \underline{R}(z) = 0$$

when

$$\frac{d^2}{dz^2} \underline{R}(z) = 0.$$

It should be emphasized that this is only an approximate criterion, useful because it obviates the need for integration, based on the concept of a "stationary phase". In general the true maximum of the kinematical integral has to be obtained by numerical integration.

3.6 Comparison of the image peak positions on various theories

We have above presented three methods for determining the peak position of the image of a dislocation. They are, in order of increasing complexity; the criterion of Cockayne et al, the kinematical theory, and the dynamical theory. In this section, detailed comprisons of the predictions of these three methods are given. We consider the images of straight dislocations. The displacement field due to such a defect in isotropic elasticity theory is given by (Hirsch et al 1965)

$$\underline{R}(r,\Phi) = \frac{1}{2\pi}\left\{ \underline{b}\,\Phi + \underline{b}_e \frac{\sin 2\Phi}{4(1-\nu)} + (\underline{b}\wedge\underline{u}) \times \ldots \right.$$

$$\left. \ldots \times \left[\frac{1-2\nu}{2(1-\nu)} \ln|r| + \frac{\cos 2\Phi}{4(1-\nu)} \right] \right\}$$

where $\underline{b}$ is its Burgers vector, $\underline{b}_e$ its edge component, $\underline{u}$ its line direction, ν Poisson's ratio and r and Φ are the polar coordinates in a plane normal to $\underline{u}$. The kinematical theory calculations were performed by a program that evaluated the integral (3.5) using a numerical procedure based on the trapezoidal rule. The dynamical calculations were obtained from essentially the program described in Chapter 5. The criterion of Cockayne et al of course, gives analytical solutions, and for a dislocation parallel to the foil plane, the image peak is predicted to occur at a distance X_w from the projection of the dislocation where

$$X_w = -\frac{\underline{g}\cdot\underline{b}}{2\pi s}\left(1 + \frac{\varepsilon}{2(1-\nu)}\right)$$

where $\varepsilon = 1$ for an edge dislocation

and $\varepsilon = 0$ for a screw dislocation.

If X_k is the corresponding position of the prediction of kinematical theory, the numerical calculations confirmed the results of Hirsch et al (1960) and Gevers (1962) namely that (for $\underline{g}.\underline{b} = 2$)

$$X_k \simeq -\frac{2.1}{2\pi s} \qquad \text{(edge dislocation)}$$

$$X_k \simeq -\frac{1.0}{2\pi s} \qquad \text{(screw dislocation)}$$

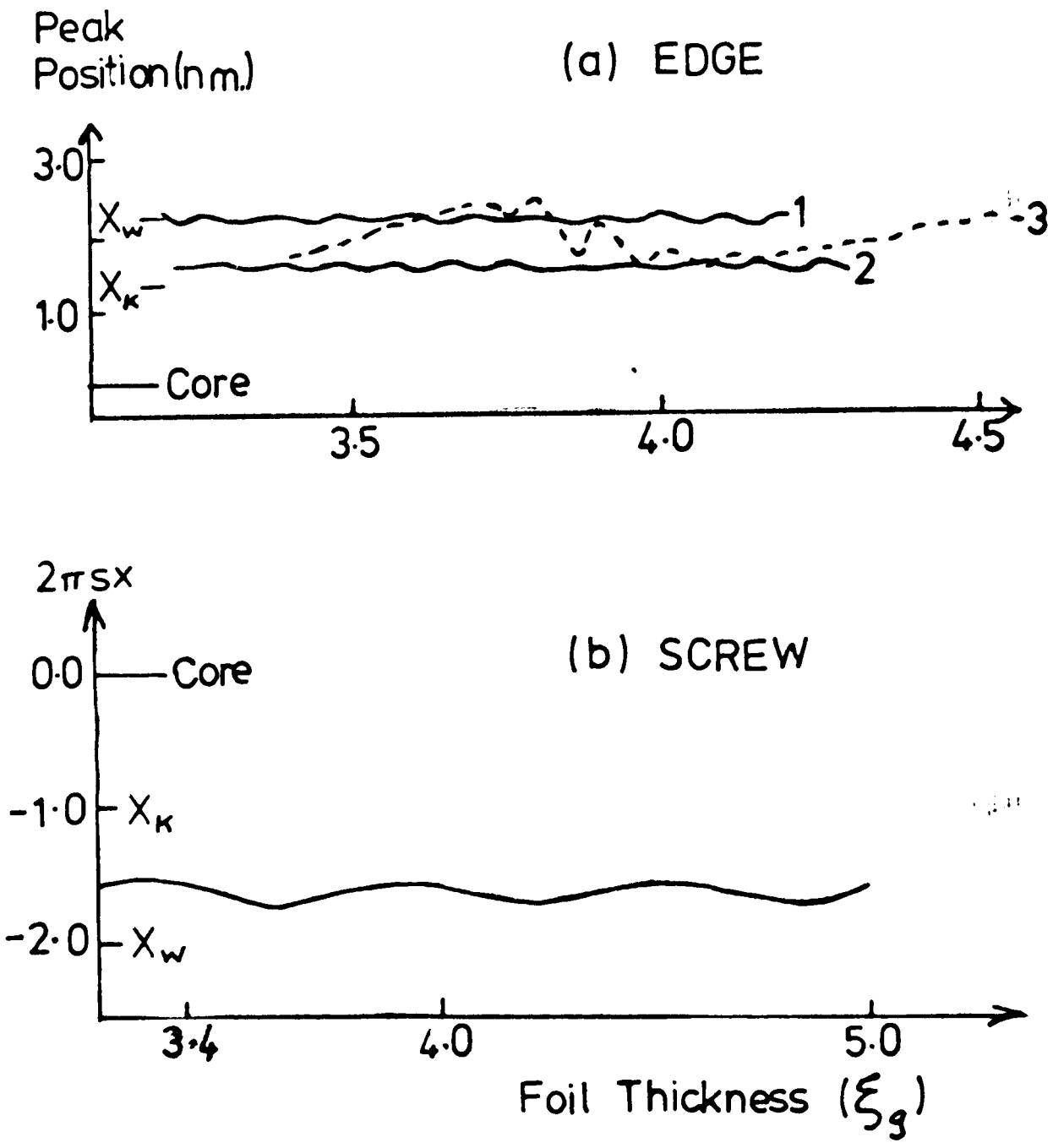

Peak
Position (nm.)
(a) EDGE
3·0
1·0
X_w
X_K
Core
1
2
3
3·5
4·0
4·5
$2\pi sx$
0·0
Core
-1·0
X_K
-2·0
X_w
(b) SCREW
3·4
4·0
5·0
Foil Thickness (ξ_g)

FIGURE 3·2

Figure 3.2

(a) A plot of the weak-beam image peak position as a function of foil thickness for an undissociated edge dislocation in copper. It can be seen that the peak position lies between X_w and X_K. Parameters $|\underline{g}.\underline{b}| = 2$; 6-beam calculations, 100kV electrons; isotropic elasticity

Curve 1, dislocation depth = $2.20\xi_g$; $\underline{g} = \bar{2}\bar{2}0$; $Sg = -0.24nm^{-1}$

Curve 2, dislocation depth = $1.56\,\xi_g$
$g = \bar{2}\bar{2}0$; $Sg = -0.25\ nm^{-1}$

Curve 3, dislocation depth = $2.20\,\xi_g$;
$g = 220$; $Sg = 0.24\ nm^{-1}$

(b) A similar plot for a screw dislocation

Dislocation depth = $2.2\,\xi_g$; $g = 2\bar{2}0$; $S_g = 0.24\,nm^{-1}$

These results, together with the variations of the dynamical theory peak positions as a function of crystal thickness are given in Fig.3.2 (a) and (b). The results for edge and screw dislocations are plotted on separate graphs. Fig.3.2(a) considers three different dislocation depths and two different diffraction conditions (see figure caption).

Both graphs indicate that to a good approximation, the image peak positions calculated on the basis of dynamical theory lie between X_K and X_W although Curve 3 for the edge dislocation oscillates quite considerably between these limits.

An interesting point about Fig.3.2(a) is that the dominant frequency of oscillation of the curves 1 and 2 is very different from that of curve 3. It is tempting to look at the dispersion surface to see whether the dominant Bloch waves in the former case have a larger separation in reciprocal space than those in the latter case. Equation (1.13) may be rewritten

$$\left([S_g]_D + \underline{\underline{4}} - [u_o + i u_o'] \underline{\underline{I}}\right)\{C_g^{(l)}\} = \gamma^{(l)}\{C_g^{(l)}\}$$

where $\gamma^{(l)} = k_z^{(l)} - K_z$ and $\underline{\underline{I}}$ is the unit matrix. ($k_z^{(l)}$ is the z-component of Bloch wave (l) and K_z the z-component of the incident electron wave-vector corrected for the effect of mean refraction). For a perfect crystal, we may find the matrix $\underline{\underline{C}}$ and the eigenvectors $\gamma^{(l)}$. The following tables show the values of two rows of $\underline{\underline{C}}$ and corresponding $\gamma^{(l)}$'s for the two cases of Fig.3.1a

ℓ	1	2	3	4	5
$\gamma^{(\ell)}$ ($\AA^{-1}$)	-4.19 x10^{-5}	-7.82 x 10^{-3}	-1.57 x 10^{-2}	-3.77 x 10^{-2}	-5.37 x 10^{-2}
$C^{(\ell)}_{000}$ ($=\psi^{(\ell)}(0)$)	-0.983	0.166	0.075	-0.010	-0.007
$C^{(\ell)}_{\bar{2}\bar{2}0}$	-0.081	-0.032	-0.996	-0.010	-0.031

Table 1

Case of Curves 1 and 2 of Fig. 3.2(a)

ℓ	1	2	3	4	5
$\gamma^{(\ell)}$ ($\AA^{-1}$)	-1.34 x 10^{-3}	-4.28 x 10^{-3}	-2.32 x 10^{-2}	-2.79 x 10^{-2}	-6.70 x 10^{-2}
$C^{(\ell)}_{000}$ ($=\psi^{(\ell)}(0)$)	0.483	-0.874	-0.022	-0.048	-0.003
$C^{(\ell)}_{\bar{2}\bar{2}0}$	0.873	0.485	-0.059	-0.013	-0.006

Table 2

Case of Curve 3 of Fig. 3.2(b)

Figure 3.3

Micrographs of extended nodes in silicon, weak-beam conditions

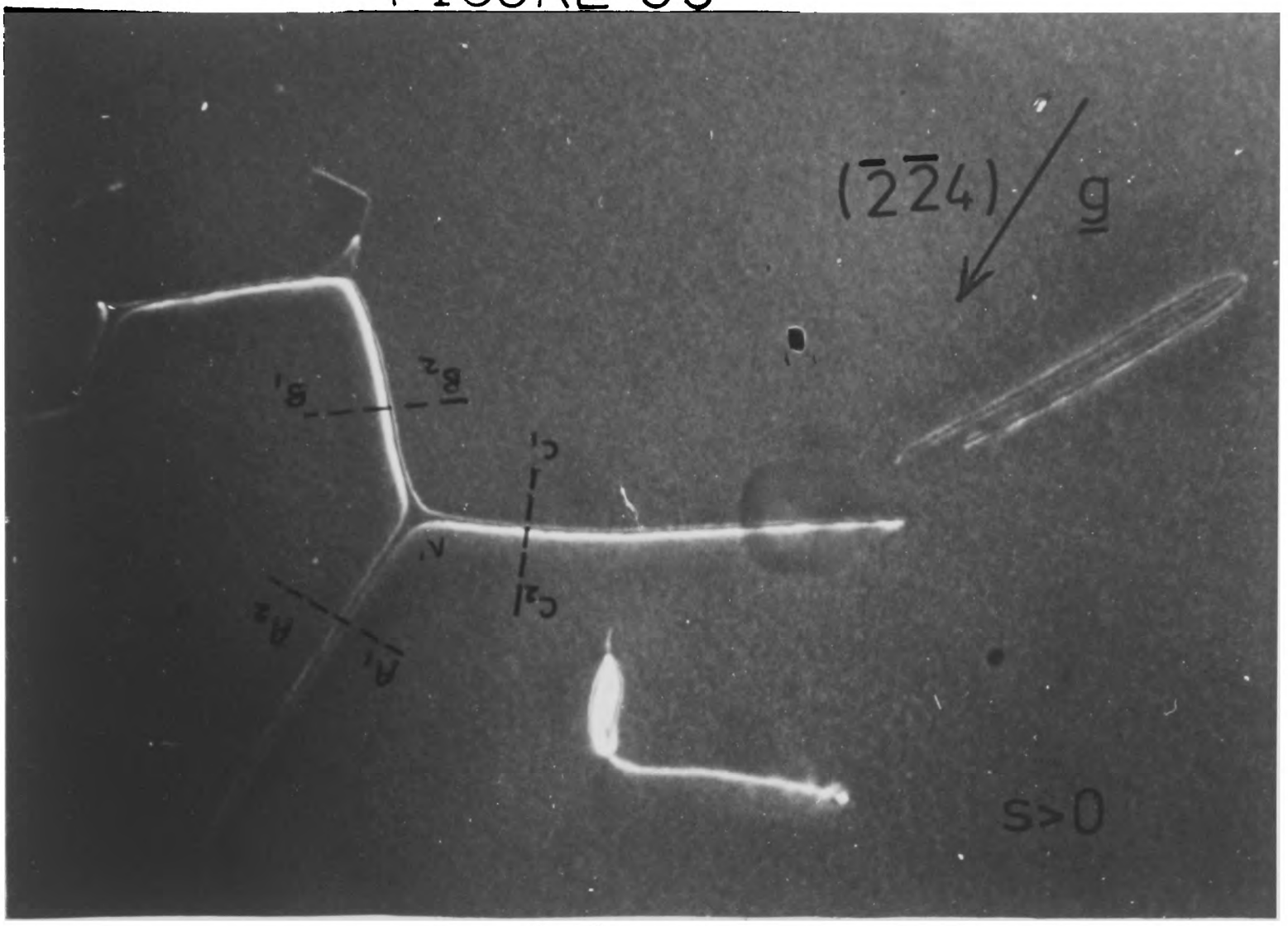
(a) $W \simeq 10$

(b) $W \simeq -10$

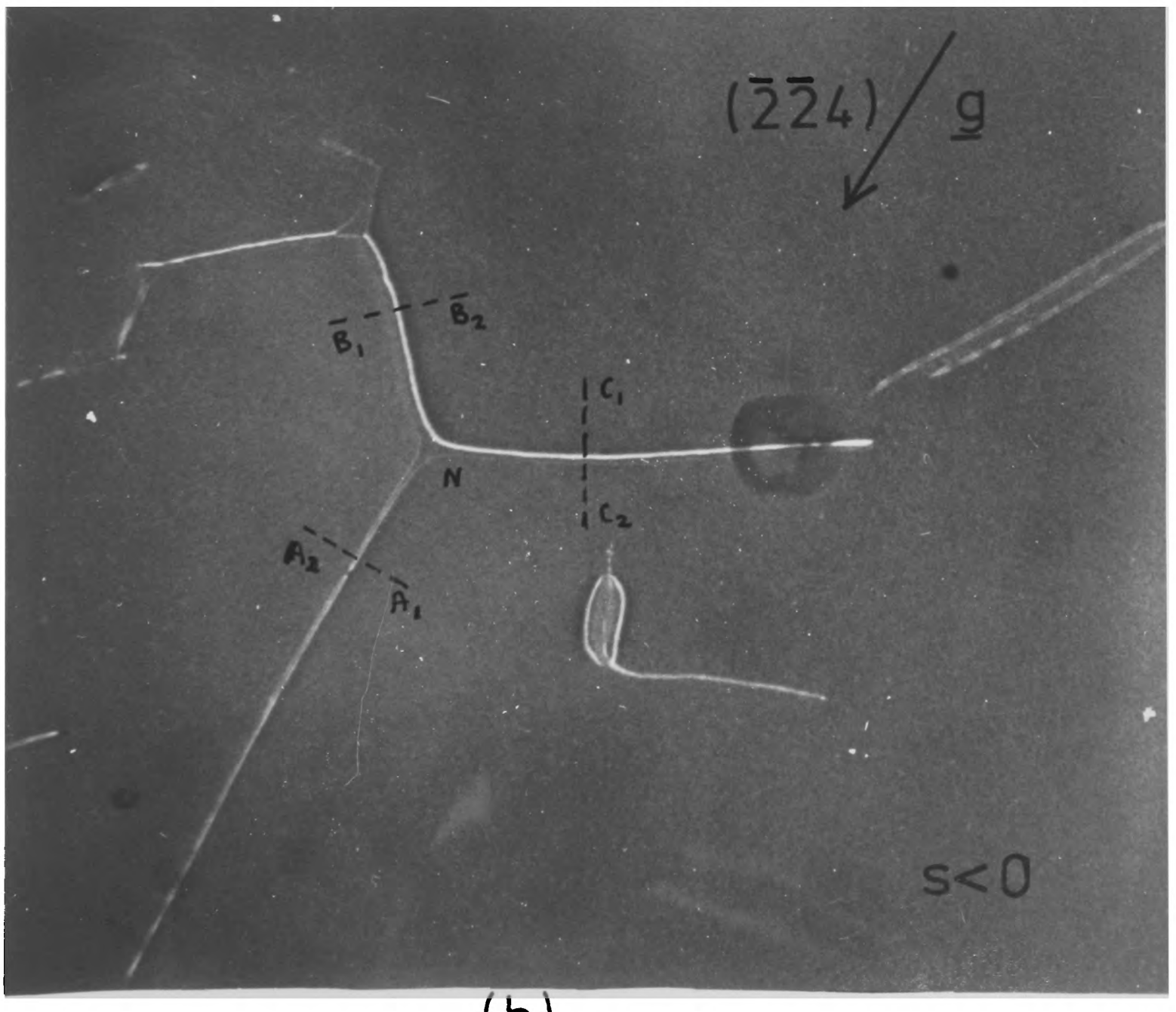
(Photographs taken by A.G.Cullis)

Foil normal [111] Operating reflection $\underline{g}$.

FIGURE 3.3



(a)



(b)

On a kinematical Bloch-wave scattering theory which appears to be valid under these weak-beam conditions, we do not expect much re-distribution of amplitudes by the defected crystal amongst the branches of the dispersion surface. Thus we would expect $\psi^{(l)}(t) \simeq \psi^{(l)}(0)$ for all l and $\phi_j(t) \simeq \sum \psi^{(l)}(t) C_g^{(l)}$ where we need only add the products which contribute appreciably to the sum. Examination of tables 1 and 2 shows that for the curves 1 and 2 we need only consider Bloch waves 1 and 3 (numbering from the top of the dispersion surface) and for curve 3 we need consider only waves 1 and 2. The beat frequencies would give rise to a periodicity in Fig.3.2(a) of about 0.1 ξ_{220} in the former case and about 0.8 ξ_{220} in the latter case. These are in fact about the frequencies observed, thus giving further support to the concept of kinematical Bloch wave scattering.

Similar arguments are applicable to Fig.3.2(b) which considers the variation of the image peak from a screw dislocation.

3.7 Weak-beam contrast from extended nodes in silicon

Figures 3.3 (a) and (b) are micrographs of an extended node in silicon, obtained under two different weak-beam conditions. Figure 3.3(a) was formed from a beam with a deviation parameter of about 10 while figure 3.3b from a beam with $w \simeq -10$. These photographas were taken by A.G.Cullis.

The great variations of the contrast amongst the different pairs of partial dislocations leading away from the node, as well as the changes of the behaviour of the images from the same pair of partials from conditions (a) to conditions (b), make these micrographs a good test case for (i) seeing whether the contrast

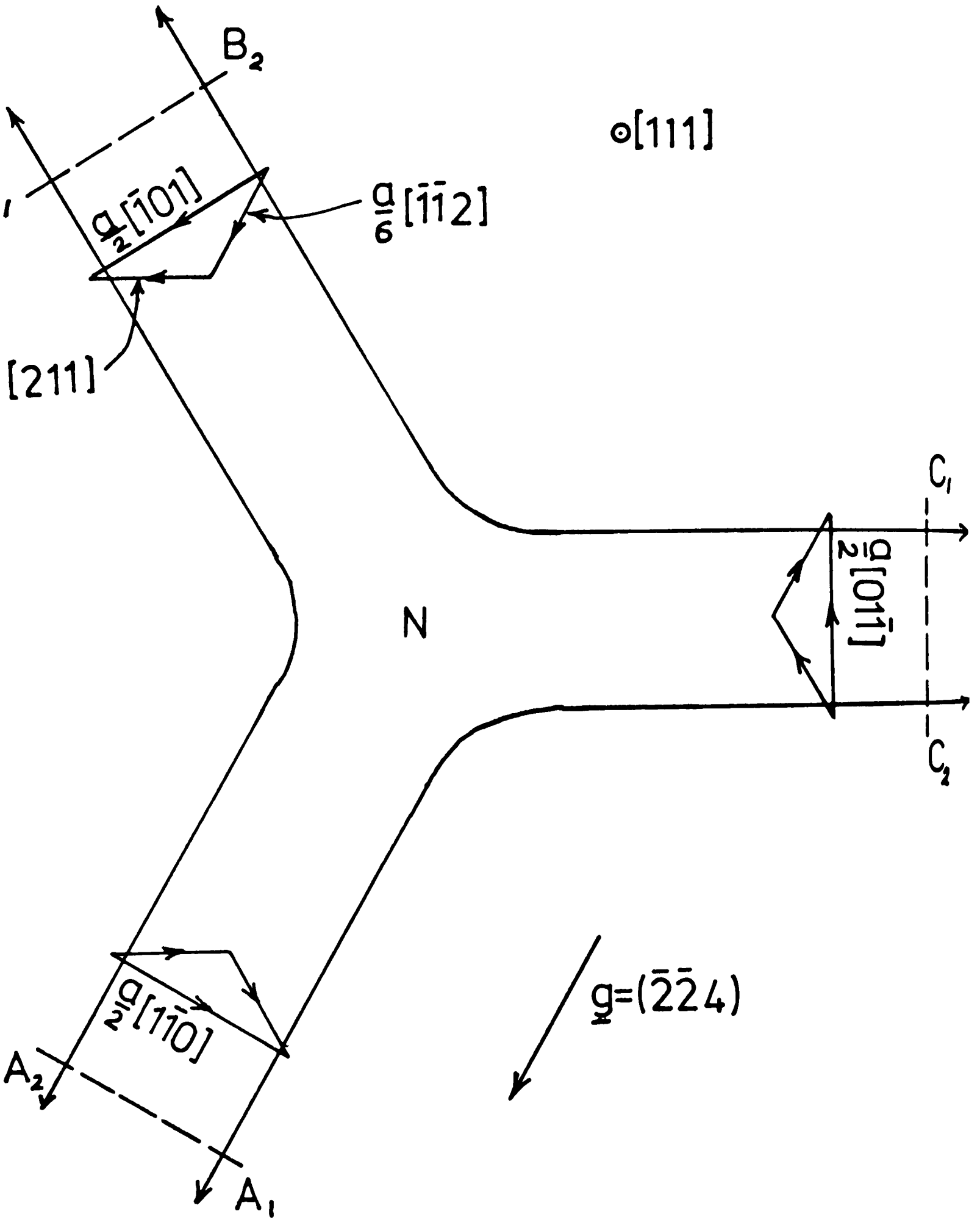


FIGURE 3·4 .

behaviour is predicted by electron diffraction theory (ii) testing the agreement of the modified kinematical theory of § 3.3.1 and 3.4.1 with the predictions of a n-beam dynamical theory.

Figure 3.4 is a schematic diagram of the partial dislocations making up the extended node and also indicates their respective Burgers' vectors.

The lines A_1A_2, B_1B_2 and C_1C_2 are marked on both the micrographs Fig.3.3(a) and (b) and the schematic representation Figure 3.4. These have directions perpendicular to each of the three pairs of partials, and cross the partials at a considerable distance from the node centre N. Figures 3.5 (a) to (f) show image profiles along these lines, calculated on both a 5-beam dynamical theory and on the modified kinematical theory. In each case the profiles are those observed when looking away from the node centre.

The plane of the node system was $(\bar{1}\bar{1}1)$. The weak reflection in which the images were formed was $(2\ 2\ 4)$. The deviation parameters of this reflection in the cases 3.3(a) and 3.3(b) were approximated by 9.89 and -10.02 respectively. If $\underline{\chi}_x$ is the componentof the incident wave vector in the direction of the systematic row of reciprocal lattice points containing $(2\ 2\ 4)$ then $\underline{\chi}_x = -0.69\ \underline{g}_{224}$ and $\underline{\chi}_x = -0.308\underline{g}_{224}$ for the two respective cases. In the former case the dynamical calculation included the effects of the reflections $(4\ 4\ 8)$, $(6\ 6\ 12)$ and $(\bar{2}\ \bar{2}\ \bar{4})$ while in the latter case the other reflections considered were $(4\ 4\ 8)$, $(\bar{4}\ \bar{4}\ \bar{8})$ and $(\bar{2}\ \bar{2}\ \bar{4})$.

Figure 3.5 (a) to (f)

Image profiles across partials leading away from extended node shown in Figure 3.4.

Dynamical theory ——

Kinematical theory — — —

Foil Thickness: $0.8\xi_g$

Depth of Defect: $0.4\xi_g$

w=10·0

w=-10·0

A_1A_2

$(\times 10^{-2})$

Intensity

4·0

2·0

B_1B_2

12·0

4·0

4·0 8·0 12·0 $(\times 10^{-2}\ \xi_g)$ 4·0 8·0 12·0

C_1C_2

14·0

6·0

Figures 3.5 (a) to (f) show good agreement between the features of the observed and calculated contrast. In addition the agreement between the dynamical and kinematical calculations is excellent. The amount of computer time taken to perform the kinematical calculations was only a fraction of that required to do the dynamical computations.

It may therefore be proposed that weak-beam computations of image contrast where the deviations from the Bragg condition are about those given here, may in future use the modified kinematical theory of § 3.3.1 without any significant loss of accuracy and with significant savings of computer time. In addition, the essentially simpler numerical procedures for evaluating the definite integrals of the kinematical theory as compared to the complicated methods of solving the coupled differential equations of dynamical theory, are likely to result is a smaller loss of accuracy through rounding-off and truncation errors.

4.1 Introduction

The dynamical theory of electron diffraction and its use in the study of intensities of diffracted beams from imperfect crystals was outlined in Chapter 1. We saw that the problem could be formulated in terms of differential equations for the amplitudes either of the diffracted beams or of Bloch waves.

It is, of course, true, that we are ultimately interested in the amplitudes, and hence the intensities, of the diffracted beams in order to determine image contrast in the electron microscope. In the case of small defect clusters, however we can make use of the fact that, in a perfect crystal, the amplitudes of the various Bloch waves remain constant throughout the crystal. Since the defects are small compared to the thickness of the crystal, deviations from crystal perfection are only considerable in the immediate vicinity of the defect.

We may thus use approximate theories applied to the Bloch wave case, based on weak or no scattering among Bloch waves in the greater part of the thickness of the crystal.

4.2 Bloch Wave scattering of lattice defects

We use notation similar to that of Wilkens, Katerbau and Ruhle (1973) and define

$$\underline{\underline{Q}}_z = \underline{\underline{C}}^{-1} \left[U_{g,z} \right]_D \underline{\underline{C}}$$

we may re-write equation (1.20) as

$$\frac{d}{dz} \psi^{(l)} = 2\pi i \sum_{l'} Q_{,z}^{l,l'} \psi^{l'} \exp\left[2\pi i \left(\Gamma^{(l')} - \Gamma^{(l)}\right) z\right] \qquad (4.1)$$

($Q_z^{l,l'}$ are the matrix elements of $\underline{\underline{Q}}$ where l specifies

the row and 1' the column) These equations were first derived for the two-beam case by Whelan (unpublished) and first appears in a paper by Howie (1963).

We thus see that the effect of the strain-field in the crystal is to redistribute amplitudes among the Bloch-waves. If the crystal is perfect $Q_z^{l,l'} = 0$ and thus the Bloch-wave amplitudes remain constant throughout the column. We define interbranch scattering as that which redistributes amplitude from Bloch-wave 1' to wave 1 where $1 \neq 1'$. Intra-branch scattering occurs for the case $1 = 1'$.

We may therefore re-write equation (4.1), separating these terms

$$\frac{d}{dz}\psi^{(l)} = 2\pi i\, Q_z^{l,l}\psi^{(l)} + 2\pi i \sum_{l' \neq l} Q_z^{l,l'}\psi^{(l')} \exp\{2\pi i(\gamma^{(l')} - \gamma^{(l)})z\} \qquad (4.2)$$

Let $\underline{\underline{Q}} = \underline{\underline{C}}^{-1}[u_n]_D \underline{\underline{C}}$

$Q^{l,l}$ are the diagonal elements of this matrix. We define the phase-factors

$$P_{\pm}^{l}(z) = \exp\left[\pm 2\pi i\{Q^{l,l}(z) - Q^{l,l}(0)\}\right]$$

and transform to new amplitudes $\phi^{(l)}(z)$ defined by

$$\psi^{(l)}(z) = \phi^{(l)}(z)\, P_+^{(l)}(z) \qquad (4.3)$$

Substitution of (4.3) in (4.2) yields

$$\frac{d}{dz}\phi^{(l)}(z) = 2\pi i \sum_{l' \neq l} Q_z^{l,l'} P_-^{l}(z)\, P_+^{l'}(z)\, \phi(z) \exp\{2\pi i(\gamma^{(l')} - \gamma^{(l)})z\} \qquad (4.4)$$

We have thus transformed to a new representation in which the amplitudes $\phi^{(l)}(z)$ are free of intra-branch scattering.

Integration of (4.4) between 0 and t gives

$$\phi^{(l)}(t) - \phi^{(l)}(0) = 2\pi i \sum_{l' \neq l} \int_0^t Q_z^{l,l'} P_-^{(l)}(z) P_+^{(l')}(z) \times \ldots$$

$$\ldots \times \phi^{(l')}(z) \exp\left\{2\pi i \left(\Gamma^{(l)'} - \Gamma^{(l)}\right) z\right\} \qquad (4.5)$$

4.2.1. First Born Approximation applied to Bloch wave scattering

The integral equation (4.5) can be treated by a First Born Approximation to give

$$\phi^{(l)}(t) = \phi^{(l)}(0) + 2\pi i \sum_{l' \neq l} \phi^{(l')}(0) \int_0^t Q_z^{l,l'} P_-^{(l)}(z) P_+^{(l)}(z) \times \ldots$$

$$\ldots \times \exp\left\{2\pi i \left(\Gamma^{(l')} - \Gamma^{(l)}\right) z\right\} \qquad (4.6)$$

and using the reverse transformation

$$\phi^{(l)}(z) = \psi^{(l)}(z) P_-^{(l)}(z)$$

we obtain from (4.6)

$$\psi^{(l)}(t) = \psi^{(l)}(0) P_+^{(l)}(t) + 2\pi i P_+^{(l)}(t) \sum_{l' \neq l} \psi^{(l')}(0) \times \ldots$$

$$\ldots \times \int_0^t Q_z^{l,l'} P_+^{(l')}(z) P_-^{(l)}(z) \exp\left\{2\pi i \left(\Gamma^{(l')} - \Gamma^{(l)}\right) z\right\} dz \qquad (4.7)$$

This equation was obtained by Wilkens, Katerbau and Ruhle (1973).

Cockayne (1972) gave a similar treatment except that he effectively applied the back transformation to equation (4.5) and then applied the First Born Approximation to the function $\psi^{(l')}(z)$ on the R.H.S. In this treatment the factor $P_+^{(l)}(z)$ on the R.H.S.

of (4.7) cancels out and we obtain, the same expression except for this factor.

There is no clear reason for considering either Wilkens' or Cockayne's treatment more accurate than the other. In any case, for small defect clusters, $P_+^{(l)}(z)$ is non-zero for only a narrow region around the defect, and it is therefore arguable that the results of the two treatments will be very similar.

4.3 The Two-Beam Case

Frequently in electron microscopy the crystal under observation is tilted such that the exact Bragg condition is satisfied for only one reflection. This is the so-called two-beam case and the intensities in the direct beam and the Bragg reflection can be calculated by considering the dynamic interaction between only these beams. In this two beam case there are only two important Bloch waves and the kinematical scattering between these Bloch waves by a defect was first considered by Wilkens (1964a,b,)

$$\psi^{(1)}(t) = \psi^{(1)}(0) - \pi i\, \psi^{(2)}(0) \int_0^t u_{g,z}(z) \exp(2\pi i\, \Delta\Gamma z)\, dz \qquad (4.8a)$$

$$\psi^{(2)}(t) = \psi^{(2)}(0) - \pi i\, \psi^{(1)}(0) \int_0^t u_{g,z}(z) \exp(-2\pi i\, \Delta\Gamma z)\, dz \qquad (4.8b)$$

where $\Delta\Gamma = \Gamma^{(2)} - \Gamma^{(1)}$

The equations are obtained by assuming $P_{\pm}^{(l)}(t) = 1$ for $l = 1$ and 2

This implies that the displacement field $\underline{R}(z) = 0$ at the bottom of the foil.

4.3.1 Black-White images of small defects

We define

$$C = \int_0^t U_{g,z}(z) \cos\{2\pi \Delta\Gamma (z - t_o)\}\, dz$$

$$S = \int_0^t U_{g,z}(z) \sin\{2\pi \Delta\Gamma (z - t_o)\}\, dz \qquad (4.9)$$

where t_o is the depth of the centre of the defect in the column.

Equations (4.8) can then be written

$$\psi^{(1)}(t) = \psi^{(1)}(o) + \pi\, \psi^{(2)}(o) \exp(2\pi i \Delta\Gamma t_o)[S - iC]$$

$$\psi^{(2)}(t) = \psi^{(2)}(o) - \pi\, \psi^{(1)}(o) \exp(-2\pi i \Delta\Gamma t_o)[S + iC] \qquad (4.10)$$

In the electron microscope however, we only observe the "Darwin" amplitudes $\phi_o(t)$ and $\phi_g(t)$. If $\underline{R}(t) = o$ equation (1.20).becomes in the two-beam case :

$$\left.\begin{aligned}\phi_o(t) &= C_o^{(1)} \psi^{(1)}(t) \exp(2\pi i \Gamma^{(1)} t) + C_o^{(2)} \psi^{(2)}(t) \exp(2\pi i \Gamma^{(2)} t)\\ \phi_g(t) &= C_g^{(1)} \psi^{(1)}(t) \exp(2\pi i \Gamma^{(1)} t) + C_g^{(2)} \psi^{(2)}(t) \exp(2\pi i \Gamma^{(2)} t)\end{aligned}\right\} \qquad (4.11)$$

4.3.2 Absorption

In general of course the Γ's will be complex and one can make the identifications

$$\Gamma^{(l)} \Rightarrow \Gamma^{(l)} + i q^{(l)}$$

$$\Delta\Gamma \Rightarrow \Delta\Gamma + i \Delta q$$

Then substitution of (4.9) into (4.10) yields,

$$\phi_o(t) = C_o^{(1)} \left\{ \psi^{(1)}(o) + \pi \psi^{(2)}(o) \exp(2\pi i \Delta\Gamma t_o) \times \ldots \right.$$
$$\left. \ldots \times \exp(-2\pi \Delta q t_o)[S - iC] \right\} \exp(2\pi i \Gamma^{(1)} t) \exp(-2\pi q^{(1)} t) + \ldots$$
$$\ldots + C_o^{(2)} \left\{ \psi^{(2)}(o) - \pi \psi^{(1)}(o) \exp(-2\pi i \Delta\Gamma t_o) \exp(2\pi \Delta q t_o) \times \ldots \right.$$
$$\left. \ldots \times [S + iC] \right\} \exp(2\pi i \Gamma^{(2)} t) \exp(-2\pi q^{(2)} t) \qquad (4.12)$$

and

$$\phi_g(t) = C_g^{(1)} \left\{ \psi^{(2)}(o) + \pi \psi^{(2)}(o) \exp(2\pi i \Delta\Gamma t_o) \exp(-2\pi \Delta q t_o) \times \ldots \right.$$
$$\left. \ldots \times [S - iC] \right\} \exp(2\pi i \Gamma^{(1)} t) \exp(-2\pi q^{(1)} t) + \ldots$$
$$\ldots + C_g^{(2)} \left\{ \psi^{(2)}(o) - \pi \psi^{(1)}(o) \exp(-2\pi i \Delta\Gamma t_o) \exp(2\pi \Delta q t_o) \times \ldots \right.$$
$$\left. \ldots \times [S + iC] \exp(2\pi i \Gamma^{(2)} t) \exp(-2\pi i q^{(2)} t) \right.$$

(4.12)

4.3.3. General expressions for amplitudes for large absorption

Hirsch (1966) first showed that when anomalous absorption is important expressions (4.12) are considerably simplified. In that case,

$$q^{(2)} \gg q^{(1)}$$

and hence $\exp(-2\pi q^{(2)} t) \ll \exp(-2\pi q^{(1)} t)$

Thus the terms including $\psi^{(2)}(o)\exp(-2\pi q^{(2)}t)$ in equations (4.11) can be neglected. We thus obtain after suitable rearrangments, and the substitution of the boundary conditions $\psi^{(1)} = C_o^{(1)}$

$$\phi_o(t) = \Big[C_o^{(1)}\Big\{ C_o^{(1)} + \pi C_o^{(2)} \exp(2\pi i \Delta\Gamma t_o) \exp(-2\pi \Delta_q t_o) \times \ldots \times [S - iC] - \pi C_o^{(2)} \exp[2\pi i \Delta k (t-t_o)] \exp[-2\pi \Delta_q (t-t_o)] \times \ldots \times [S+iC]\Big\}\Big] \exp(2\pi i \Gamma^{(1)} t) \exp(-2\pi q^{(1)} t) \qquad (4.13a)$$

and

$$\phi_g(t) = \Big[C_g^{(1)}\Big\{ C_o^{(2)} + \pi C_o^{(2)} \exp(2\pi i \Delta\Gamma t_o) \exp(-2\pi \Delta_q t_o) \times \ldots \times [S - iC]\Big\} - \Big\{ C_g^{(2)} C_o^{(1)} \exp[2\pi i \Delta\Gamma (t-t_o)] \exp[-2\pi \Delta_q (t-t_o)] \times \ldots \times [S+iC]\Big\}\Big] \exp(2\pi i \Gamma^{(1)} t) \exp(-2\pi q^{(1)} t) \qquad (4.13b)$$

4.3.4 Defects near electron entry surface

For defects near the top surface of the foil $\exp\{-2\pi \Delta_q (t-t_o)\}$ $\ll \exp\{-2\pi \Delta_q t_o\}$ and we can thus neglect the third terms within the curly brackets.of both equations 4.13a and 4.13b

The intensities are then given by

$$|\phi_o(t)|^2 = C_o^{(1)*} C_o^{(1)} \{ C_o^{(1)*} C_o^{(1)} + \ldots$$

$$\ldots + 2\pi \, Re\,(C_o^{(1)*} C_o^{(2)}) [S\cos(2\pi \Delta\Gamma t_o) + C\sin(2\pi \Delta\Gamma t_o)] \times \ldots$$

$$\ldots \times \exp(-2\pi \Delta q t_o)\} \exp(-4\pi q^{(1)} t)$$

(4.14 a)

and,

$$|\phi_g(t)|^2 = C_g^{(1)*} C_g^{(1)} \{ C_o^{(2)*} C_o^{(2)} + 2\pi [S\cos(2\pi \Delta\Gamma t_o) + \ldots$$

$$+ C\sin(2\pi \Delta\Gamma t_o)] \exp(-2\pi \Delta q t_o)\} \exp(-4\pi q^{(1)} t)$$

(4.14 b)

where in this first order treatment, terms in S^2 and C^2 have been neglected, and it has been assumed that the imaginary parts of the coefficients $C_g^{(i)}$ are small compared to their real parts.

In each of the expressions equation 4.14(a) and 4.14(b), the first terms within the curly brackets represent background intensity. The contribution due to the defect scattering is provided by the second terms. Even in this case where absorption is considered, the coefficients $C_g^{(i)}$ are closely approximated by their two-beam values, viz:-

$$\begin{pmatrix} C_o^{(1)} & C_o^{(2)} \\ C_g^{(1)} & C_g^{(2)} \end{pmatrix} \equiv \begin{pmatrix} \cos\beta/2 & \sin\beta/2 \\ -\sin\beta/2 & \cos\beta/2 \end{pmatrix} \quad (4.15)$$

where at the Bragg reflecting position, $\beta = \pi/2$ (see Hirsch et al., 1965, p.200). This approximation is also frequently employed when calculating the absorption coefficients from a matrix element containing the original Bloch eigenvectors, and is of standard use in perturbation theory in general. These values for $C_g^{(i)}$ indicate that the factor $Re\,(C_o^{(1)*} C_o^{(2)})$ in equation (4.14a) is positive. Thus the functional form of the contribution of defect scattering to $|\phi_o(t)|^2$ and

$|\phi_g(t)|^2$ is identical (though they differ by the value of a constant). This indicates that when a defect is near the electron entry surface of a foil, its bright- and dark-field images are similar in form.

4.3.5 Defects near the electron exit surface

In the case of defects near the electron exit surface,

$$\exp(-2\pi\Delta q\, t_o) \ll \exp(-2\pi\Delta q[t-t_o])$$

and thus the second terms in equations 4.13 are negligible, and a similar analysis gives,

$$|\phi_o(t)|^2 = |C_o^{(1)}|^2 \{ |C_o^{(1)}|^2 - 2\pi\, Re(C_o^{(1)*} C_o^{(2)}) \times \ldots$$
$$\ldots \times [S\cos\{2\pi\Delta\Gamma(t-t_o)\} - C\sin\{2\pi\Delta\Gamma(t-t_o)\}] \times \ldots$$
$$\ldots \times \exp(-2\pi\Delta q[t-t_o])\} \exp(-4\pi q^{(1)} t)$$

(4.16 a)

and

$$|\phi_g(t)|^2 = \{ |C_g^{(1)}|^2 |C_o^{(2)}|^2 - 2\pi\, Re(C_g^{(1)*} C_o^{(2)*} C_g^{(2)} C_o^{(1)}) \times \ldots$$
$$\ldots \times [S\cos\{2\pi\Delta\Gamma(t-t_o)\} - C\sin\{2\pi\Delta\Gamma(t-t_o)\}] \times \ldots$$
$$\ldots \times \exp(-2\pi\Delta q[t-t_o])\} \exp(-4\pi q^{(1)} t)$$

(4.16 b)

The first terms of R.H.S.'s of (4.16(a) and (b) again represent background intensity. From equation (4.15) it is easy to see that the factor $Re(C_o^{(1)*} C_o^{(2)})$ in equation (4.16a) is positive

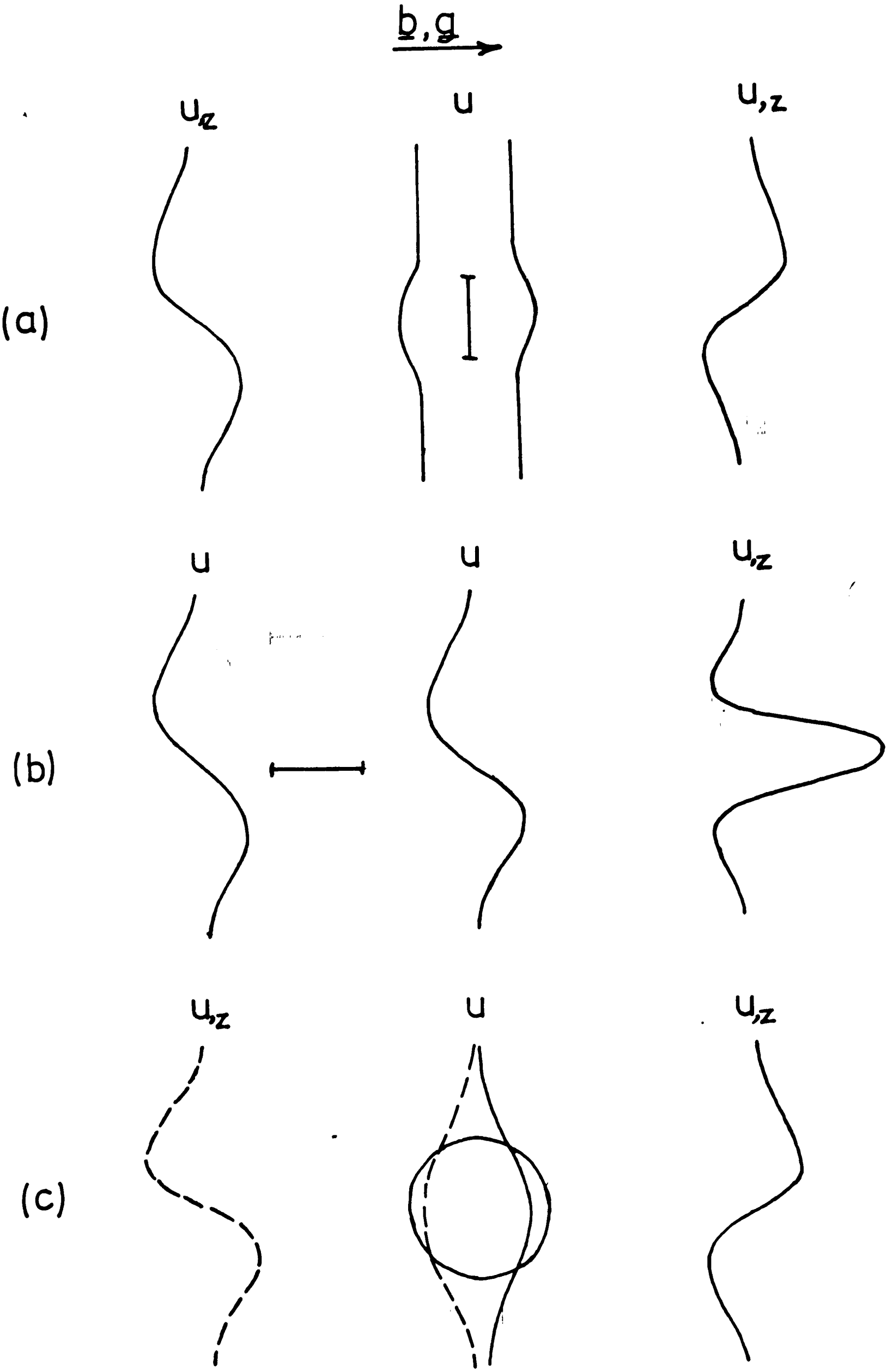


FIGURE 4·1

while the factor $Re\left(C_g^{(1)*} C_o^{(2)} C_g^{(2)} C_o^{(1)}\right)$ in equation (4.16b) is negative. Therefore, the functional forms of the second terms in (4.16(a) and (b) are identical, but their coefficients have opposite signs. Thus a region of an electron microscope specimen which gives supra-background intensity in bright-field would give sub-background intensity in dark field. Hence crystal defects near the electron-exit surface of a foil produce bright- and dark-field images which are complementary.

4.4 Contrast from some special defects

When the function $u_{g,z}(z)$ is either symmetric or anti-symmetric about the centre of the defect, equations (4.14) and (4.15) are further simplified. If $u_{g,z}$ is symmetric, it is easy to see from equations (4.9) that $S = 0$. If $u_{g,z}$ is anti-symmetric $C = 0$.

4.4.1 Edge-on Frank Loop

Figure 4.1(a) shows schematically the bending of the lattice planes around a Frank loop and also the variation of its derivative $u_{g,z}(z)$. The latter is clearly anti-symmetric about the loop centre. Thus $C \doteq 0$. Also since $u_{g,z}(z)$ changes sign from one side of the loop to the other, S will have opposite signs for a given depth t_o. This gives rise to the so-called "black-white" contrast with the intensity above background on one side of the loop and below background on the other. Also, if we define a vector $\underline{l}$ whose direction is from the centre of the "black" lobe to the centre of the "white" one, we see that the direction of $\underline{l}$ reverses at depths

$\frac{1}{4}\xi_g$, $\frac{3}{4}\xi_g$, $\frac{5}{4}\xi_g$, ..., $\frac{(2n-1)}{4}\xi_g$, ...

from each of the foil surfaces. (see equation 4.15) (We define $\xi_g = \frac{1}{\Delta\Gamma}$). We also see that the dark-field image of a loop near the lower surface of the foil has $\underline{l}$ in the same direction as an image (bright or dark-field) of a loop near the top surface.

4.4.2 Edge-on pure shear loop

An edge-on pure shear loop has $u_{g,z}$ antisymmetric about the loop centre. See figure 4.1(c) Then C = 0. It is easy to see that this leads to the vector $\underline{l}$ reversing direction at depths $\frac{1}{2}\xi_g$, ξ_g, $\frac{3}{2}\xi_g$, ..., $\frac{n}{2}\xi_g$, ... from either surface.

4.4.3 Flat-on pure shear loop

Figure 4.1(b) shows that in this case $u_{g,z}$ is symmetric and hence that as with the edge-on Frank loop S = 0. Now however, C has the same sign for both sides of the loop. Hence simple "black-white" contrast is not found. On the basis of this approximate theory, pure white or pure black images are expected, with transitions from one to another taking place at depths

$\frac{1}{4}\xi_g$, $\frac{3}{4}\xi_g$, ..., $\frac{(2n-1)}{4}\xi_g$, ...

4.5 Summary

The approximate theory above based on the concept of kinematical scattering of Bloch waves gives a good physical picture of the scattering processes and predicts the broad features of the images of small defects. However in order to obtain fine details of the contrast, for example, concerning the border between the white and the black lobes, it is necessary to perform a full dynamical theory calculation. The next chapter shows how this theory may be used to produce computer simulated images of lattice defects.

Chapter 5

COMPUTER SIMULATION OF ELECTRON MICROSCOPE IMAGES

FLOW CHART for DYNAMICAL THEORY PROGRAM

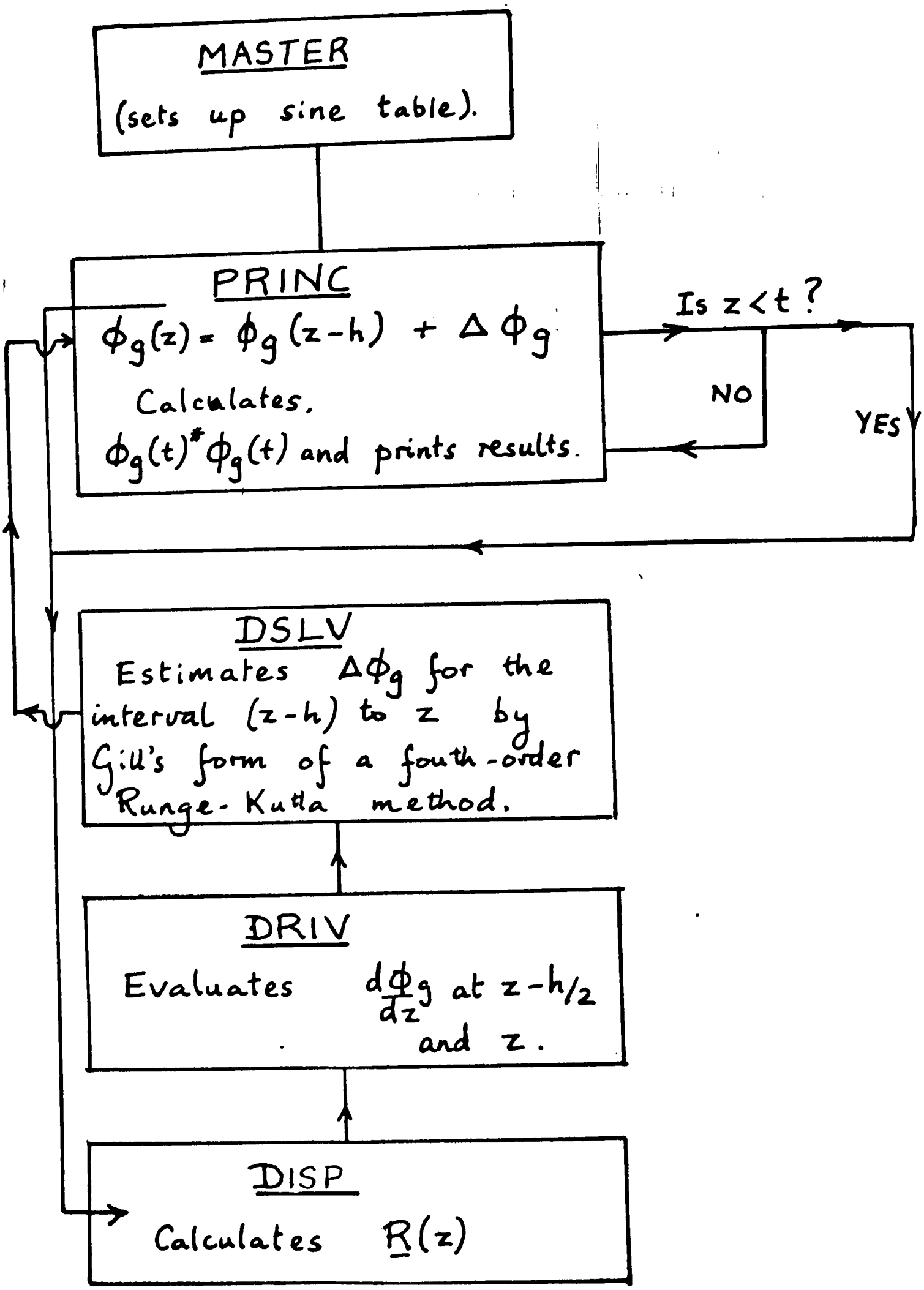


FIGURE 5.1

5.1 Introduction

The last chapter showed how the Bloch wave formulation of dynamical theory may be used to obtain approximate analytical expressions for image contrast. This chapter shows how the Darwin formulation may be used to produce image contrast, with the aid of appropriate numerical techniques. In addition, the use of a display system for producing close likenesses of the simulated image to the corresponding experimental micrographs is described.

5.2 The dynamical theory computer program

A flow chart, showing the various segments of the program is shown in figure 5.1. The program described below uses the column approximation. The program may be modified to obviate the need for invoking this approximation. In that case an extra segment, called by CORRECwould be required. All computations described in this thesis use the column approximation. The purposes and the modes of operation of the various segments of this program are described below. The program used was a modified version of one written by Howie and Swann.

5.2.1 The MASTER segment

The calculation begins by following instructions in this segment. The main purpose of this segment is to set up a table of values of $\sin\theta$ where θ takes 1251 discrete values between 0 and $9/4$. The values of $\sin\theta$ are stored in a COMMON block so that they may be used by other segments. This is a time-saving

device, and as will be seen later the loss of accuracy can be made minimal. Finally the PRINC subroutine is called.

5.2.2 The PRINC subroutine

This is the main and controlling segment of the program. Its functions are summarized below.

READS INPUT parameters:

1. No. of atoms per unit cell.
2. Positions of atoms in unit cell.
3. Humphreys and Hirsch(1968) parameters for absorption coefficients.
4. Parameters for contrast levels of graph plotter.
5. Value of π to 10 sig. figs.
6. Accelerating voltage.
7. Step-length for Runge-Kutta calculation.
8. Lattice parameter.
9. Poisson's ratio.
10. Smith and Burge (1962) atomic scattering factors.
11. Foil normal.
12. Reciprocal lattice vectors of diffracted beams in calculation.
13. Component of incident wave-vector in plane of $\underline{g}$.
14. Foil thickness.
15. No. of thicknesses for which calculation is required.
16. Increment between these thicknesses.
17. Values of X and Y at each column. (The z-axis is normal to the foil).

Normalizes relevant vectors

Calculates structure factor for the input reflections, and hence the extinction distances.

Calculates absorption coefficients.

Calculates deviation parameter s.

Sets initial values of diffracted-beam amplitudes, i.e.

$$\phi_0(0) = 1 \quad ; \quad \phi_g(0) = 0 \qquad \text{for all } \underline{g} \neq 0$$

and also sets independent variable, $z = 0$.

If $z <$ thickness, segment DSLV is called.

If the values of $\phi_g(z)$ are fed into DSLV, the values of $\phi_g(z+h)$ are returned.

The process is continued until $z = t$.

Then the intensities $I_g(t) = \phi_g(t)\,\phi_g^*(t)$

are calculated and written.

Finally the graph plotting is performed by placing the picture points on a grid and drawing equal intensity contours through them.

5.2.3 Subroutine DSLV

This consists of a fourth-order Runge-Kutta method of advancing the solution of the system of n coupled differential equations by an amount $\Delta z = h$ There exists a whole family of fourth-order Runge-Kutta methods. The one used in a particular case depends on the characteristics of the problem. The most convenient for the system of equations (1.25) is Gill's method (1951).
A critical discussion of Runge-Kutta methods in general and Gill's method in particular is given in § 5.3.3.

5.2.4 Subroutine DRIV

This subroutine is concerned with evaluating the R.H.S. of equations (1.25). Real arithmetic is used throughout and therefore equation (1.25) is decomposed into its real and imaginary parts. Then the complex exponentials are converted into sine functions (the cosine functions may be regarded as sine functions displaced along the abcissae by $\pi/2$ radians). Use is then made of the sine table set up in the MASTER segment. If the angle lies between tabulated values of the sine function, use is made of an interpolation procedure based on trigonometric formulae and a small-angle series expansion for sine and cosine functions. Another consequence of separately using the real and imaginary parts is that the N complex differential equations are replaced by 2N real coupled differential equations.

Each evaluation of the R.H.S. of (1.25) requires knowledge of the $\underline{R}(z)$, the value of the displacement field in each column at a depth z. These values of $\underline{R}(z)$ have to be obtained by calling a separate subroutine DISP.

5.2.5 Subroutine DISP

This subroutine depends upon the nature of the defect in the foil. The form of the subroutine for a number of straight parallel dislocations is described in Chapter 3. Chapter 6 describes that for a dislocation loop and Chapter 8 that for a stacking fault tetrahedron.

5.3 Methods for numerically solving coupled ordinary differential equations

5.3.1 Runge-Kutta methods

Perhaps the commonest type of method used is the class of techniques known as Runge-Kutta processes. Starting with initial values of the ordinates, they predict the values of these quantities at the end of a step by evaluating the gradient at various intermediate positions in the step. The order of the process depends on the number of terms in the Taylor series expansion about the initial point. If h is the length of the step, and the highest power of h used is m, then the order of the process is m.

It has been found that the most suitable Runge-Kutta methods are those of order 4. Due to the degrees of freedom available in choosing various constants used in the process, it is possible to use several different fourth-order processes.

5.3.2 Kutta-Merson process

Head (1973) uses the Kutta-Merson process (see Merson 1957). This method permits easy estimation of the truncation error per step, thus enabling routines to be written for automatically choosing an optimum step length for each region of the integration. It integrates the equations

$$\frac{d}{dz}\phi_M \doteq f_M(z, \phi_1, \phi_2, \cdots) \qquad M = 1 \text{ to } 2N$$

where z is the independent variable and ϕ_M's are the dependent variables. If the step length is h, Merson has shown that the increment in ϕ_M is,

$$\delta\phi_M = \frac{1}{2}(K_{M,1} + 4K_{M,4} + K_{M,5}) + O(h^5)$$

where,

$$K_{M,1} = \tfrac{1}{3}\cdot h\, f_M(z\ ,\ \phi_1\ ,\ \phi_2\ ,\ \dots\ )$$

$$K_{M,2} = \tfrac{1}{3}\cdot h\, f_M\left(z+\tfrac{h}{3}\ ,\ \phi_1 + K_{1,1}\ ,\ \phi_2 + K_{2,1}\ ,\ \dots\right)$$

$$K_{M,3} = \tfrac{1}{3}\, h\, f_M\left(z+\tfrac{h}{3}\ ,\ \phi_1 + \tfrac{1}{2}\cdot K_{1,1} + \tfrac{1}{2}\cdot K_{1,2}\ ,\right.$$

$$\left.\phi_2 + \tfrac{1}{2}\cdot K_{2,1} + \tfrac{1}{2}\cdot K_{2,2}\ ,\ \dots\right)$$

$$K_{M,4} = \tfrac{1}{3}\, h\, f_M\left(z+\tfrac{h}{2}\ ,\ \phi_1 + \tfrac{3}{8} K_{1,1} + \tfrac{9}{8} K_{1,2}\ ,\ \dots\right)$$

$$K_{M,5} = \tfrac{1}{3}\, h\, f_M\left(z+h\ ,\ \phi_1 + \tfrac{3}{2} K_{1,1} - \tfrac{9}{2} K_{1,3} + 6 K_{1,4}\ ,\ \dots\right)$$

and an estimate of ε, the error in δY_M is,

$$5\varepsilon = \left| K_{M,1} - \tfrac{9}{2} K_{M,3} + 4 K_{M,4} - \tfrac{1}{2} K_{M,5} \right|$$

The chief drawback of this method when used to solve the equations (1.25) is the fact that the functions f_M have to be evaluated at three different values of z, namely $z + \frac{h}{3}$, $z + \frac{h}{2}$ and $z + h$ for each step. In the context of the dynamical theory program described in § 5.2, this means that SUBROUTINE DISP would be called three times per step. Now in the applications described in this thesis, DISP is the longest subroutine and thus the overall running time of the program would be large.

Gill's process

Gill (1951) proposed an alternative fourth-order Runge-Kutta process which only requires the evaluation of the function f_M at two points per step. This process consists of evaluating the following quantities in the order given (putting $z = \phi_{00}$)

$$K_{M0} = h f_M(\phi_{00}, \phi_{10}, \dots), \quad r_{M1} = \tfrac{1}{2} \cdot K_{M0} - w Q_{M0} + e(r_{M1})$$

$$\phi_{M1} = \phi_{M0} + r_{M1}, \quad Q_{M1} = Q_{M0} + 3 r_{M1} - \tfrac{1}{2} \cdot K_{M0}$$

$$K_{M1} = h f_M(\phi_{01}, \phi_{11}, \dots), \quad r_{M2} = \left[1 - \sqrt{\tfrac{1}{2}}\right](K_{M1} - Q_{M1}) + e(r_{M2})$$

$$\phi_{M2} = \phi_{M1} + r_{M2}, \quad Q_{M2} = Q_{M1} + 3 r_{M2} - \left[1 - \sqrt{\tfrac{1}{2}}\right] K_{M1}$$

$$K_{M2} = h f_M(\phi_{02}, \phi_{12}, \dots), \quad r_{M3} = \left[1 + \sqrt{\tfrac{1}{2}}\right](K_{M2} - Q_{M2}) + e(r_{M3})$$

$$\phi_{M3} = \phi_{M2} + r_{M3}, \quad Q_{M3} = Q_{M2} + 3 r_{M3} - \left[1 + \sqrt{\tfrac{1}{2}}\right] K_{M2}$$

$$K_{M3} = h f_M(\phi_{03}, \phi_{13}, \dots), \quad r_{M4} = \tfrac{1}{6}(K_{M3} - 2 Q_{13}) + e(r_{M4})$$

$$\phi_{M4} = \phi_{M3} + r_{M4}, \quad Q_{M4} = Q_{M3} - 3 r_{M4} - \tfrac{1}{2} K_{13}$$

where e represents the error, and Q_{M4} becomes Q_{M0} for the succeeding step. The optimum value of w was found to be 1. In this process z only takes the values $z + \frac{h}{2}$ and $z + h$ during any function evaluations per step.

The truncation error expression is too unwieldy for convenient evaluation. Therefore this method is not used with an automatic step length optimization routine. However, use of the registers Q enables the errors to be minimized.

5.3.4 Comparison of Kutta-Merson and Gill's processes

We have seen that the main advantage of Gill's process is that the SUBROUTINE DISP needs to be called only twice per step. Its main disadvantage compared to the Kutta-Merson process is that it cannot easily be used with a variable step-length routine to take advantages of regions where the quantities ϕ may be varying slowly.

Now experimentally, accuracy in the intensities of greater than 10% is not easily obtained. Therefore ultra-high accuracy in intensities is not important in the computer simulation work. The most important factor is speed.

Identical computations of image intensity from typical defects were performed, using both the Kutta-Merson and Gill's processes. It was found that Gill's process was considerably faster. It was therefore decided to use Gill's method for all the computations described in this thesis.

5.4 Interpolation Scheme

The main output from the computer programme described in this Chapter is in the form of intensities in various diffracted beams for each column of electron path. The intensities have the magnitudes they would have if unit amplitude was incident on the top surface of the foil.

As might be imagined from the form of the differential equation solving routines of 5.3, the programme is rather lengthy and time-consuming. In fact, in a typical case, say for a $2\,\xi_g$ thick copper foil, calculation of intensities at the bottom of 100 columns takes about $2\frac{1}{2}$ minutes of computer time on the I.C.L. 1906A computer in Oxford. It was decided that this was about the maximum feasible amount of time expendable in simulating a single electron micrograph.

Thus for a two-dimensional micrograph, it is only feasible to compute intensities for a (10 x 10) grid of columns. If these are spaced so as to cover the entire area of the simulated micrograph, an interpolation scheme can be used to obtain the intensities at a large number of intermediate points on the micrograph.

Use is made of the four-point interpolation formula given by Abramowitz and Stegun (1965)

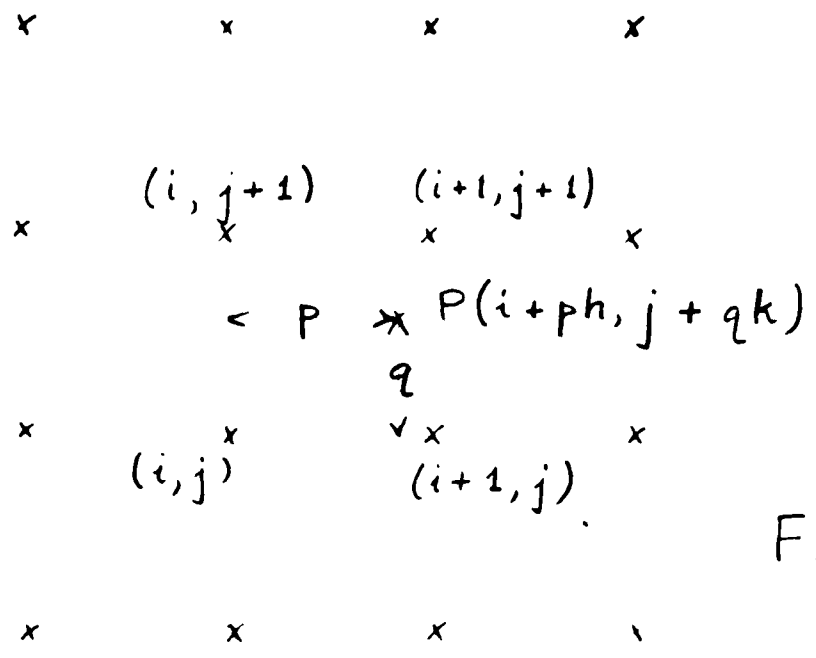


FIGURE 5.2

Figure 5.2 shows a two-dimensional array of points where the intensity is known. The "horizontal" spacing between the points is h and the "vertical" spacing k. Let P be the point whose coordinates are $(i+ph, j+qk)$. Then if $I(i+ph, j+qk)$ is the intensity at P, it is written in terms of the intensities of the square of points immediately surrounding it thus

$$I(i+ph, j+qk) = (1-p)(1-q)\,I(i,j) + \ldots$$
$$+ p(1-q)\,I(i+1, j) + q(1-p)\,I(i, j+1) + \ldots$$
$$\ldots + pq\,I(i+1, j+1) + O(h^2)$$

In this manner, in most of the simulated micrographs in this thesis, the calculated (10 x 10) array was enlarged to a (180 x 180) array of picture points at which values of intensity are known.

5.5 Relationship between density of final photographic print and electron intensity

Using the SC4020, described in 5.6 it is possible to produce various shades of grey in a graduated scale of photographic density on the simulated micrograph. Using diffraction theory we can calculate electron intensity at the lower foil surface. If we assume that the lenses in the electron microscope are perfect, these are also the theoretical electron intensities (except for a scaling term) on the (theoretical) micrograph. Before effective computer simulation can be performed, it is necessary to know the relationship between the electron intensity and the photographic density on the final print. This relationship is obtained by means of the following argument, which is dependent on three different physical stages.

5.5.1 In the electron microscope

Let E be the electron intensity impinging on a point of the photographic plate and D be the photographic density of that point.

Then $$D = k E \qquad (5.1)$$

where k is a constant

(see Valentine, 1966).

5.5.2 In the enlarger

Consider the transmission of light through the plate. Let I_o be the incident light intensity and I_1 be the transmitted intensity. Then the transmission coefficient is $T = \frac{I_1}{I_o}$ and by definition,

$$D = \ln (1/T) \qquad (5.2)$$

and hence from (5.1)

$$kE = \ln\left(I_o / I_1\right)$$

and

$$I_1 = I_o \exp(-kE) \qquad (5.3)$$

5.5.3 On the final (positive) print

If D_p is the density of the print, conventional photographic theory gives

$$D_p = \gamma\left(\ln I_1 - \ln k'\right)$$

where k' is the film speed and γ the contrast.

Hence from (5.3)

$$D_p = \gamma\left\{\ln\left[I_o \exp(-kE)\right] - \ln k'\right\}$$

$$= \gamma\left\{\ln I_o - kE - \ln k'\right\}$$

$$= -\gamma kE + A \qquad (5.4)$$

where the constant $A = \gamma\left\{\ln\left(I_o/k'\right)\right\}$

This establishes the relationship we sought.

5.6 The SC4020 Plotter

This instrument is capable of plotting dots of various shades of grey (ranging from the blank white page to black) at any location within a grid of (1024 x 1024) equally spaced addressable positions. The shades of grey are linearly spaced on a scale of photographic density.

In order to reproduce reasonable micrographs, it was found necessary only to plot points at every third addressable position. In 5.4 we saw that the interpolation process produces a (180 x 180) array of intensities. This in easily acommodated within the grid of addressable positions even when dots were placed at only every third position.

5.7 Adjustment of contrast levels

Equation (5.4) can be written

$$D_p = -BE + A$$

In matching micrographs with corresponding computer simulations, A and B can be regarded as adjustable parameters. If a standard developing technique is used for all electron micrographs, it should in theory, be possible to calculate A and B (see Maher, Perrin, and Bullough, 197). Where such standard methods do not exist, as in the author's laboratory, where developing and printing of electron micrographs are performed by individual microscopists under a wide variety of conditions, it is clearly not feasible to calculate A and B for each case.

In adjusting A and B for reasonable simulation of black-white contrast (conditions which prevail in most micrographs in this thesis), the most important consideration is the level of background intensity (i.e. intensity from undeformed regions in the crystal). Since it is required to display approximately equally prominently the black and white lobes, the background grey level is taken to be at the middle of the scale. Frequently such a procedure displaces the brightest intensities off the one end of the grey scale. This is justified since this simulates the effect of saturation on micrographs.

Chapter 6

CONSTRUCTION OF DISPLACEMENT FIELDS FOR POLYGONAL DISLOCATION LOOPS

Let $x_i \quad (i = 1, 2, 3)$ be orthogonal cartesian coordinates. The stress σ_{ij} is defined as the jth component of the force per unit area acting on a plane whose normal is parallel to the x_i direction. Then, it is easy to show, that if there are no internal torques present,

$$\sigma_{ij} = \sigma_{ji} \tag{6.1}$$

Also if f_i is the ith component of a body force per unit volume,

$$\frac{\partial \sigma_{ij}}{\partial x_j} + f_i = 0 \tag{6.2}$$

using the Einstein summation convention. These are the equilibrium equations.

Bodies deform in response to stresses. If the displacements at a point $\underline{r}$ are u_i, the strains are defined by

$$\varepsilon_{ij} = \frac{1}{2}\left(\frac{\partial u_i}{\partial x_j} + \frac{\partial u_j}{\partial x_i}\right) \tag{6.3}$$

Stiff rotations of elements,

$$\omega_{ij} = \frac{\partial u_i}{\partial x_j} - \frac{\partial u_j}{\partial x_i} \tag{6.4}$$

are only caused by external torques.

6.2.2 Linear Elasticity

In the approximation of linear elasticity, the stresses depend linearly on the strains, that is

$$\sigma_{ij} = c_{ijkl}\, \varepsilon_{kl} \tag{6.5}$$

The coefficients C_{ijkl} are the elastic constants, and the four suffixes imply that any material requires for its description, 81 elastic constants. However, all these elastic constants are not independent. For example, from equation (6.3) we have,

$\varepsilon_{ij} \equiv \varepsilon_{ji}$ and using equation (6.1), it follows that,

$$C_{ijkl} = C_{jikl} = C_{ijlk} = C_{jilk} \qquad (6.6a)$$

Also since the elastic contribution to the Helmholtzfree energy is given by

$$dF = C_{ijkl}\ \varepsilon_{kl}\ d\varepsilon_{ij}$$

Hence $$\frac{\partial^2 F}{\partial \varepsilon_{ij}\ \partial \varepsilon_{kl}} = C_{ijkl}$$

Now since the order of differentiation is immaterial, it follows that $$C_{ijkl} = C_{klij} \qquad (6.6b)$$

The relations (6.6a) and (6.6b) reduce the number of independent elastic constants to 21. By substituting equation (6.3) and equation (6.6a) into equation (6.5), it follows that

$$\sigma_{ij} = C_{ijkl}\ \frac{\partial u_k}{\partial x_l}$$

(The Einstein convention is used throughout this Chapter).

In the case of cubic crystals, the number of independent elastic constants is reduced still further from 21 to 3. Since the axes are invariant with respect to 90° rotations about the cube axes, $C_{iiii} = C_{11}$ (say), $C_{iijj} = C_{12}$ (say) and $C_{ijij} = C_{44}$ (say) for $i \neq j$. All other elastic constants are zero since the sign of ε_{ij}, $i \neq j$ cannot affect the value of σ_{ii} Thus $C_{iiij} = 0$ etc.

If the crystal is also elastically isotropic, the number of independent elastic constants is reduced still further to 2, since the relationship, $2c_{44} = c_{11} - c_{12}$ is satisfied. The factor $A = \frac{2c_{44}}{c_{11} - c_{12}}$ which is known as the anisotropic ratio is thus unity for isotropic crystals.

Frequently used constants for isotropic crystals are μ, λ and ν known as Lamé's constant, the shear modulus and Poisson's ratio respectively. They are defined by the relationships.

$$\mu = c_{44} = \frac{1}{2}(c_{11} - c_{12})$$

$$\lambda = c_{12}$$

$$\nu = \frac{\lambda}{2(\mu + \lambda)} = \frac{c_{12}}{2(c_{44} + c_{12})}$$

6.3 Green's Function of Elasticity

The tensor Green's function $u_{ij}(\underline{r})$ of elastic displacements is defined as the ith component of the displacement at $\underline{r}$ caused by a unit force acting in the jth direction at the origin.

Then a continuous distribution of forces $f_j(\underline{r})$ in an elastic medium causes displacements

$$u_i(\underline{r}) = \int u_{ij}(\underline{r} - \underline{r}') f_j(\underline{r}') \, d^3\underline{r}' \qquad (6.7)$$

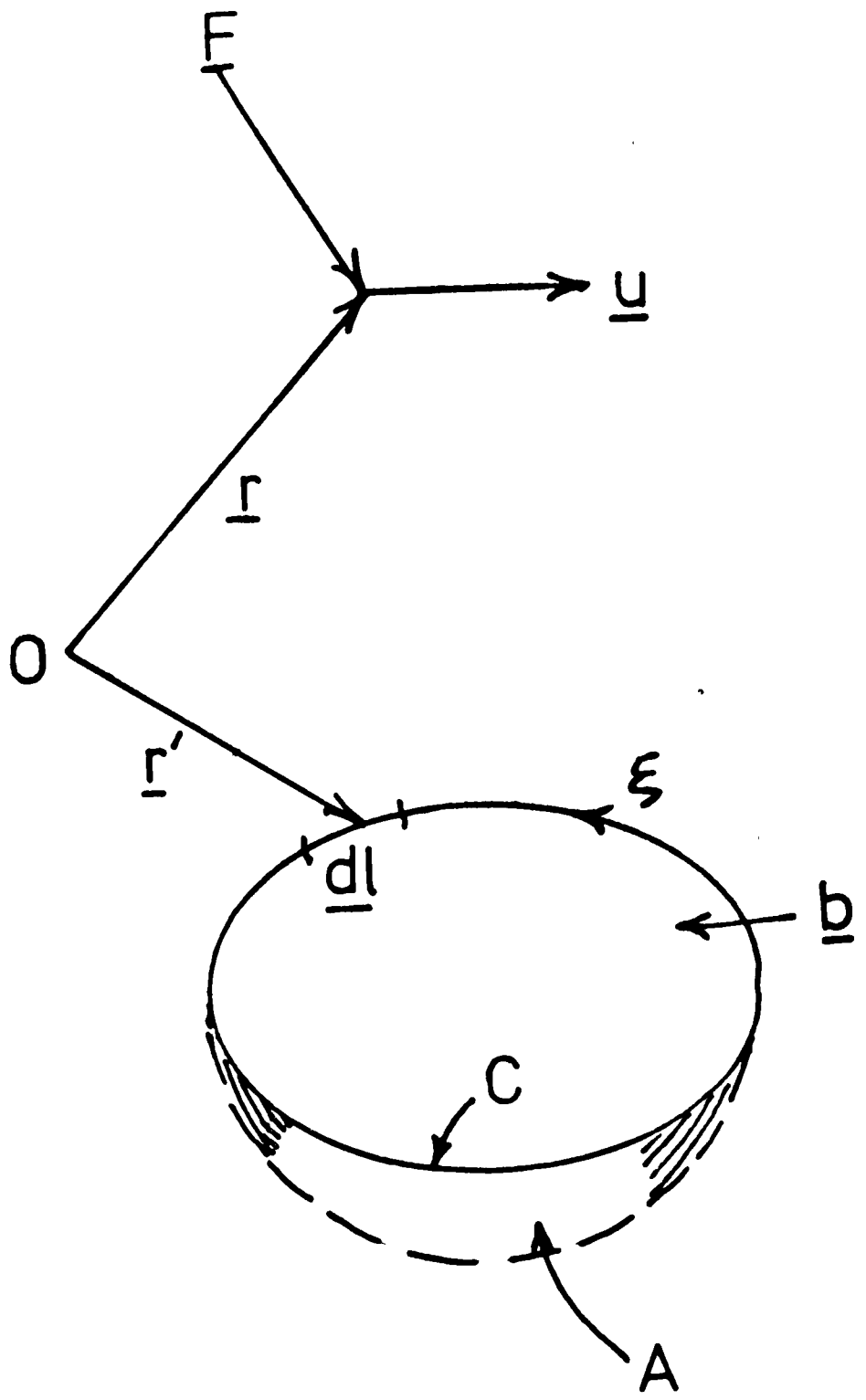


FIGURE 6.1

6.4 Application of the Green's Function method for curved dislocations

Figure 6.1 shows a closed dislocation loop C of Burgers' vector $\underline{b}$ in an infinite medium. Suppose that a displacement $\underline{u}(\underline{r})$ is produced at a point $\underline{r}$ due to the formation of the loop. If a point force $\underline{F}$ acts at $\underline{r}$ the work done is $W = F_m u_m(\underline{r})$ (6.8) where F_m and u_m are Cartesian components of $\underline{F}$ and $\underline{u}(\underline{r})$

Now from a theorem concerning internal energy in a system, in linear elasticity, this is also the work done on the surface A.

i.e. $$W = -\int_A dA_j\, b_i\, C_{ijkl}\, \frac{\partial}{\partial x'_l} F_m\, u_{mk}(\underline{r}' - \underline{r}) \qquad (6.9)$$

where summation over i,j,k and l is understood. If $F_{m'} = \delta_{m',m}$ then equating (6.8) and (6.9), and cancelling F_m from both sides, we obtain,

$$u_m(\underline{r}) = -\int_A dA_j\, b_i\, C_{ijkl}\, \frac{\partial}{\partial x'_l}\, u_{mk}(\underline{r}' - \underline{r}) \qquad (6.10)$$

Equation (6.10) is generally valid in an anisotropic material.

6.5 Isotropic case

All the computer calculations in this thesis are concerned with the case where the elastic medium is assumed to be isotropic. This approximation considerably simplifies the elasticity theory expressions. In this case, the use of Stokes' Theorem, and rearrangement (see Hirth and Lothe 1968) of (6.10) yields,

$$u(\underline{r}) = \underline{b}\,\phi - \frac{1}{4\pi}\oint_C \frac{\underline{b} \wedge d\underline{\ell}'}{R} + \frac{1}{8\pi(1-\nu)}\,\mathrm{grad}\oint_C \frac{(\underline{b} \wedge \underline{R}).\, d\underline{\ell}'}{R} \qquad (6.11)$$

where $\phi = \frac{1}{4\pi}\oint_C \frac{\underline{R}\,.\,d\underline{A}}{R^3}$ is the solid angle subtended by the positive side of A at $\underline{r}$. Here $d\underline{l}'$ is an infinitesimal element along the dislocation line, and ν is Poisson's ratio.

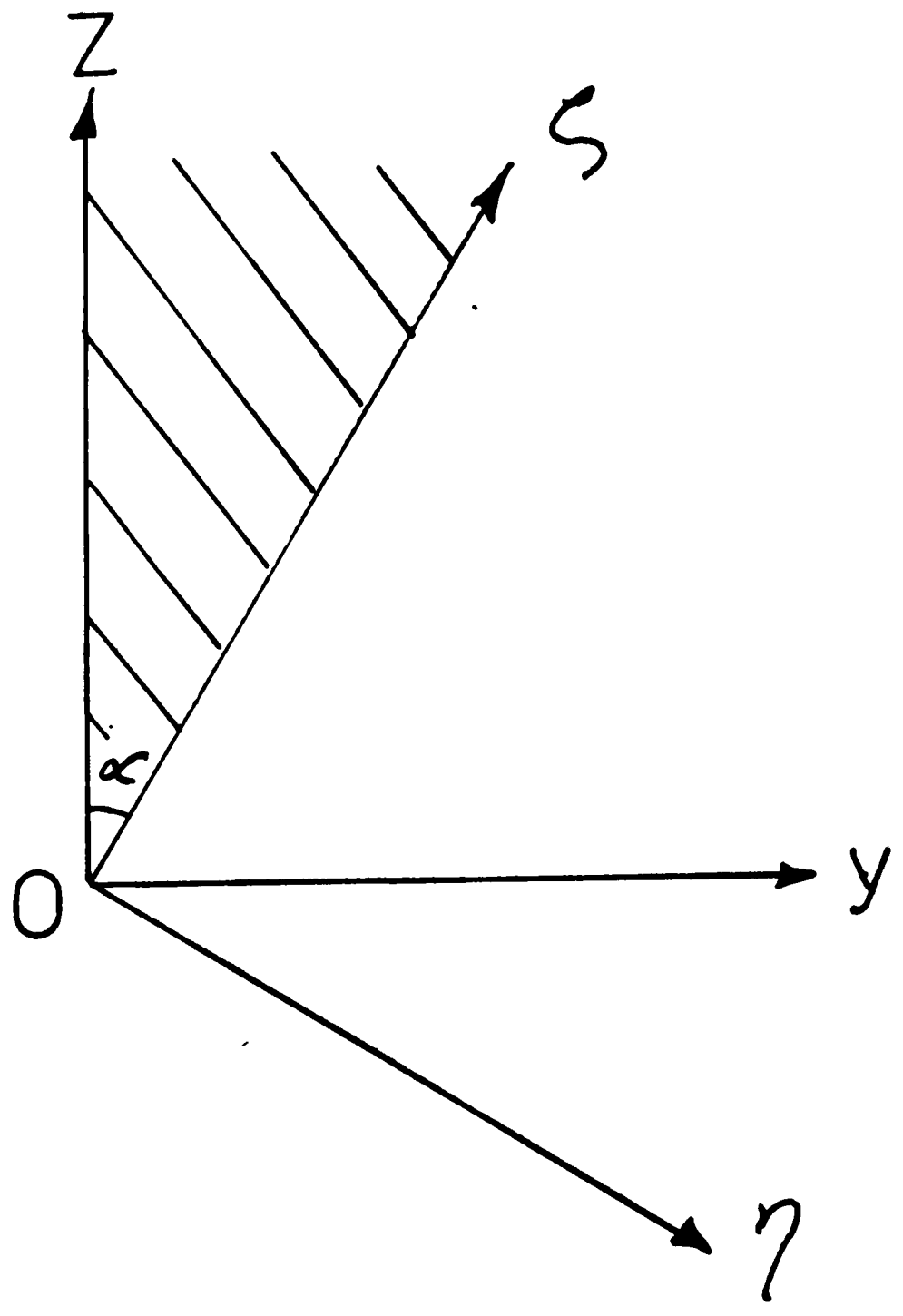


FIGURE 6·2

Equation (6.11) was first derived by Burgers. The first term gives a discontinuity $\Delta \underline{u} = \underline{b}$ over the surface A, consistent with the operation of cutting and displacing A. The other two terms are continuous except at the dislocation line.

Equation (6.11) provides a general method of finding the displacement field due to an arbitrarily shaped dislocation or array of dislocations, by integrating along the dislocation line.

6.6 The Angular Dislocation

An angular dislocation consists of two semi-infinite arms of straight dislocations, with identical Burgers vector, meeting at a point. Figure 6.2 illustrates this. Oz and $O\zeta$ are the semi-infinite arms and the shaded (infinite) area consists of the cut and displaced region.

Yoffe (1960) has applied equation (6.11) to evaluate the displacement field due to the angular dislocation. ϕ is now the angle subtended at a point P (x,y,z) by the shaded area shown, if we wish to find the displacement field at P.

Thus $$\phi = \frac{1}{4\pi} \iint \frac{x}{R^3}\, dy'\, dz'$$

where $$R^2 = x^2 + (y-y')^2 + (z-z')^2$$

By the use of the stereographic projection and spherical trigonometry it can be elegantly shown (see Appendix II) that,

$$\phi = \frac{1}{4\pi}\left(\tan^{-1}\left\{\frac{y}{x}\right\} - \tan^{-1}\left\{\frac{\eta}{x}\right\} + \tan^{-1}\left\{\frac{x\, r \sin\alpha}{x^2\cos\alpha + y\eta}\right\}\right) \qquad (6.12a)$$

when x is positive. When x is negative obviously,

$$\phi = -\frac{1}{4\pi}\left(\tan^{-1}\left\{\frac{y}{x}\right\} - \tan^{-1}\left\{\frac{\eta}{x}\right\} + \tan^{-1}\left\{\frac{|x|\, r \sin\alpha}{x^2\cos\alpha + y\eta}\right\}\right) \qquad (6.12b)$$

6.6.1 Burgers' vector in the x-direction

Let the components of the displacement at the point P be (u,v,w). Then if the Burgers' vector is $\underline{b}$ in the direction of x, the displacements are

$$u = b\phi + \frac{b}{8\pi(1-\nu)}\left\{\frac{xy}{r(r-z)} - \frac{x\eta}{r(r-\zeta)}\right\}$$

$$v = \frac{b}{8\pi(1-\nu)}\left\{\frac{\eta\sin\alpha}{r-\zeta} - \frac{y\eta}{r(r-\zeta)} + \frac{y^2}{r(r-z)} + \cdots\right.$$

$$\left.\cdots + (1-2\nu)[\cos\alpha\,\ln(r-\zeta) - \ln(r-z)]\right\}$$

$$w = \frac{b}{8\pi(1-\nu)}\left\{\frac{\eta\cos\alpha}{r-\zeta} - \frac{y}{r} - \frac{\eta z}{r(r-\zeta)} + \cdots\right.$$

$$\left.\cdots - (1-2\nu)\sin\alpha\,\ln(r-\zeta)\right\} \qquad (6.13)$$

where α is the angle between the semi-infinite arms of the angular dislocation.

It will be noticed that in the expression for w, the sign of the last term on the R.H.S. is opposite to that given by Yoffe. The form gives above is, in fact, correct, as was also pointed out by Hokanson (1963).

6.6.2 Burgers' vector in the y-direction

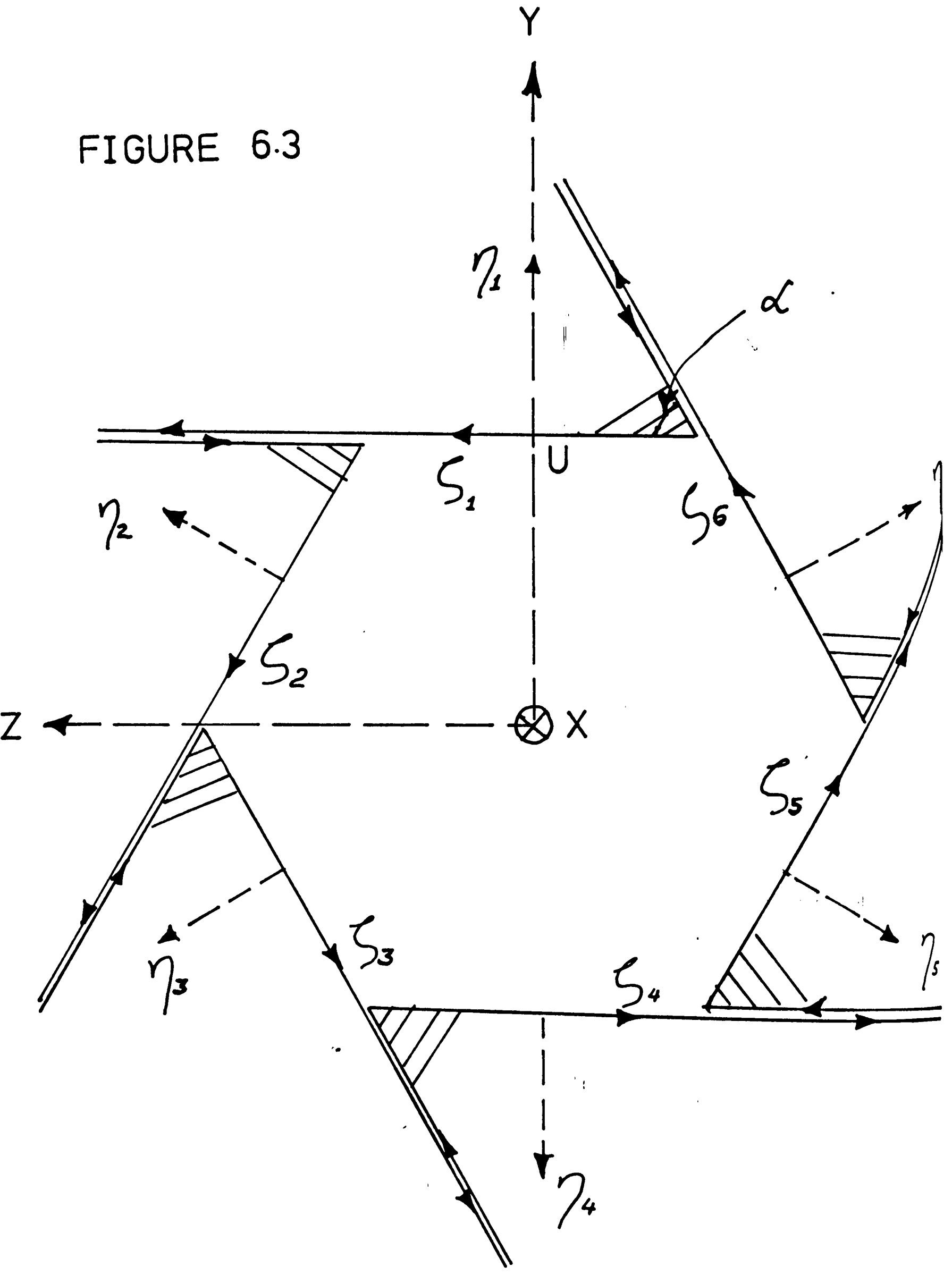
When the Burgers' vector is of magnitude $\underline{b}$ in the y-direction, the expressions are,

$$u = \frac{b}{8\pi(1-\nu)}\left\{\frac{x^2\cos\alpha}{r(r-\zeta)} - \frac{x^2}{r(r-z)} + \cdots\right.$$

$$\left.\cdots - (1-2\nu)[\cos\alpha\,\ln(r-\zeta) - \ln(r-z)]\right\}$$

$$v = b\phi + \frac{bx}{8\pi(1-\nu)}\left\{\frac{y\cos\alpha}{r(r-\zeta)} - \frac{\sin\alpha\cos\alpha}{r-\zeta} - \frac{y}{r(r-z)}\right\}$$

FIGURE 6.3



CONSTRUCTION OF HEXAGONAL LO

FROM ANGULAR DISLOCATIONS

$$w = \frac{bx}{8\pi(1-\nu)}\left\{\frac{z\cos\alpha}{r(r-\zeta)} - \frac{\cos^2\alpha}{(r-\zeta)} + \frac{1}{r}\right\} \qquad (6.14)$$

6.6.3 Burger's vector b in the z-direction

$$u = \frac{b\sin\alpha}{8\pi(1-\nu)}\left\{(1-2\nu)\ln(r-\zeta) - \frac{x^2}{r(r-\zeta)}\right\}$$

$$v = \frac{bx\sin\alpha}{8\pi(1-\nu)}\left\{\frac{\sin\alpha}{r-\zeta} - \frac{y}{r(r-\zeta)}\right\}$$

$$w = b\phi + \frac{bx\sin\alpha}{8\pi(1-\nu)}\left\{\frac{\cos\alpha}{(r-\zeta)} - \frac{z}{r(r-\zeta)}\right\}$$

(6.15)

6.6.4 Angular Dislocation with general Burgers' vector

The displacement field due to the dislocation of arbitrary Burgers' vector can be formed by linearly summing the displacement fields due to each of its components. Thus equations (6.13), (6.14) and (6.15) fully determine the displacement field of any angular dislocation.

6.7 Displacement field due to a polygonal loop of arbitrary Burgers vector

Figure 6.3 shows how a hexagonal loop may be built from six angular dislocations, placed with their vertices at the numbered points, and oriented as shown. If the Burgers' vectors of all the angular dislocations are identical, then clearly the outer arms will produce no effect since they consist of two mutually opposite dislocations that are positionally coincident.

6.7.1 Position and Orientation of the Loop in the foil

The displacement field for the polygon is set up relative to the right-handed Cartesian system of axes whose origin is at the centre of the loop. The Y- and the Z- axes lie in the plane of the loop and the X-axis is perpendicular to it. In order to accurately position and orient the loop in the foil, it is necessary to define say a Cartesian system of coordinates whose origin is at the top surface of the foil. Suppose that they are defined by means of a right-handed system of vectors $(\hat{Q}, \hat{R}, \hat{S})$. Let $\hat{S}$ be the vector pointing opposite to the direction of propogation of the electron beam, and $\hat{Q}$ and $\hat{R}$ lie on the surface of the foil. Then if the coordinates of the point P are (q,r,s) in this system and (x,y,z) in the system of axes on the loop, the latter coordinates are related to the former by the relationships.

$$\begin{bmatrix} x \\ y \\ z \end{bmatrix} = \begin{bmatrix} \hat{X}.\hat{Q} & \hat{X}.\hat{R} & \hat{X}.\hat{S} \\ \hat{Y}.\hat{Q} & \hat{Y}.\hat{R}. & \hat{Y}.\hat{S} \\ \hat{Z}.\hat{Q} & \hat{Z}.\hat{R} & \hat{Z}.\hat{S} \end{bmatrix} \begin{bmatrix} q \\ r \\ (S + d) \end{bmatrix}$$

where d is the depth of the centre of the loop below the foil surface.

6.7.2 Coordinate systems for the individual angular dislocations of the loop

In order to calculate the complete displacement field at P, it is necessary to calculate the contributions from each angular dislocation. Equations (6.13) to (6.15) can be used for this purpose only if the coordinates of P are known in systems of axes whose origins lie on each individual angular dislocation.Fig.6.3.

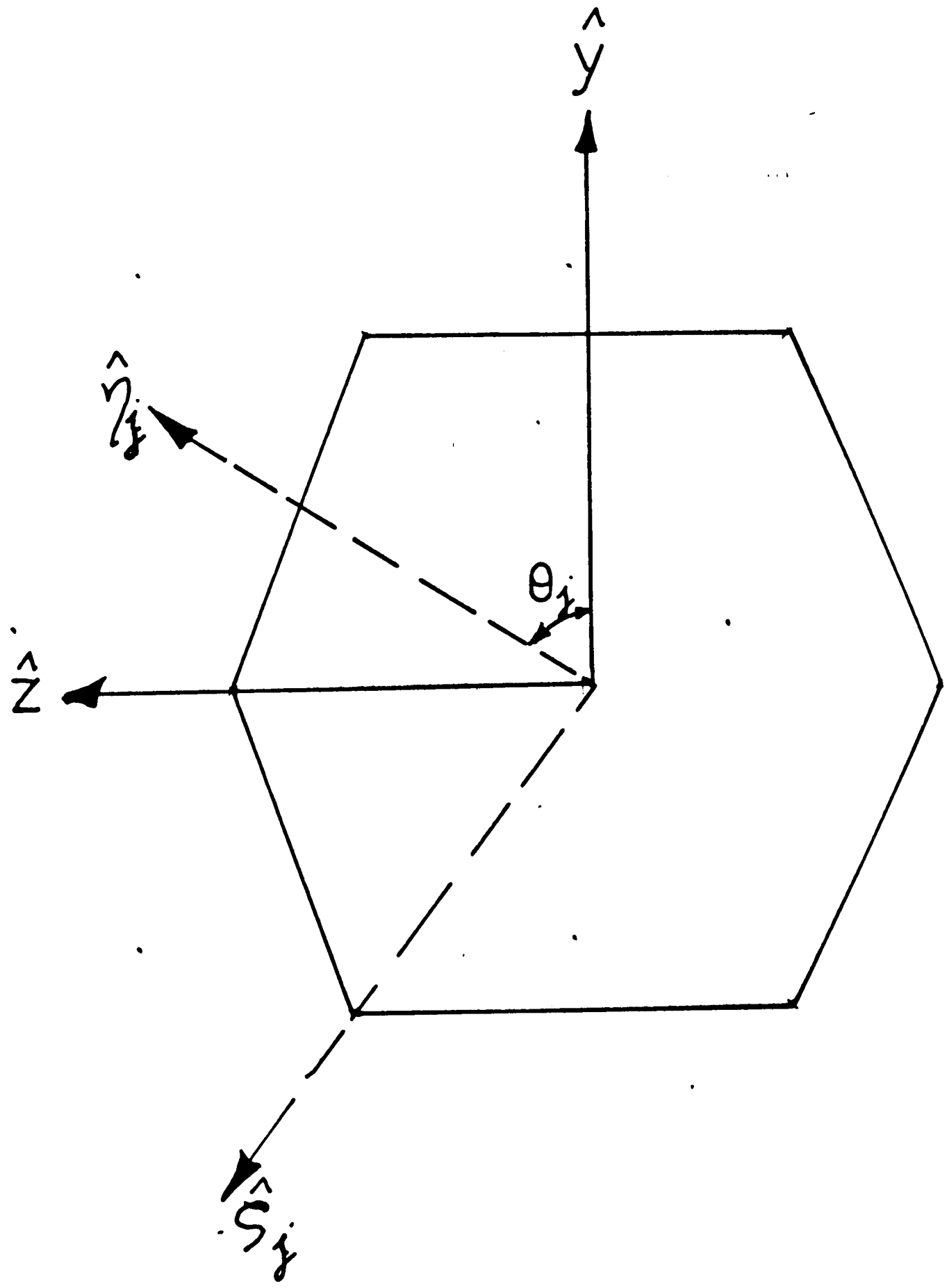


FIGURE 6·4

indicates these systems, which are defined by the set of unit vectors ($\hat{x}$, $\hat{\eta}_j$, $\hat{\zeta}_j$) where j takes any one of the values from 1 to n (n being the number of sides of the polygon).

Let the coordinates of P in these systems be (x, η_j, ζ_j). Clearly the x-coordinate requires no transforming. η_j and ζ_j are related to y and z by,

$$\begin{bmatrix} \eta_j + h\cos\alpha/2 \\ \zeta_j \end{bmatrix} = \begin{bmatrix} \hat{Y}.\hat{\eta}_j & \hat{z}.\hat{\eta}_j \\ \hat{Y}.\hat{\zeta}_j & \hat{z}.\hat{\zeta}_j \end{bmatrix} \begin{bmatrix} y \\ z \end{bmatrix}$$

where h is the distance from the centroid of the polygon to a vertex, and $\alpha = 2\pi/n$. If θ_j is the angle between the general axis $\hat{\eta}_j$ and $\hat{Y}$ (see figure 6.4) then the matrix above may be written,

$$\underset{=j}{A} = \begin{bmatrix} \cos\theta_j & \sin\theta_j \\ -\sin\theta_j & \cos\theta_j \end{bmatrix}$$

where $\theta_j = (j-1)2\pi/n$.

6.7.3 Displacement field due to each angular dislocation in loop

Let (u_j, v_j, w_j) be the components in the directions of the axes $(x, \eta_{j+1}, \zeta_{j+1})$ of the displacement field contributed by the jth angular dislocation at the point P. Let $(b_{xj}, b_{\eta_{j+1}j}, b_{\zeta_{j+1}j})$ be the components of the Burgers vector of this angular dislocation (with respect to the same axes). The vector (u_j, v_j, w_j) may be evaluated from equations (6.13) to (6.15) if the vector (b_{xj} $b_{\eta_{j+1}j}$ $b_{\zeta_{j+1}j}$)

is known and if we make the identifications

$$\zeta \Rightarrow \eta_{j+1}$$

$$z \Rightarrow (\varsigma_{j+1} + h \sin \alpha/2)$$

$$\eta \Rightarrow \eta_1$$

$$\varsigma \Rightarrow (\varsigma_j - h \sin \alpha/2)$$

on the right hand sides. The only exception to this rule occurs when i = n. Then η_{j+1} and ς_{j+1} are redefined as η_1 and ς_1 respectively. This is necessary to close the polygon. The x- coordinate is unaltered.

6.7.4 Burgers' vector components for each angular dislocation

In order to use equation (6.13) to (6.5) it is necessary to find the vectors ($b_{x\,j}$ $b_{\eta j+1,j}$ $b_{\varsigma j+1,j}$) in terms of the Burgers vector components for the whole loop, (B_x , B_y , B_z), expressed with respect to the axes (X,Y,Z).

It is easy to see that $b_{x\,j} = B_x$ for all j,

and that

$$\begin{bmatrix} b_{\eta j+1,j} \\ b_{\varsigma j+1,j} \end{bmatrix} = \underline{C}_j \begin{bmatrix} B_x \\ B_z \end{bmatrix}$$

where

$$\underline{C}_j = \begin{bmatrix} \cos \phi_j & \sin \phi_j \\ -\sin \phi_j & \cos \phi_j \end{bmatrix}$$

where

$$\phi_j = j \cdot 2\pi/n.$$

It will be noted that $(\phi_j - \theta_j) = 2\pi/n$

where θ_j is the angle needed to define the matrix $\underline{\underline{A}}$.

6.7.5 Displacement field due to whole loop

Let (U,V,W) be the displacement field components for the whole loop at the point P, in the directions of the axes (X,Y,Z) respectively. Then

$$u = \sum_{j=1}^{n} u_j$$

and

$$\begin{pmatrix} v \\ w \end{pmatrix} = \sum_{j=1}^{n} \begin{bmatrix} \hat{Y}.\hat{\eta}_{j+1} & \hat{Y}.\hat{\zeta}_{j+1} \\ \hat{Z}.\hat{\eta}_{j+1} & \hat{Z}.\hat{\zeta}_{j+1} \end{bmatrix} \begin{bmatrix} v_j \\ w_j \end{bmatrix}$$

In fact the matrix on the right-hand side can be shown to be equal to C_j^{-1}, so

$$\begin{pmatrix} V \\ W \end{pmatrix} = \sum_{j=1}^{n} \underline{\underline{C}}_j^{-1} \begin{pmatrix} v_j \\ w_j \end{pmatrix}$$

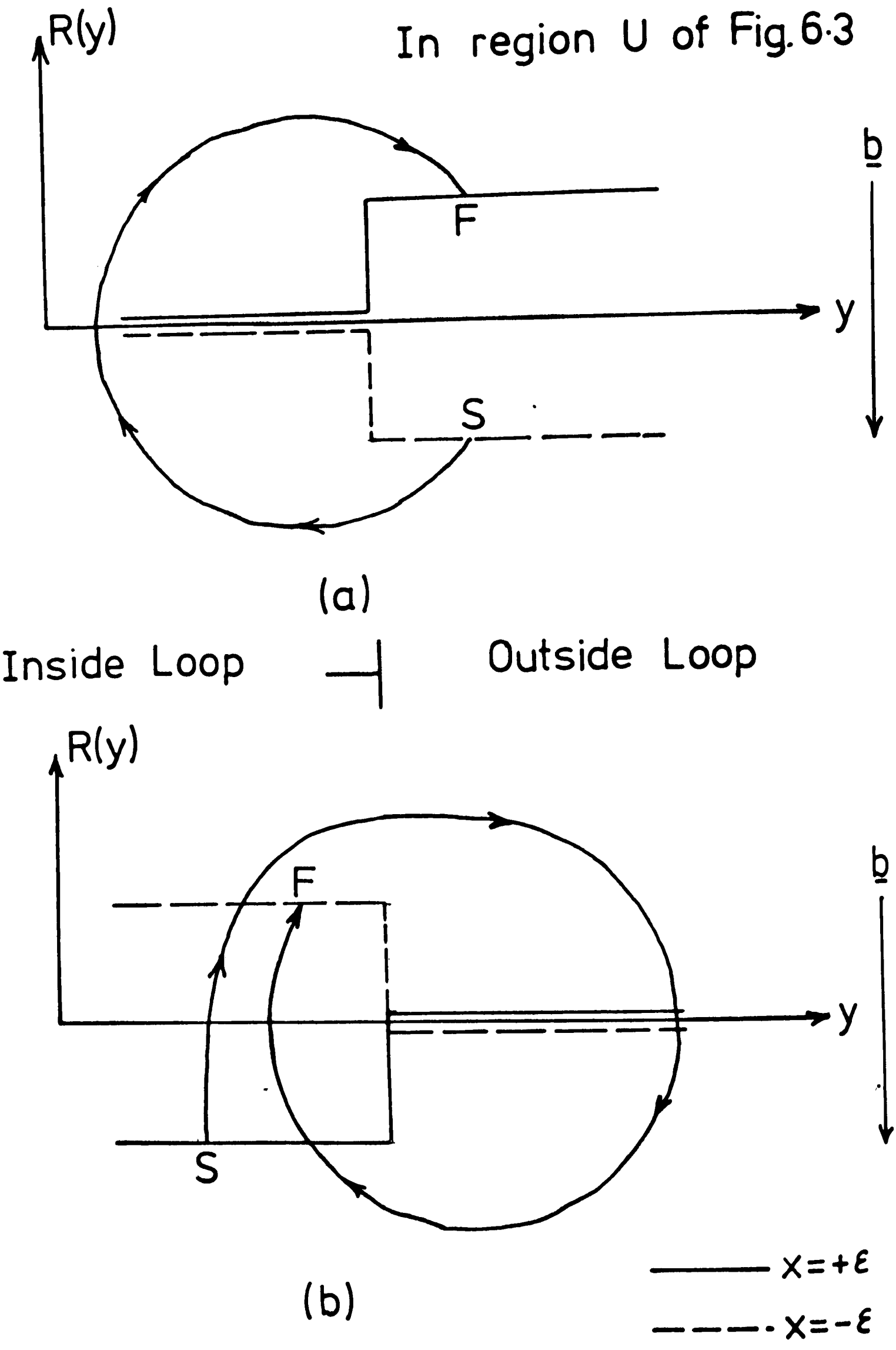

R(y)
In region U of Fig. 6·3
b
F
y
S
(a)
Inside Loop
Outside Loop
R(y)
F
b
y
S
x=+ε
x=-ε
(b)

FIGURE 6·5

6.7.6 Insertion of correct stacking-fault

Yoffe's (1960) expressions for the displacement field due to an angular dislocation imply a jump in the displacement field in the sector formed within the angle α bounded by the two semi-infinite arms. Addition of the displacement field contributions from all the angular dislocations forming a loop (see Fig.6.3) therefore produces a jump in the displacement field in the (infinite) area in the plane defined by the loop but not enclosed by it. All the faulted loops we shall consider, however, have stacking-faults, completely enclosed by the loop. In order to create the displacement field due to such loops therefore it is necessary to transfer the cut region in the elastic continuum from the outside to the planar region inside the loop.

A method of doing this is illustrated in Figure 6.5. The displacement field modulus R is plotted as a function of the coordinate y for the region u of figure 6.3. In this region the y-axis crosses a dislocation line.

The unbroken line is the graph for $x = \xi$ and the broken line that for $x = -\xi$ where ξ is a small qunatity approaching zero. Fig.6.5(a) is the situation when the cut is in the region outside the loop and Fig.6.5(b) when the cut is inside the loop. As can be seen from the Burgers circuits, the Burgers vectors are identical in both cases. It is not difficult to see from the diagrams that case (a) is converted into case (b) by shifting all the displacements in the region $x < 0$ by $-\underline{b}$

relative to the displacements in the region $x \geqslant 0$

This process preserves the original strain field but shifts the cut in the elastic continuum from the region outside to the region inside the loop. If $\underline{b}$ is not equal to a lattice vector, a stacking-fault of fault vector $\underline{b}$ is thus automatically introduced into the planar region bounded by the loop.

6.7.7 Components of displacements in crystallographic directions

If we require to use these expressions for the displacement field together with the dynamical theory computer program described in Chapter 5, we shall require to form the products $\underline{g} \cdot \underline{R}$ where $\underline{g}$ is the reciprocal lattice vector of any of the reflections considered, and $\underline{R}$ is the displacement field due to the defect. Now $\underline{g}$ is usually specified by its Miller indices $(h\ k\ \ell)$ where these indices are the projections of the vector $\underline{g}$ on the (100), (010) and (001) directions in reciprocal space. The product $\underline{g} \cdot \underline{R}$ is therefore easily formed if $\underline{R}$ is specified by its components in these directions. Let us suppose that the components of $\hat{X}$ in these directions are (x_h, x_k, x_ℓ) respectively, with similar notations for $\hat{Y}$ and $\hat{Z}$. Then if the corresponding components of R are R_h, R_k, R_ℓ,

$$\begin{bmatrix} R_h \\ R_k \\ R_\ell \end{bmatrix} = \begin{bmatrix} x_h & y_h & z_h \\ x_k & y_k & z_k \\ x_\ell & y_\ell & z_\ell \end{bmatrix} \begin{bmatrix} u \\ v \\ w \end{bmatrix}$$

6.8 Summary

The method described above enables the construction of the displacement field due to a regular polygonal dislocation loop of arbitrary Burgers vector. Thus, not only Frank loops, but also loops with shear components of Burgers vector may be studied. Also since the number of sides of the polygon is specified only by the parameter n, it is in principle possible to study loops with such a large number of sides that they approximate to a circular loop.

When used in conjunction with the dynamical theory computer program described in the last chapter, it is possible to predict or verify the images of loops, observed in the electron microscope. The position and the orientation of the loops in the foil may be controlled by parameters fed into the program.

Chapter 7

COMPUTER SIMULATED IMAGES FROM POLYGONAL DISLOCATION LOOPS

7.1 Introduction

A crystal cannot exist at any finite temperature in a state of complete perfection. At any finite temperature, the statistical distribution of thermal energy amongst its atoms implies a finite probability of a local concentration of energy in a group of atoms to form a lattice defect. The simplest type of imperfections are the point defects known as vacancies and interstitials. A vacancy is formed when an atom is missing from its position in a perfect lattice and an interstitial when an atom is lodged between a group of atoms originally in their perfect lattice sites.

By the use of statistical mechanics it is possible to find an expression for the Helmholtz free energy of a crystal with a certain concentration of a particular type of point defect. The equilibrium concentration may be found by minimizing this function, and yields the expression, (where C_r is the concentration of point defects of type r; the factor $\exp(\Delta S_f^r/k)$ is referred to as the entropy factor; U_f^r is the formation energy of each defect, k is Boltzmann's constant and T is the absolute temperature),

$$C_r = \exp(\Delta S_f^r/k)\exp\{-U_f^r/kT\} \qquad (7.1)$$

In the formation of a vacancy, it is found (see e.g. Thompson, 1969) that the magnitude of the relaxation of the atoms surrounding it is much smaller than during the formation of an interstitial. It is therefore found that U_f^V the formation energy of a vacancy is much smaller than U_f^I, the corresponding quantity for an interstitial. Thus for any given temperature T, C_V, the concentration

of vacancies would be much greater than C_I, that of interstitials, if the system is in thermodynamic equilibrium.

During the quenching of a crystal from a high temperature, the greater concentration of point defects appropriate to the higher temperature is frozen in at the lower temperature (see e.g. Bauerle and Koehler, 1957, Hirsch, Silcox, Smallman and Westmacott, 1958). Subsequent annealing at an intermediate temperature results in a migration of the point defects. One of the effects of this migration is the mutual annihilation of defects of opposite type (i.e. vacancies and interstitials) if they approach one another. The frequency of such annihilations is increased by the strain-fields around these defects, which leads to an attractive force between them. Even if all the extra interstitials are destroyed by such a mechanism the greater concentration of vacancies ensures that there will remain a larger number of such defects than are appropriate to the intermediate temperature. These extra vacancies are mutually attracted and tend to agglomorate to form vacancy clusters.

Another factor influencing the events that take place during an annealing experiment is the greater rate of migration of interstitials. In fact one finds that the jump rate, namely the rate at which a point defect moves to a neighbouring site, is given by an expression of the form

$$\frac{dn_r}{dt} = \nu \exp\left(\Delta S_m^r / k\right) \exp\left(-U_m^r / kT\right) \qquad (7.2)$$

where ν is the oscillation frequency of the defect, the first exponential is an entropy term and U_m^r is the energy of migration of the defect of type r. It is found that $U_m^I \ll U_m^V$ where the I and V refer to interstitials and vacancies respectively. Thus interstitials

are more likely to be lost at surfaces than vacancies.

7.2 The most likely form of vacancy clusters

If γ is the surface energy of unit area of the crystal, it can be shown (see Thompson, 1969) that the formation energy U_f^{sphere} of a spherical void of n atoms is given by,

$$U_f^{sphere} = \left(6\sqrt{\pi} \cdot n\Omega\right)^{\frac{2}{3}} \gamma \qquad (7.3)$$

where Ω is the volume occupied by one atom in the crystal. The formation energy U_f^{disc} of a flat circular void of n vacancies is,

$$U_f^{disc} \simeq 2n\Omega^{2/3}\gamma \qquad (7.4)$$

Thus $$U_f^{disc} / U_f^{sphere} \sim 0.44 n^{1/3} \qquad (7.5)$$

Therefore for a given large n, a sphere has a lower formation energy than a disc.

Now collapse of a disc shaped void in its central region to reunite the exposed surfaces releases a large amount of surface energy. The resulting configuration is a dislocation loop. The formation energy of such a loop, U_f^{loop} is,

$$U_f^{loop} \simeq 2\sqrt{n\pi} \cdot \Omega^{1/3} \mu b^2 \qquad (7.6)$$

where μ is the shear modulus of the crystal and $\underline{b}$ the Burgers vector of the bounding dislocation line.

Thus

$$\frac{U_f^{loop}}{U_f^{sphere}} \rightarrow \frac{\mu b^2}{\gamma} \frac{2\pi^{1/6}}{6^{2/3} n^{1/6} \Omega^{1/3}} \qquad (7.7)$$

showing that for large, n, the loop has the lowest formation energy. One would thus expect that in a quenching and annealing experiment, vacancy type dislocation loops are likely to be formed. They tend to form on close-packed planes since vacancies tend to cluster on such planes because, as might be imagined, the formation energy of discs on such planes is lower.

7.3 Irradiation by high-energy particles

When a crystal is bombarded by high-energy particles, energy is transferred to lattice atoms. One may regard the transfer of energy as occurring by means of collisions. If a lattice atom receives more than a certain critcal energy E_d it will be displaced from its lattice site leaving a vacancy. The displaced atom, known as the "primary knock-on" of energy E_p may go directly into an interstitial site or if sufficiently energetic may cause further displacements. These displaced atoms may produce further displacements and so on, the whole process being known as the "displacement cascade". From a simple model based on the assumption that the colliding particles behave as "hard spheres", Kinchin and Pease (1955) have shown that the number of displaced atoms $\nu(E_p)$ in the collision cascade for a given primary knock-on energy E_p is given approximately by the formulae,

$$\nu(E_p) = 0 \qquad \text{if} \quad E_p < E_d$$

$$\nu(E_p) = 1 \qquad \text{if} \quad 2E_d > E_p > E_d$$

$$\nu(E_p) \simeq E_p/2E_d \qquad \text{if} \quad E_p > 2E_d.$$

The nature of the damage produced in a material thus depends crucially on E_p.

In nuclear reactors, fission neutrons have typically energies of the order 1.5 MeV. Particle accelerators typically produce protons and electrons with energies of the order of a MeV . Although the energies of these particles are all the same order of magnitude, the types of damage they produce in crystals differ greatly due to the different magnitudes of the primary recoil energies E_p. Now if the mean free path of the incident particle in the solid is much greater than the interatomic spacing, the primary event (namely the collision between the incident particle and a lattice atom) can be treated by classical mechanics. If E is the energy of the incident particle and M_1 and M_2 the masses of the target atom and the projectile respectively, it can be shown classically that the maximum possible primary recoil energy is,

$$E_{p,max} = \frac{4 M_1 M_2}{(M_1 + M_2)} \cdot E$$

From this argument alone therefore it is not difficult to see that typical E_p's for neutrons will be considerably higher than that for electrons (for a given E). Thus for 1MeV incident particles, a primary event for electrons causes only one or two interstitial vacancy-pairs, but a similar event in the case of neutron irradiation causes a number of such defects of the order of a thousand. Thus electron irradiation produces a dispersed distribution of defects but neutron irradiation produces large clusters of defects.

In the latter case frequently the knocked-in atoms cause "focussed collision sequences" (see Thompson, 1969). These are processes whereby atoms sequentially replace one another along a close-packed row, and the final interstitial is ejected from the row at some considerable distance from the point at which the sequence began.

Therefore most of the interstitials could be transported a great distance from the region of the initial collisions, and be left in a diffuse cloud surrounding a "depleted zone" containing an excess of vacancies. The higher migration rate of the interstitials could then cause them to be lost at surfaces and other sinks, while the high concentration and low rate of migration of the vacancies cuase them to form clusters, of which a substantial number would be expected to be dislocation loops lying on close-packed planes, by the arguments of 7.2.

7.4 Dissociation of loops

In materials with low stacking-fault energy such as copper and silver, the loops have a tendency to dissociate by the Silcox-Hirsch mechanism described in Chapter 8. Jenkins (1973) suggested that nearby foil surfaces could have great bearing on the manner in which the dissociation occurs. Favourable directions of dissociation were argued by consideration of image dislocations. The ultimate consequence of the process is the creation of a stacking-fault tetrahedron. In many materials however this final stage is not reached by some defects and they take up intermediate configurations described by Jenkins (1973). One of the consequences of Jenkins' theory is that in ⟨111⟩ foils tetrahedra have apices pointing away from the nearby foil surface.

Calculations of the displacement field due to defects of this intermediate type are rather complicated, and in this thesis, the electron microscope images from only polygonal dislocation loops (of edge and mixed character) and stacking-fault tetrahedra are considered.

7.5 Images from small defect clusters

Contrast from dislocation loops depends crucially on whether their dimensions are large or small compared witb the extinction distance. In the former case a more or less sophisticated application of the "classical" properties of dislocation contrast (e.g. as developed by Hirsch et al (1965)) suffices for understanding the qualitative features of the contrast. In the latter case, the image properties are most easily understood by considerations of Bloch wave scattering, outlined in Chapter 4.

7.5.1 "Kinematic" Images

The earliest studies of the small defect clusters were performed under so-called "kinematic" imaging conditions (i.e. when no Bragg reflection is strongly excited and an image is formed with the incident beam). Pashley and Presland (1961) observed black dots in gold foils irradiated with 0^- ions inside the microscope. Makin and co-workers (1961, 1962, 1963) observed large well resolved dislocation loops of perfect Burgers vector $\underset{\sim}{b} = \frac{a}{2}\langle 110 \rangle$ and also a high density of black spots, in neutron-irradiated copper. In this thesis we shall be concerned primarily with the small defects. The shapes of the black dots were unfortunately rather unspecific and did not yield much crystallographic information about the defects.

7.5.2 "Dynamic" Images

Important progress was made when Essmann and Wilkins (1964) demonstrated that the black dots on the "kinematic" images show a characteristic black-white structure if the foils are imaged under two-beam dynamical contrast conditions (i.e. with the excitation error $s_g = 0$ for one Bragg reflection). Black-White images were also observed by Ashby and Brown (1963) from larger spherical inclusions.

7.5.3 Qualitative features of contrast

So as to be able to draw conclusions about the nature of the lattice defects from the types of observed black-white images, a summary of our present knowledge of the nature of contrast from small defects is presented below.

Small defect clusters at present observable in the electron microscope are of the following types:

(i) Voids

(ii) Spherical inclusions

(iii) Dislocation loops

(iv) Stacking-fault tetrahedra

Type (iv)will be considered in the next chapter.

-

(i) Voids

These are small volumes of the crystal totally unoccupied by lattice atoms. They may be filled with a gas (e.g. helium) and are then called bubbles. Such defects give rise to virtually no long range displacement field and are therefore not observed by the type of diffraction contrast mechanism described in chapter 4.

On the contrary their existence is revealed by phase contrast (see Hirsch et al., 1965, p.243 and p.244).

(ii) Spherical Inclusions

Historically the interpretation technique for small defect clusters was greatly influenced by the work of Ashby and Brown (1963) on contrast from large coherent precipitates of either positive or negative volume misfit. They showed that in agreement with the calculations of Phillips and Livingston (1962), when the precipitate is in the middle of the foil, a coffee-bean like contrast is expected, which resembles the double-arc contrast from an inclined loop. Two dark, approximately elliptically shaped parts of the contrast figure are separated by a "line of no contrast" perpendicular to the operating reflection .

If the inclusion lies within ξ_g of one of the surfaces however, anomalously wide images are expected. These consist of a white part on one side of the line of no-contrast and a black part on the other. We define a vector $\underline{l}$ as that joining the centre of the black part to the centre of the white one. Then Ashby and Brown found that $\underline{g}.\underline{l} > 0$ for inclusions with negative volume misfit (i.e. of "vacancy" type), and vice versa, on the dark-field images. According to the rules, discussed in Chapter 4, the sign of $\underline{g}.\underline{l}$ in bright-field is the same as that in dark field for inclusions near the top surface of the foil and reversed for those near the bottom. These are often known as the Ashby-Brown rules.

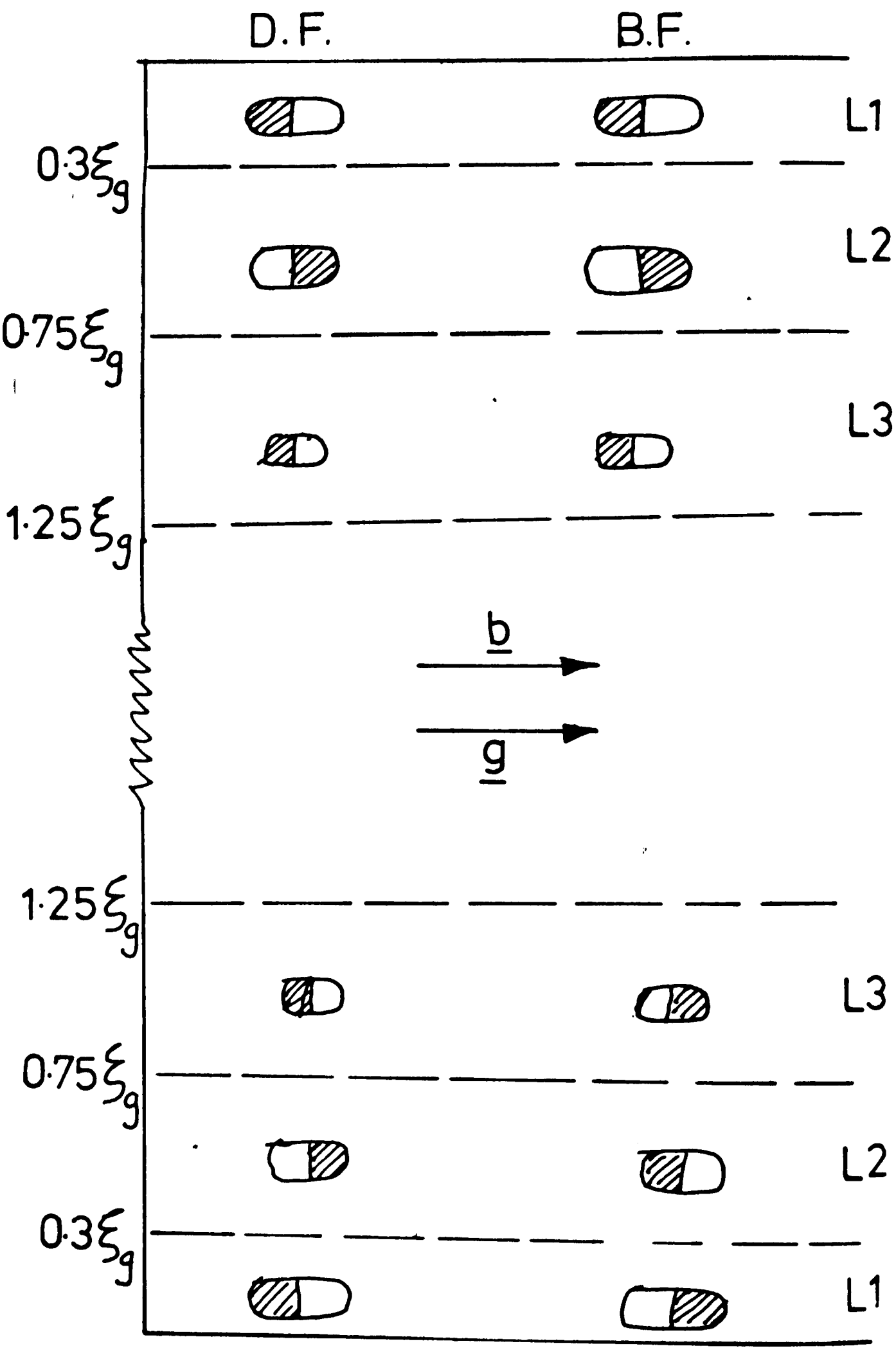

Vacancy Loops and Tetrahedra
D.F.
B.F.
L1
L2
L3
0·3ξg
0·75ξg
1·25ξg
b
g
1·25ξg
L3
0·75ξg
L2
0·3ξg
L1

FIGURE 7·1

(iii) Dislocation loops

The work of Essmann and Wilkens (1964), Ruhle, Wilkens and Essmann (1965), Ruhle(1967) and McIntyre and Brown (1966) led to the establishment of the following properties of "dynamical" images of dislocation loops.

(a) A loop oriented with $\underset{\sim}{g}\,\underset{\sim}{b} \neq 0$ with its centre close to one of the foil surfaces reveals black-white contrast under dynamical conditions. The direction of $\underset{\sim}{l}$ is between that of $\underset{\sim}{g}$ and the projection of $\underset{\sim}{b}$ onto the image plane.

(b) The sign of $\underset{\sim}{g}.\underset{\sim}{l}$ depends on the distance of the loop centre from the nearest foil surface and on the nature of the loop (i.e. whether of vacancy or interstitial type). The variation is summarized in fig.7.1.

(c) The sign of $\underset{\sim}{g}.\underset{\sim}{l}$ in the first layer on either surface agrees with the predictions of the Ashby-Brown rule.

(d) The depth oscillations of the black-white contrast are damped by anomalous absorption, which depends on the ratio $\xi_g / \xi_g' \sim 0.1$ Thus the black-white contrast is only observable in the first two (or three) layers.

(e) The contrast when the loop lies near the borders between the layers L1,L2, ... etc. consists of a black dot with no observable structure.

(f) The line of no contrast coincides with the trace of the loop habit plane on the image plane if and only if the loop habit plane is perpendicular to the image plane.

7.5.4 Depth dependence of $\underset{\sim}{g}\,\underline{l}$

Comparison of 7.53(iii) and 7.5.3(iii) shows that for large spherical inclusions, we do not expect oscillations of the sign of $\underline{g}.\underline{l}$ with the depth of the centre of the defect from the nearer foil surface (behaviour of type α) whereas for dislocation loops, such behaviour is expected (type β). McIntyre and Brown (1966a) and Chik, Wilkens and Ruhle (1967) studied the reaons for this difference in behaviour. Both groups found that the transition from type α to type β is due to the neighbouring traction-free surface which modifies the strain-fields. Behaviour of type α is, in fact, to a first approximation, linearly superimposed on that of type β . Both types of contrast are in phase for strain centres in layers L1, L3, ... and hence for these layers the signs of $\underline{g}.\underline{l}$ are not changed. They are antiphase in layers L2, L4, ... The prevalence of either type depends on the value of the dimensionless normalized misfit parameter

$$P = \Delta V\, g\pi / \xi_g^2$$

where ΔV represents the volume misfit of the strain centre, such that $\Delta V = b R_L^2 \pi$ for a Frank loop and $\Delta V = 4\pi\varepsilon R_s^3$ for a spherical inclusion. R_L and R_S are the radii of the loop and sphere respectively and 3ε is the relative volume misfit $\Delta V/V$ of the inclusion. When $P < 1$, type β behaviour predominates, and when $P > 1$ type α does so.

For dislocation loops if $\underset{\sim}{g}.\underline{b} = 1$ then the condition $P > 1$ implies $R_L > \xi_g$. This is clearly impossible for loops in layer L2, since the inner boundary of L2 is only $0.75\,\xi_g$ from the surface. Thus we would expect the depth oscillations of $\underset{\sim}{g}.\underline{l}$ to always occur for unresolved dislocation loops (i.e. with $R_L \ll \xi_g$).

We do not bother to consider behaviour in L4 since from property of 7.53(iii) we see that usually the black-white character of the contrast is not observable in this layer due to anomalous absorption.

7.6 Displacement Field due to a Dislocation Loop (Review)

(a) Isotropic Media

7.6.1 The infinitesimal loop

The displacement field due to an infinitesimal loop can be regarded as that due to a finite loop at distances large compared with the size of the loop. Expressions for the displacement field were first given by Eshelby (1957). Similar formulae were given by Kroupa (1963).

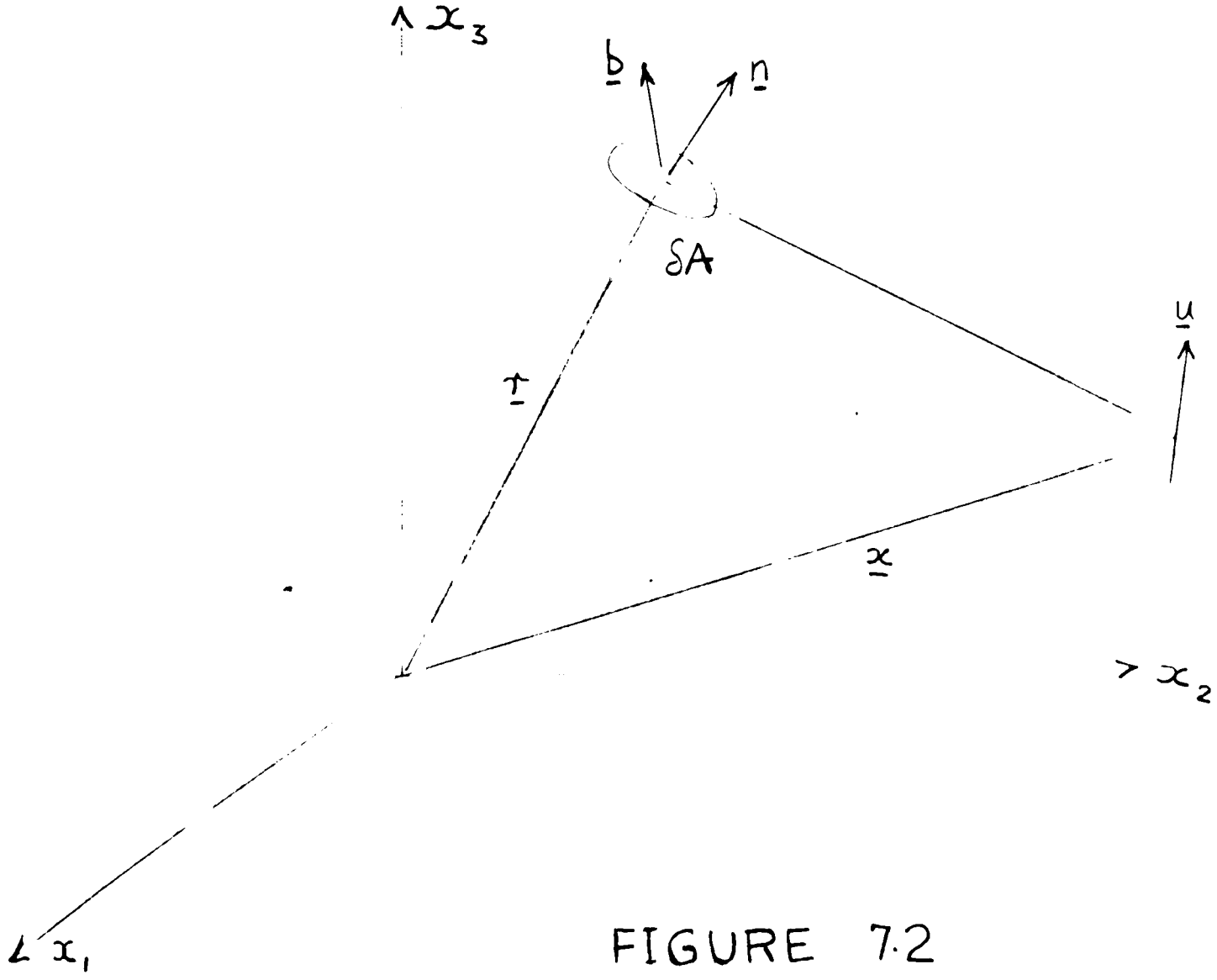


FIGURE 7.2

With the notation in fig.7.2, Kroupa showed that the displacement field $\underline{u}$ at a point specified by the position vector $\underline{x}$ could be written

$$\underline{u} = \frac{-\delta A}{8\pi(1-\nu)\,\rho^2}\left\{\frac{(1-2\nu)}{\rho}\left[\underline{n}\cdot(\underline{b}\cdot\underline{\rho} + \underline{n}\wedge(\underline{b}\wedge\underline{\rho})\right] + \ldots \right.$$
$$\left. \ldots + 3(\underline{b}\,\underline{\rho})(\underline{n}\cdot\underline{\rho})\,\underline{\rho}/\rho^3\right\}$$

where

$$\underline{\rho} = \underline{x} - \underline{r} \quad ; \quad \rho = |\underline{x} - \underline{r}|$$

ν is Poisson's ratio, δA is the area of the loop and $\underline{b}$ is the Burgersvector.

Bacon and Groves (1970) have expressed the displacement field in terms of the elastic Green's function.

7.6.2 Finite Circular Edge Loop

The displacement field due to a circular edge dislocation loop has been derived by Kroupa (1960) and Bullough and Newman (1960) from the form of the biharmonic stress function χ which satisfies the equation $\nabla^4\chi = 0$ subject to the boundary conditions for the loop.

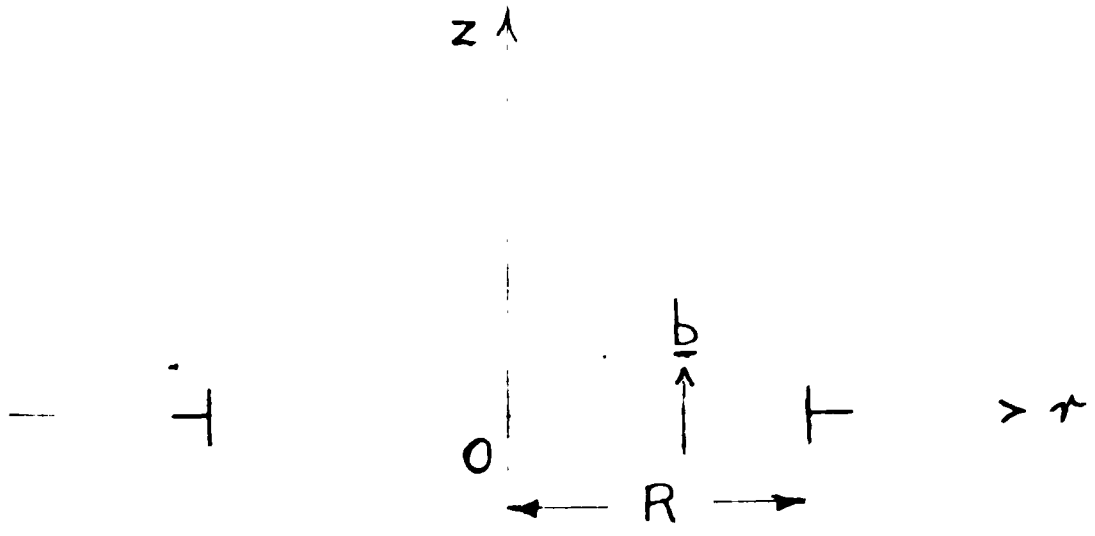


FIGURE 7.3

In the system of cylindrical coordinates illustrated in Fig.7.3, consider the loop of radius R described by the equations $Z = 0$ and $r = R$. If the components of the stress tensor in the coordinate system are σ_r , σ_θ , σ_z , $\tau_{r\theta}$, τ_{rz} and $\tau_{\theta z}$, and those of the displacement are u_r, u_θ , u_z . If the Bergers' vector $\underline{b}$ is in the z-direction, these functions are independent of θ and symmetric with respect to the plane $z = 0$. It is therefore sufficient to find the solution to this function in the upper half-space ($z > 0$) subject to the boundary conditions,

(1) $$u_z(r, 0) = -\frac{1}{2} b \qquad \text{for} \quad 0 \le r < R$$

$$u_z(r, 0) = 0 \qquad \text{for} \quad r > R$$

(2) $$\tau_{rz}(r, 0) = 0$$

on the plane $z = 0$

It is also required that all components of stress and displacement approach zero as $z \to \infty$ and $r \to \infty$

This problem has been solved by Kroupa (1960) using the method of Hankel transformations for cylindrical symmetry, as elaborated in Sneddon's book (1951). The solution for the displacement components is,

$$u_r(\rho, \zeta) = \frac{b}{4(1-\sigma)} \left[(1-2\sigma) I_1^\circ - \zeta I_1' \right]$$

$$u_z(\rho, \zeta) = -\frac{b}{4(1-\sigma)} \left[2(1-\sigma) I_0^\circ + \zeta I_0' \right]$$

$$u_\theta(\rho, \zeta) = 0$$

where σ is Poisson's ratio, $\rho = r/R$, $\zeta = z/R$ and

$$I_j^i(\rho,\zeta) = \int_o^\infty t^i J_j(t\rho) J_1(t) e^{-t\zeta} dt \qquad (7.8)$$

Many functions of this type may be evaluated from their relationships to certain elliptic integrals (see Eason et al, 1959, Watson, 1922).

7.6.3 Finite Circular Shear Loop

Ohr (1972) applied the Green's function method to derive the displacement field due to a shear dislocation loop. Substitution of the elastic Green's function for an isotropic medium (Love, 1927) into equation (6.10), shows that the displacement field due to a loop is given in terms of the surface integral

$$Q = \int_S \frac{dx_1' \, dx_2'}{\underline{r} - \underline{r}'}$$

where S is the area of the loop.

Gray (1919) has shown that

$$Q = 2\pi R I_o^{-1}(e,|\zeta|)$$

Thus by combining the expressions he derived for the field due to a pure shear loop in terms of the Lipschitz-Hankel integral defined by equation (7.8) above, with that from a pure edge loop given by Kroupa (1960), Ohr (1973) was able to obtain expressions for the displacement field due to a finite circular loop of arbitrary Burgers vector, subject to the limitations of isotropic elasticity.

(b) 7.6.4 Anisotropic Media

The displacement field due to a dislocation loop in an anisotropic medium has been calculated by Indenbom and Orlov (1967) by the use of Lothe's Theorem (Lothe, 1967, Brown, 1967). These

authors reduced the problem to one of calculating derivatives with respect to the line orientation of the distortions produced by an infinite straight dislocation.

Making use of an integral representation for the Green's function of anisotropic elasticity, and by means of ingenious mathematical methods, Willis (1970) has been able to find an expression for the displacement field due to a general elliptical loop in a more explicit form. Willis' method does not involve the use of Lothe's Theorem but requires the solution of a sextic equation for each short segment of the dislocation line, and a contour integral over a circle where the integrand contains the sextic roots.

Ohr (1974) has given an alternative formulation which expresses the displacement field in the form of a double integral which has to be evaluated numerically.

7.7 Computer Simulation of Images (Review)

McIntyre (1967) has used the infinitesimal loop model of 7.6.1 to calculate line profiles of contrast from the dynamical theory by finding solutions to the Howie-Whelan equations. Wilkens and Ruhle (1972) used Kroupa's (1963) displacement field for an infinitesimal loop but attempted to find the two-dimensional distribution of intensity in the image plane. The intensities were calculated on an argument based on the kinematical Bloch wave scattering theory (see e.g. Chapter 4). The combination of these two simplified models enabled an analytic solution for the intensities to be obtained to a first order. The results were displayed as equal intensity contours.

This method enabled the study of images of loops of mixed character (Haussermann, Ruhle and Wilkens, 1972).

Bullough, Maher and Perrin (1970) have used the isotropic elasticity model for a circular edge loop (see 7.62) and calculated intensities from the Howie-Whelan equations (1.19). The results have been displayed by a method very similar to that described in this thesis, namely by a half-tone technique using a Stromberg-Carlson 4060 plotter.

Ohr (1973) has used his formulae for an elastically isotropic shear loop (Ohr 1972) to calculate contrast from loops of mixed character in niobium. He also employed the Howie-Whelan equations for intensity determination but displayed his results as line profiles. The computer simulated images reported later in this Chapter which use the displacement field model of Chapter 6, are in good agreement with Ohr's calculations.

7.8 Computer Simulation of dark field images (Present work)

7.8.1 Hexagonal Frank loops in Copper

We saw in s 7.3 that irradiation of a crystal by say 1 MeV neutrons gives rise to vacancy-type dislocation loops on close-packed planes. In an fcc material , the $\{111\}$ planes are the closest packed. The formation of a loop by the eating away of a $\{111\}$ layer results in a fault in the stacking sequence of the A B C layers (using the conventional means of specifying the $\{111\}$ layers, as in Hirth and Lother (1968)). The result is the Frank sessile loop which encloses areas of stacking fault of fault vector $\underset{\sim}{R} = \frac{a}{3}\langle 111\rangle$ as illustrated in fig.7.4.

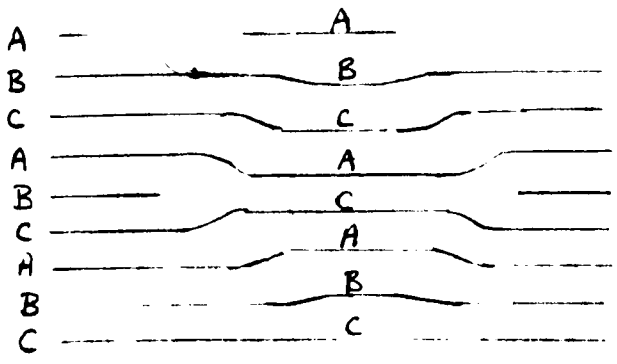


FIGURE 7.4

Using the methods described in Chapter 6, the displacement field due to a hexagonal Frank loop was constructed and the computer simulation method of Chapter 5 was employed to produce the following dark-field images (under dynamical conditions i.e. $S_g = 0$)

(a) Edge-on Loops

(i) Depth Dependence (111 Reflection at ⟨110⟩ pole).

Figs 7.5 and 7.6 illustrate the depth dependence of the images of edge-on Frank loops. The values of the various parameters such as size, Burgers vector, foil thickness etc. are described in the caption. From the definition of the parameter h in Chapter 6, it is clear that the diameter of a hexagonal loop is about twice this value.

The black-white nature of the contrast is clearly visible. Figures 7.5(a), (b) and (c) correspond to loops at depths of $0.5\,\xi_g$ ξ_g and $1.5\,\xi_g$ from the top (electron-entry) surface. The thickness of the foil was $2\xi g$. Thus fig. 7.5(a) and (c) correspond to defects in the layers L2 counting from the top and bottom surfaces respectively. Figure 7.5(b) corresponds to the defect at the centre of the foil and in layer L3. It is clear that the variation of $\underset{\sim}{g}\,\underset{\sim}{l}$ is exactly as predicted by figure 7.1. The modified Ashby-Brown rule for

dislocation loops described in 7.5.3(iii) states that $g \underline{l}$ is positive on the dark-field images in either of the layers L1, for vacancy loops. This implies that $g \underline{l} < 0$ on the dark field images for loops in layers L2, (assuming $g // \underline{b}$) Figs.7.5(a) and (c) show this very behaviour. Naturally $g . \underline{l} > 0$ for dark field images in layer L3, as shown by Fig.7.5(b).

ii) Loop Depth Around 1/4 ξ_g

Since surface relaxation effects were not taken into account in the calculations, the boundary between the layers L1 and L2 would be expected to lie at a depth of 1/4 ξ_g. Figure 7.6 shows the results of an investigation of contrast from a loop, the depth of whose centre varies in the range 1/8 ξ_g to 1/4 ξ_g. It can be seen that the transition to black-dot contrast at the boundary is quite gradual and involves a continuous diminution of the strength of the black-white contrast.

iii) Size Dependence

In Fig.7.5 it can be seen that the "line of no contrast", which separates the bright and dark lobes is not straight. In fact in this case the white lobe appears to extend into the black lobe. This appears to contradict the predictions of the kinematical Bloch wave theory of Chapter 4, which predicts that for an edge-on Frank loop the line of no contrast should be straight, and lie on the projection of the loop plane on the image plane.

However, it will be remembered that that theory used a First Born Approximation to calculate the Bloch wave amplitudes after scattering from the defect. Now it is well known in the case where

this approximation is used in the theory of scattering of radiation from an atom say, that its validity depends crucially upon the scattering cross-section of the atom being small (as was pointed out in Chapter 1). In fact, the Optical Theorem shows that the first Born approximation is only exact for the case where the scattering cross-section is identically zero!

It would therefore be expected that if the loop is made smaller the line of no contrast would become straighter as predicted by the kinematical Bloch wave scattering theory.

Fig.7.7 illustrates the dependence of the contrast from an edge-on Frank loop as a function of its size. The parameter h was given the values 25Å, 20Å and 15Å respectively. A gradual transition to a nearly straight line of no-contrast for the case of $h = 15$Å vindicates the above arguments based on the Born Approximation. (The loops of Fig.7.6 all have the parameter $h = 15$Å) Fig.7.7(d) is a magnified version of Fig.7.7(c) and shows that even for $h = 15$Å the line of no contrast is not exactly straight.

(iv) Images in different reflections

Figure 7.8 illustrates how the dark-field image from an edge-on Frank loop changes as the vector $\underline{g}$ of the operating reflection is rotated in the image plane. Figs 7.8(i), (iii) and (iv) form a sequence of images for increasing angular deviation of the vector $\underline{g}$ from the Burgers vector direction $\underline{b}$. The quantity $\underline{g} \cdot \underline{b}$ is respectively $-\frac{4}{3}$, $-\frac{2}{3}$ and $-\frac{1}{3}$

In Figs. 7.8(i), (ii) and (iii) a unique vector $\underline{\ell}$ can be defined (since there are only one white lobe and one black lobe) and in both cases, the direction of $\underline{\ell}$ lies between those of $-\underline{b}$ and $\underline{g}$.

In Fig.7.8 (iv), a subsidiary white lobe has begun to appear, but if one defines $\underline{\ell}$ as the vector joining the centres of the most prominent black and white lobes, then again the direction of $\underline{\ell}$ lies between those of $-\underline{b}$ and $\underline{g}$.

Figure 7.8(ii) is a magnified version of Figure 7.8(i) plotted in order to show up more clearly the region near the central "line of no contrast".

Figures 7.9 to 7.12 show experimental micrographs of self-ion irradiated copper at this orientation. The operating reflections are marked on the micrographs. By concentrating on a particular defect and observing the type of image produced in each of these reflections, it is possible, with the aid of computer simulated images like those shown in figure 7.8, to identify the planes on which they lie (assuming most of the prominent defects are Frank loops). The circled defects in figures 7.9 to 7.12 are labelled by the planes on which they are thought to lie (using Thompson's notation, see e.g. Chapter 8). Thus the defect image marked c on figure 7.10 clearly corresponds to the simulated image shown in figure 7.8 (iii) and that marked a on figure 7.11 to figure 7.8(iv).

Figure 7.13 shows an edge-on Frank loop viewed at a $\langle 211 \rangle$ - type orientation with $\underline{g}.\underline{b} = 0$. The loop is viewed by the so-called residual contrast. Only the components of the displacement field in a direction perpendicular to $\underline{b}$ contribute to the contrast. Since these components are weak compared to the components parallel to $\underline{b}$, the images would be expected to be considerably weaker than those for which $\underline{g}.\underline{b} \neq 0$. The image has been plotted using a different scale of contrast in order to bring out clearly the details of the "butterfly" shape. This type of image is known as a "butterfly" image. The greatest intensity in such an image, was only about a

fifth of that from a similar loop in an edge on orientation with $\underline{g} \perp \underline{t}$

Such experimental images have been observed by Eyre, Maher and Perrin (1974).

(b) i) Inclined Loops-variation with $\underline{g}$

At the [110] orientation, from the point of view of an incident electron beam, there are two edge-on {111} planes and two {111} planes which are inclined to the direction of the beam. Most investigations so far have concentrated on the edge-on Frank loops which give rise to strong black-white contrast under two beam conditions as shown in the preceding sections. The inclined loops are however also capable of producing black-white images, though of less contrast.

Figure 7.14 shows the results of image computations for these defects, observed under the conditions of the strongly excited reflections (111), (002) and (220). The pictures on the left are images from loops sloping into the paper towards the left and those on the right, the converse. It can be seen that in all cases the $\underline{\ell}$ vectors (defined as the vectors joining the centres of the main dark and bright regions) are nearly parallel to $\underline{g}$. This is very different from the variation of $\underline{\ell}$ with $\underline{g}$ for the case of edge-on Frank loops as described in the last section. The corresponding experimental images are those marked b on figures 7.9 to 7.12. These loops may lie on either of the Thompson planes b or d since the resolution on the experimental micrographs is insufficient to reveal much more detail than directions of $\underline{\ell}$.

In fact, this aspect of the contrast behaviour of inclined Frank-loops closely resembles that of a small spherical inclusion, and as we shall see in Chapter 8, that of the stacking-fault tetrahedron.

An interesting question then arises as to how an inclined Frank loop may be distinguished from a stacking-fault tetrahedron. Section 7.8.1(b)(iii) discusses one method which may have a chance of experimental success.

(ii) Depth Dependence

Consider the image in figure 7.14 of a Frank loop on a (111) plane at a depth in the foil of $\frac{1}{8}\xi_g$ where $g = (\bar{2}02)$ and ξ_g the two-beam extinction distance of the reflection g. A series of images of loops in this configuration but at different depths in the region of $\frac{1}{4}\xi_g$ are shown in Fig.7.15. The images seem to be nearly anti-symmetric about the depth $\frac{1}{4}\xi_g$ implying a similar layer structure as exists for the case of edge-on Frank loops. It will be observed that exactly at the depth $\frac{1}{4}\xi_g$, the intensity is purely above background, and would be worthy of experimental investigation.

(iii) Frank loops at ⟨100⟩ orientation

At a ⟨100⟩ orientation all the {111} planes are inclined to this direction. The different type of images given by Frank loops on three of these planes are shown in Figure 7.16. The image from the fourth plane is a mirror image of that shown in figure 7.16(c). It can be seen that these three varieties of images are all mutually distinguishable (especially 7.16(c) from 7.16(a) or 7.16(b). Thus imaging in $\underset{\sim}{g} = (022)$ would not only cause the vector $\underset{\sim}{\ell}$ to turn through a right angle (following $\underset{\sim}{g}$) but would also give a slightly different type of image.

It will be seen in Chapter 8 that a stacking fault tetrahedron in such an orientation would cause $\underline{\ell}$ to turn through a right angle as $\underline{g}$ is changed from $(02\bar{2})$ to (022) but would otherwise cause the image features to remain virtually identical. Thus at a $\langle 100 \rangle$ orientation it will be easier to distinguish between an inclined loop and a tetrahedron than at a $\langle 110 \rangle$ orientation.

7.8.2 Dislocation loops in B.C.C. Metals

In B.C.C. Metals, the condensation of point defects is expected to occur on the most densely packed $\{110\}$ planes resulting in a faulted loop of Burgers vector $\frac{a}{2}[110]$. The large stacking fault energy in such a configuration often causes shear ajong the $[001]$ direction which results in the formation of a perfect loop with Burgers vector $\underline{b} = \frac{1}{2}[111]$

Also possible is a shear in a $[1\bar{1}0]$ direction which creates a loop with $\underline{b} = a[100]$. Burgers vectors $\underline{b} = \frac{a}{2}\{110\}$ and $\underline{b} = a\{100\}$ are perfect lattice vectors and consequently such loops contain no stacking-fault. They are therefore glissile and may move along their slip cylinders so as to minimize the lengths of their dislocation lines (for energy reasons) This minimum configuration occurs when the loop normal $\underline{n}$ turns round to be parallel with the Burgers vector $\underline{b}$.

Let the shear process be represented by the following equation,

$$\underline{b}_1 + \underline{b}_2 \rightarrow \underline{b}_t$$

where b_1 is the initial Burgers vector, $\underline{b}_2$ is the shear Burgers vector and $\underline{b}_t$ is the total Burgers vector after shear.

Then $\underline{b}_1 . \underline{b}_2 = 0$. The two different types of shear processes which can occur are exemplified by the following equations

$$\frac{a}{2}[110] + \frac{a}{2}[001] \rightarrow \frac{a}{2}[111]$$

$$\frac{a}{2}[110] + \frac{a}{2}[1\bar{1}0] \rightarrow a[100]$$

Let us also assume, following Haussermann, Ruhle and Wilkens (1972,b), that after shear, the loop normal $\underline{n}$ either remains parallel to $\underline{b}_1$ or rotates such as to be parallel to $\underline{b}_t$. We can thus construct the following table describing all possible loop configurations in b.c.c. metals.

	b_t	n parallel to	No. of possible configurations
1	$\frac{a}{2}\langle 110\rangle$	$b_t = b_1$ (no shear)	6
2	$a\langle 100\rangle$	b_1	12
3	$\frac{a}{2}\langle 111\rangle$	b_1	12
4	$a\langle 100\rangle$	b_t	3
5	$\frac{a}{2}\langle 111\rangle$	b_t	4
		Total	37

An exhaustive study of contrast from dislocation loops in b.c.c. metals therefore requires the consideration of 37 different cases. Fortunately energetic and other considerations narrows down the number of configurations expected to be observed practically

condition for the $(12\bar{1})$ reflection.

Calculations using polygonal loop model of Chapter 6

Calculations were performed for a polygonal loop whose X-, Y- and Z-axes were oriented parallel to the [110], [1$\bar{1}$0] and [001] directions respectively. Identical diffraction conditions to those used by Ohr were employed, and the depth of the centre of the loop in the foil was made $\frac{\xi_g}{8}$, $\frac{\xi_g}{4}$, $\frac{\xi_g}{2}$, $\frac{3}{4}\xi_g$, ξ_g successively and the bright field images simulated for each case. Fig.7.17 shows images obtained for each of these cases. Good agreement with Ohr's results is obtained. This seems to indicate that the images expected from circular and hexagonal loops are almost identical.

It thus appears that if images of the sort predicted from our calculations and Ohr's are experimentally observed, it would not be possible to tell from this sort of black-white contrast, whether the loops are circular or hexagonal.

It should perhaps be emphasized that if Haussermann's (1972a) arguments are valid (concerning the probability of slip of perfect loops), the loops in Ohr's configuration are not likely to be plentiful in a thin foil (since the foil normal and the Burgers vector make only a small angle relative to one another, assuming the foil normals are close to the orientation parameter [113]). In view of this consideration, it was decided to examine a case where $\underline{b}$ was perpendicular to the nearby foil normal and this is described in the next section.

in thin foils. For instance, as pointed out by Haussermann (1972a), if the Burgers vector of a perfect loop is perpendicular to a nearby foil surface, there is a reasonable probability that the loop would slip out to the surface. Thus in practical cases only the perfect loops with Burgers vectors nearly parallel to nearby foil surfaces need be considered. Secondly, shear processes themselves are affected by a nearby surface. Shears whose vectors point toward the surface are more likely, due to the possibility of surface relaxation, which lowers the energy barrier to such a process.

Calculated contrast from loops with shear components

Previous work

Wilkens and Ruhle (1972) have used the expression for the displacement field due to an infinitesimal loop given in 7.6.1 to calculate the contrast expected from loops with shear components of Burgers vector. Ohr (1972) has derived expressions for the displacement field due to a finite dislocation loop in terms of the functions $I_j^i(\rho, \zeta)$ described in 7.6.2.

The method described in Chapter 6 enables the displacement field due to a polygonal loop with shear components of Burgers vector to be constructed. All three methods assume elastic isotropy.

Ohr (1973) has calculated line profiles of image contrast expected from loops with shear components, using his expressions for the displacement field. He considered the case of niobium which is a B..C.C. material and the common $\underline{b} = \frac{a}{2}[111]$ loops on (110) planes. These calculations, were performed on the computer for a foil of thickness 1000Å and loop radius 25Å. The foil plane was taken as the (113) plane oriented to satisfy the exact Bragg

condition for the $(12\bar{1})$ reflection.

Calculations using polygonal loop model of Chapter 6

Calculations were performed for a polygonal loop whose X-, Y- and Z-axes were oriented parallel to the [110], [1$\bar{1}$0] and [001] directions respectively. Identical diffraction conditions to those used by Ohr were employed, and the depth of the centre of the loop in the foil was made $\frac{\xi_g}{8}$, $\frac{\xi_g}{4}$, $\frac{\xi_g}{2}$, $\frac{3}{4}\xi_g$, ξ_g successively and the bright field images simulated for each case. Fig.7.17 shows images obtained for each of these cases. Good agreement with Ohr's results is obtained. This seems to indicate that the images expected from circular and hexagonal loops are almost identical.

It thus appears that if images of the sort predicted from our calculations and Ohr's are experimentally observed, it would not be possible to tell from this sort of black-white contrast, whether the loops are circular or hexagonal.

It should perhaps be emphasized that if Haussermann's (1972a) arguments are valid (concerning the probability of slip of perfect loops), the loops in Ohr's configuration are not likely to be plentiful in a thin foil (since the foil normal and the Burgers vector make only a small angle relative to one another, assuming the foil normals are close to the orientation parameter [113]). In view of this consideration, it was decided to examine a case where $\underline{b}$ was perpendicular to the nearby foil normal and this is described in the next section.

An interesting feature of the configuration studied by Ohr is that the image plane normal z, the Burgers vector b and the loop plane normal n are coplanar. This implies that the projections of $\underline{b}$ and $\underline{n}$ onto the image plane are identical. Now this condition also holds for inclined Frank loops, such as those whose contrast is shown in figures7.14 and 7.15. It is thus to be expected that the perfect loops in Ohr's configuration would produce contrast having some similarities to those of figures 7.14 and 7.15. Comparison with Figure 7.17 reveals many similarities.

Main types of contrast from perfect loops with shear components

Consider a system of Cartesian axes with the x- and y-axes in the image plane and the z-axis as the image plane normal. Let the reciprocal lattice vector $\underline{g}$ point along the x-axis. Then Haussermann et al (1972b) state that there are four different types of images obtained under the following conditions:

(i) If the directions of the loop plane normal $\underline{n}$ and $\underline{b}$ the Burgers vector are sufficiently close to the $\pm$ x-axes, the image consists of one black and one white lobe roughly symmetric with respect to a mirror line drawn through the lobe centres. This is known as a "normal" black-white image.

(ii) With increasing n_y and b_y components, the lines of no-contrast between the main lobes becomes roughly S-shaped and the main lobes become extrusions. This is known as a "weakly distorted" image.

(iii) If $\underline{n}$ and $\underline{b}$ lie sufficiently close to but not exactly inside the yz plane, or if one of the dire ctions lies inside the yz plane with the other one deviating appreciably from this plane, the images show subsidiary lobes comparable in size to the main lobes (although still smaller). The subsidiary

lobes streak in the directions of $\pm \underline{g}$. This type of image is known as "strongly distorted".

(iv) If both $\underline{a}$ and $\underline{b}$ lie in the yz plane, the images have a "butterfly" shape of three pairs of black-white lobes centred on one point. In this case the lobes extending parallel or anti-parallel to the x-axis are shorter and narrower than the other four lobes. This is also sometimes known as a "three-fold symmetric" image.

Contrast calculations for loops in molybdenum with b perpendicular to foil normal

Contrast from loops with $\underline{b}$ lying in the image plane was calculated and the results are shown in Figures 7.18 and 7.19. The important parameters are given in the captions and show that in this case the loop plane is edge-on. Strong-beam images in the reflections $(0\bar{1}\bar{1})$ (200), $(\bar{2}1\bar{1})$ and $(21\bar{1})$ are shown in Figure 7.18 and those for opposite $\underline{g}$ are shown in Figure 7.19.

The effect of reversing $\underline{g}$ is seen to be mainly the conversion black lobes into white and vice-versa.

In the images on the left-hand sides of figures 7.18 and 7.19 $\underline{n}$ and $\underline{b}$ are oriented quite close to the direction of $\underline{g}$ but nevertheless have appreciable components in the y-direction (using the Cartesian axes system of 7.8.2). The images would thus be expected to be of the "weakly distorted" category and this is, in fact, observed.

In the top right-hand side images of figures 7.18 and 7.19 , $\underline{n}$ lies in the y-z plane but $\underline{b}$ deviates appreciably from this plane. In the bottom righ-hand side images of figures 7.18 and 7.19 , $\underline{b}$ lies in the y-z plane but $\underline{n}$ deviates appreciably. Thus both these conditions would be expected to produce the "strongly distorted" images described in 7.8.2(iii) The pictures are good examples of this type of image.

Experimental micrographs of irradiated molybdenum observed in these reflections with the foil orientation near [011] are shown in figure 7.20. The different types of images obtained from the same defect are illustrated. The particular foil orientation used to produce each image is indicated by the vector $\underline{Z}$.

Reasonably good agreement with the computed images of figures 7.18 and 7.19 can be seen. The slight differences might be attributable to the fact the foils for the computed images were orientated exactly at [011].

FIGURE 7.5

FRANK LOOP (EDGE-ON) (Cu)

Depth Dependence -

Layer structure

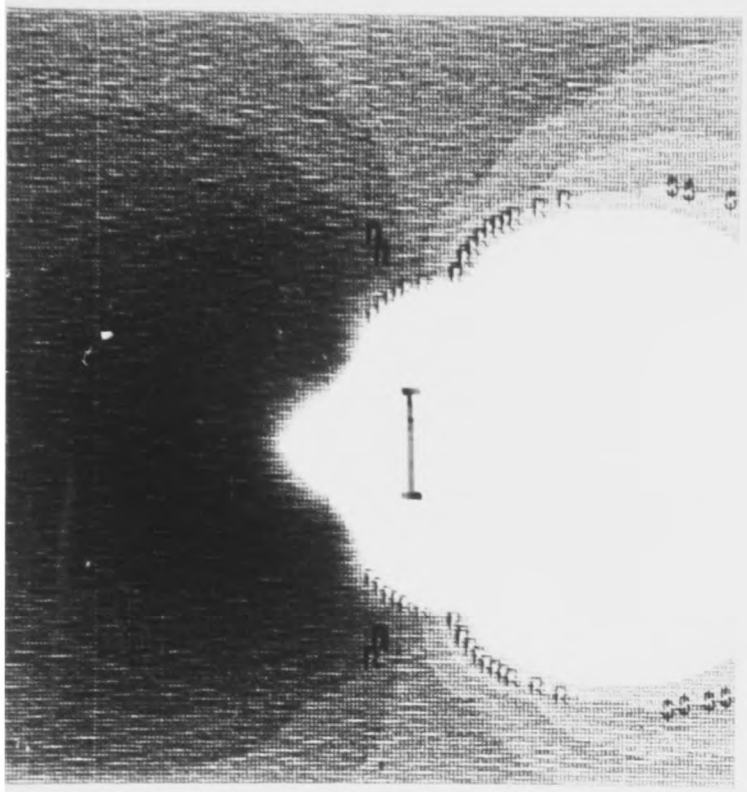
$\underline{Z} = [110]$

$\underline{g} = (\bar{1}1\bar{1})$

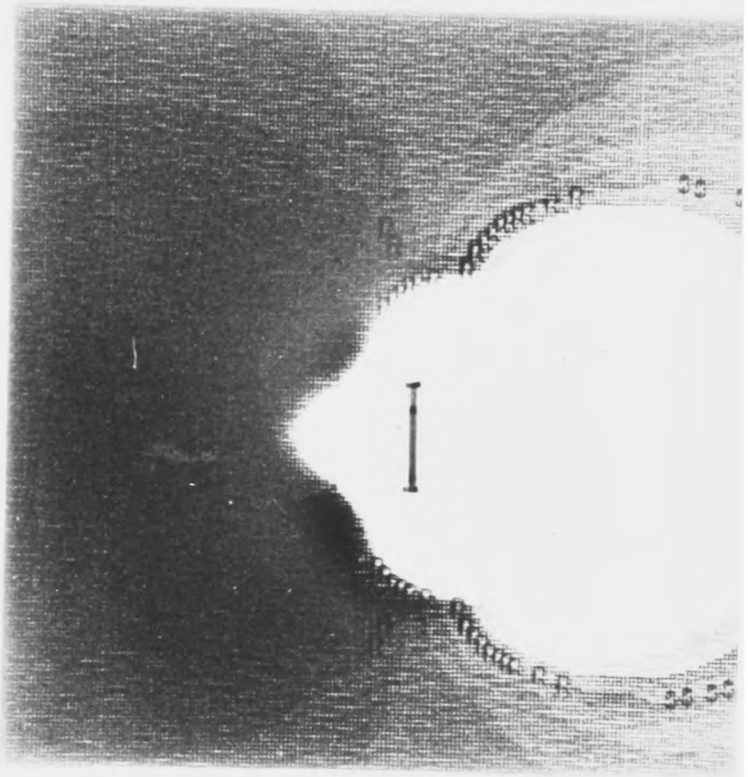
$\underline{b} = a/3[\bar{1}1\bar{1}]$

$h = 30\text{Å}$

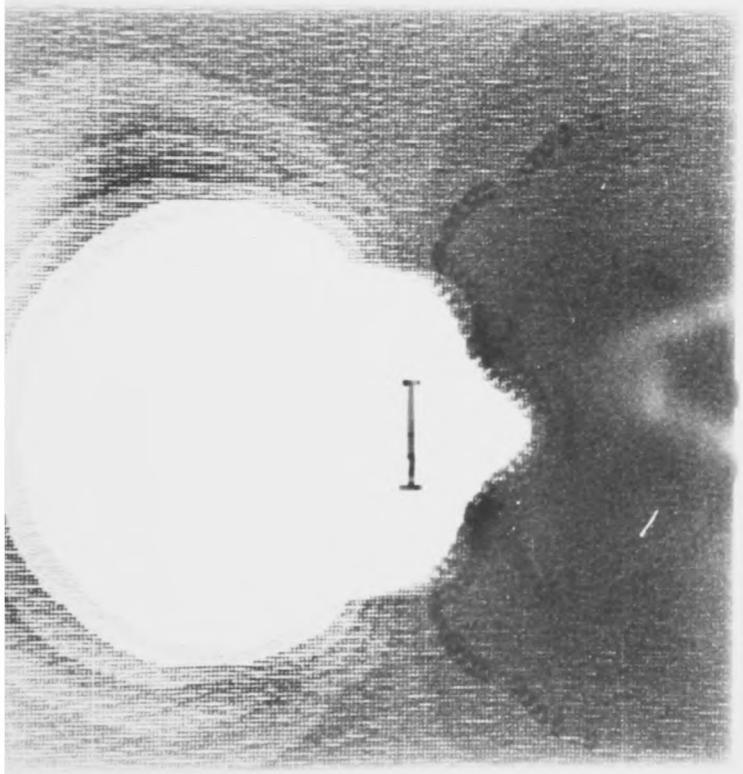
$t = 2\xi_g$



(a) $d = 0.5\,\xi_g$ (L2)



(c) $d = 1.5\,\xi_g$

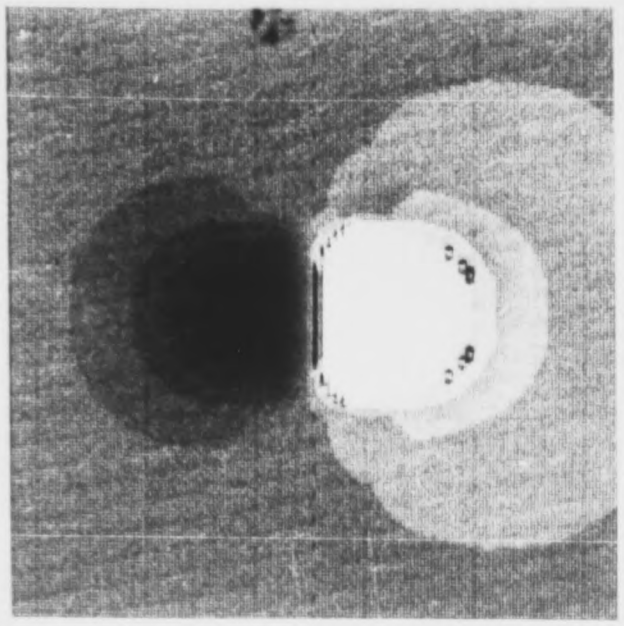


(b) $d = 1.0\,\xi_g$ (L3)

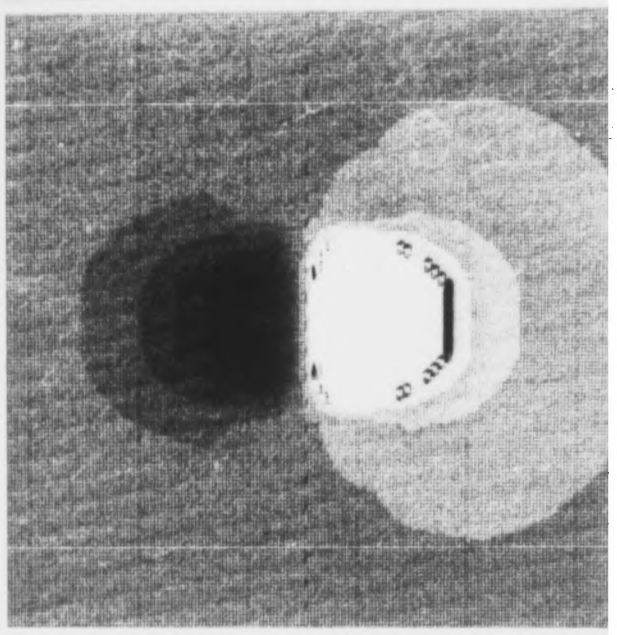
$\underline{g}$

FIGURE 7.6

FRANK LOOPS (Edge-On)

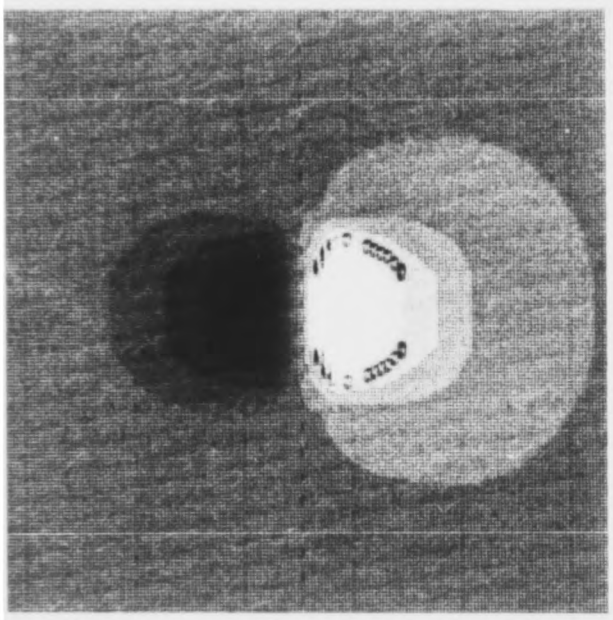


$d = 1/8\,\xi_g$

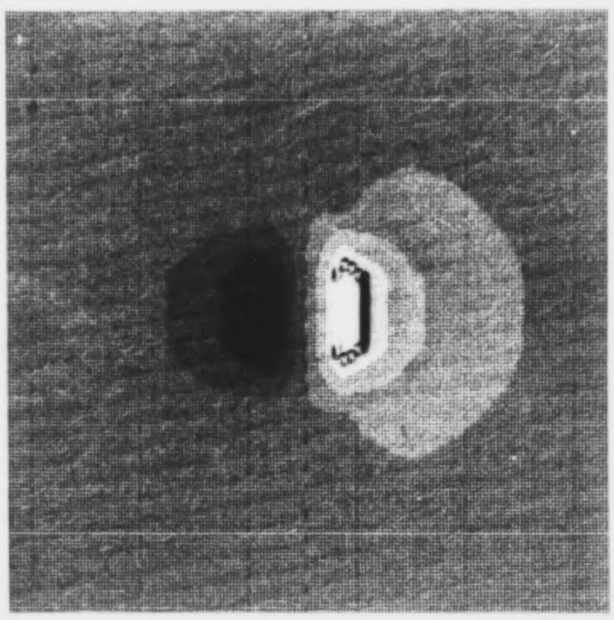


$d = 5/32\,\xi_g$

Depth Dependance

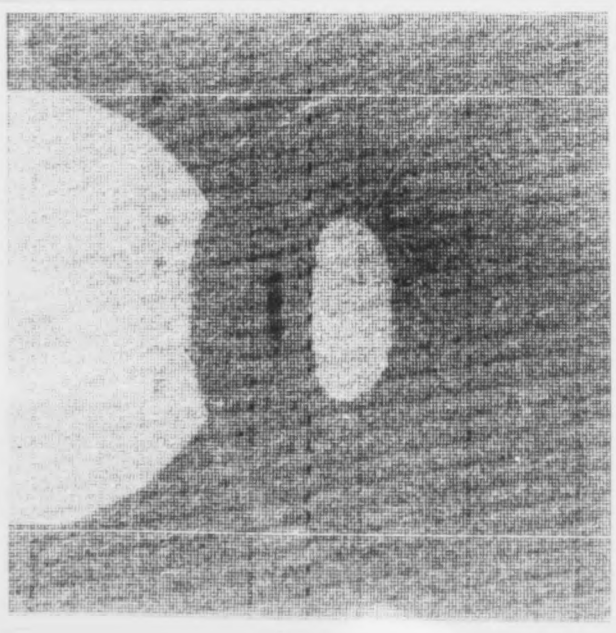


$d = 6/32\,\xi_g$



$d = 7/32\,\xi_g$

$\underline{g} = (111)$



$d = 1/4\,\xi_g$

$h = 15\text{Å}$

FIGURE 7.7

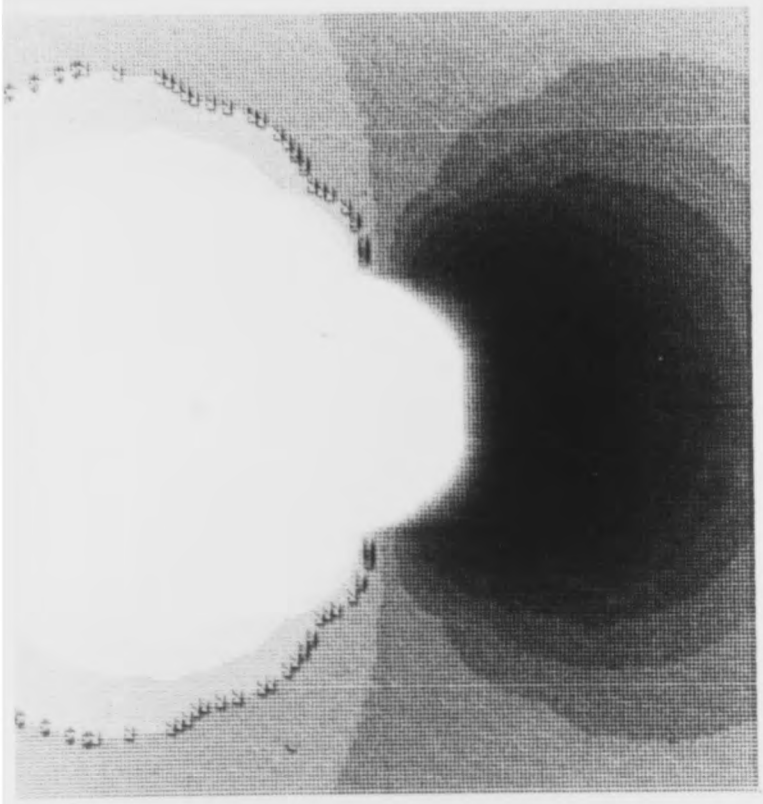
FRANK LOOPS (EDGE-ON)

Size Dependance

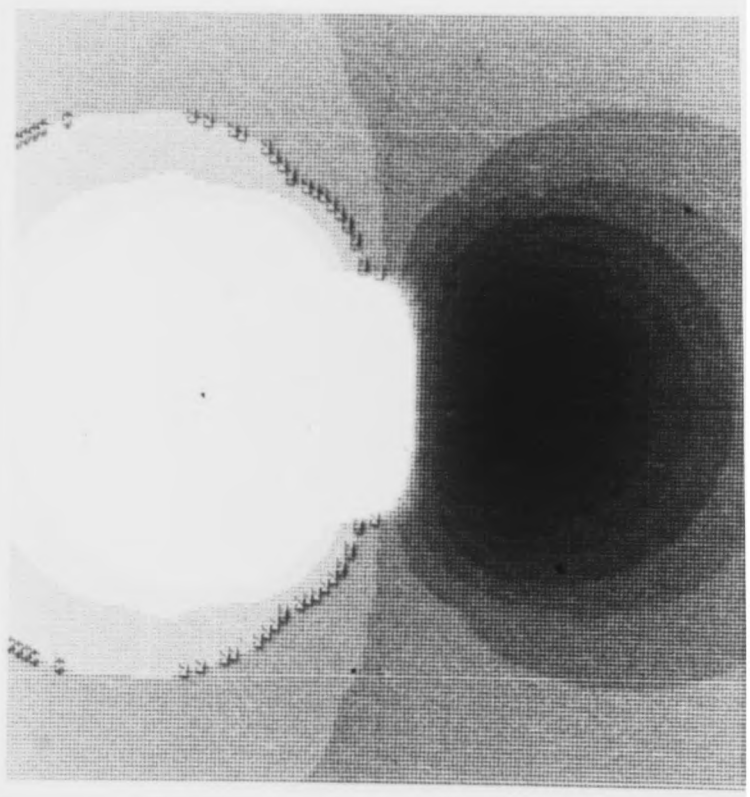
$t = 2\xi_g$

$d = \xi_g$ (Layer L3)

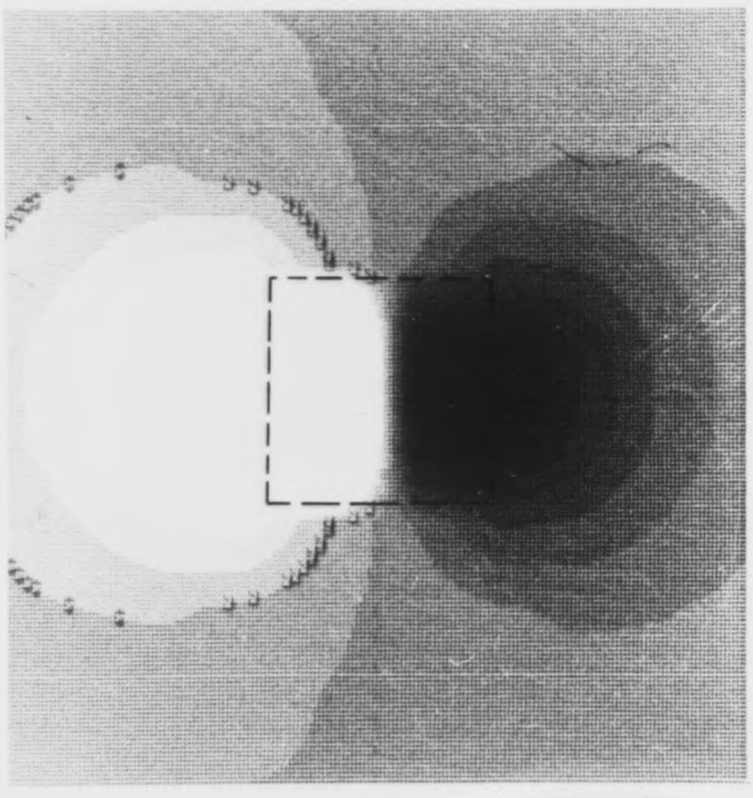
$\underline{g}$



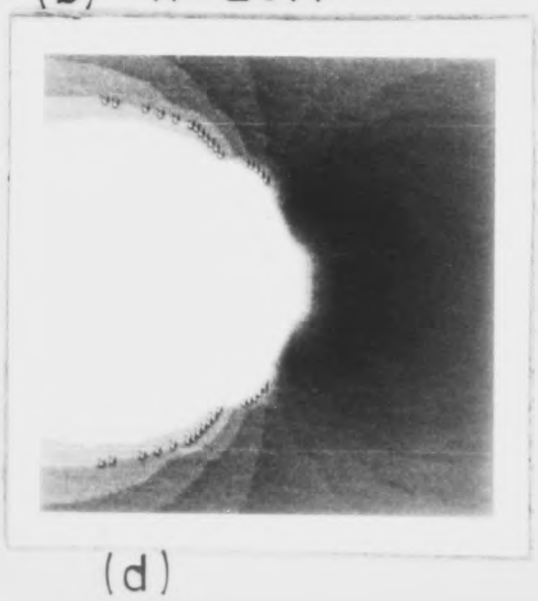
(a) h = 25Å



(b) h = 20Å



(c) h = 15Å

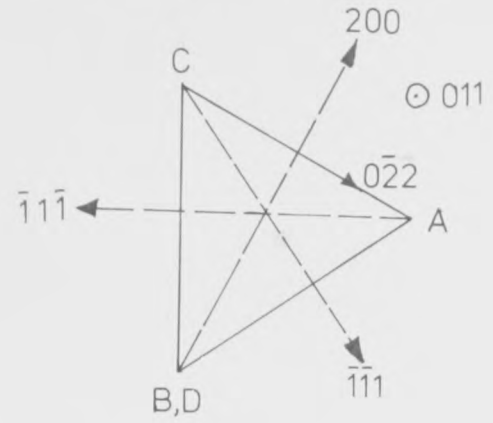


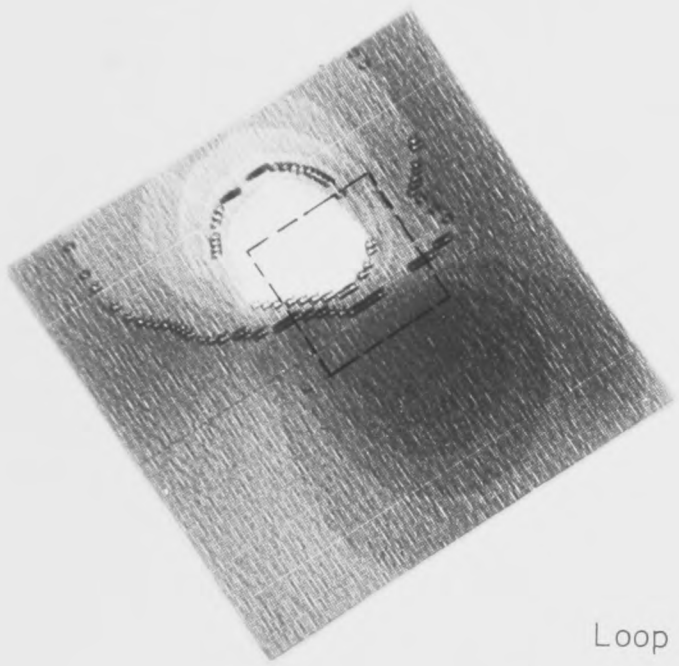
(d)

FIGURE 7.8

FRANK LOOPS (EDGE-ON)

Different Bragg Reflections

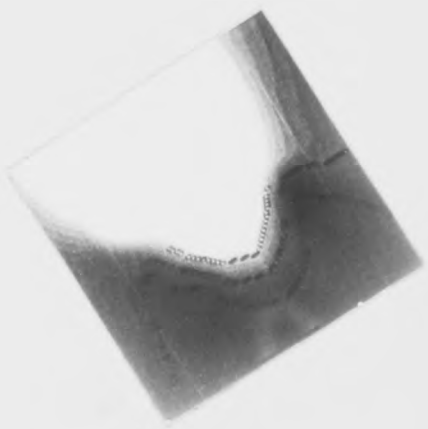




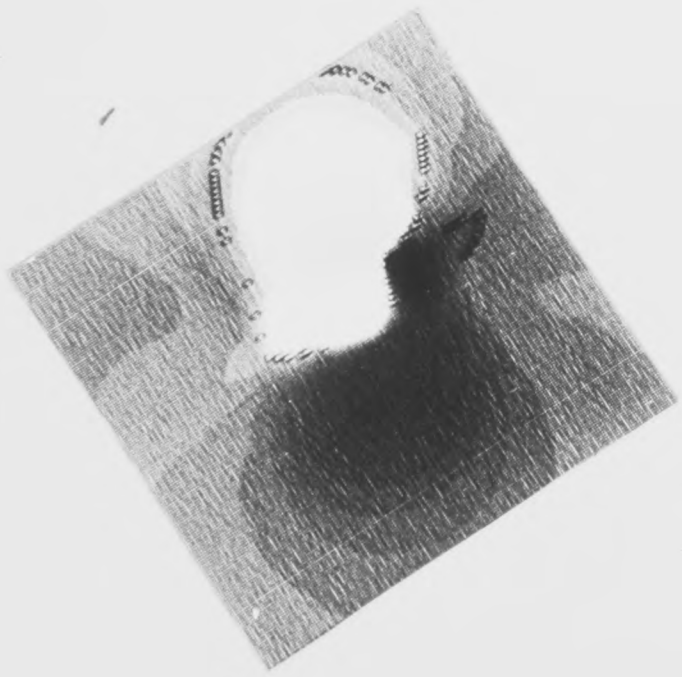
(i)

Loop Plane c ,

$\underline{g}=(02\bar{2})$, $\underline{g}.\underline{b}=-4/3$, h=30Å , $d=\xi_g$



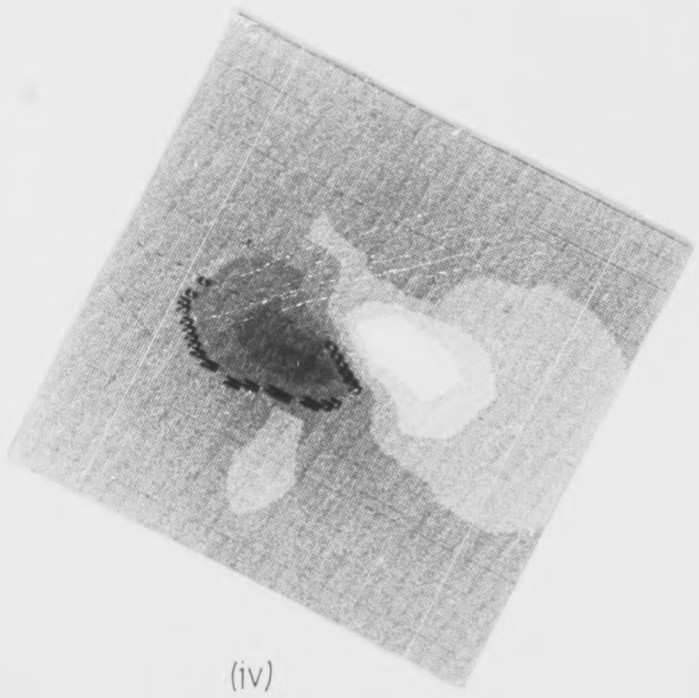
(ii)



(iii)

Loop Plane c , $\underline{g}=(200)$,

g.b=-2/3 , h=30Å , $d=\xi_g$



(iv)

Loop Plane a , $g=(\bar{1}\bar{1}1)$,

g.b=-1/3 , h=15Å , $d=1/8\,\xi_g$

FIGURE 7.9

Experimental Micrograph of self-ion irradiated copper (Photograph taken by A.Y. Stathopoulos).

Strong-beam conditions, $\underline{g}$ is the operating reflection.

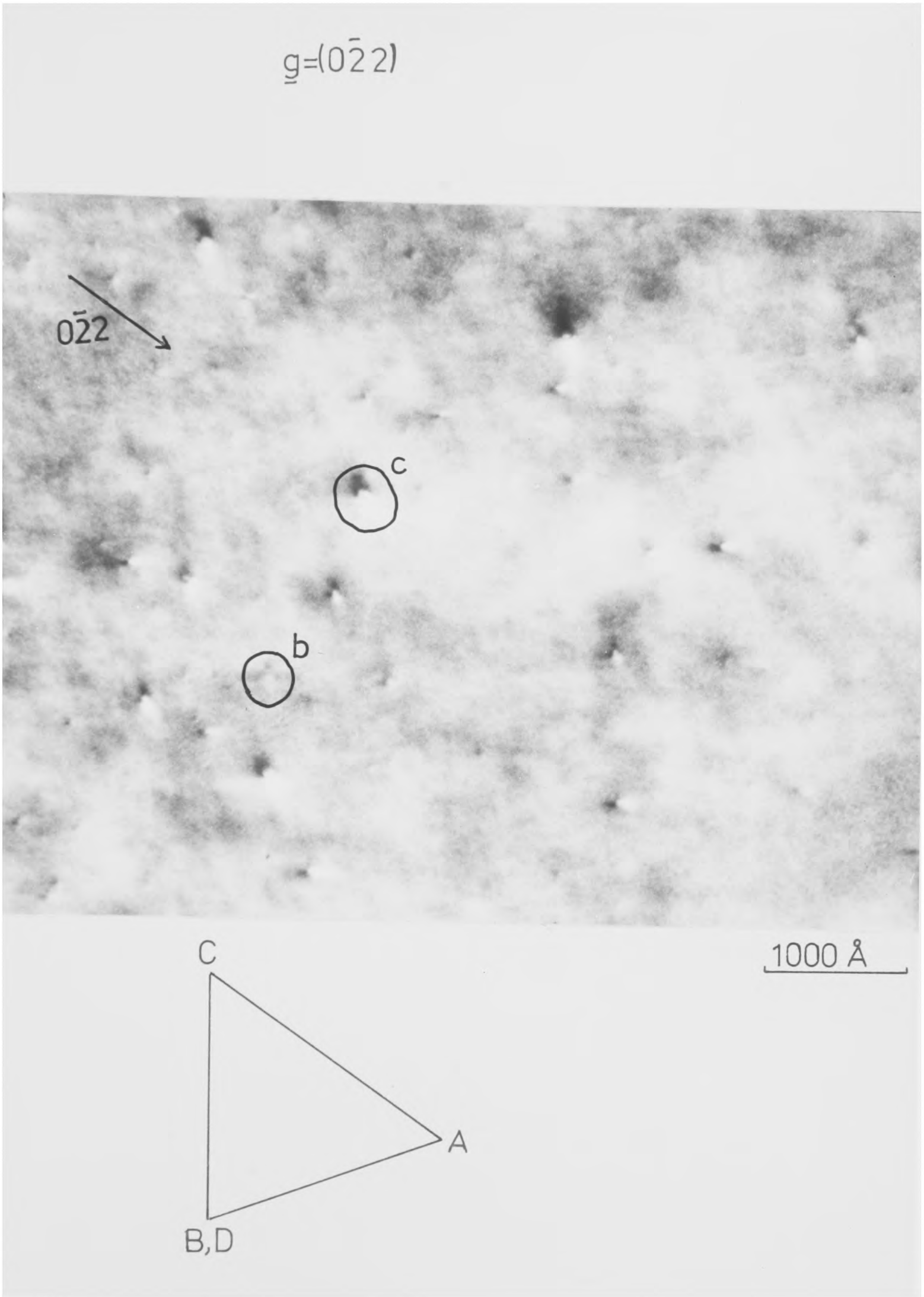
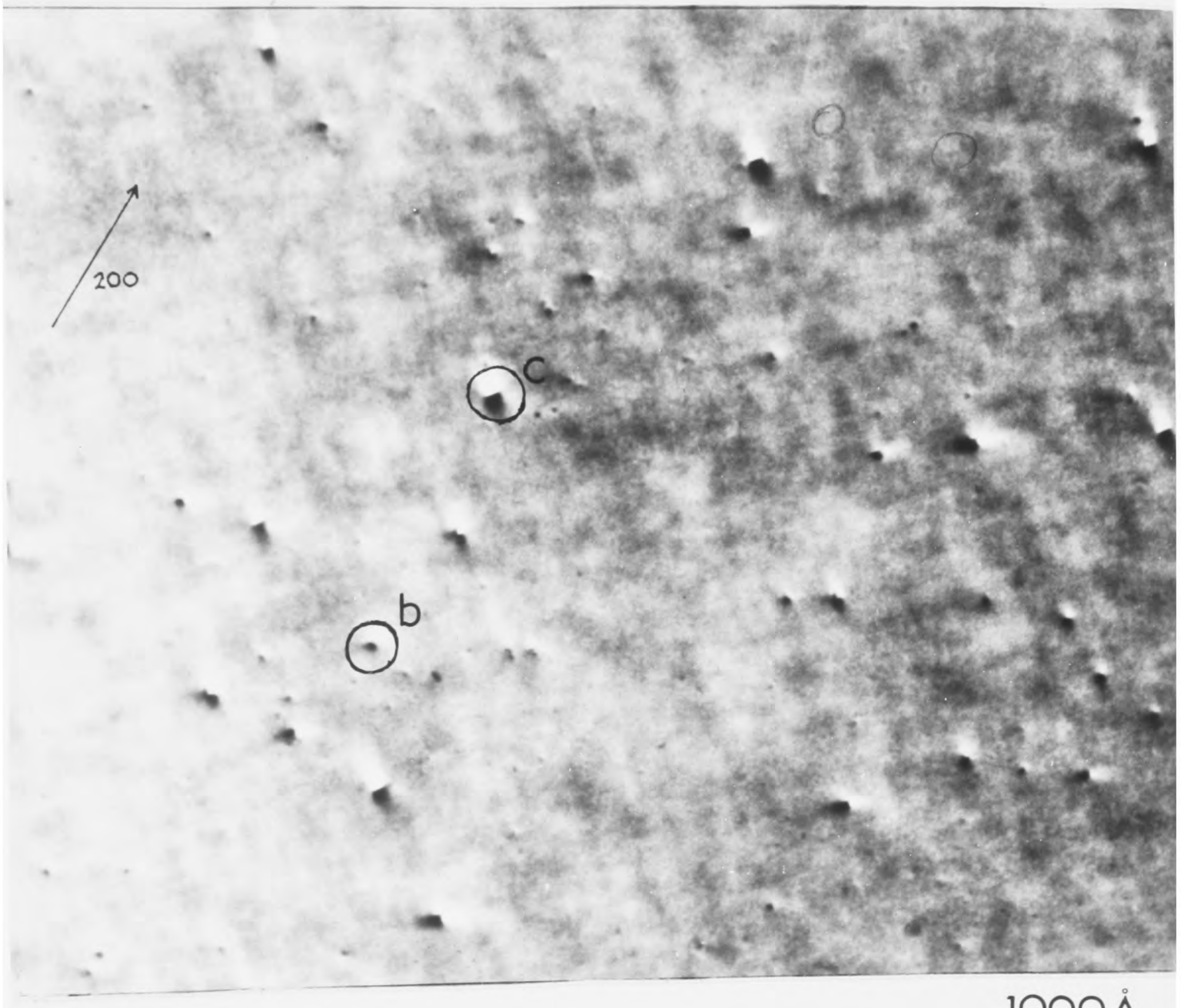

g=(0$\bar{2}$2)
0$\bar{2}$2
c
b
C
A
B,D
1000 Å

FIGURE 7.10

Experimental Micrograph of self-ion irradiated copper.
(Photograph taken by A.Y. Stathopoulos)

Strong beam conditions, $\underline{g}$ is the operating reflection.

$\underline{g}$=(200)



1000 Å

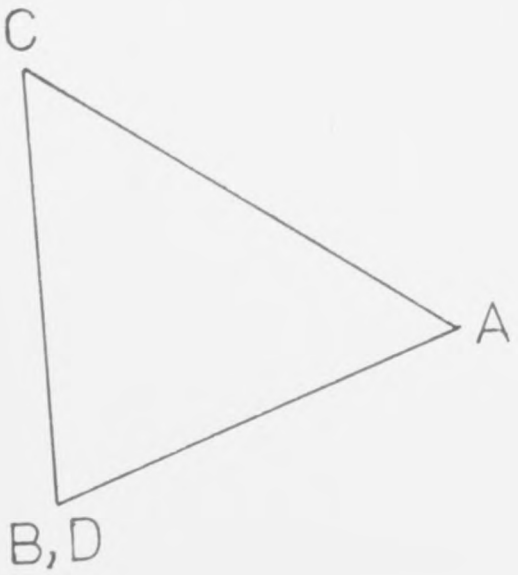
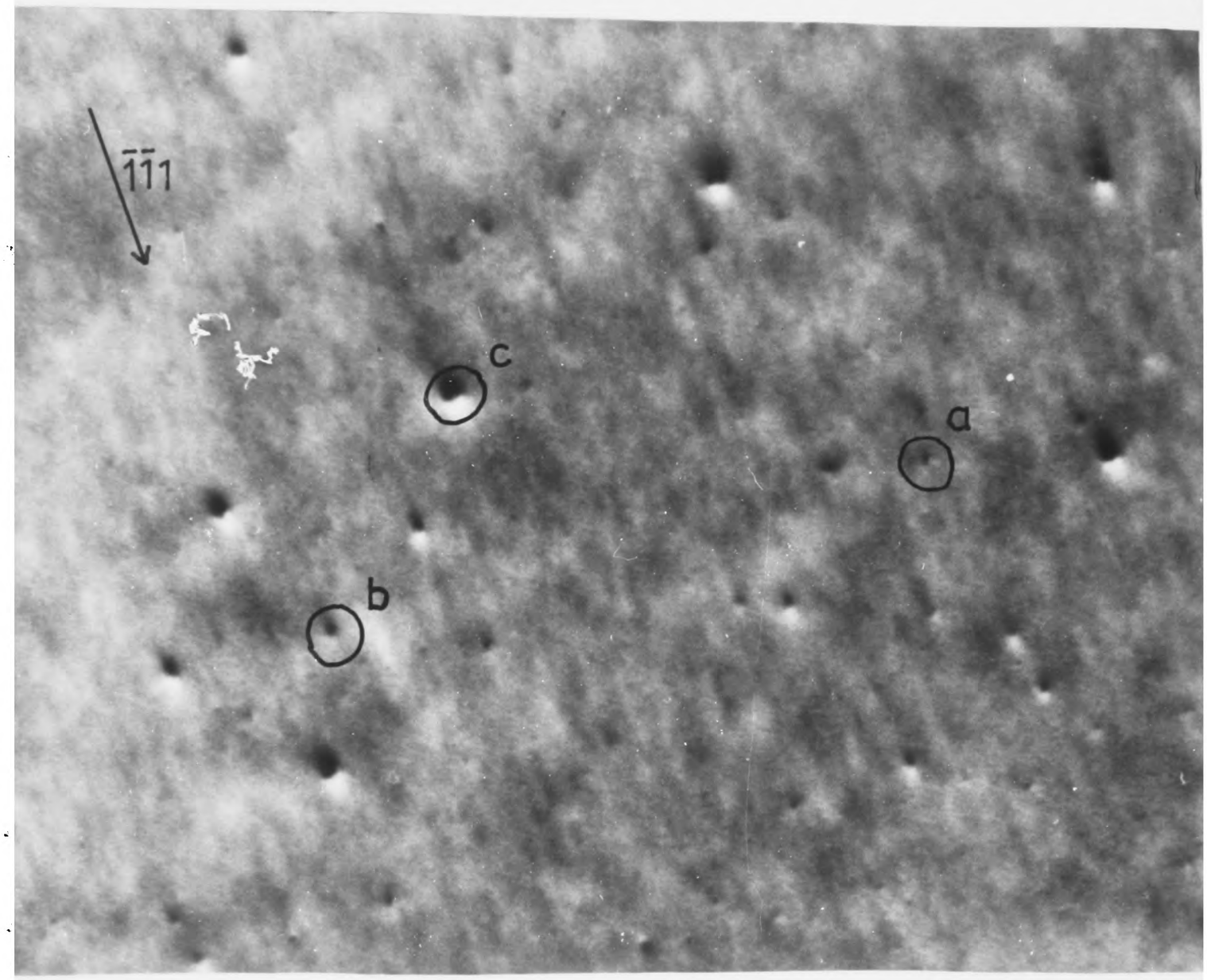


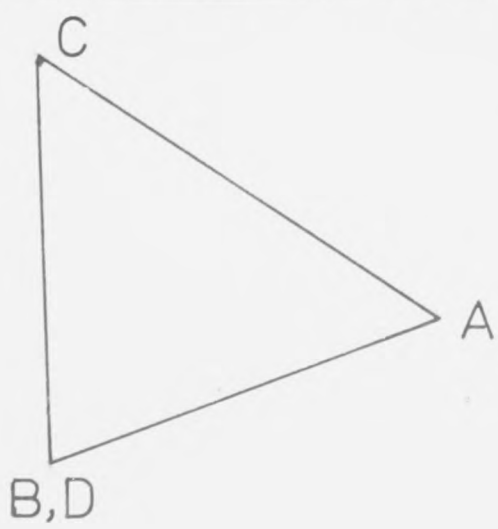
FIGURE 7.11

Experimental Micrograph of self-ion irradiated copper (Photograph taken by A.Y. Stathopoulos).

Strong-beam conditions, $\underline{g}$ is the operating reflection

$\underline{g} = (\bar{1}\bar{1}1)$





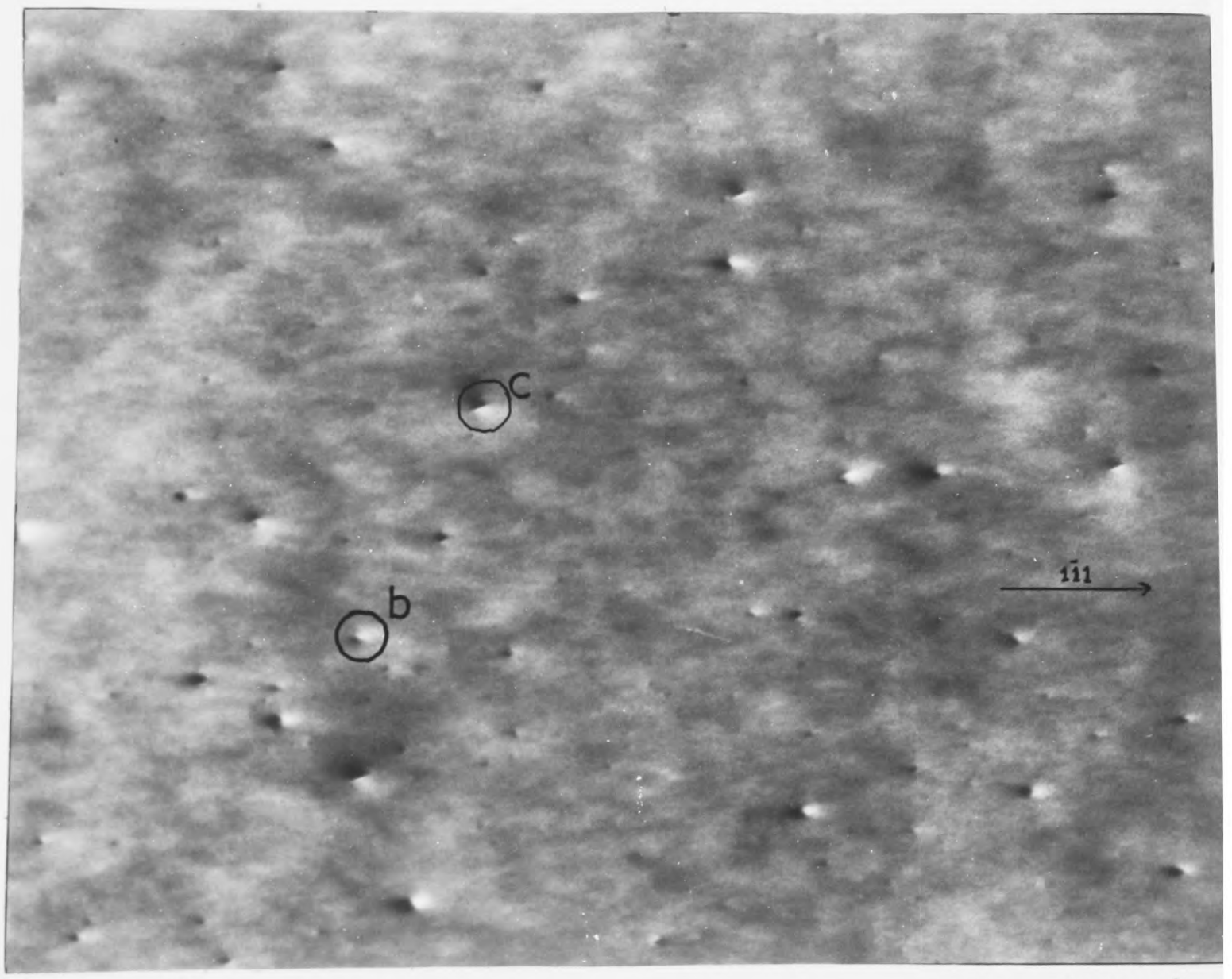
1000 Å

FIGURE 7.12

Experimental Micrograph of self-ion irradiated copper.
(Photograph taken by A.Y.Stathopoulos).

Strong-beam conditions, $\underline{g}$ is the operating reflection.

$\underline{g}=(1\bar{1}1)$



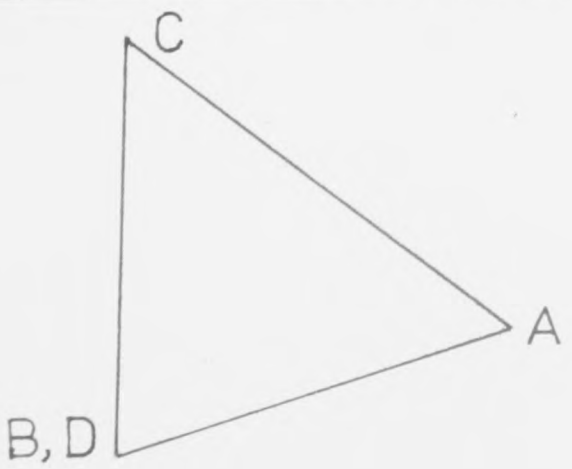


FIGURE 7.13

FRANK LOOP (EDGE-ON)

"Butterfly" Image

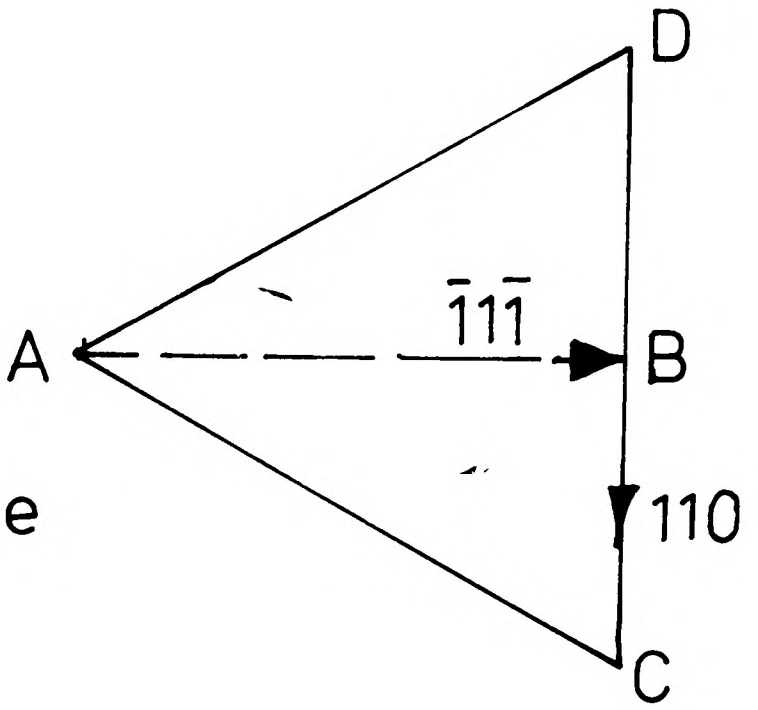
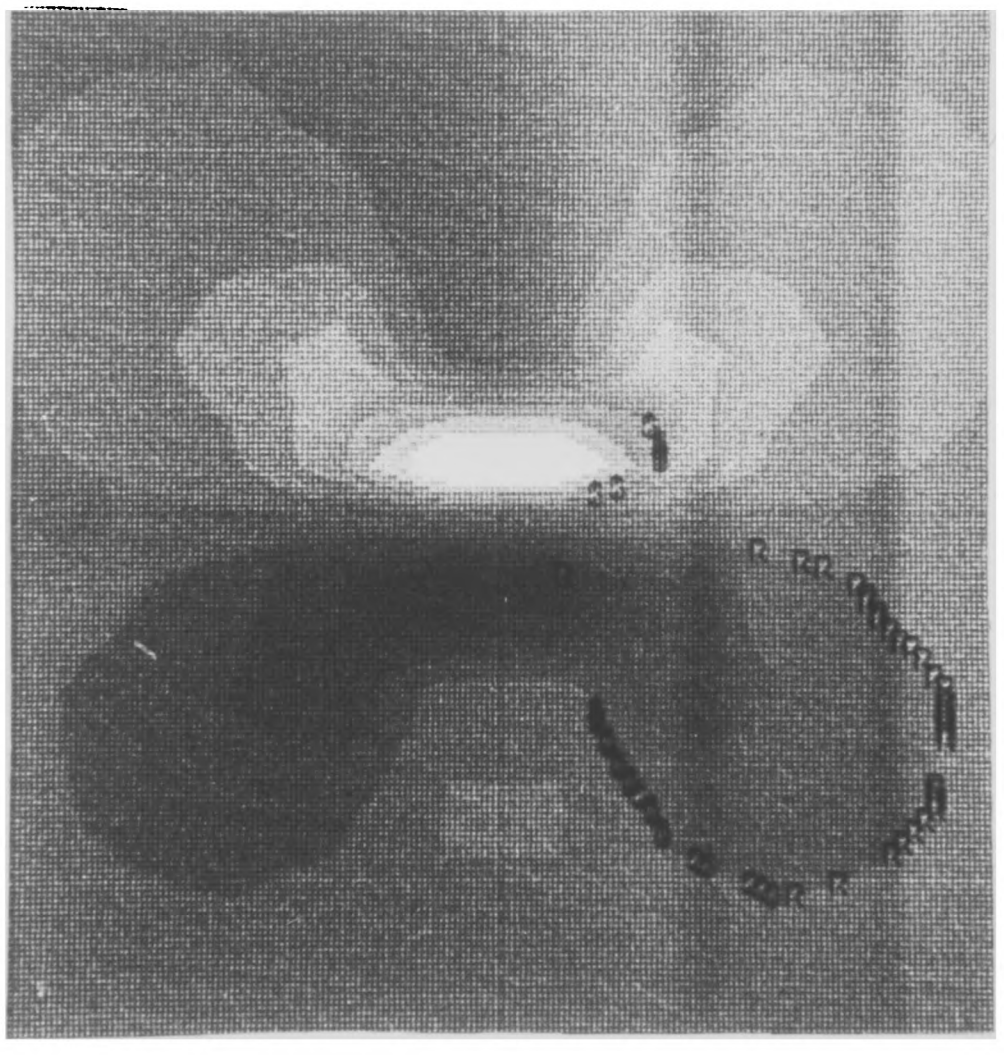


Image Plane Normal
⊙ $\bar{1}12$

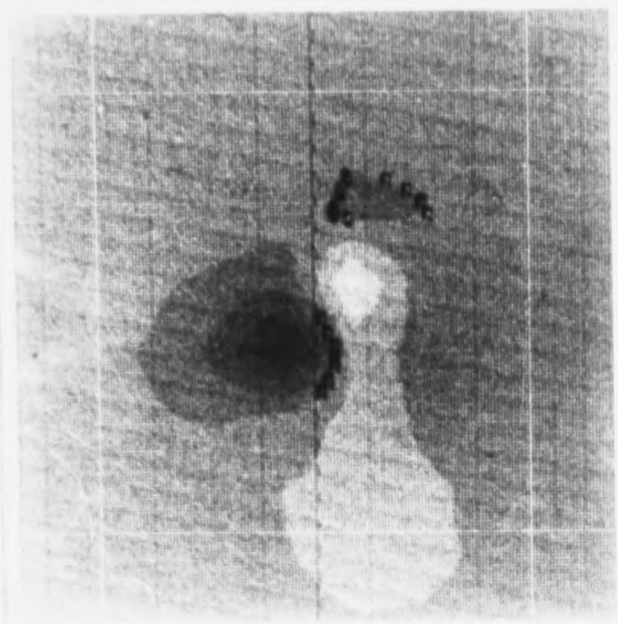


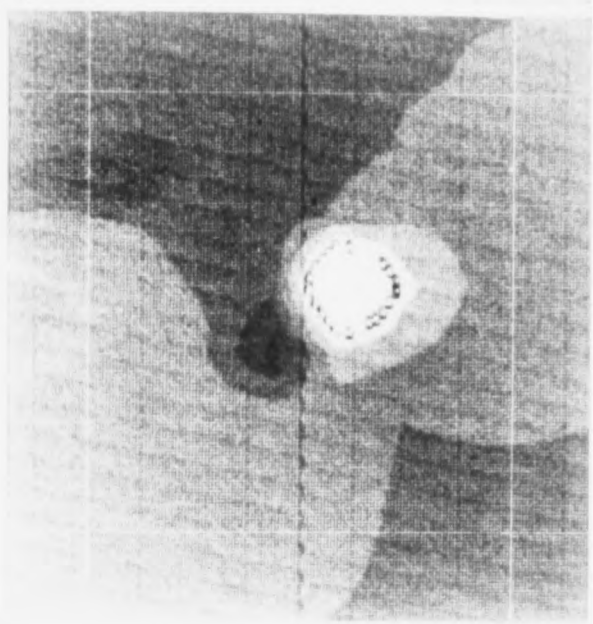
Loop Plane a, $\underline{g}=(220)$, $\underline{g}.\underline{b}=0$
$h=30\text{Å}$, $d=\xi_a$

FIGURE 7.14

FRANK LOOPS (INCLINED)

$\underline{Z} = [110]$

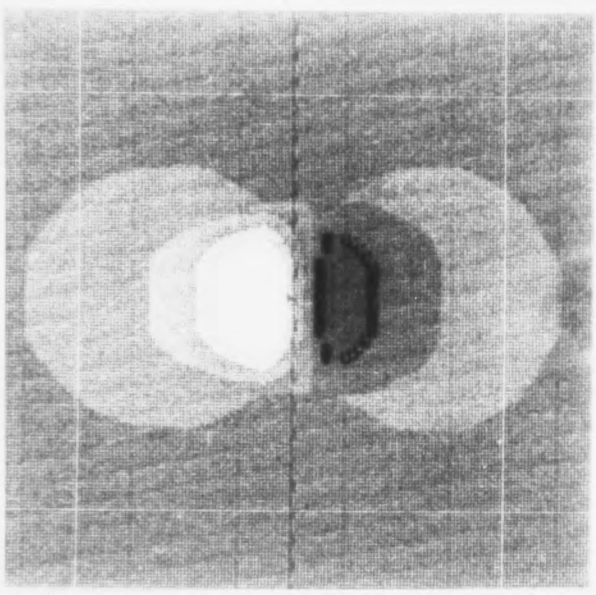


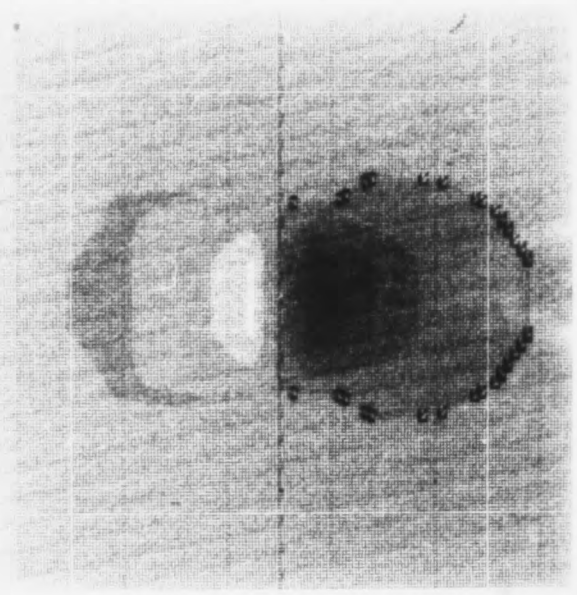


$\underline{b} = a/3[111]$

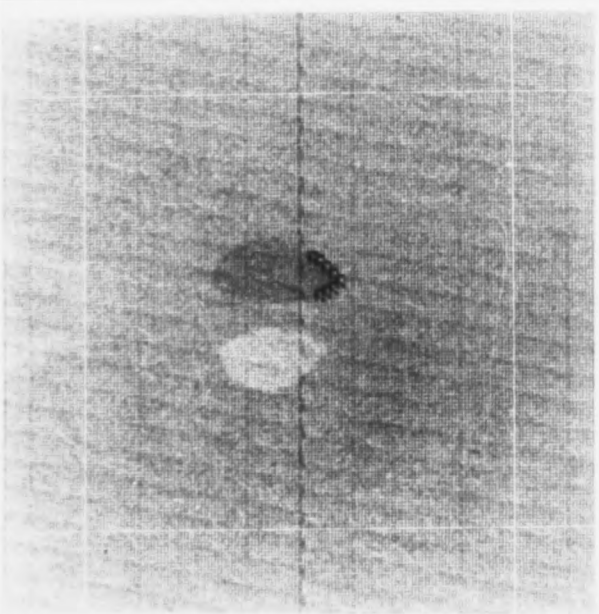
$\underline{b} = a/3[11\bar{1}]$

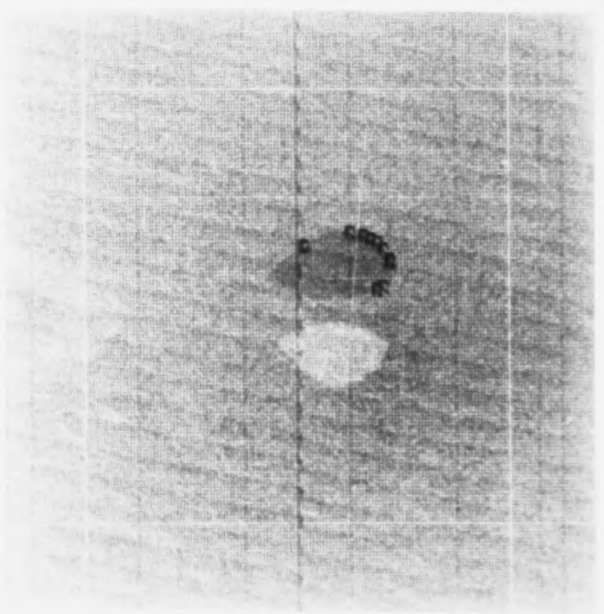
$\underline{g} = (\bar{1}1\bar{1})$





$\underline{g} = (002)$





$\underline{g} = (220)$

FIGURE 7.15

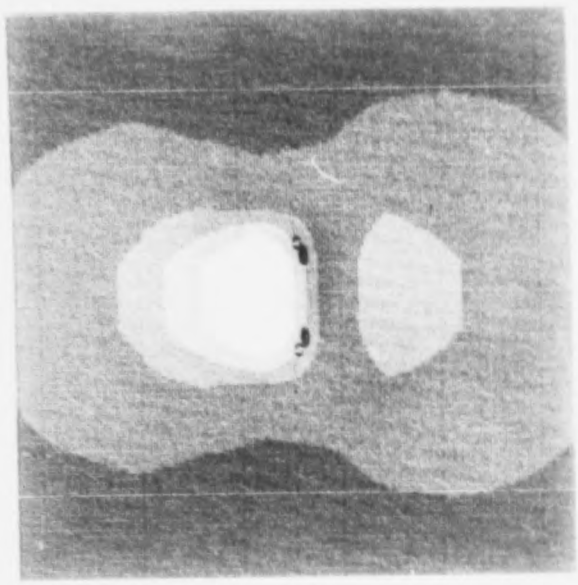
INCLINED FRANK LOOP - Depth Dependence (Cu)

Thickness $2\xi_g$

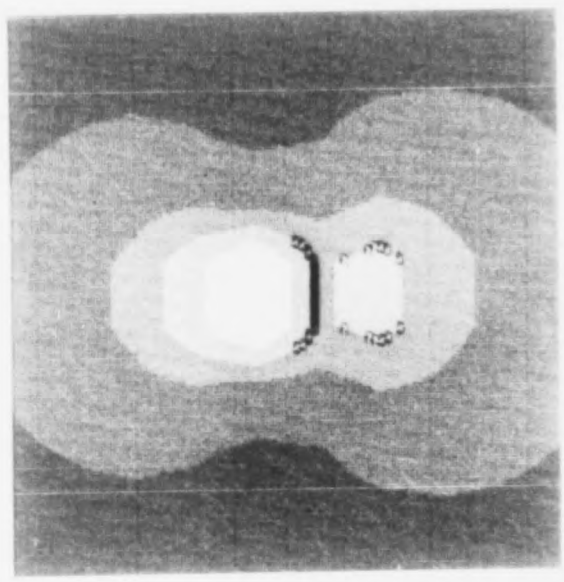
$\underline{b} = a/2[111]$

$\underline{Z} = [110]$

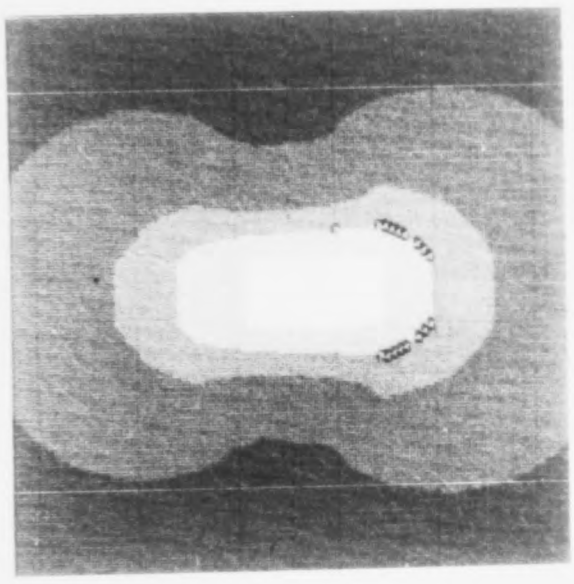
$\underline{g} = (002)$ ←



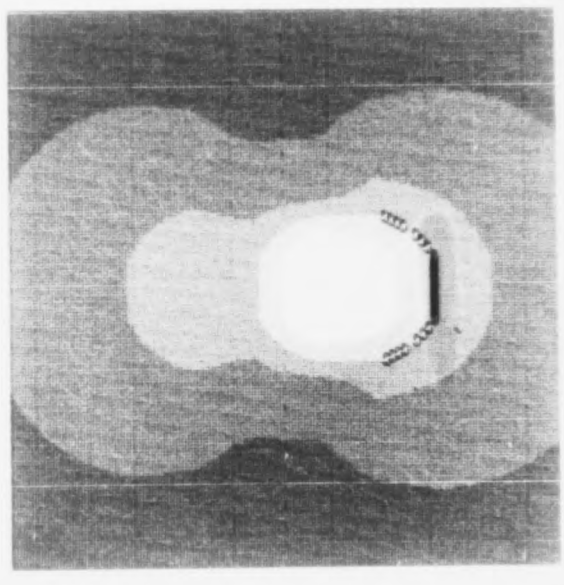
$d = 6/32\ \xi_g$



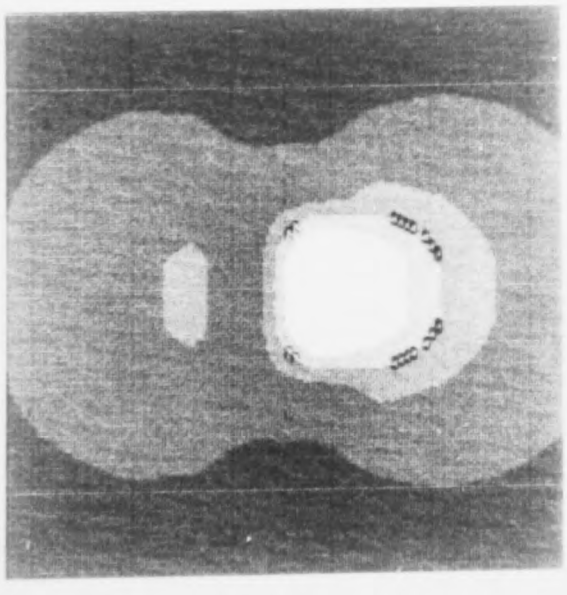
$d = 7/32\ \xi_g$



$d = 8/32\ \xi_g = 1/4\ \xi_g$



$d = 9/32\ \xi_g$

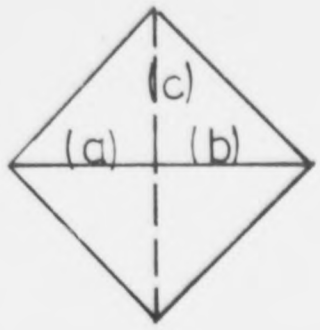


$d = 10/32\ \xi_g$

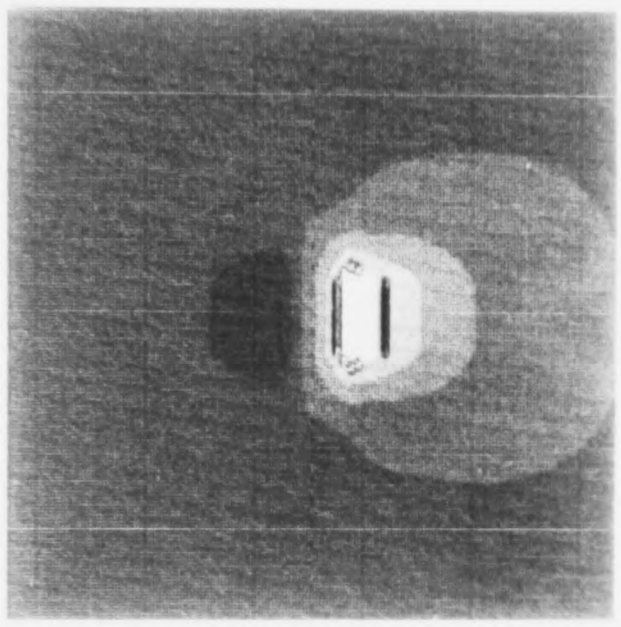
FIGURE 7.16

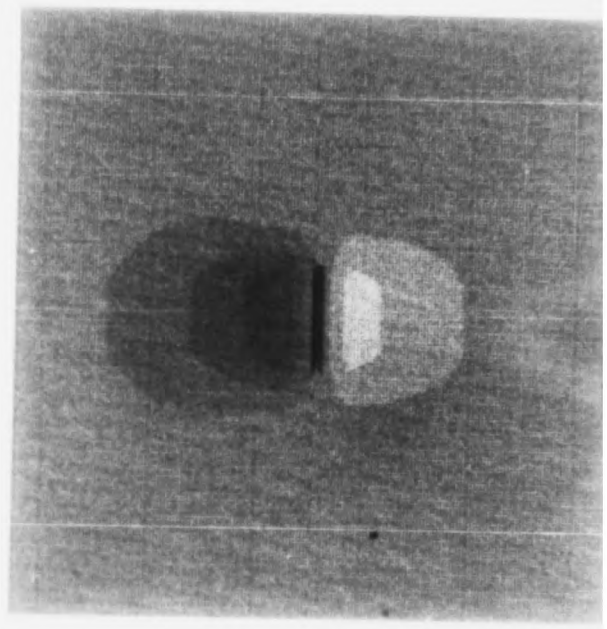
FRANK LOOPS

$\underline{Z} = [100]$



$\underline{g} = (02\bar{2})$





(a) $\underline{n} = [\bar{1}\bar{1}1]$

(b) $\underline{n} = [\bar{1}1\bar{1}]$



(c) $\underline{n} = [111]$

FIGURE 7.17

PERFECT LOOPS (Nb)

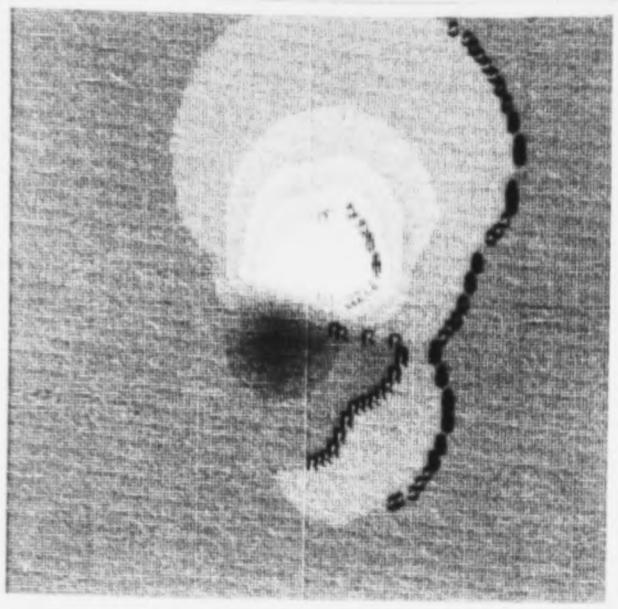
$\underline{Z}=[113]$

$\underline{n}=[110]$

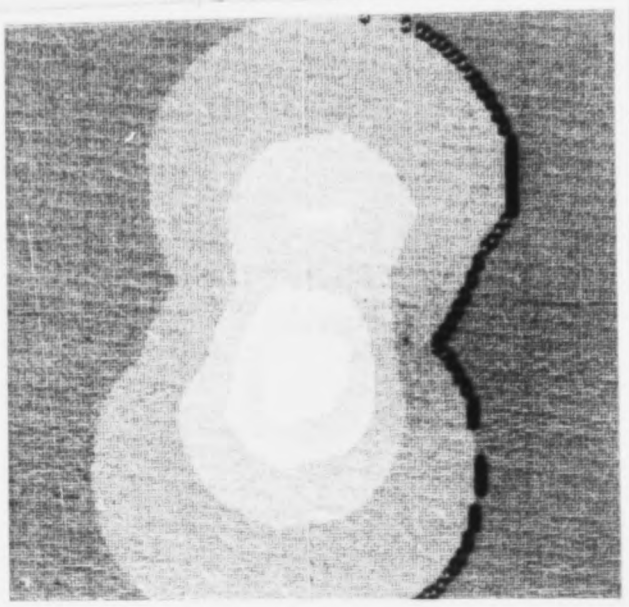
$\underline{b}=[111]a/2$

$h=20\,Å$

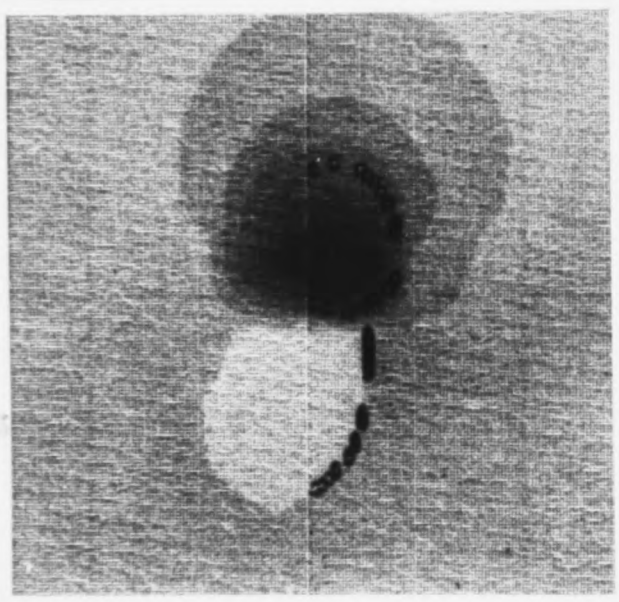
Intersection of loop plane with image plane ----



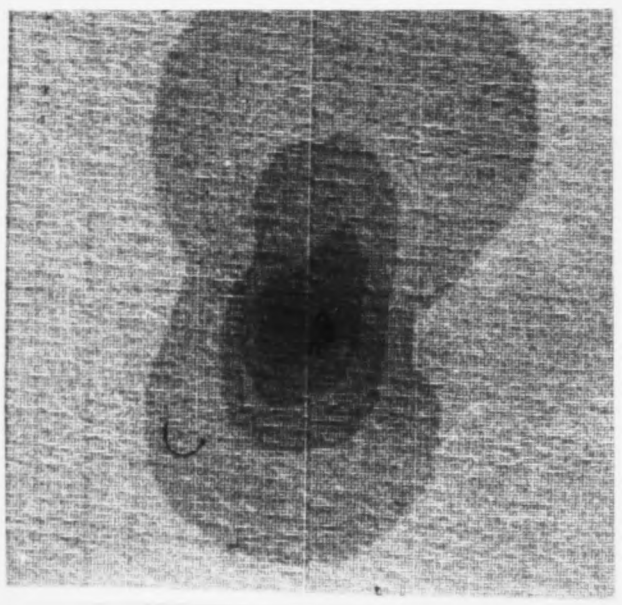
(a) $d=1/8\,\xi_g$



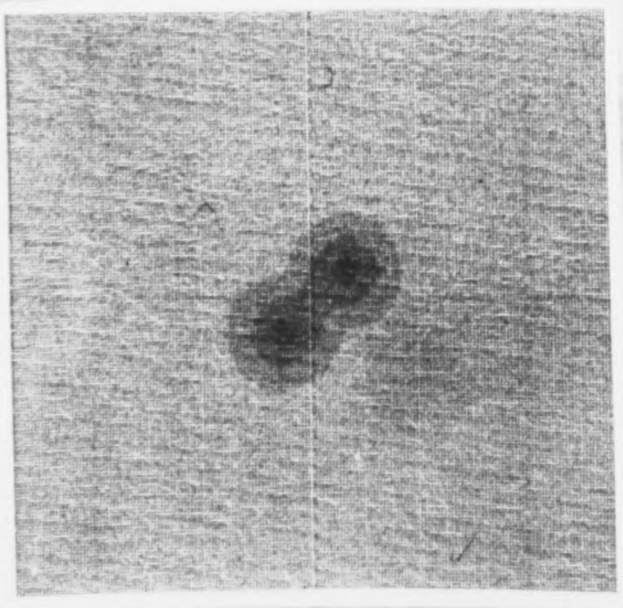
(b) $d=1/4\,\xi_g$



(c) $d=1/2\,\xi_g$



(d) $d=3/4\,\xi_g$



(e) $d=\xi_g$

$\underline{g}=(12\bar{1})$

$(\underline{n},\underline{Z})=64^\circ$

$\underline{Z},\underline{n},\underline{b}$ coplanar

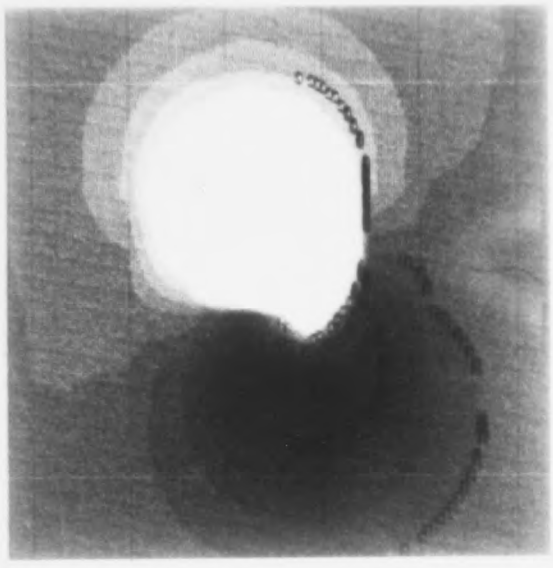
FIGURE 7.18

PERFECT LOOP (EDGE-ON) (I) (Mo)

image plane normal [011]
depth $1/8\,\xi_g$
thickness $2\,\xi_g$
size 25Å (h)

$\underline{b}=a/2[\bar{1}1\bar{1}]$

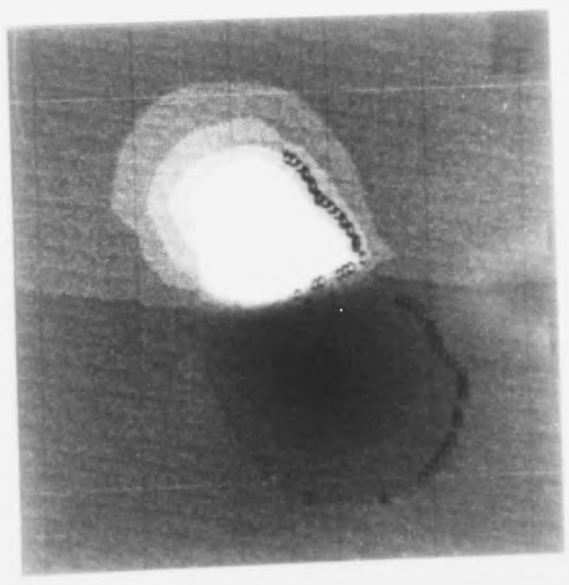
$\underline{n}=[01\bar{1}]$

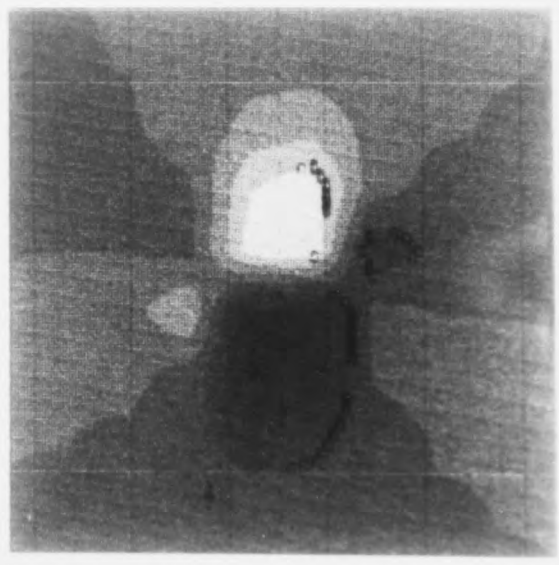




$\underline{g}=(01\bar{1})$

$\underline{g}=(200)$





$\underline{g}=(\bar{2}1\bar{1})$

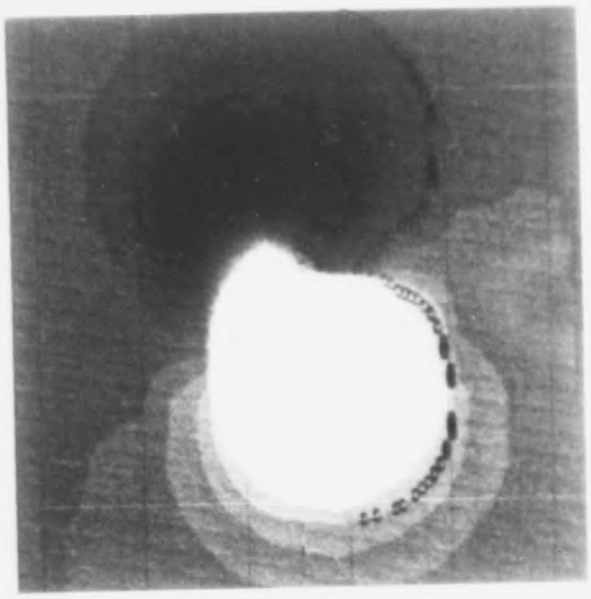
$\underline{g}=(211)$

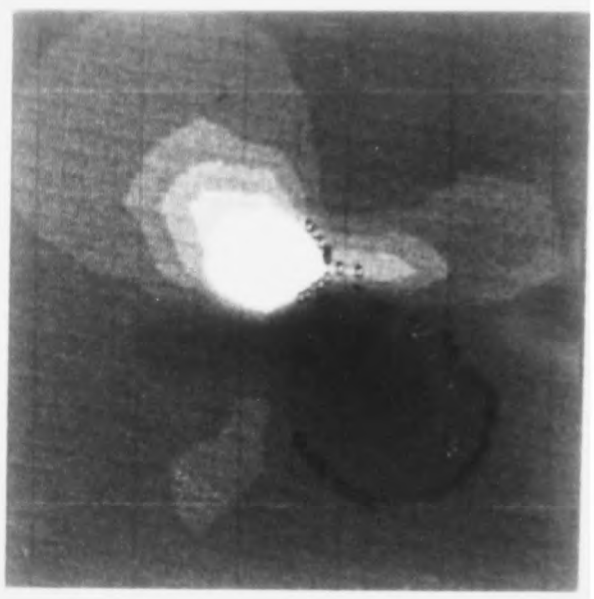
FIGURE 7.19

PERFECT LOOP (EDGE-ON) (II) (Mo)

$\underline{n}=[01\bar{1}]$

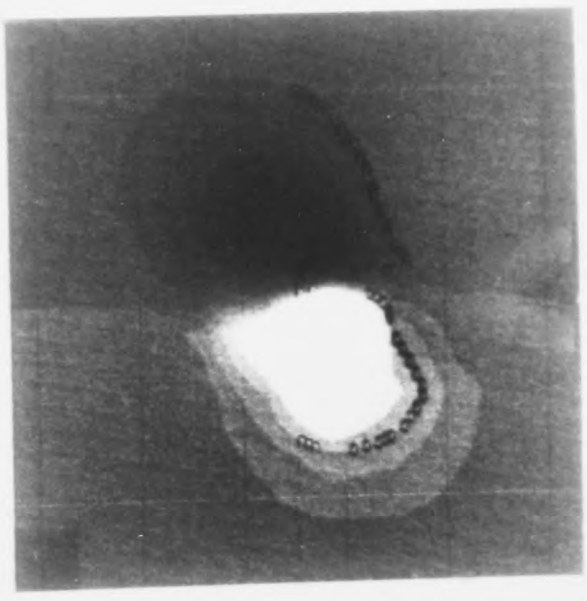
$\underline{b}=a/2[\bar{1}1\bar{1}]$

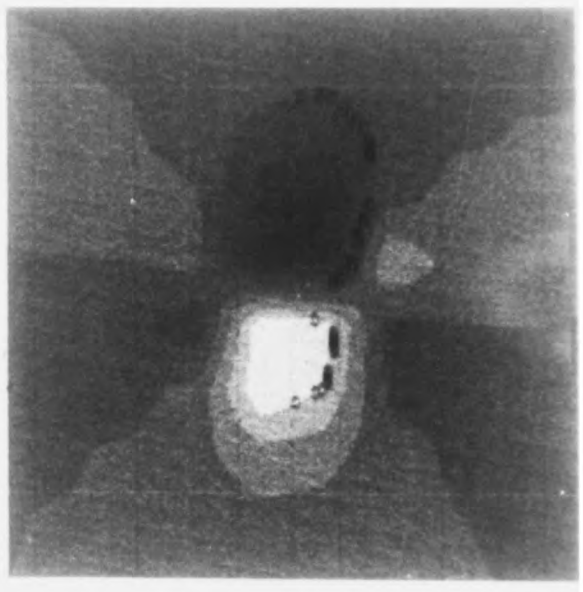




$\underline{g}=(0\bar{1}1)$

$\underline{g}=(\bar{2}00)$





$\underline{g}=(2\bar{1}1)$

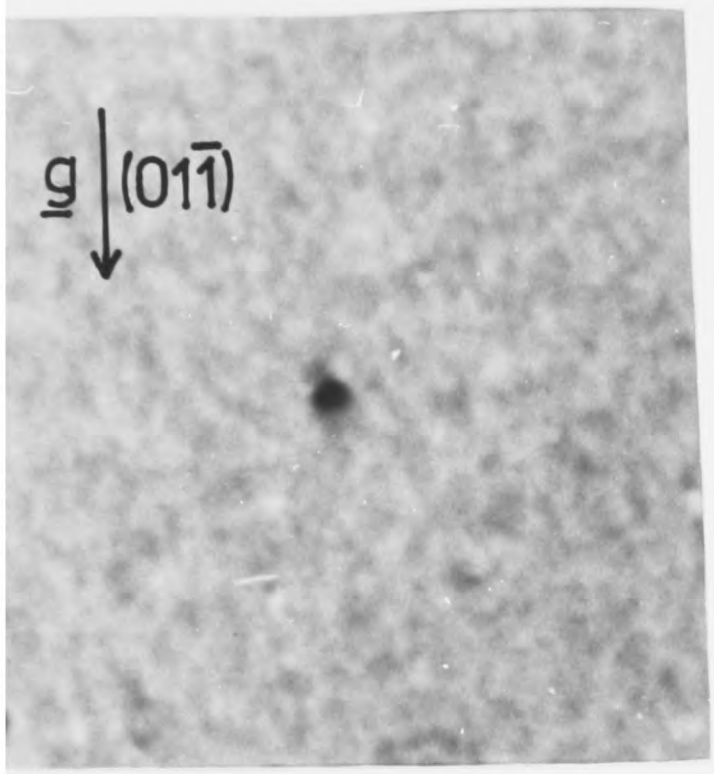
$\underline{g}=(\bar{2}\bar{1}1)$

FIGURE 7.20

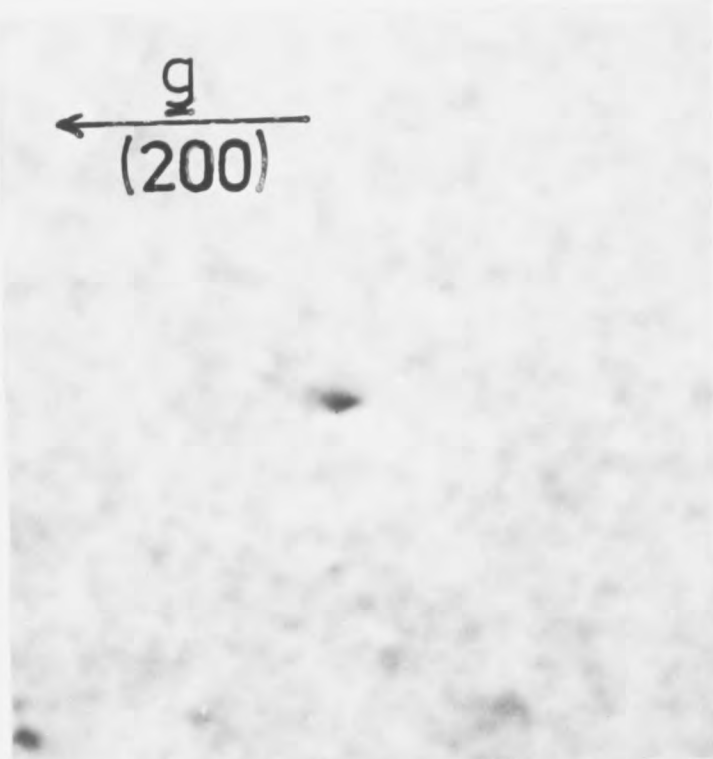
Experimental Micrographs of same defect in ion-irradiated molybdenum in different strongly excited (i.e. S = 0) reflections $\underline{g}$ (Photograph taken by C.A.English).

EXPERIMENTAL IMAGES (Mo)

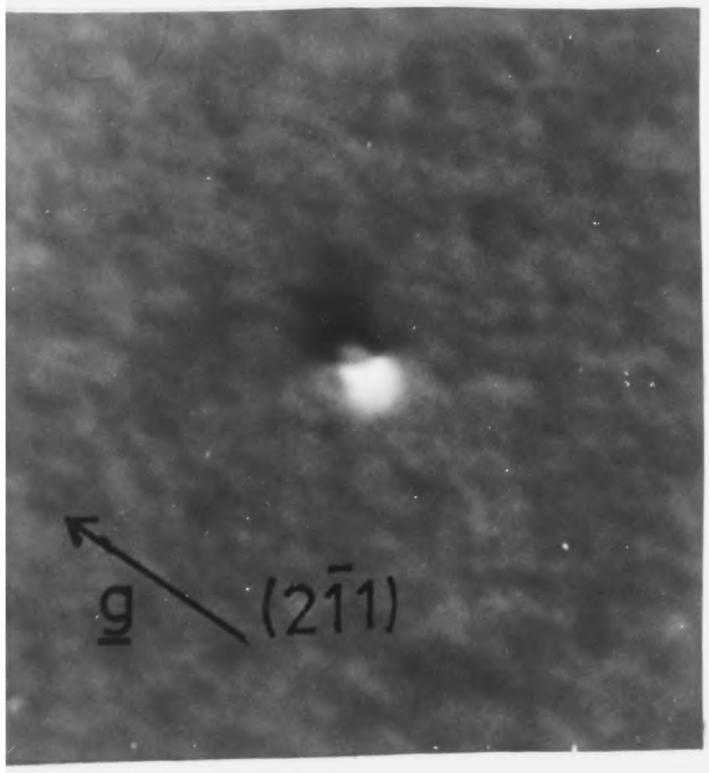
Near [011] orientation



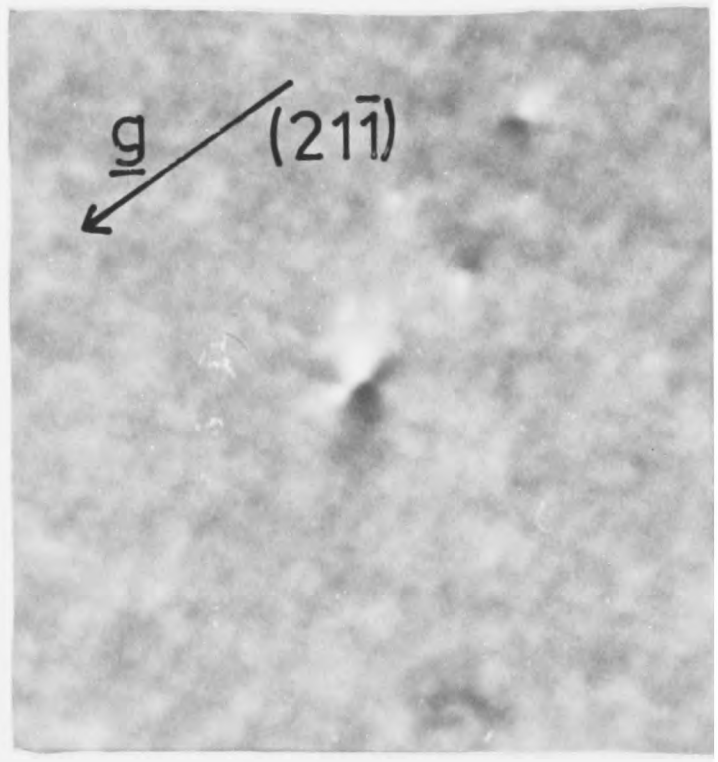
$\underline{Z}$=[$\bar{1}$55]



$\underline{Z}$=[032]



$\underline{Z}$=[$\bar{1}$35]



$\underline{Z}$=[$\bar{1}$53]

Chapter 8

IMAGE CONTRAST FROM STACKING-FAULT TETRAHEDRA

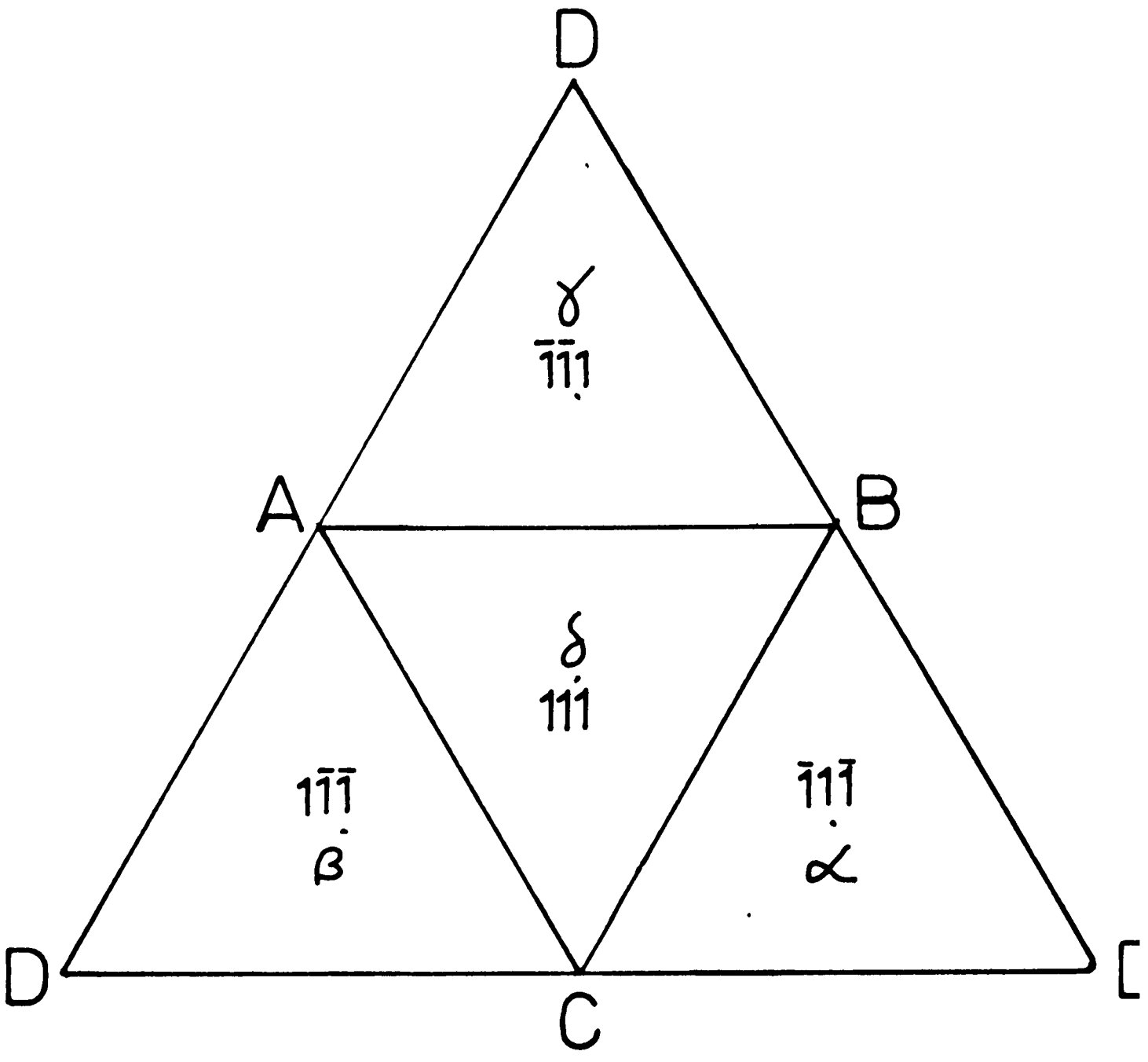


FIGURE 8·1

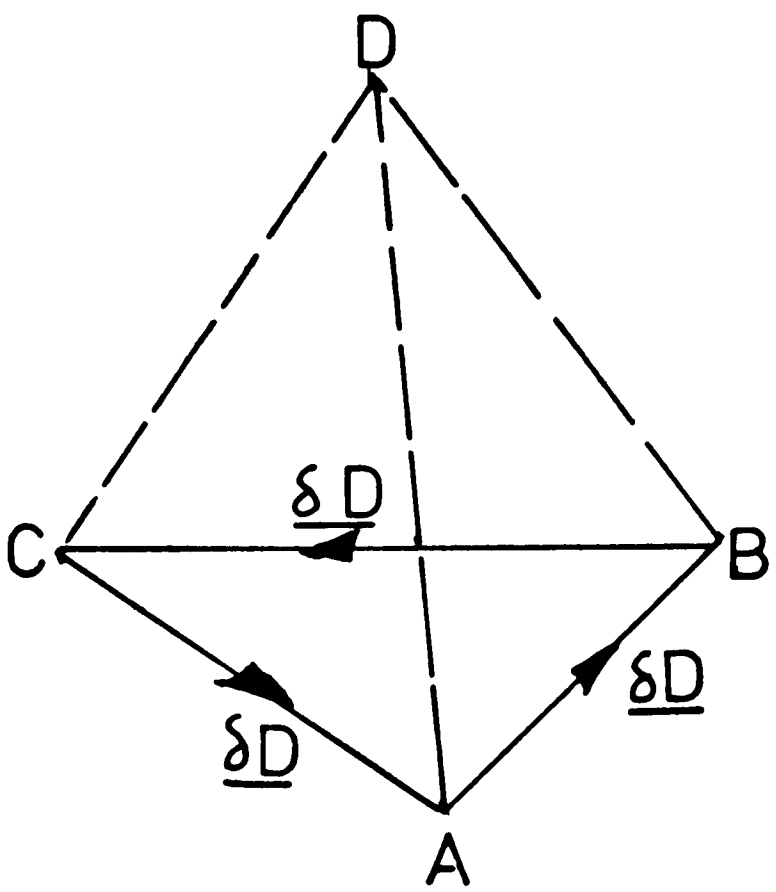
Image contrast from stacking-fault tetrahedra

8.1 Introduction

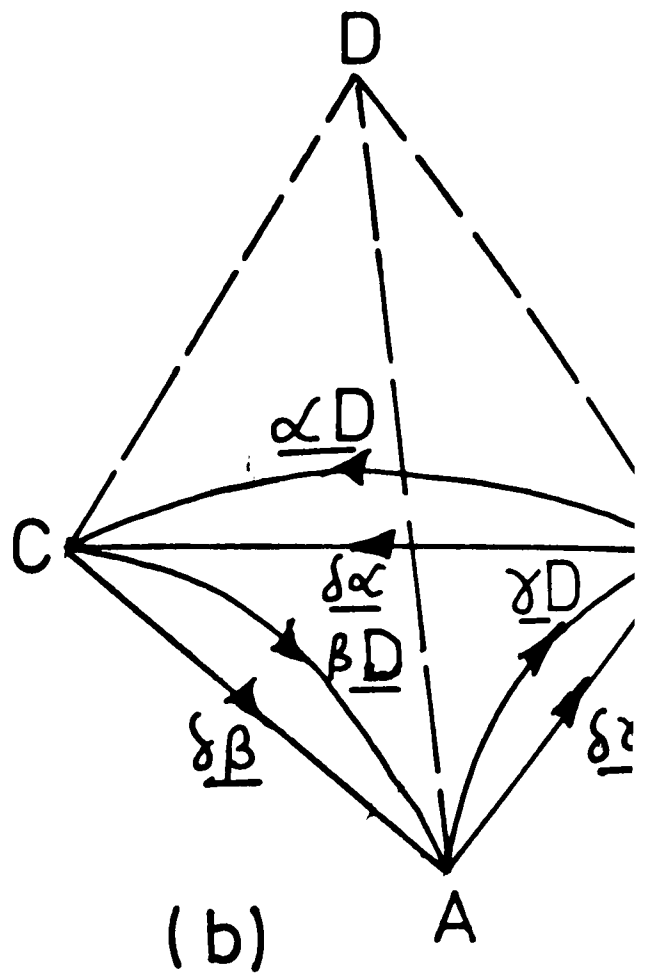
Stacking-fault tetrahedra are found in low stacking-fault energy f.c.c. crystals. They consist of regular tetrahedra whose facies lie on the four $\{111\}$- type planes. They have been observed in the transmission electron microscope after quenching of the specimen in gold by Silcox and Hirsch (1959), Chik (1966), Jenkins (1973)- in silver by Smallman, Westmacott and Coiley (1959)- and in nickel-cobalt alloys by Mader and Simsch (1960).

The description of the stacking-fault tetrahedron and similar defects is greatly aided by the representation known as the Thompson tetrahedron (Thompson, 1953)). A model of this tetrahedron which is capable of being made out of cardboard say, correctly describes the three-dimensional relationship between the important planes and directions in a f.c.c. material. Figure 8.1 shows such a model, opened out at the corner D and spread out flat. The four faces of the tetrahedron represent the four possible $\{111\}$ glide planes. The outward drawn normals to these faces are $[111]$, $[\bar{1}1\bar{1}]$, $[1\bar{1}\bar{1}]$ and $[\bar{1}\bar{1}1]$. These planes are labelled d, a, b and c respectively on the outer surface and $\bar{d}$, $\bar{a}$, $\bar{b}$ and $\bar{c}$ on the inner surface. Their midpoints are denoted by δ, α, β and γ, and the vertices opposite these midpoints by D, A, B and C respectively.

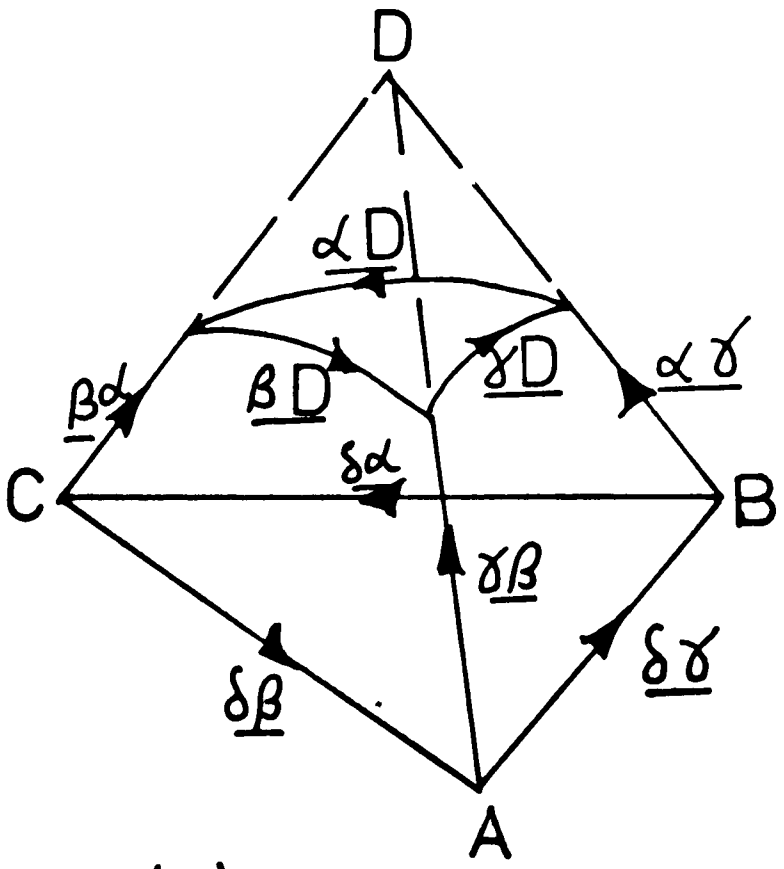
The physical nature of the stacking-fault tetrahedron is best understood by considering a possible mechanism for its formation.



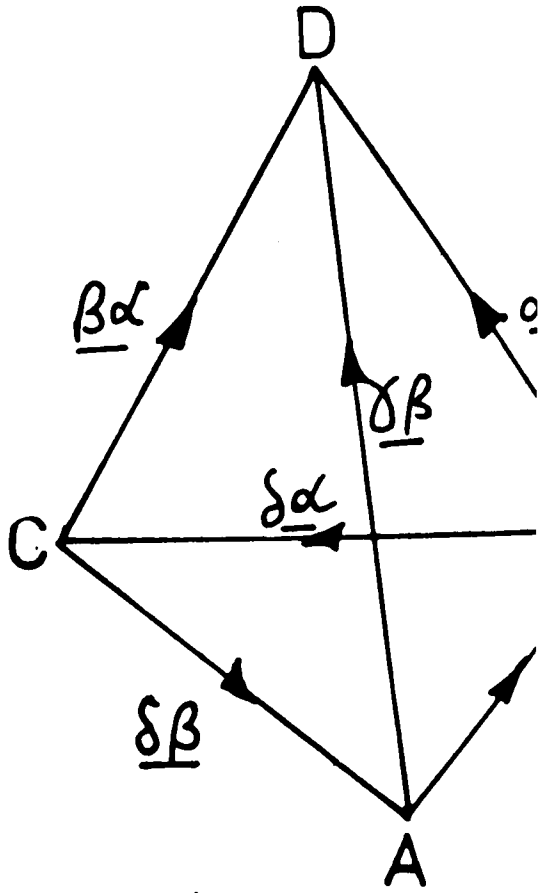
(a)



(b)



(c)



(d)

FIGURE 8.2

Four stages in such a process are illustrated in Fig.8.2. These diagrams use the notation of the Thompson Tetrahedron to specify planes and directions in the crystal. Fig. 8.2(a) depicts a triangular Frank loop of Burgers' vector $\underline{b} = \frac{a}{3}[111]$, lying on the plane d. Let us represent this Burgers vector by the vector $\underline{\delta D}$. If the diagram is to represent a vacancy-type loop (i.e. one with an intrinsic stacking-fault), the dislocation line directions must be as shown. Line directions in the opposite sense would represent an interstitial-type loop (i.e. one with an extrinsic stacking-fault).

The dislocations in the directions, BC, CA and AB (i.e. the $\langle 110 \rangle$-type directions) can dissociate with a decrease in elastic energy according to the reactions,

$$\underline{\delta D} \rightarrow \underline{\delta\alpha} + \underline{\alpha D} \qquad (8.1\ A)$$

$$\underline{\delta D} \rightarrow \underline{\delta\beta} + \underline{\beta D} \qquad (8.1\ B)$$

and $$\underline{\delta D} \rightarrow \underline{\delta\gamma} + \underline{\gamma D} \qquad \text{respectively (8.1.C)}$$

where the first terms on the R.H.S.'s represent the Burgers vectors of stair-rod dislocations and the second terms, those of Shockley partials. In more conventional terms, equation (8.1.c) say, can be written

$$\frac{a}{3}[\bar{1}\bar{1}\bar{1}] \rightarrow \frac{a}{6}[\bar{1}\bar{1}0] + \frac{a}{6}[\bar{1}\bar{1}\bar{2}]$$

Frank partial — Stair-rod — Shockley partial

The appearance of the defect after this initial dissociation is illustrated in Fig.8.2(b). The Shockley partials are formed by shearing processes on the planes a,b, and c respectively.

The shear vector is equal to the Shockley partial Burgers vector, and the process causes the Shockley partials to be bowed out from the vertices A,B and C as shown in the diagram.

Energy considerations frequently cause the Shockley partials to glide further up the planes a, b and c to produce the configuration illustrated in figure 8.2(c). The interactions of neighbouring Shockley partials along the lines AD, BD and CD result in the formation of stair-rod dislocations along these lines. These reactions may be represented by equations of the type

$$\beta D + D\alpha \rightarrow \beta\alpha$$

If conditions are favourable, a complete stacking-fault tetrahedron (see Fig.8.2(d)) is formed when the glide of the Shockley partials cause them to reach the vertex D.

In fact, stacking-fault tetrahedra can be produced by a variety of methods, e.g. by heavy ion irradiation, and by deformation. Alternative mechanisms of their creation are the glide or cross-slip of jogged dislocations (Loretto, Clarebrough and Segall, 1965).

8.2 The Nature of the Stacking-faults

An interesting question is, what type of stacking faults are thus formed on each of the faces of the tetrahedron? The original Frank loop on face d contained an intrinsic fault specified by the vector δD. The other faces are formed by shear processes and thus have fault vectors of the type αD. Inspection of the Thompson Tetrahedron however shows that $\alpha D = \alpha A + AD$

Now αA is a vector of type $\frac{a}{3}\langle 111\rangle$ and AD one of type $\frac{a}{2}\langle 110\rangle$. In a f.c.c. material, the latter is a perfect lattice vector (i.e. translation by such a vector reproduces the original lattice).

Thus faults described by vectors αD and αA are identical physically. Thus the stacking faults on the faces d, a, b and c are δD , αA , βB and δC respectively, indicating that the stacking-fault tetrahedron is a defect symmetrical with respect to each of its four faces. If the fault on the original Frank loop was of intrinsic-type, the faults on the other faces will also be of this type.

Let 0 be the centroid of a Thompson tetrahedron. Consider four equilateral triangular, vacancy-type edge loops, placed on the Thompson planes a, b, c and d such as to touch each other along their sides to form a tetrahedron. If the dislocation line directions for each of these component loops are anti-clockwise, when viewed from the positive sides of a, b, c and d, and the Burgers vectors are $O\alpha$, $O\beta$, $O\gamma$ and $O\delta$ respectively, it is not difficult to see that at the points where the sides of these triangular loops are in contact, there are formed the stair-rod dislocations of the stacking-fault tetrahedron,

$$e.g. \quad \beta O + O\alpha \rightarrow B\alpha \quad etc.$$

This provides a method of constructing the strain-field due to a stacking fault tetrahedron, from that of a triangular edge loop by suitable further matrix rotations of axes. If we use the method of constructing the displacement field due to a dislocation loop described in Chapter 6, however, the discontinuous jump in the displacement field on crossing the plane of theloop from positive x to negative x is $\underline{b}$, the Burgers vector of the loop. For the face d, say, this would be $\delta\delta$. However since $|D\delta|$ is the spacing of two adjacent close-packed (111)-type planes, in a f.c.c lattice, $O\delta$ does not correspond to any physically realizable fault vector in the crystal.

This problem can be overcome when it is realized that the equations of elasticity do not completely determine the displacement field of a defect. What is determined is the strain field in regions where the strain is non-singular. A constant of integration introduces an element of arbitrariness into the displacement-field. In problems involving straight dislocations and dislocation loops, say, every point in the material can be joined to any other point by a path not involving a discontinuous jump in the displacement field. This does not hold for a stacking-fault tetrahedron. Any path from inside the tetrahedron to outside it must pass through a jump in the displacement field. Whereas, in the former problem, consistency with the equations of elasticity involve the same constant of integration for the whole crystal, in the latter case, consistency could be ensured even if the constants of integration for the parts inside and outside the tetrahedron were different. The singularities in the strain-field remain on the faces a, b, c and d and the magnitudes of the jumps in the displacement-field at each face can be controlled by the relative values of the constant of integration.

For example, consider the addition of a displacement of magnitude $\underline{D}\underline{O}$ to all the material inside the tetrahedron, while retaining the values of the displacements outside. Then the jump in the displacement an face d becomes,

$$\underline{D}\underline{O} + \underline{O}\underline{\delta} \rightarrow \underline{D}\underline{\delta}$$

which is the fault vector of an intrinsic fault in a f.c.c. material. The jumps on the other faces then become ,

$$\underline{D}\underline{O} + \underline{O}\underline{\alpha} \rightarrow \underline{D}\underline{\alpha} = \underline{D}\underline{A} + \underline{A}\underline{\alpha}$$

$$\underline{D}\underline{O} + \underline{O}\underline{\beta} \rightarrow \underline{D}\underline{\beta} \quad \underline{D}\underline{E} + \underline{B}\underline{\beta}$$

and $$\underline{D}\underline{O} + \underline{O}\underline{\gamma} \rightarrow \underline{D}\underline{\gamma} - \underline{D}\underline{C} + \underline{C}\underline{\gamma}$$

Now $\underline{DA}$, $\underline{DB}$ and $\underline{DC}$ are perfect lattice vectors in a f.c.c. material and thus the jumps on the faces a,b, and c can be described by the fault vectors $A\underline{\alpha}$, $B\underline{\beta}$, and $C\underline{\gamma}$ which are, of course, intrinsic fault vectors.

The next section describes in detail the method of constructing the displacement-field due to the stacking-fault tetrahedron, using the method outlined above.

8.3 The displacement field due to stacking-fault tetrahedron

Using methods identical to those described in Chapter 6,we may construct the displacement field due to a triangular edge loop. All we require to do to the formulae for the displacement field of polygonal loop of general Burgers vector is to make the number of sides $n = 3$ and to make the shear components of the Burgers vector, B_y and B_z, each zero.

Suppose that we require to construct the displacement field due to a stacking fault tetrahedron lying on the Thompson planes a,b,c and d.

We require in order to completely characterize the displacement field, to specify the depth of its centroid from the "upper" foil surface, and its size.

8.3.1 Position of the tetrahedron in the foil

This is the analogous stage to that described in 6.7.1. for the loop. For the tetrahedron, it is clear that its centroid lies on the X_f-axis of each of its component triangular faces. (f takes the values 1 to 4). Let its S distance from the origins of each of the (X_f, Y_f, Z_f) type coordinate systems on each of the triangular faces be d_c. Then it is not difficult to see that (using the same notation as in 6.7.1)

$$q\hat{Q} + r\hat{R} + s\hat{S} = -d\hat{S} + d_c\hat{X}_f + x_f\hat{X}_f + y_f\hat{Y}_f + z_f\hat{Z}_f \qquad (8.1)$$

and we thus obtain the matrix relation

$$\begin{pmatrix} [x_f + d_c] \\ y_f \\ z_f \end{pmatrix} = \begin{pmatrix} \hat{Q}.\hat{X}_f & \hat{R}.\hat{X}_f & \hat{S}.\hat{X}_f \\ \hat{Q}.\hat{Y}_f & \hat{R}.\hat{Y}_f & \hat{S}.\hat{Y}_f \\ \hat{Q}.\hat{Z}_f & \hat{R}.\hat{Z}_f & \hat{S}.\hat{Z}_f \end{pmatrix} \begin{pmatrix} q \\ r \\ s+d \end{pmatrix} \qquad (8.2)$$

This enables the coordinates (x_f, y_f, z_f) of a general point P in the (X_f, Y_f, Z_f) coordinate system of each loop to be found in terms of its coordinates (q,r,s) in the coordinate system whose origin is at the top surface of the foil. The depth of the centroid of the tetrahedron below this foil surface is specified by d. If ℓ is the length of each edge of the tetrahedron, it is not difficult to see with the aid of elementary trigonometry that, $d_c = \frac{1}{4}\sqrt{5/6}\ \ell$. Thus specification of the edge length of the tetrahedron results in automatic positioning of the centroids of each triangular face relative to the centroid of the tetrahedron.

8.3.2 Coordinate axes for each triangular face

Let f = 1, 2, 3 and 4 correspond to the faces a, b, c and d respectively of the Thompson tetrahedron. Then, bearing in mind that the Y_f axes must be perpendicular to one of the edges of the triangular loop, it is easy to specify the axes (X_4, Y_4, Z_4) by inspection of the Thompson tetrahedron. Suppose that we choose the axes $[111]$, $[2\bar{1}\bar{1}]$ and $[01\bar{1}]$ respectively. Normalization of these vectors is performed in the computer. Examination of the Thompson tetrahedron shows that any vector on face d can be transformed to a vector on face a by rotation through π about the axis $[010]$. Similarly vectors on the faces b and c can be generated from (X_4, Y_4, Z_4) by rotation about $[100]$ and $[001]$ respectively. The matrices for rotation through π about the axes $[100]$, $[010]$ and $[001]$ are,

$$\underline{\underline{M}}_2 = \begin{bmatrix} 1 & 0 & 0 \\ 0 & -1 & 0 \\ 0 & 0 & -1 \end{bmatrix}, \quad \underline{\underline{M}}_1 = \begin{bmatrix} -1 & 0 & 0 \\ 0 & 1 & 0 \\ 0 & 0 & -1 \end{bmatrix}$$

and

$$\underline{\underline{M}}_3 = \begin{bmatrix} -1 & 0 & 0 \\ 0 & -1 & 0 \\ 0 & 0 & 1 \end{bmatrix}$$

and thus,

$$\begin{pmatrix} \hat{X}_f \\ \hat{Y}_f \\ \hat{Z}_f \end{pmatrix} = \underline{\underline{M}}_f \begin{pmatrix} \hat{X}_4 \\ \hat{Y}_4 \\ \hat{Z}_4 \end{pmatrix}$$

for $f = 1, 2$ and 3.

This determination of the coordinate axes on each face of the tetrahedron enables the use of equation (8.2) to determine the coordinates (x_f, y_f, z_f) f = 1 to 4 of the point P, for each face. Substitution in the formulae of Chapter 6 then enables the evaluation of the displacement field (R_{hf}, R_{kf}, R_{lf}) at P, referred to the <100> crystallographic directions for each face. The field outside the tetrahedron is then given by

$$\underline{R} = \underline{R}' = \begin{bmatrix} R_h \\ R_k \\ R_l \end{bmatrix} = \sum_{f=1}^{4} \begin{bmatrix} R_{hf} \\ R_{kf} \\ R_{lf} \end{bmatrix} \qquad (8.3)$$

8.3.3 Insertion of correct fault-vectors

We saw in 8.1 that when the displacement field of the tetrahedron is calculated as above, intrinsic faults may be inserted on all the faces if the displacement of any point within the tetrahedron is increased by a vector of the type $\underline{DO}$. If $\underline{b}_d$ is the Burgers vector of the component loop on the face d, $\underline{DO} = \frac{3}{4} \underline{b}_d$, and thus the correct displacement field is given not by equation (8.1) for the region outside, but by

$$\underline{R} = \underline{R}' + \frac{3}{4} \underline{b}_d \qquad (8.4)$$

for the region inside the tetrahedron. This implies that an atom at the centre of a tetrahedron occupies an interstitial site of the perfect lattice that would exist in the absence of the tetrahedron.

A suitable criterion for use in the computer programme for deciding whether equation (8.3) or equation (8.4) is applicable makes use of the solid angle ϕ of equation (6.12). This is the solid angle subtended by the arms of an angular dislocation at the point (P) at which the displacement field is being evaluated. For an n-sided loop constructed as described in Chapter 6, there will be n such angles. Their sum ϕ_s is the solid angle subtended by the

whole area outside the loop, and this is positive on the side of the loop for which x is positive and vice versa. For any arbitrary point near a tetrahedron, there are four such quantities $\phi_{s,m}$ where $m = 1$ to 4, corresponding to the four faces. A necessary and sufficient condition for P being inside the tetrahedron is that every one of the qualities

$$\phi_{s,m} \quad , \quad m = 1 \text{ to } 4 \text{ is negative.}$$

8.4 Alternative method for tetrahedron displacement field

This alternative method also involves adding the displacement fields due to triangular loops on the faces a,b,c and d. However, the Burgers vector of the loop on face d, say, is now made D_{δ} and those of the loops in the other faces are D_{α}, D_{β}, and D_{γ} respectively That is, the loop on one of the faces is of Frank type while the others are Shockley type shear loops. The stair-rods on the sides, AB, BC and CA are then formed by reactions of the type

$$\delta D + D\alpha \rightarrow \delta\alpha$$

and those on the sides AD, BD and CD by such reactions as

$$\gamma D + D\beta \rightarrow \gamma\beta$$

It will be noticed that this method dispenses with the need to make further adjustments for the stacking-faults, since the displacement jumps automatically created on the faces would already produce intrinsic faults in f.c.c. materials.

Although this method also theoretically produces a defect which is symmetric with respect to each of the faces a,b,c and d, computationally the process is not symmetric, and due to rounding off errors etc., produced a displacement field which is not quite symmetric on the ICL1906A computer at Oxford. For this reason, this method was not used in the computer simulation work described

later in this Chapter.

8.5 Computer Simulations

8.5.1 Vacancy type tetrahedron (a) At a ⟨110⟩ orientation

Figs. 8.3 and 8.4 illustrate the contrast expected from a stacking-fault tetrahedron at the [110] orientation which lies in the middle of layer L1 (i.e. at a depth of $\frac{1}{8}\xi_g$). Also shown are corresponding experimental images. The parameter h for each of the triangular faces is 20Å for the computed images, the reflections considered are of {200}, {220} and {111}- type. It can be seen that for a tetrahedron of this size the behaviour of the directions of the black-white streaking vector $\underline{\ell}$ is very similar to that expected from a spherical inclusion. That is, $\underline{\ell}$ appears to remain parallel to $\underline{g}$ as $\underline{g}$ takes on several different orientations. This is not unexpected. Under strong-beam conditions, a small tetrahedron (here small implies small compared to ξ_g) is imaged mainly by the scattering of electrons from the long-range strain-field and not the stacking faults on each face. It is well known that the long-range strain-field of a stacking-fault tetrahedron asymptotically approaches the form of that from a spherical inclusion.

The experimental micrograph taken with loop plane normal [110] in reflection (200) shows a V-shaped sharp line of no-contrast separating the black and white lobes. Insufficient resolution in Figs.8.3(b) and (c) do not reveal this contrast. An image simulation restricted only to the central region of Fig.8.3(b) is shown in Fig.8.3(a). Here the V-shape is clearly visible thus indicating that many experimentally observed V-shaped lines of no contrast may arise from stacking-fault tetrahedra.

(b) Tetrahedron at a 100 orientation

Figure 8.5 shows images of a stacking-fault tetrahedron observed at the [100] orientation in the reflections $(02\bar{2})$ and (022). In both cases the streaking directions are seen to be parallel to the $\underline{g}$-vector of the reflection and to be virtually of the same form.

8.5.2 Comparison between Frank loops and Tetrahedron at [100] orientation

Comparison of Figures 8.5 and 7.11 makes possible the differentiation between the images of Frank loops and tetrehedra at this orientation. Figure 7.11 shows that at the [100] orientation, there are essentially three different types of Frank loop images (depending on the habit plane of the loop), when the reflection $(02\bar{2})$ is used. Viewing the same area in the perpendicular reflection $\underline{g} = (022)$ results not only in the direction of streaking ($\underline{l}$) turning round by 90^{o} but also the image types exemplified by Figs.8.5(a) and (c) are interchanged. For the stacking-fault tetrahedron, the only effect is the rotation of the vector $\underline{l}$ by 90^{o}.

8.5.3 Depth Dependence

In 7.4.5 we saw that whether the contrast from a small defect cluster showed an oscillation with its depth in the foil depended on the value of a dimensionless normalized misfit parameter P. We also saw that for a dislocation loop observed by its balck-white contrast, the condition $P < 1$ always holds and there are thus always reversals of the sign of black-white contrast with depth. Now a stacking-fault tetrahedron is formed from a Frank-loop by pure shear processes. Thus the values of P for a tetrahedron and a Frank

loop of similar linear dimensions are similar and we would expect similar depth oscillations of the black-white contrast as for the case of the Frank loop.

Computer calculations were performed for a ⟨110⟩ orientation to verify this and the behaviour was found to be as shown in Figure 7.1.

8.5.4 The interstitial-type tetrahedron

We have so far only been concerned with the case of the vacancy-type tetrahedron, that is, the tetrahedron formed by shear of a vacancy-type Frank loop. Since almost all the visible loops formed after irradiation by 1.5 MeV neutrons are of vacancy-type it is not surprising that the stacking-fault tetrahedron formed from these loops are of vacancy-type and thus have faces of intrinsic stacking faults.

Electron irradiation is however capable of producing interstial-type tetrahedron, that is tetrahedra which could be created by shear processes acting on interstitial-type Frank loops. Such tetrahedra have faces of extrinsic stacking faults.

An interstitial-type stacking-fault tetrahedron may be constructed by the methods described earlier in this chapter if the Burgers vectors $\underline{b}$ of the constituent edge-loops are of opposite sign to those used in the construction of the vacancy-type tetrahedron The vector describing the subsequent shifting of the material inside the tetrahedron thus also automatically reverses.

Now information about a lattice defect is fed into the diffraction contrast equations by means of the scalar quantity $\underline{g}.\underline{R}$

We have already seen in Chapter 7 that reversing the sign of $\underline{g}$ alone reverses the sign of the contrast (i.e. black regions became white regions and vice-versa). In the case of all the defects we have considered so far $\underline{R} \propto \underline{b}$. Thus reversing the direction of $\underline{b}$ alone reverses the direction of $\underline{R}$ and thus the sign of $\underline{g}.\underline{R}$, and hence the sign of the contrast.

Thus intrinsic-type and vacancy-type tetrahedra of the same depth in a foil show opposite signs of contrast (i.e. the vector $\underline{\ell}$, if it can be defined, is reversed). This behaviour is summarized in Figure 7.1, and computer calculations were performed to verify this prediction.

8.5.5 Differentiation between interstitial-type and vacancy-type tetrahedra

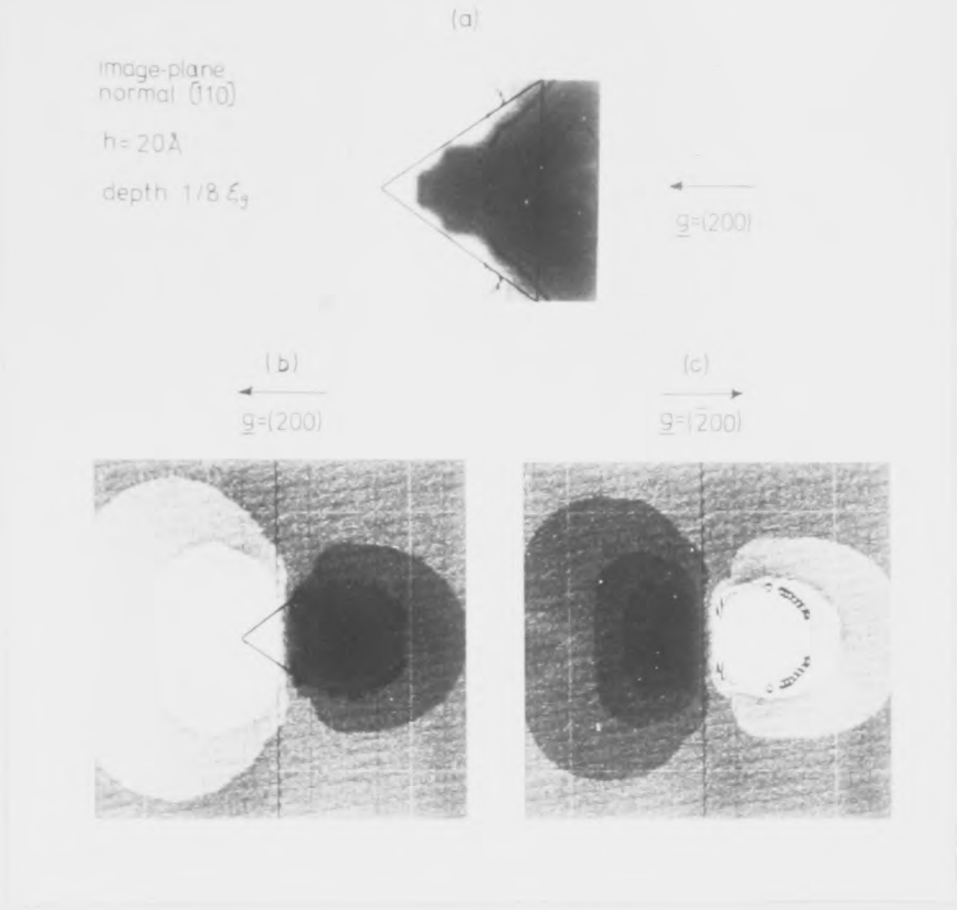
In this Chapter some methods have been suggested for identifying and differentiating between stacking-fault tetrahedra and dislocation loops, from the behaviour of their black-white contrast on strong-beam dark field micrographs. In order to differentiate between intrinsic-type and vacancy-type tetrahedra however it is necessary also to know their depths in the foil. The arguments of the last two sections and figure 7.1 show that the contrast from a vacancy-type tetrahedron in layer L1 can be virtually identical with that of an intrinsic type tetrahedron in layer L2. Once the depth of the defect has been found however (say by steroscopic methods) it is a simple matter to determine the nature of the stacking-fault tetrahedron by use of the information in figure 7.1.

Figure 8.3

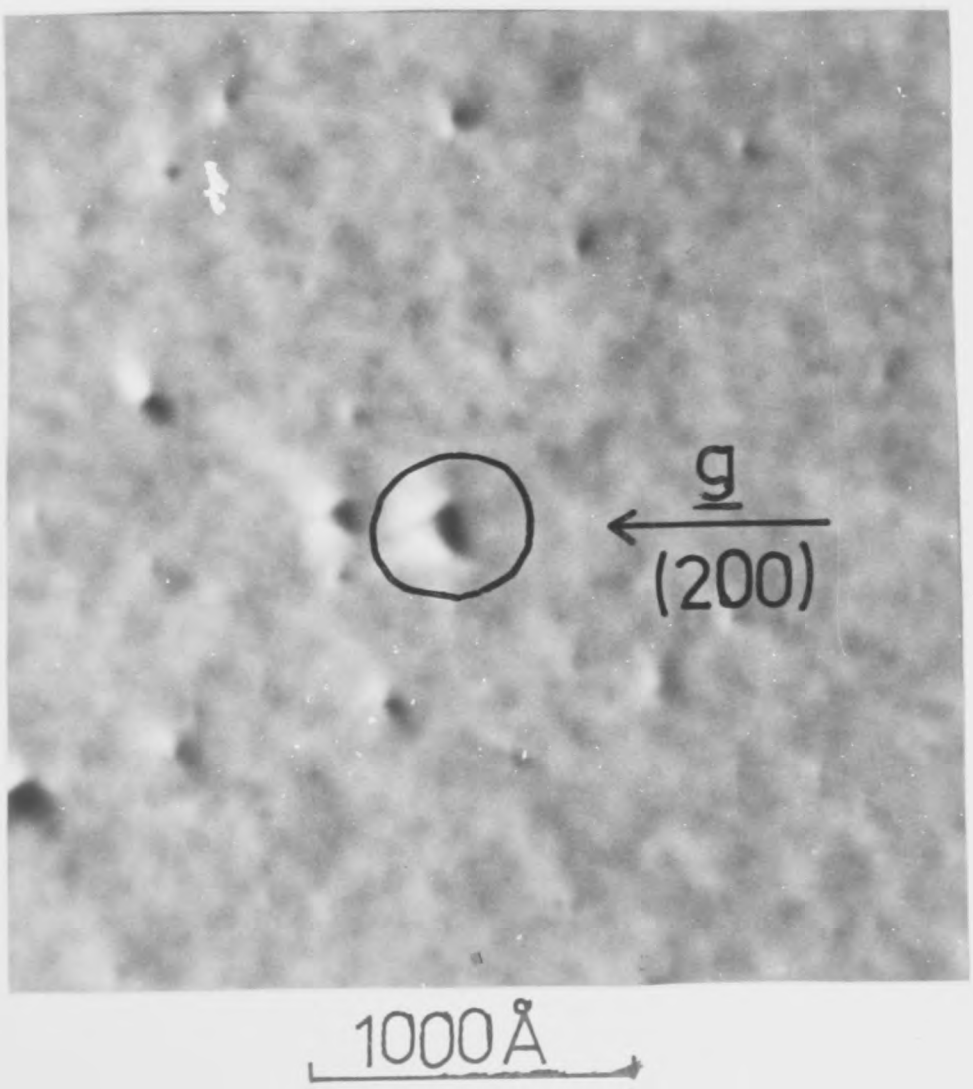
Experimental Micrograph of ion-irradiated Cu-1 at % Al
(Photograph taken by A.Y.Stathopoulos).

Strong-beam conditions. Reflection $\underline{g}$.

STACKING-FAULT TETRAHEDRON



Computed Images (Cu)



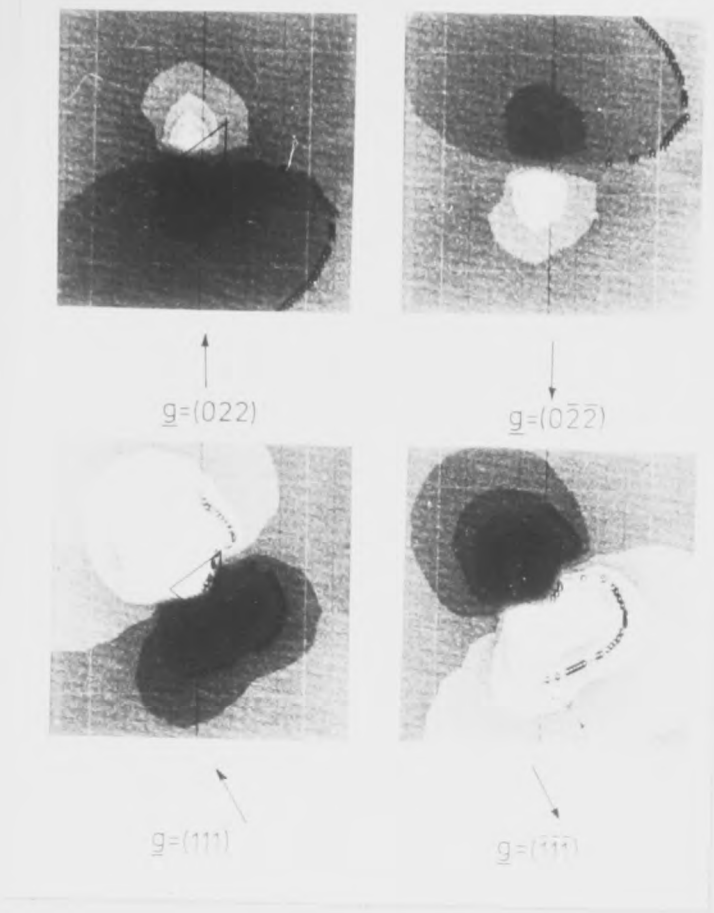
Experimental Image (Cu-1% Al)

Figure 8.4

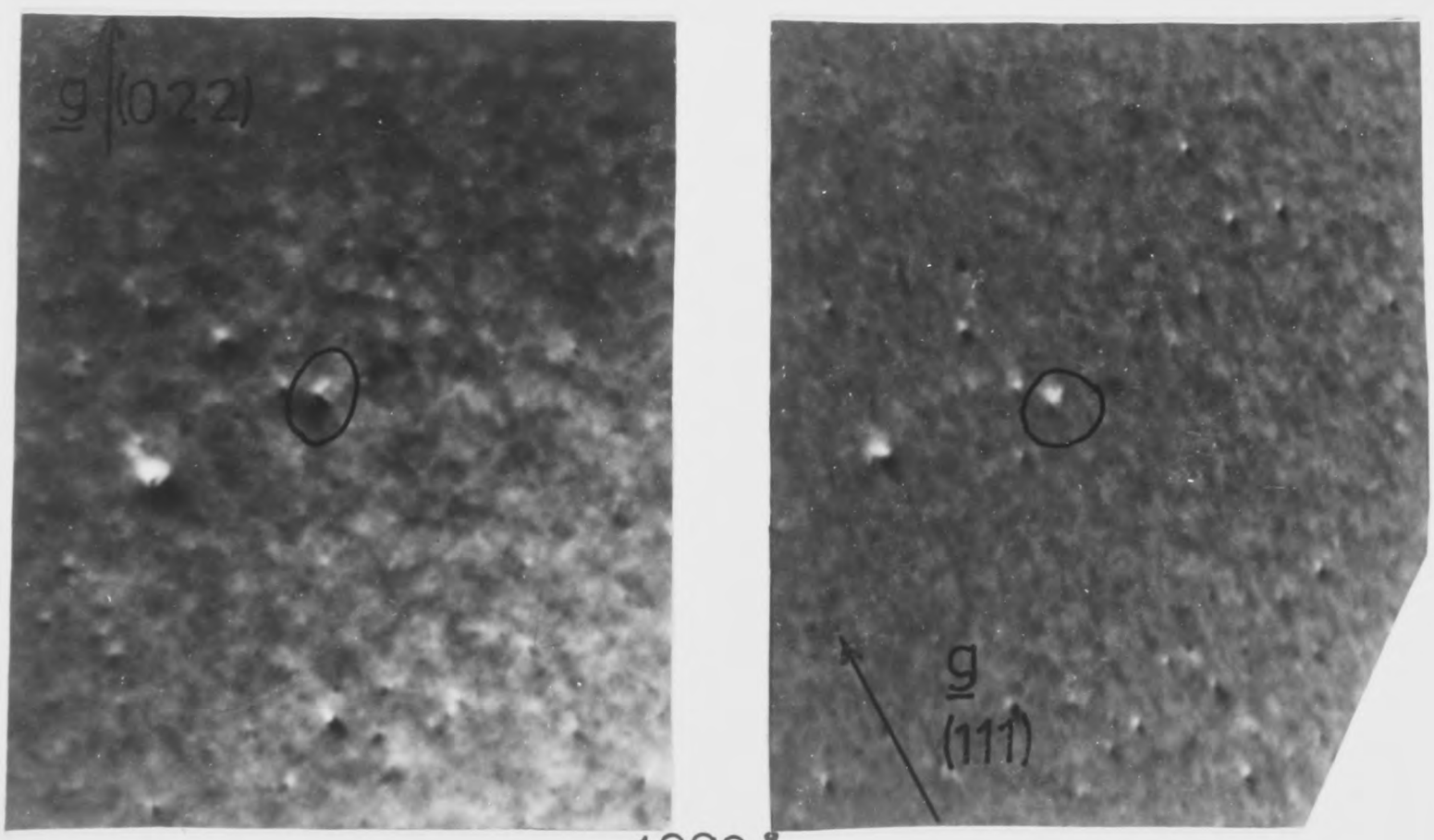
Experimental Micrographs of ion-irradiated Cu-1 at % Al (Photographs taken by A.Y.Stathopoulos).

Strong-beam conditions. Reflection $\underline{g}$.

STACKING-FAULT TETRAHEDRON (Cu)



Computed Images



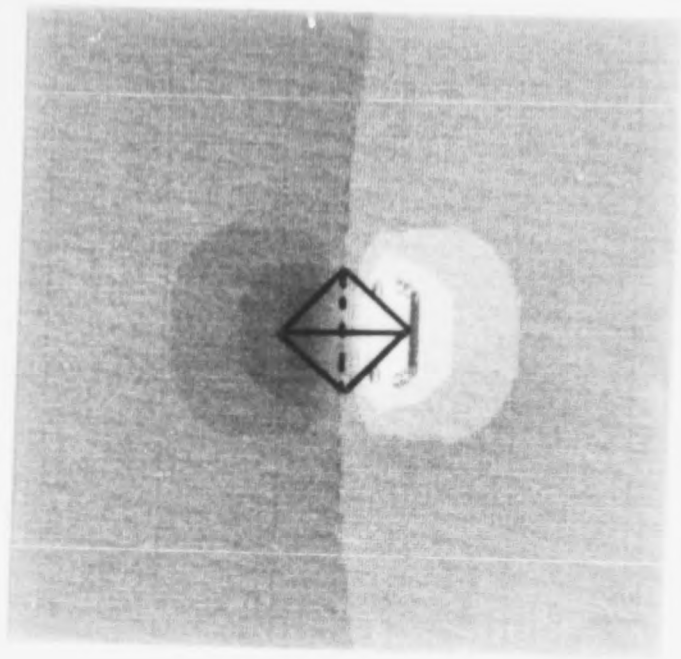
Experimental Images

Figure 8.5

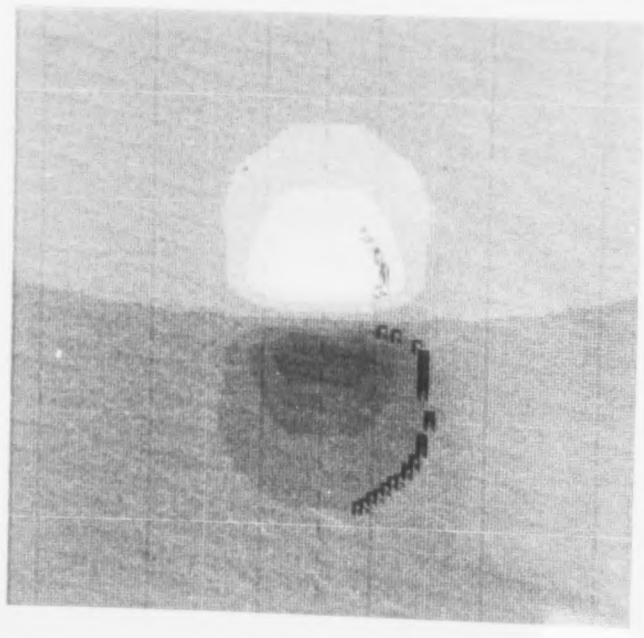
STACKING-FAULT TETRAHEDRON

$\underline{Z} = [100]$





$\underline{g} = (02\bar{2})$



$\underline{g} = (022)$

Chapter 9

PRESENT CONCLUSIONS AND REMAINING PROBLEMS

9.1 Summary of results of the thesis

(i) The discrepancy noted by Fukuhara (1966) between the dynamical diffraction theory of Sturkey and Bethe's eigenvalue approach is not due to numerical approximations made by Sturkey but is due to the fact that Sturkey's theory refers to positron diffraction (except for particle-anti-particle annihilation).

(ii) Weak-beam images of defects calculated from kinematical theory are shown to be in very good agreement with the images calculated from a many-beam dynamical theory if the kinematical theory intensities are reduced by the attenuation due to the mean absorption coefficient.

(iii) Yoffe's method of the construction of the displacement field due to a polygonal dislocation loop is shown to be a practical method for loops with arbitrary amounts of edge and shear components. An extension of the method has been used to find the displacement field due to a stacking-fault tetrahedron.

(iv) When the direction between $\underline{g}$ and $\underline{b}$ is not very large the image of an edge-on Frank loop in copper is characterised by a vector $\underline{\ell}$ having a direction between those of $\underline{g}$ and $\underline{b}$. When $\underline{g}\,\underline{b} = 0$ the "butterfly" image formed has a maximum intensity lower by a factor of about 1/5 than that of the above mentioned image type. These predictions agree with the experimental evidence found by Stathopoulos (private communication).

(v) As the diameter of an edge-on Frank loop is reduced the line of no-contrast becomes straighter in accordance with the predictions of a theory based on the kinematical scattering of

Bloch waves.

(vi) As the depth of an edge-on Frank loop is varied so as to approach the boundary between the layers L1 and L2, the strength of the black-white contrast and the size of the contrast figure are greatly reduced.

(vii) The computed images from perfect loops with shear components of Burgers vector give good agreement with the main features of calculations by Ohr (1973) and Haussermann et al (1972) which were based on different models of the displacement fields. Both the "weakly distorted" and "strongly distorted" images of Haussermann were found and compared well with the experimental images of English (private communication).

(viii) The images of both inclined Frank loops and stacking-fault tetrahedra at a [110] orientation are characterized by $\underline{\ell}$-vectors which remain nearly parallel to $\underline{g}$ as $\underline{g}$ is rotated in the image plane. At this orientation a tetrahedron observed in a (200) reflection has a line of no-contrast which is V-shaped and traces the projection of the tetrahedron on the image plane. These results are also in good agreement with the experimental results of Stathopoulos.

(ix) The images of tetrahedra and inclined Frank loops may be distinguished by their different symmetry properties when observed in two mutually perpendicular $\{220\}$ reflections at a $\langle 100 \rangle$ orientation.

(x) Vacancy and interstitial type tetrahedra may be distinguished, if their depths are known, by essentially the same methods as those used for vacancy and interstitial loops, since they also show similar depth reversals of the vector $\underline{1}$.

9.2 Suggestions for further work

All the computer simulated images displayed in this thesis were calculated for strong two-beam diffraction conditions. An obvious extension of the method is a study of the same defects under weak-beam conditions, perhaps using the modified kinematical theory of Chapter 3 to compute intensities. Since the contrast details under such conditions are likely to be much finer, it would be necessary to compute intensities at the bottom of a much more finely spaced grid of columns. This would require considerably more computer time or a faster computer. A modification of the interpolation routine would have to be employed. This would judiciously interpolate between computed picture points only if the spatial variation of intensity in that region was small. Otherwise the intermediate intensities would be calculated. Use of a plotter capable of producing a greater number of grey levels would also improve the quality of the images.

Another extension of the present work is the use of anisotropic elasticity theory to calculate the displacement fields. One of the methods described in Chapter 7 might be employed.

A practical problem from the nuclear energy industry is the preferential expansion of zirconium alloys along the c-axis of the hexagonal unit cell during irradiation. This is accompanied by a corresponding contraction in the basal plane such as to keep the volume of the material constant. There is speculation that this is due to the formation of interstial dislocation loops on the basal planes and vacancy loops in planes containing the c-axis.

The results of experimental electron microscope investigations in conjunction with the computer simulation techniques described in this thesis may provide a resolution of this question.

APPENDIX I

Derivation of the integral equation of scattering

In chapter 2, section 2.1 we were concerned with the problem of the scattering of an electron by an isolated atom. The incident wave-function ψ_0 satisfies euqation (2.2) and the total wave-function after scattering satisfies equation (2.1).

We define the scattered wave-function by $\psi_s(\underline{r}') = \psi(\underline{r}') - \psi_0(\underline{r}')$

Then subtraction (2.2) from (2.1) gives

$$(\nabla^2 + 4\pi^2\chi^2)\,\psi_s(\underline{r}') = -4\pi^2 u(\underline{r}')\,\psi(\underline{r}') \qquad (a)$$

Now consider the function $G(\underline{r}, \underline{r}')$ which satisfies the following equation

$$(\nabla^2 + 4\pi^2\chi^2)\,G(\underline{r}, \underline{r}') = -\delta(\underline{r} - \underline{r}') \qquad (b)$$

where the R.H.S. is a Dirac delta function.

$G(\underline{r}, \underline{r}')$ is known as the Green's function for the operator $(\nabla^2 + 4\pi^2\chi^2)$ and it can be shown that

$$G(\underline{r}, \underline{r}') = G(|\underline{r} - \underline{r}'|)$$

$$= \frac{\exp(2\pi i \chi |\underline{r} - \underline{r}'|)}{4\pi |\underline{r} - \underline{r}'|}$$

Forming $G \times (a.) - \psi_s \times (b.)$ and integrating over a volume bounded by a surface S, we have

$$\int [G(\underline{r}, \underline{r}')\nabla^2\psi_s(\underline{r}') - \psi_s(\underline{r}')\nabla^2 G(\underline{r}, \underline{r}')]\, d^3\underline{r}'$$

$$= -4\pi^2 \int u(\underline{r}')\,\psi(\underline{r}')\,G(\underline{r}, \underline{r}')\, d^3\underline{r}' + \int \delta(\underline{r} - \underline{r}')\,\psi_s(\underline{r}')\, d^3\underline{r}'$$

Now by Green's Theorem, L.H.S. is

$$\int [G(\underline{r},\underline{r}')\,\underline{\nabla}\,\psi_s(\underline{r}') - \psi_s(\underline{r}')\,\nabla G(\underline{r},\underline{r}')]\,d^3\underline{r}'$$

and if ψ_s is suitably behaved (i.e. vanishes sufficiently rapidly when S becomes large) then the surface integral $\rightarrow$ 0 as $S \rightarrow \infty$

$$\text{Now, } \int \delta(\underline{r}-\underline{r}')\,\psi_s(r')\,d^3\underline{r}' = \psi_s(\underline{r})$$

$$\therefore \quad \psi_s(\underline{r}) = 4\pi^2 \int u(\underline{r}')\,\psi(\underline{r}')\,G(\underline{r},\underline{r}')\,d^3\underline{r}'$$

$$\psi(\underline{r}) = \psi_0(\underline{r}) + 4\pi^2 \int u(\underline{r}')\,\psi(\underline{r}')\,G(\underline{r},\underline{r}')\,d^3\underline{r}'$$

This is the integral equation of scattering, quoted as equation (2.4) in Chapter 2.

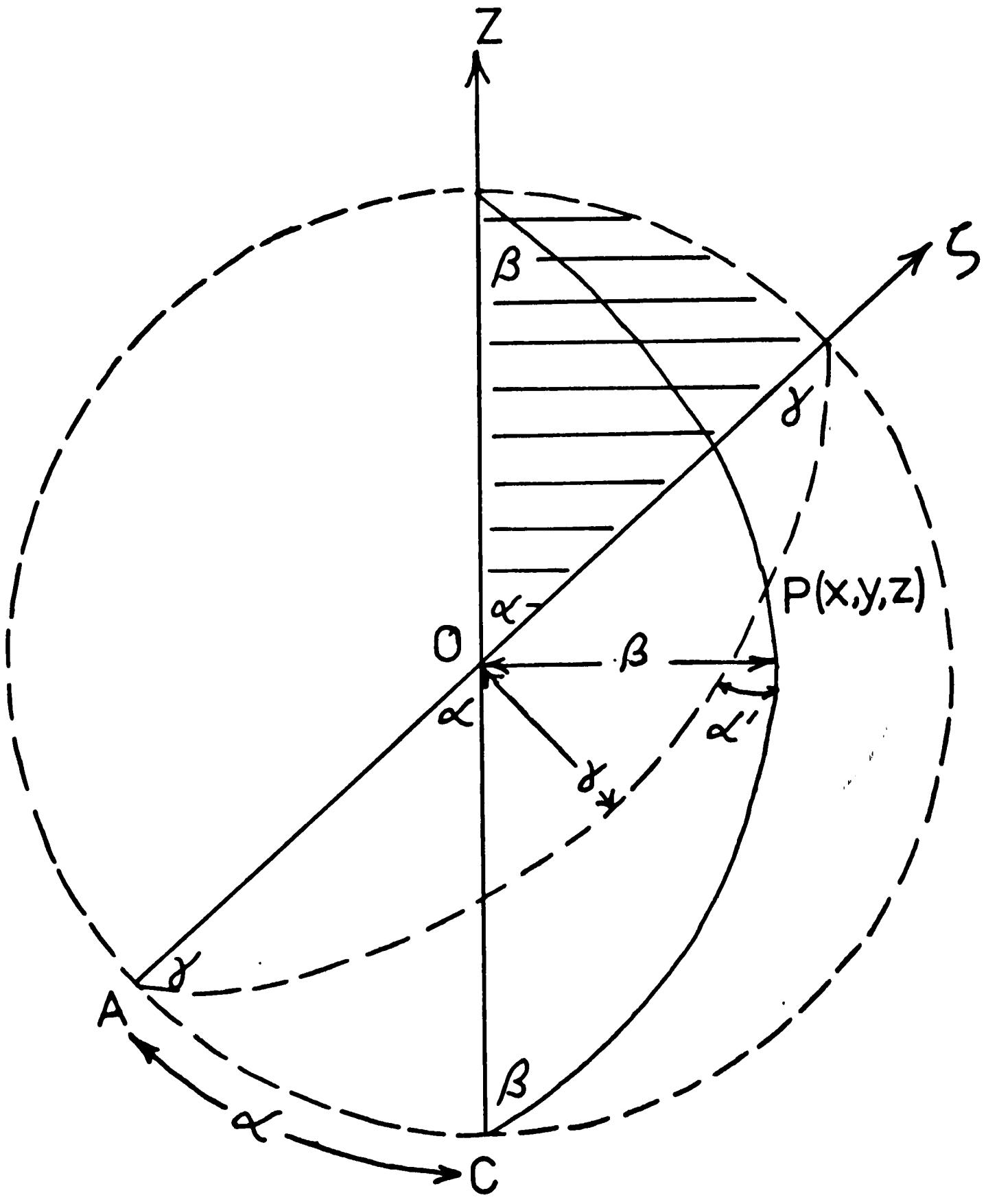


FIGURE A.2

Appendix II

Solid Angle subtended by an angular dislocation

Let Oz and $O\zeta$ define the positions of the arms of the angular dislocation. We require to know the solid angle subtended at P(x,y,z) by (shaded) area enclosed by the arms of the angular dislocation. This solid angle (ϕ) is clearly equal to that subtended at the centre of the sphere (i.e. at 0) by the spherical triangle APC. From spherical trigonometry,

$$\phi = \sum \text{corner angles of APC} - \pi$$

$$= (\pi/2 + \beta) + (\pi/2 - \gamma) + \alpha' - \pi$$

$$= \beta - \gamma + \alpha'$$

Also application of the cosine rule to APC gives,

$$\cos\alpha' = -\cos(\pi/2 + \beta)\cos(\pi/2 - \gamma) + \sin(\pi/2 + \beta)\sin(\pi/2 - \gamma)\cos\alpha$$

$$= \sin\beta\sin\gamma + \cos\beta\cos\gamma\cos\alpha$$

$$= \frac{y}{\sqrt{x^2+y^2}} \cdot \frac{\eta}{\sqrt{x^2+\eta^2}} + \frac{x}{\sqrt{x^2+y^2}} \cdot \frac{x}{\sqrt{x^2+\eta^2}} \cos\alpha$$

Hence, $$\tan^2\alpha' = \frac{(x^2+y^2)(x^2+\eta^2) - (y\eta + x^2\cos\alpha)^2}{(y\eta + x^2\cos\alpha)^2}$$

and substituting $$\eta = \cos\alpha - z\sin\alpha$$

we obtain, $$\tan\alpha' = \frac{xr\sin\alpha}{(y\eta + x^2\cos\alpha)}$$

Inspection of fig.A2 also shows that

$$\beta = \tan^{-1}\left(\frac{y}{x}\right) \quad , \quad \gamma = \tan^{-1}\left(\frac{\eta}{x}\right)$$

Hence $$\phi = \tan^{-1}\left(\frac{y}{x}\right) - \tan^{-1}\left(\frac{\eta}{x}\right) + \tan^{-1}\left(\frac{xr\sin\alpha}{y\eta + x^2\cos\alpha}\right)$$

which is equation 6.12(b) of chapter 6.

APPENDIX III

The matrix of the eigenvectors C for different types of fundamental matrix A

Consider the eigenvalue equation

$$\underline{\underline{A}}\ \underline{\underline{C}} = \underline{\underline{C}}\left[\gamma^{(i)}\right]_D$$

Hence

$$\underline{\underline{C}}^{-1}\underline{\underline{A}}\ \underline{\underline{C}} = \left[\gamma^{(i)}\right]_D \qquad (1)$$

We examine two cases:

(i) $\underline{\underline{A}} = \underline{\underline{A}}^T$ (symmetric matrix, real or complex)

(ii) $\underline{\underline{A}} = (\underline{\underline{A}}^*)^T$ (Hermitian matrix)

Case (i)

Taking the transpose of equation (1) we have,

$$\underline{\underline{C}}^T\ \underline{\underline{A}}^T\ (\underline{\underline{C}}^{-1})^T = \left[\gamma^{(i)}\right]_D$$

and using condition (i) we obtain

$$\underline{\underline{C}}^T\ \underline{\underline{A}}\ (\underline{\underline{C}}^{-1})^T = \left[\gamma^{(i)}\right]_D$$

This will clearly be consistent with (1) if,

$$\underline{\underline{C}}^{-1} = \underline{\underline{C}}^T$$

That is, the matrix of the eigenvectors of $\underline{\underline{A}}$ is orthogonal.

Case (ii)

Taking the complex conjugate of equation (1), we have

$$(\underline{\underline{C}}^{-1})^*\ \underline{\underline{A}}^*\ \underline{\underline{C}}^* = \left[\gamma^{(i)}\right]_D \qquad (2)$$

(since the eigenvalues of a Hermitain matrix are real). Taking the transpose of equation (2),

$$(\underline{\underline{C}}^*)^T (\underline{\underline{A}}^*)^T \{(\underline{\underline{C}}^{-1})^*\}^T = [\gamma^{(i)}]_D$$

and using condition (ii)

$$(\underline{\underline{C}}^*)^T \underline{\underline{A}} \{(\underline{\underline{C}}^{-1})^*\}^T = [\gamma^{(i)}]_D$$

This will be consistent with (1) if,

$$\underline{\underline{C}}^{-1} = (\underline{\underline{C}}^*)^T$$

That is, the matrix of the eigenvectors of $\underline{\underline{A}}$ is unitary.

N.B. Strictly speaking, these conditions on the matrix $\underline{\underline{C}}$ are only demanded in the case where all the eigenvalues are distinct. If some of the eigenvalues are degenerate however, a suitable linear combination of the degenerate eigenvectors may be chosen in order to satisfy these relations.

REFERENCES

Abramowitz M. & Stegun I.A. (1965)
Handbook of Mathematical Functions, Dover.

Ashby M.F. & Brown L.M. (1963a, b)
Phil.Mag., 8, 1038,1649

Bacon D.J. & Groves P.P. (1970)
Fundamental Aspects of Dislocation Theory.
Ed.Simmons J.A., de Wit R., & Bullough R.
Washington Nat.Bureau of Standards, p.35.

Bauerle J.E. & Koehler J.S. (1957)
Phys.Rev., 107, 1493.

Bethe H.A. (1928)
Ann.Phys.Lpz, 87, 55.

Boersch H. (1942)
Z.Phys., 118, 706.

Boersch, H. (1943)
Z.Phys., 121, 746.

Boersch, H. (1944)
Kolloid Z., 106, 169.

Borrmann, G (1941)
Z.Phys., 42, 157.

Borrmann, G. (1950)
Z.Phys., 127, 297.

Brimhall, J.L.(1971)
Workshop Conf. on Microscopy of Cluster Nuclei in
Defected Crystals, Chalk River, Canada (CNRL-622-1)

Brinkman J.A. (1954)
J.Appl.Phys., 25, 961

Brown, L.M. (1964)
Symposium on Electron Microscopy, Modena Ed.
Paolo Buffa, CNR, Rome.

Brown, L.M. (1967)
Phil.Mag., 15, 363.

Bullough, R., Maher, D.M., & Perrin, R.C. (1970)
UKAEA Research Group Report AERE R 6348

Bullough R. and Newman R.C. (1960)
Phil.Mag., 5, 921.

Chik, K.P. (1966)
Phys.Stat.Sol., 16, 685.

Chik, K.P., Wilkens M. and Ruhle M. (1967)
Phys.Stat.Sol., 23, 113

Cockayne, D.J.H. (1972)
Z.Naturf., 274, 452

Cockayne D.J.H., Jenkins M.L. and Ray I.L.F. (1971)
Phil.Mag., 24, 1383.

Cockayne D.J.H., Ray I.L.F. and Whelan M.J. (1968)
Proc. 4th Eur.Reg.Conf. on Electron Microscopy,
Rome, p.129.

Cockayne, D.J.H., Ray I.L.F. and Whelan M.J. (1969)
Phil.Mag., 20, 1265

Cowley, J.M. and Moodie A.F. (1957)
Acta Cryst., 10, 609.

Darwin, C.G. (1914a,b)
Phil.Mag., 27, 315, 675.

Darwin, C.G. (1922)
Phil.Mag., 43, 800.

De Ridder R. and Amelinckx S. (1971)
Phys.Stat.Sol.(b), 43, 541.

Eason, G., Noble, B. and Sneddon I.N. (1959)
Phil.Trans.Roy.Soc., A247, 529.

Eshelby, J.D. (1957)
Proc.Roy.Soc., A241, 376.

Essmann U. and Wilkens M. (1964)
Phys.Stat.Sol., 4, K53.

Ewald P.P. (1916 a, b, 1917)
Ann.Phys., 46, 117; 49, 1; 54, 519.

Ewald P.P. (1920, 1924)
Z.Phys., 2, .232; 30, 1

Ewald, P.P. (1925)
Physik Zeitsch., 26, 29

Eyre, B.L., Maher, D.M. and Bartlett (1971)
Phil.Mag., 23, 409.

Eyre, B.L., Maher, D.M. and Perrin R.C. (1974)
Proc. 8th Int.Cong. on Electron Microscopy.
Canberra, Australia, p.436.

Fujimoto, F. (1959)
J.Phys.Soc. Jap., 14, 1558.

Fujiwara K. (1959)
J.Phys.Soc.Jap., 14, 1513.

Fukuhara A. (1965)
Proc.Phys.Soc., 86, 1031.

Fukuhara A. (1966)
J.Phys.Soc. Jap., 21, No.12, 2645.

Gevers, R. (1962)
Phil.Mag., 7, 59.

Gill, S. (1951)
Proc. Camb.Phil.Soc., 47, 96.

Goodman, P. and Moodie A.F. (1974)
Acta Cryst., A30, 280.

Gray, A (1919)
Phil.Mag., 38, 201.

Hashimoto H., Howie A. and Whelan M.J. (1962)
Proc.Roy.Soc., A269, 80.

Haussermann F (1972 a,b,c)
Phil.Mag., 25, 537, 561, 583.

Haussermann F., Ruhle M. and Wilkens M. (1972)
Phys. Stat.Sol. (b), 50, 445.

Head, A.K., Humble, P., Clarebrough L.M., Morton, A.J. and Forwood C.T. (1973) Defects in Crystalline Solids, Vol.7, North-Holland Publishing Company, Amsterdam.

Heidenreich R.D. (1949)
J.Appl.Phys., 20, 993

Heidenreich R.D. and Sturkey L. (1945)
J.Appl.Phys., 16, 97.

Hillier, J. and Baker R.F. (1942)
Phys.Rev., 61, 722.

Hirsch, P.B. (1966)
Unpublished lecture to Harwell Symposium on "Nature of Small Defect Clusters".

Hirsch, P.B., Howie A., Nicholson R.B., Pashley D.W. and Whelan M.J. (1965) Electron Microscopy of Thin Crystals, Butterworths.

Hirsch, P.B., Howie A. and Whelan M.J. (1960) Phil.Trans.Roy.Soc., 252, 499.

Hirsch P.B., Silcox J., Smallman R.E. and Westmacott K.H. (1958) Phil.Mag., 3, 897.

Hirth J.P. and Lothe J. (1968) Theory of Dislocations, McGraw-Hill, New York.

Hokanson J.L. (1963) J.Appl.Phys., 34, No.8, 2337.

Honjo, G. (1953) J.Phys.Soc.Jap., 8, 776.

Honjo, G. and Mihama, K. (1954) J.Phys.Soc.Jap., 9, 184.

Howie, A. (1963) Proc.Roy.Soc., A271, 268.

Howie, A. and Bazinski Z.S. (1968) Phil.Mag., 17, 1039.

Howie A. and Whelan M.J. (1961, 1962) Proc.Roy.Soc., A263, 217; A267, 206.

Humphreys C.J. and Hirsch P.B. (1968) Phil. Mag., 18, 115

Indenbom, V.L. and Orlov, S.S. (1967) Zh.éksp.teor.Fiz., Pis'ma, 6, 826.

Jenkins, M.L. (1972) Phil.Mag., 26, 747.

Jenkins, M.L. (1973) D.Phil. Thesis, Oxford.

Jenkins M.L., Cockayne D.J.H. and Whelan M.J. (1973) J.Microsc., 98, pt.2, 155.

Kinchin G.H. and Pease R.S. (1955) Rep.Prog.Phys., 18, 1

Kroupa F. (1960) Czech.J.Phys., B10, 284.

Kroupa F. (1963) Czech.J.Phys., A13, 301.

Loretto M.H., Clarebrough L.M. and Segall R.L. (1963) Phil.Mag., 11, 459.

Lothe J. (1967)
Phil.Mag., 15, 353

Love A.E.H. (1927)
Mathematical Theory of Elasticity, C.U.P., p.185.

Mader, S. and Simsch E. (1960)
Proc.Eur.Reg.Conf. on Electron Microscopy, Delft, p.379.

Maher, D.M. and Eyre, B.L. (1971)
Phil.Mag., 23, 409.

Maher, D.M., Perrin, R.C. and Bullough R. (1971)
Phys.Stat.Sol. (b), 43, 707.

Makin M.J. and Manthorpe (1963)
Phil.Mag., 8, 1725.

Makin M.J., Whapman A.D. and Minter F.J. (1961, 1962)
Phil.Mag., 6, 465; 7, 285.

MacGillarry C.H. (1940)
Physica, 7, 329.

McIntyre K.G. (1967)
Ph.D.Thesis, Cambridge.

McIntyre K.G. and Brown (1966a,b)
(a) J.Phys.Rad., 27, C3-178.
(b) Symposium on Nature of Small Defects, Harwell
AERE Report R5269, p.351.

Merson R.H. (1957)
Conf.Data Processing and Automatic Computing Machines
(W.R.E., Salisbury, Australia).

Metherell, A.J.F. and Fisher, R.M. (1969)
Phys.Stat.Sol., 32, 551.

Moliére K. (1939)
Ann. Phys. Lpz., 34, 461.

Mott, N.F. and Massey H.S.W. (1949)
Theory of Atomic Collisions, O.U.P.

Ohr, S.M. (1972)
J.App.Phys. , 43, 1361.

Ohr, S.M. (1973)
Proc.Int.Conf. on Defects and Defect Clusters in
B.C.C. Metals and their Alloys, Ed.Arsenault, R.J.;
Nat.Bureau of Standards, Gaithersburg, Maryland, U.S.A.
p.62.

Ohr S.M. (1974)
Phys.Stat.Sol. (b), 64, 317

Pashley D.W. and Presland A.E.B. (1961)
Phil.Mag.,6, 1003.

Phillips V.A. and Livingston J.D. (1962)
Phil.Mag.,7, 969.

Ray, I.L.F. and Cockayne D.J.H. (1971)
Proc.Roy.Soc.,A325, 543.

Ray, I.L.F. and Cockayne, D.J.H. (1973)
J.Microsc.,98, 170.

Ruhle, M. (1967a,b)
Phys.Stat.Sol. 19, 263, 279.

Ruhle, M. (1969)
Proc.Symposium on Rad.Dam. in Reactor Materials,
Vienna, Vol.I, p.113.

Ruhle M., Wilkens M. and Essmann U. (1965)
Phys.Stat.Sol., 11,819.

Schrodinger E. (1926)
Ann.Phys.,79, 361.

Silcox, J. and Hirsch P.B. (1959)
Phil.Mag., 4, 72.

Smallman, R.E., Westmacott, K.H. and Coiley, J.A. (1959)
J.Inst.Met., 88, 127.

Smith G.H. and Burge R.E. (1962)
Acta Cryst.,15, 182.

Sneddon J.N. (1951)
Fourier Transforms, McGraw-Hill, New York.

Stobbs W.M. and Sworn C.H. (1971)
Phil.Mag., 24, 1365.

Sturkey, L. (1962)
Proc. Phys. Soc., 80, 321.

Thompson M.W. (1969)
Defects and Radiation Damage in Metals, C.U.P.

Thompson, N. (1953)
Proc. Phys.Soc., 66B, 481.

Tournarie M. (1962)
J.Phys.Soc.Jap., 17, Suppl. BII, p.98.

Valentine R.C. (1966)
Adv. in optical and electron microscopy Vol. I
p.180, Academic Press, London and New York.

von Laue M. (1946)
Acta Cryst., 2, 106.

Watson G.N. (1922)
Theory of Bessel Functions, C.U.P.

Whelan M.J. and Hirsch P.B. (1957a, b)
Phil.Mag., 2, 1121, 1303.

Wilkens M. (1964a,b)
Phys.Stat.Sol., 5, 175; 6, 939.

Wilkens M. (1966)
Phys.Stat.Sol., 13, 529.

Wilkens M. (1970)
Modern Diffraction and Imaging Techniques in Materials
Science, Ed.Amelincks S.et al., North-Holland.

Wilkens, M. (1970)
Vacancies and Interstitials in Metals, Ed.Seeger et al.
North-Holland, p.485.

Wilkens, M., Katerbau K.-H and Ruhle M. (1973)
Z.Naturf., 28a, No.5, 681.

Wilkens, M. and Ruhle M. (1966)
Proc.6th Int.Cong. on Electron Microscopy, Kyoto,
Vol. I, p.77.

Wilkens, M. and Ruhle M. (1972)
Phys.Stat.Sol.(b), 49, 749.

Wilkens M., Ruhle, M. and Haussermann F. (1967)
Phys. Stat.Sol., 22, 689.

Wilkens, M., Ruhle M. and Hausserman F. (1971)
Proc. of Workshop Conference on Microscopy of
Cluster Nuclei in Defected Crystals, CRNL-622-1,
Chalk River, Canada.

Willis J. (1970)
Phil.Mag., 21, 931.

Wilson, M.M. (1970)
D.Phil.thesis, Oxford.

Yoffe, Elizabeth H. (1960)
Phil.Mag., 5, 161.

Yoshioka H. (1957)
J.Phys. Soc. Jap., 12, 618.